PERIODIC FLOW HYDRODYNAMIC RESISTANCE PARAMETERS FOR VARIOUS REGENERATOR FILLER MATERIALS AT CRYOGENIC TEMPERATURES

A Dissertation
Presented to
The Academic Faculty

by

Matthew D. Perrella

In Partial Fulfillment
of the Requirements for the Degree
Doctor of Philosophy in the
School of Mechanical Engineering

Georgia Institute of Technology

December 2017

PERIODIC FLOW HYDRODYNAMIC RESISTANCE PARAMETERS FOR VARIOUS REGENERATOR FILLER MATERIALS AT CRYOGENIC TEMPERATURES

Approved by:

Dr. Mostafa Ghiaasiaan, Advisor
School of Mechanical Engineering
Georgia Institute of Technology

Dr. Devesh Ranjan
School of Mechanical Engineering
Georgia Institute of Technology

Dr. Zhuomin Zhang
School of Mechanical Engineering
Georgia Institute of Technology

Dr. Mitchell Walker II
School of Aerospace Engineering
Georgia Institute of Technology

Dr. Ali Kashani
Research and Development
Atlas Scientific

Date Approved: August 23, 2017

To my parents, Guy and JoAnn Perrella

ACKNOWLEDGEMENTS

I would like to thank my advisor, Dr. Mostafa Ghiaasiaan for his outstanding guidance and support through the course of my work at Georgia Tech. I am very grateful to have been a part of the GT Cryolab, and without his wisdom and experience none of my work would have been possible. I would also like to thank the other members of the GT Cryolab, both current and former. To my lab mates, Veera Manek, Michael Baldwin, and Tao Fang I would like to express my thanks for the comradery, insight, and assistance they have provided to me over the years. I would also like to especially thank past members of the GT Cryolab who offered tremendous help in the conduction of this research. Specifically I would like to thank Dr. Tom Mulcahey and Dr. Ted Conrad for their hours of guidance and assistance via telephone in how to conduct the experiments and design the simulations needed for this work. I would like to thank Dr. Mihir Pathak, Mallik Ahmed, Gilbran Alvarez, and the members of the Madison Cryogroup for their contributions to the NASA Early Stage Innovations project and separate effects testing of the $Er_{0.5}Pr_{0.5}$ regenerator. I would also be remiss for neglecting to mention my numerous other friends and colleagues at Georgia Tech who provided additional assistance and made my time here a truly enjoyable experience. Lastly, I would like to thank my family for their continual love and support especially my parents, Guy and JoAnn Perrella for their advice and encouragement and my wife, Nella, for her unyielding patience and inspiration.

TABLE OF CONTENTS

LIST OF TABLES

LIST OF FIGURES

NOMENCLATURE

Variables

A_f	Regenerator flow area [m^2]
A_c	Regenerator cross-sectional area [m^2]
C_2	Fluent inertial resistance [1/m]
c_3	Sage leading coefficient of $1/\mathrm{Re}_{d_h}$ term
c_f	Forchheimer inertial coefficient [-]
c_P	Constant-pressure specific heat [J/K]
c_v	Constant-volume specific heat [J/K]
d_h	Hydraulic diameter [m]
d_s	Sphere diameter [m]
d_w	Wire diameter [m]
E	Extensive energy [J]
F	Sage total frictional pressure gradient [Pa/m]
f	Sage/ Darcy dimensionless friction factor [-]
f	Frequency [Hz]
g	Gravitational acceleration [m/s^2]
h	Enthalpy [J/kg]
K	Darcy permeability [m^2]
K	Sage local loss coefficient [-]
k_c	Coverage factor [-]

L	Length of porous medium [m]
$\dot{m}$	Mass flow rate [kg/s]
$\dot{m}_{\text{peak}}$	Peak mass flow rate [kg/s]
N	Number of samples
P	Pressure [Pa]
$\dot{Q}$	Heat transfer rate [W]
R_{He}	Ideal gas constant for helium [J/(kg K)]
Re_{d_h}	Hydraulic diameter-based Reynolds number [-]
$\text{Re}_{\sqrt{K}}$	Pore-based Reynolds number [-]
S_i	Fluent momentum source term [Pa/m]
S_x	Wetted perimeter of porous medium [m]
s	Entropy [J/K]
T	Temperature [K]
t	Time [s]
U_A	Random uncertainty/ resolution
U_B	Bias uncertainty/ accuracy
U_C	Combined uncertainty
u	Axial velocity [m/s]
u_D	Darcian velocity in axial direction [m/s]
u_s	Superficial velocity in axial direction [m/s]
u_{peak}	Peak velocity in axial direction [m/s]
V	Volume [m^3]

v	Specific volume [m^3/kg]
$\dot{W}$	Power [W]
x	Axial coordinate

Symbols

A	Leading coefficient of Re_{d_h} term [-]
B	Leading coefficient of $\mathrm{Re}_{d_h}^2$ term [-]
Γ	Non-dimensionalized momentum source term [-]
ΔP	Instantaneous pressure drop across regenerator [Pa]
ΔP_{peak}	Peak instantaneous pressure drop across regenerator [Pa]
α	Fluent permeability [m^2]
β	Fluent viscous resistance $(1/\alpha)$ [1/m^2]
ε	Porosity of porous medium
ϕ	Phase angle [rad]
γ	Ideal gas specific heat ratio
ρ	Density [kg/m^3]
$\langle\ \rangle$	Volume averaged quantity
$\vec{}$	Vector
$\overline{=}$	Tensor

Notations

1D	One dimensional/ unidirectional
2D	Two dimensional/ axisymmetric
3D	Three dimensional
$_{0.5}$	50%
#400	Four hundred meshes per square inch
#325	Three hundred and twenty-five meshes per square inch
BPTC	Basic Pulse Tube Cooler
$_{C}$	Cold
CHX	Cold Heat Exchanger
CFD	Computational Fluid Dynamics
Cu	Copper
ErPr	Erbium Praseodymium
Exp	Experimental
FFT	Fast Fourier Transform
GUI	Graphical User Interface
$_{H}$	Hot
$_{in}$	Inlet
ITPTC	Inertance Tube Pulse Tube Cooler
JT	Joule-Thomson Cooler
NIST	National Institute of Science and Technology
$_{out}$	Outlet

P_1	Upstream pressure
P_2	Downstream pressure
PTC	Pulse Tube Cooler
PWG	Pressure Wave Generator
Regen	Regenerator
Sim	Simulation
SS	Stainless Steel
SSD	Sample Standard Deviation
SV	Surge Volume
WHX	Warm Heat Exchanger

SUMMARY

The regenerator is a critical component of all Stirling and Pulse Tube cryocoolers. It generally consists of a microporous metallic or rare-earth filler material contained within a cylindrical shell, which exchanges heat with an oscillating flow of high-pressure gas. The accurate modeling of the hydrodynamic and thermal behavior of different regenerator materials is crucial to the successful design and optimization of Stirling and Pulse Tube cryocoolers. Previous investigations have used experimental measurements at steady and periodic flow conditions in conjunction with pore-level CFD analysis to determine the pertinent hydrodynamic resistance parameters for the porous medium, namely the Darcy permeability and Forchheimer coefficients. Due to the difficulty associated with experimental measurements at cryogenic temperatures, most of the past investigations were performed at ambient temperature conditions. These results are assumed to be accurate for cryogenic temperatures since, for fully-developed flow, the Darcy permeability and Forchheimer coefficient should depend only on the geometry of the porous medium and temperature-independent flow characteristics such as the Reynolds number. There is, however, a pressing need to determine these so-called hydrodynamic resistance parameters for several regenerator filler materials under prototypical conditions and verify the validity of the foregoing assumption.

The objective of this investigation is to examine the effect of cryogenic temperatures on the hydrodynamic resistance parameters of microporous structures that are commonly used as cryocooler regenerator fillers. Regenerators filled with several commonly-applied regenerator filler materials including spherical $Er_{0.5}Pr_{0.5}$ powder,

#400SS wire mesh, and #325SS wire mesh are studied under periodic helium flow at cryogenic temperatures for a range of frequencies and mean operating pressures. The instantaneous pressure oscillations upstream and downstream of each regenerator as well as the instantaneous mass flow rates downstream are analyzed using a Fast Fourier Transform, and the experimental results are analyzed using a combined experimental and CFD-assisted methodology. First, the dimensionless Darcy friction factor, f, is calculated based on the maximum instantaneous pressure drop across each regenerator. These results are correlated with respect to the hydraulic diameter-based Reynolds number, and for each filler material the friction factor is shown to be independent of mean operating pressure, frequency, and temperature. Correlations for friction factor are developed based on the least-squares method and presented for all regenerator filler materials across the entire experimental range. Sage, an industry standard, one-dimensional cryocooler optimization software, is then used to simulate the entire test section and flow through the regenerator filler materials to validate the values for Darcy friction factor determined from experimental measurements. Sage's built in optimization tool is used to match the oscillating pressure boundary conditions across each regenerator with the experimental results, and the Darcy friction factor values obtained from simulation are compared to those calculated from the experimental pressure drop measurements and are shown to be in good agreement. The experimental and simulation results are then compared to previous correlations for Darcy friction factor that were developed at ambient temperature conditions for all three regenerator filler materials and shown to be in good agreement.

The experimental and simulation results are next used to calculate values for the momentum source term, S_i, which represents the total frictional pressure gradient through the porous media and is comprised of the viscous and inertial resistance terms for the medium. The momentum source term is non-dimensionalized based on the hydraulic diameter of the porous filler material and the properties of the working fluid, i.e., high-pressure helium. The non-dimensionalized momentum source term is correlated as a function of the hydraulic diameter-based Reynolds number with a second order polynomial. The resulting model is then used to calculate the viscous and inertial resistance coefficients, which are shown to be independent of pressure, frequency, and temperature. In order to confirm the validity of the viscous and inertial resistance coefficients, a two-dimensional axisymmetric CFD model is then created using the ANSYS Fluent code to simulate the periodic flow of helium through the porous media and compare the simulation results with experimental measurements for each regenerator. Other aspects of the CFD analysis including the appropriateness of the selected boundary conditions and multi-direction flow effects are accounted for. By comparing the momentum source term to the standard Forchheimer-Darcy law for flow through porous media, values for the popular Darcy permeability, K, and Forchheimer inertial coefficient, c_f, which are common in the literature, are determined for the entire range of mean operating pressures and temperatures under consideration and also shown to be independent of temperature.

To demonstrate the importance of regenerator hydrodynamic resistance on overall cryocooler performance, a case study is shown for the design and optimization of a 20W at 20K, two-stage pulse tube cryocooler. The design process consisted of multiple

iterations whereby the individual components of the cooler such as the regenerators, heat exchangers, and inertance networks were systematically optimized using industry-standard tools including Regen 3.3 and ISOHX software from NIST, and the one-dimensional Sage cryocooler modeling software. The 20W at 20K cooler design is also simulated three-dimensionally using ANSYS Fluent CFD software to detect the presence of undesirable secondary flow effects, specifically streaming and jetting through the pulse tube. The friction factor developed through the testing of the $Er_{0.5}Pr_{0.5}$ regenerator is utilized in the simulation of the 20W at 20K cooler and the influence of the regenerator hydrodynamic resistance on the overall cooler performance is examined.

CHAPTER 1. INTRODUCTION

1.1 Definition of Cryogenics

Cryogenics refers to the application of science and engineering at extremely low temperatures. Generally, anything operating at or below 123 K is considered to be within the realm of cryogenics. Within this region, many common gasses such as methane, oxygen, nitrogen, hydrogen and helium exist as liquids. In order to reach and maintain these extremely low temperatures a special class of refrigerators known as cryocoolers is used. Conventional refrigeration systems which pump a liquid refrigerant in a closed loop are not suitable for cryogenic applications because the refrigerant would naturally freeze. Replacing the liquid refrigerant with a gaseous working fluid presents its own challenges in terms of pumping power requirements and the heat transfer capabilities of the gas. Every aspect of the cooler from the pumping mechanism to the heat exchangers must be carefully designed to address these challenges. Cryocoolers can be divided into two classes: recuperative, or steady flow, cryocoolers and regenerative, or oscillating flow, coolers. Recuperative cryocoolers are thus named due to the distinctive counter-flow heat exchanger which is crucial to their operation. These coolers may use pure or mixed gases as their working fluid and include Joule-Thomson, Brayton, and Claude style cryocoolers. Regenerative coolers such as Stirling, Pulse-Tube, and Gifford-McMahon styles, operate by cyclically compressing and expanding a gaseous working fluid, usually helium, along a series of tubes, orifices, and heat exchangers. The namesake of the regenerative cryocooler and its most crucial components is the regenerator. The regenerator acts as a sort of precooler for the working fluid and is

located between the warm and cold ends of the cooler. The physical design of the regenerator and heat exchangers including the aspect ratios, volumes, and pore structure must be carefully tuned to produce the desired cooling effect. Regenerative coolers are more complex, but they generally offer improved performance and efficiency compared to the recuperative class of coolers. Within the realm of regenerative cryocoolers, Stirling and Pulse-Tube styles are of particular interest. Stirling cryocoolers operate based on an approximation of the Stirling cycle for engines and heat pumps. They possess a set of opposed pistons which operate 90 degrees out of phase in order to induce the correct mass flow to pressure phase relationship within the working fluid to create the desired cooling effect. Pulse Tube coolers operate on a similar principle except that the cold end compressor is replaced with a hydrodynamic piston which consists of a Pulse Tube, Heat Exchanger, Inertance Tube and Surge Volume. This allows Pulse Tube coolers to maintain higher reliability and longer operating life at the expense of cycle efficiency. Each class and style of cryocooler has a particular realm of applicability based on its input power requirements, cooling duty, and physical robustness. Cryocoolers may operate at temperatures as low as 5K up to 100K and can produce cooling powers anywhere from the milliwatt to megawatt scale.

1.2 Applications of Cryogenics

Cryocoolers and cryogenic refrigeration in general are often considered to be enabling technologies because, while they are not a purely scientific pursuit in and of themselves, they allow for technological and scientific advances in many other areas. One of the earliest applications of cryogenics, and one that is still prevalent to this day is the preservation of food, biological materials, and even human tissue. The benefit of

preserving food with refrigeration may be well known today, but in the early 1900s the advent of flash freezing fruits and vegetables allowed greater access to these vitamin-rich foods to greater proportions of the population at lower prices than ever before, improving the quality of life for countless people. Cryogenic temperatures are also used to preserve biological samples such as viruses, bacteria, and cells which enable advances in medical and biological technology. More recently, cryopreservation of human cells and tissue has become a subject of intense interest. Once considered the realm of science fiction, the preservation of human sperm, eggs, and even stem cells using cryogenic temperatures is now common place. This enables advanced treatments in areas as diverse as fertility, nerve damage, and even rare cancers and genetic disorders. Contrary to popular belief, the ability to preserve an intact human body through cryogenic freezing is still far off, but incredible advancements have been made in the area of organ cryopreservation which could drastically extend the shelf life of donated organs such as livers, kidneys, and hearts and thereby dramatically increase the number of potential transplant recipients. In addition to preserving human tissues, cryogenics can also be used to destroy targeted cells within the body with minimal damage to the human subject. This technique has already gained widespread success in applications such as cardiovascular ablation and chronic bronchitis therapy.

Another indispensable use of cryogenic technology is the densification and liquefaction of various gases. Liquid nitrogen can now be produced in bulk to provide cryogenic cooling for various scientific and industrial applications. Liquefaction processes have also been successfully applied to natural gas thereby increasing the energy density of this clean-burning fuel to make its shipping and transportation costs

competitive with less environmentally friendly options such as petroleum. Perhaps even more consequentially, in the 1950s cryogenics was instrumental in the development of the fusion bomb by providing the massive amounts of liquid hydrogen needed to fuel the weapons. The technological means to liquefy hydrogen was once a closely-guarded secret because it allowed countries to develop weapons with hundreds of times the destructive power of the original fission bombs used in World War II. Liquid hydrogen is still widely used as the primary fuel source for space rockets and satellites due to its extremely high energy density. Further advancements in hydrogen production and liquefaction could also contribute to the rise of a hydrogen-based transportation sector in the future. Cryogenic engineering is also found at the cutting edge of electrical engineering and computer science. Cryogenic temperatures are necessary to operate superconducting electronics and electromagnets, magnetic resonance imaging (MRI), magnetic levitation, and superconducting motors. Cryogenics is also a crucial factor in the study and development of quantum theory and quantum computing.

Cryocoolers are perhaps most prevalent in the aerospace and defense industries were they are used extensively for thermal imaging and infrared-sensing technologies. Coolers in this class are frequently referred to as tactical cryocoolers. Similar to a visible light camera, infrared sensors can be washed-out or over-exposed by too much radiation entering the aperture. In order to prevent this phenomenon, the entire housing of the infrared detector must be cooled to cryogenic temperatures. Larger sensors will necessarily require larger housings which possess a greater thermal mass and require more powerful cooling. Similar detectors are also used to generate thermal images of Earth's land masses and oceans and can even take images of deep space. Space

cryocoolers use the same basic operating principles as their tactical counterparts, but must be far more robust in order to provide the longer life expectancies required for space equipment.

1.3 Grand Challenges

In order to support advancements in these diverse areas, cryocooler technology must continue to improve. As with many areas of engineering, crucial advancements in cryogenics will not depend on a single drastic breakthrough, but on steady, incremental improvements to existing technology over time. As coolers become smaller, cheaper, and more powerful they will enable innovations that were previously thought to be impossible. Several of the most enticing applications of cryogenic technology including superconducting electronics, quantum computing, and tissue preservation are already possible on a small scale but will require additional advancements in cryocooler capability in order to make their implementation a reality. The grand challenges of cryocooler engineering moving forward are the miniaturization of the coolers themselves, and the design of high-capacity coolers. Both of these objectives present their own unique challenges in terms of cooler design and optimization.

The miniaturization of cryocoolers is beneficial in many areas and especially for tactical applications. An increase in operating temperature for infrared detectors in recent years has allowed engineers to decrease the total physical footprint of the infrared detector system including the integrated cryocooler. However, as a cryocooler is miniaturized its performance tends to suffer due to the increased boundary layer and dead volume loses relative to the cooler's size [1,2]. The decreased size also exacerbates

losses through the regenerator due to the increased thermal gradient and can greatly complicate the manufacturing process. On the other end of the spectrum, the design of high-capacity cryocoolers offers challenges of its own. In general, the easiest way to increase the cooling capacity of a Stirling or Pulse Tube cryocooler is to increase the total size of the components. This implies increasing the diameter as well as the length while maintaining approximately the same aspect ratios. Although this approach may seem straight-forward, simply increasing the size of the cryocooler components leads to additional losses and three-dimensional effects that are not well understood. Within non-porous components, such as the Pulse Tube of a Pulse Tube cryocooler, increasing the diameter will enable circulation within the pulse tube due to buoyancy forces acting on working fluid [3]. This circulation can drastically reduce the performance of a pulse tube cooler by establishing a heat transfer mechanism between the warm and cold heat exchangers effectively short-circuiting the cooler operation. This phenomenon is mostly an issue when the cooler operates at an orientation other than perfectly vertical, which is necessary in many industrial applications [3]. Ideally, Stirling and Pulse Tube coolers would operate one-dimensionally along their axis with fluid properties such as velocity, pressure, and temperature being uniform across the cross section. In practice, however, sharp edges, orifices, and step changes in flow area can all lead to secondary, three dimensional flow effects which may be detrimental to the cooler performance. One particularly troublesome issue is streaming, where flow exiting one component of the cooler is concentrated into a high velocity stream by a flow restriction such as a sharp edge which allows hot gas to penetrate into a cold zone killing the cooler.

Whether one is designing miniaturized or high-capacity cryocoolers the hydrodynamic behavior within the porous components such as the heat exchangers and regenerators plays an important role. Proper characterization of the fluid dynamics within the porous media is essential to accurately modeling the performance of any Stirling or Pulse Tube cryocooler, especially miniaturized and high-capacity designs where frictional losses through the medium and streaming effects within the porous zones can have detrimental effects for the overall cooler performance. Of particular interest to designers and researchers are the pressure drop mass flow rates through the regenerator and heat exchanger filler material. These characteristics are often predicted using dimensionless numbers known as hydrodynamic resistance parameters. The most famous of such parameters which is used extensively in fundamental fluid dynamics is the Darcy friction factor, f. In practice, it is often convenient to separate the total frictional effects within the porous medium into its component parts, namely the viscous and inertial components of the hydrodynamic resistance. In most studies of porous media hydrodynamics, the viscous resistance is represented by the Darcy permeability term while the inertial resistance is represented by the Forchheimer coefficient. Except for well-defined and idealized geometries, it is not possible to determine these parameters analytically, even for laminar flow, due to the complex geometry of the porous medium. Researchers must rely on detailed numerical simulations or experimental measurements to determine the pressure drop and velocity of the flow through the porous media and thereby calculate appropriate values for the hydrodynamic resistance parameters. This work will investigate several common materials that are typically used in cryocooler regenerators. Experimental measurements of the pressure drop across the porous samples

were taken for each of the specified materials at multiple operating pressures and frequencies for temperatures ranging from ambient conditions to typical cryocooler cold tip operating temperatures. Experimental measurements at cryogenic temperatures have been avoided in the past due to the difficulty associated with cooling the experimental apparatus and the challenges of taking reliable data while maintaining cryogenic temperatures. Measurements at cryogenic temperatures are important, however, to ensure that the hydrodynamic resistance parameters calculated for a porous medium at ambient conditions will still be suitable when the medium is cooled to its actual operating temperature. The experimental measurements were then compared to numerical simulations using Sage [4] cryocooler modeling software and ANSYS Fluent [5,6] to determine the values of the Darcy friction factor, Darcy permeability term, and Forchheimer inertial resistance coefficient. Finally, correlations were developed to predict these hydrodynamic resistance parameters across a wide range of operating conditions which can be used to design and optimize the next-generation of cryocoolers.

CHAPTER 2. BACKGROUND

2.1 Cryocooler Types and History

Cryocoolers in use today can be divided into two basic types or classes, recuperative and regenerative. Recuperative cryocoolers utilize the steady flow of a compressed gas through an expansion valve to absorb heat in much the same way as a traditional refrigeration cycle except that the thermodynamic cycle for a recuperative cooler operates mostly above the vapor dome. Coolers in this class are simple, robust, and power and include Joule-Thompson, Brayton, and Claude cryocoolers (Figure 1). Recuperative cryocoolers get their name from the counter-flow heat exchanger that is essential to their operation. The working fluid passes from the compressor or other pressure source through the pre-cooling heat exchanger and then through the expansion valve. It then absorbs heat from the target and passes back through the heat exchanger and either back to the compressor or is exhausted. This basic design has numerous advantages. It allows the compressor to be placed far from the target area. It has no moving parts at the cold end of the cooler and, owing to its steady-flow operation, has virtually no vibration [7]. Coolers of this style have been in widespread use since the 50s and have been successfully used in tactical and space applications with infrared detectors. To spite their many advantages, recuperative style cryocoolers do possess some drawbacks. The compression ratios required for successful operation can be rather high (200:1) leading to other complications such as poor efficiencies at temperatures below approximately 90K [7], and the coolers themselves tend to be quite large compared to the alternatives.

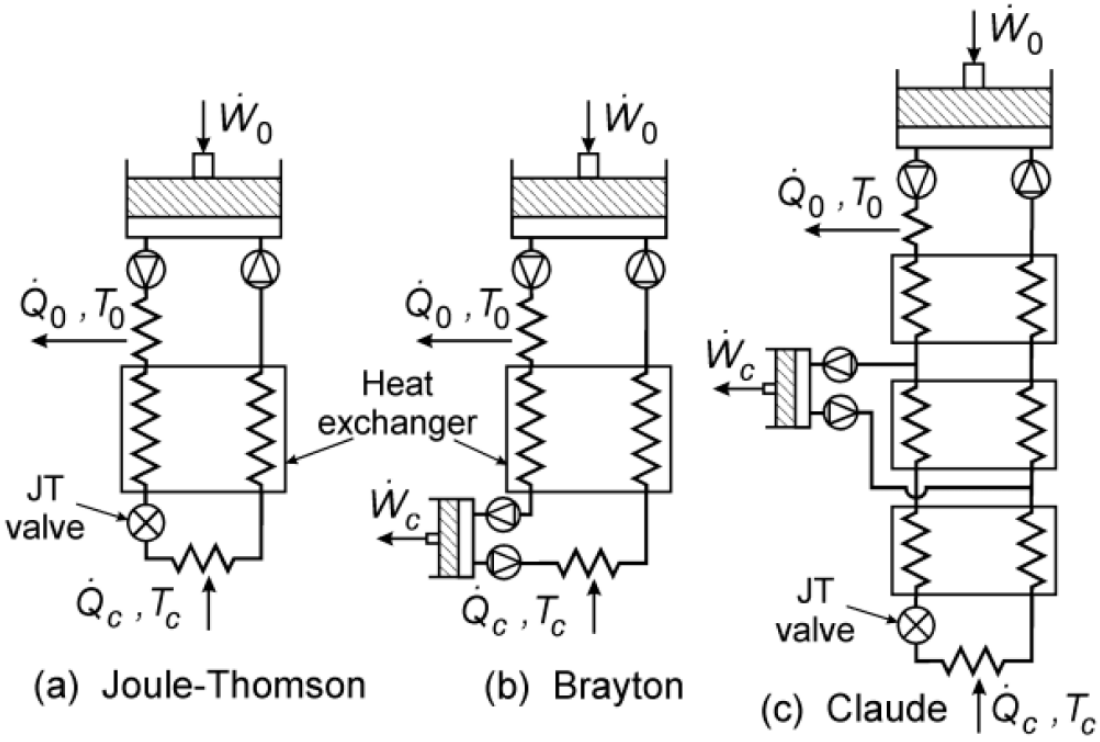

Figure 1. Schematics of Recuperative Cryocoolers from [8]

Whenever lower temperatures or higher efficiencies are desired, recuperative coolers ultimately lose out to regenerative-type devices such as Gifford-MacMahon, Stirling, and Pulse Tube Cryocoolers (Figure 2). Regenerative coolers utilize an oscillating flow of high-pressure gas, usually high-purity helium, which passes back and forth along a series of heat exchangers, tubes, and offices to generate the desired cooling effect. Unlike recuperative-type coolers, which use classic shell-in-tube style heat exchangers, the heat exchangers in regenerative-type cryocoolers are often composed of hollow cylinders packed with some type of porous material such as a wire mesh, metal foam, or packed beds of spheres. The working fluid passes through this porous media and exchanges heat with the filler material each cycle. The careful design of the porous media is essential to the successful operation of the regenerative cooler.

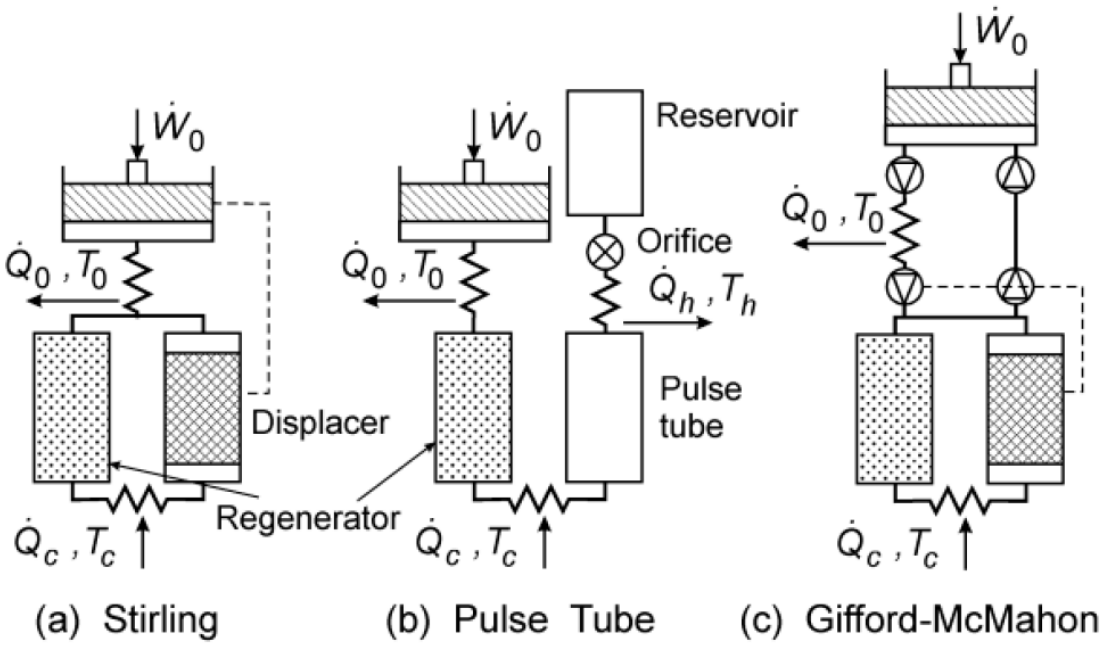

Figure 2. Schematics of Regenerative Cryocoolers from [8]

The Stirling cryocooler is the basis for all regenerative-type cryocoolers. The Stirling cryocooler operates based on the ideal Stirling cycle for a heat engine or heat pump [9]. A simplified schematic of the Stirling cryocooler is shown in Figure 3, and Figure 4 provides a pictographic representation of the Stirling cycle for a cryocooler. The thermodynamic processes coinciding with the pictographic representation are shown in Figure 5 on Pressure-Specific Volume and Temperature-Entropy diagrams.

1) First, the warm-end piston compresses the working fluid into the warm heat exchanger or WHX, which consists of a cylindrical shell packed with a porous medium such as wire mesh or metal felt. As the gas is compressed, it exchanges heat with the porous medium in the WHX which rejects excess heat to the ambient.
2) As the warm-end piston continues to move to the right, the cold-end piston begins to move to the right at the same time with the same frequency and amplitude as the

warm-end piston but 90° out of phase. Both pistons then move in tandem, forcing the working fluid through the regenerator, which is also packed with a porous medium. The regenerator acts as a precooler for the gas entering the cold heat exchanger (CHX) so the gas is close to the cold operating temperature as it enters the CHX.

3) When the warm-end piston is at its zenith, the cold-end piston continues to move to the right, expanding the gas within the cold heat exchanger and causing it to absorb heat from the target.
4) Finally, the warm-end and cold-end pistons move in tandem back to the original starting position. Thermal energy absorbed by the regenerator during phase 2-3 is picked up by the cooled gas and transferred to the warm heat exchanger to be rejected at the beginning of the next cycle.

The position of the warm-end and cold-end pistons can be described as a sinusoid with a specified amplitude, frequency, and phase. The derivative of the position function, naturally, is the velocity of the piston which will coincide with the instantaneous mass flow rate at any location in the cooler. Since the density of the working fluid changes with varying temperature, the pressure oscillations will necessarily be out of phase with the mass flow oscillations due to conservation of mass [10]. In a properly designed cooler, the mass flow and pressure will be in phase near the center of the regenerator, the mass flow will lead the pressure at the warm end by approximately 30°, and the mass flow will lag the pressure at the cold end by approximately 30° [10].

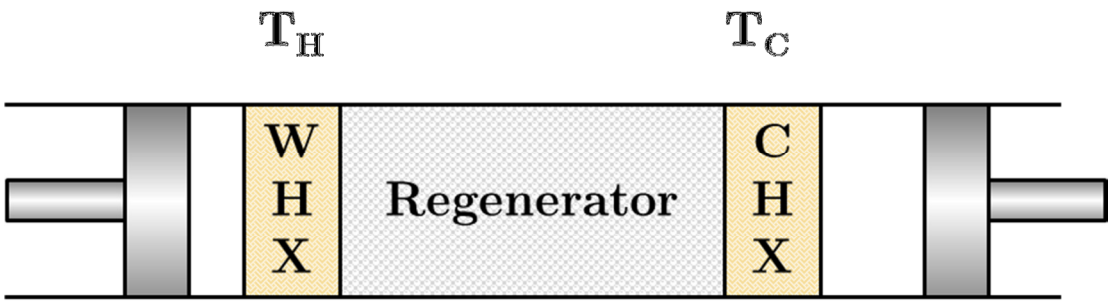

Figure 3. Simplified schematic of Stirling cryocooler from [3]

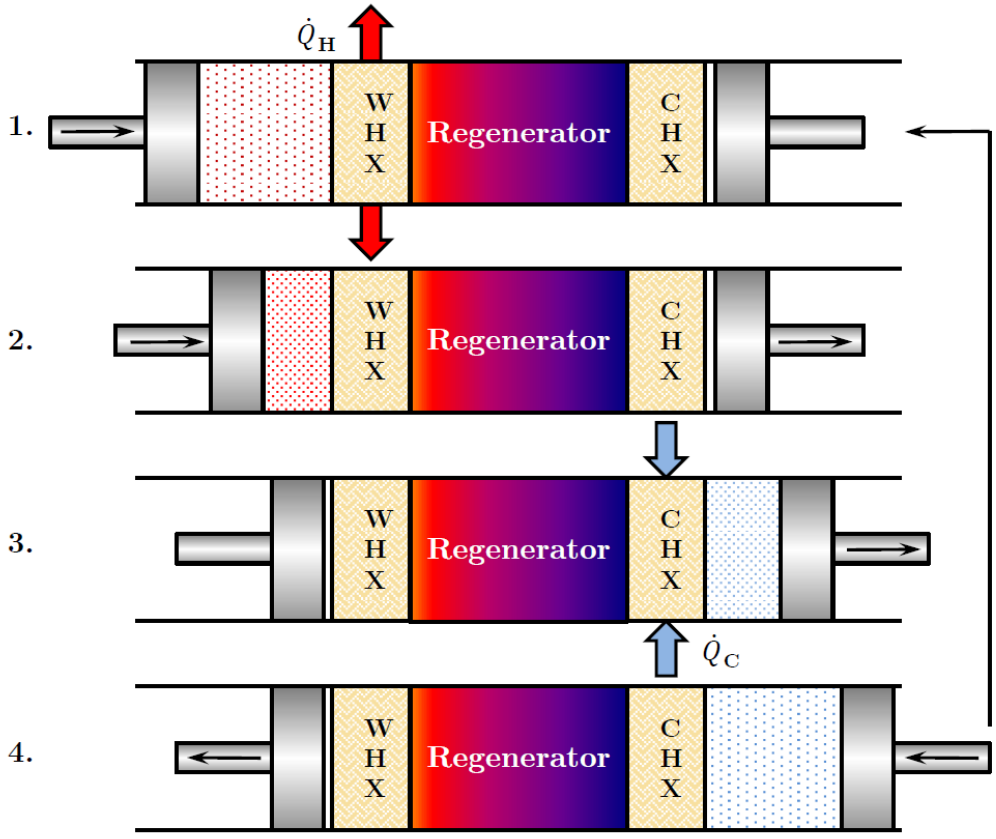

Figure 4. Pictographic representation of the Stirling cycle for cryogenic refrigeration from [3]

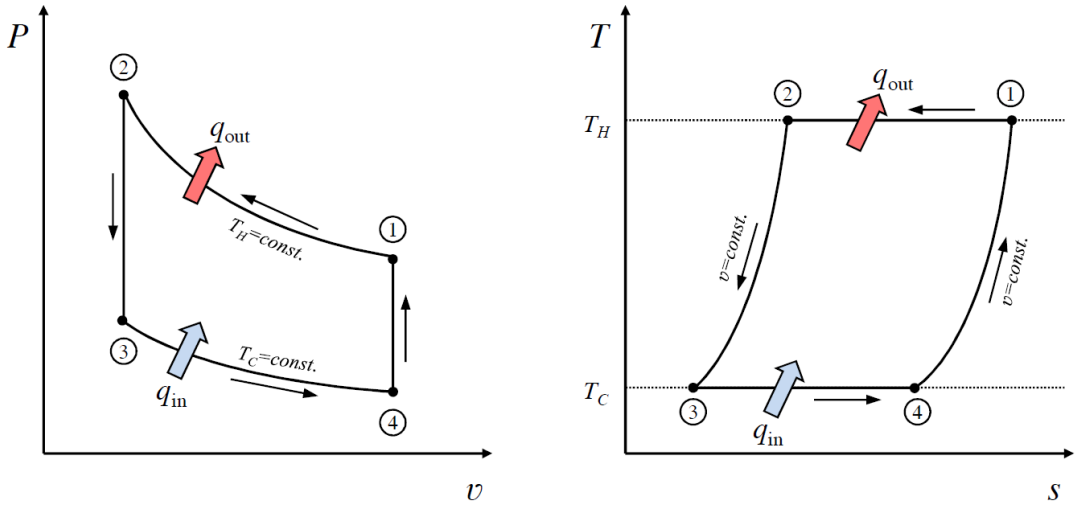

Figure 5. Ideal Stirling cycle on *P-v* and *T-s* diagrams from [3]

While the concept of utilizing the Stirling cycle as a refrigerator had existed for some time, it was not successfully implemented until the late 1800s [11] and it wasn't until the mid-1900s that the process was used for air liquefaction [12]. Stirling cryocoolers are still very prevalent today especially in the defense industry for use as tactical coolers due to their high efficiencies and inherently compact design compared to recuperative coolers. In fact, as material properties and manufacturing techniques continue to improve, much of the cutting-edge work with Stirling machines focuses on reducing the size and power requirements to smaller and smaller scales. This, in turn, is enabling smaller, lighter, and cheaper infrared detectors for the defense and public sectors.

In spite of their many appealing qualities, Stirling coolers are not without their drawbacks. The most challenging feature of a Stirling cryocooler is the cold-end piston and accompanying seals. It is very difficult for a piston-seal assembly to operate reliably at cryogenic temperature due to the increased stress on the materials. Most seal materials like plastics and rubber become brittle at low temperatures and are prone to failure from

fatigue. The thermal expansion coefficients of the different materials in the assembly can also cause interference and wearing, and the piston itself imparts additional heat loads to the CHX through frictional effects and heat-shuttling from the piston housing. Another style of cryocooler known as the Pulse Tube Cryocooler or PTCs is prevalent in several areas, such as the space industry for example, for its ability to mitigate these concerns by eliminating all moving parts at the cold end of the cooler. The first Pulse Tube Cryocoolers were proposed by Gifford and Longsworth in the 1960s, and were known as Basic Pulse Tube Cryocooler or BPTCs [13]. The basic pulse tube cryocooler consists of a warm-end piston, warm heat exchanger, regenerator, and cold heat exchanger just like a Stirling cryocooler, but instead of a cold-end piston the BPTC possesses a single hollow cylinder or pulse tube, at its cold end (Figure 6). The WHX, regenerator, and CHX of a BPTC are filled with a porous medium in the same manner as a Stirling cooler. Heat is absorbed from the target through the CHX, pumped through the regenerator, and rejected at the WHX.

The BPTC was discovered partially by accident, and although it was the first style of PTC to be developed, its operating principle is fundamentally different from that of a Stirling cryocooler [8]. Without a piston-cylinder assembly at the cold end of the cooler the BPTC cannot actively control the phase difference between the mass flow and pressure at the cold end of the cooler, which is essential to the operation of the Stirling cycle. Instead, the BPTC relies on a net enthalpy transfer away from the CHX through the pulse tube (to the right) due to heat transfer with the pulse tube wall itself [14]. This operating principle only works at low frequencies of 1-2 Hz, and is much less efficient than a comparable Stirling cooler and is not capable of as low of temperatures [8].

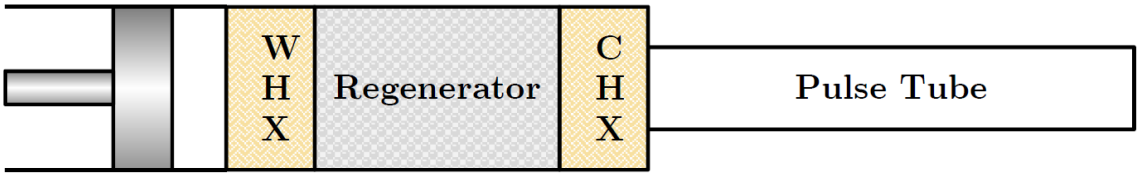

Figure 6. Schematic of Basic Pulse Tube Cryocooler from [3]

Although early PTRs were much less efficient than comparable Stirling coolers, the numerous advantages of having no moving parts at the cold end of the cooler inspired many researches to continue searching for ways to improve the BPTC. In the early 1980s, Milulin, et al. devised a variation of the BPTR by adding a sharp-edged office and larger compressible volume to the right-hand side of the pulse tube [15]. A similar modification was developed by Radebaugh et al. where a needle valve was placed between the pulse tube and compressible volume to allow for active tuning of the flow impedance [16]. This variation of the pulse tube cooler became known as the Orifice Pulse Tube Refrigerator or OPTR (Figure 7). Unlike the BPTR, the OPTR operating principle is identical to that of the Stirling cryocooler with the cold end piston replaced by the pulse-tube, orifice, and surge volume. Together, these three components act as a sort of hydrodynamic piston to create the proper mass flow rate to pressure phase relationship at the exit of the CHX in order to generate the desired cooling effect. The shuttle heat transfer with the pulse tube wall that is essential to the operation of the BPTR actually becomes a loss for the OPTR [8]. There is however, a net enthalpy flow through the Pulse tube (to the right), which is rejected by the secondary WHX.

The most recent adaptation of the Pulse tube cooler replaces the phase-shifting orifice with a long, narrow tube called the inertance tube (Figure 8). This style of cooler is known as the inertance tube pulse tube cooler or ITPTR. Proper design of the

inertance tube creates the desired pressure to mass flow phase shift at the right-hand-side of the pulse tube without the negative effects of a sharp-edged orifice such as streaming [17–20]. The ITPTR is currently the most popular configuration of the Pulse tube cooler in use today and can produce temperatures from 20-100K and cooling powers from 0.1-1000W, comparable to available Stirling coolers [7]. Depending on the application, OPTRs and ITPTRs are available in a variety of configurations that reduce the overall footprint of the cooler and allow the cold finger to be placed in close proximity to the target (Figure 9). Similar to Stirling coolers, much of the cutting edge work with PTRs revolves around reducing the size or increasing the power of the device. While most miniaturized coolers available today are Stirling type machines, there has been much work in the miniaturization of pulse tube coolers [2]. The key drawback to PTC minimization, however, is the increased boundary layer losses within the pulse tube as the diameter of the component is decreased leading to lower efficiency [21]. Another area of interest is increasing the cooling power of Pulse tube coolers especially for space applications where PTCs are valued for their reliability and long life. This leads to a host of other challenges as increasing the cooling capacity calls for increasing the size of the heat exchangers and pulse tube which can lead to secondary flows, streaming, and tilt-sensitivity due to buoyancy and circulation [3].

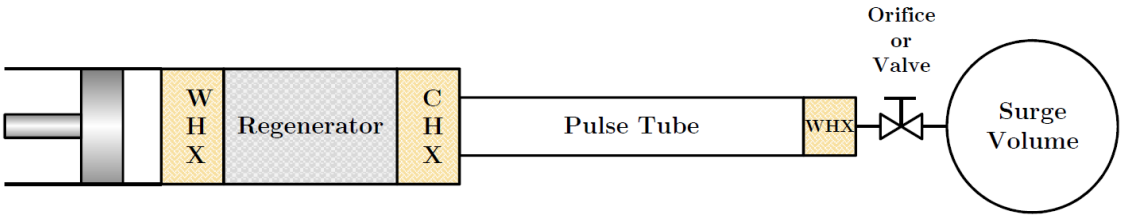

Figure 7. Schematic of Orifice Pulse Tube Refrigerator from [3]

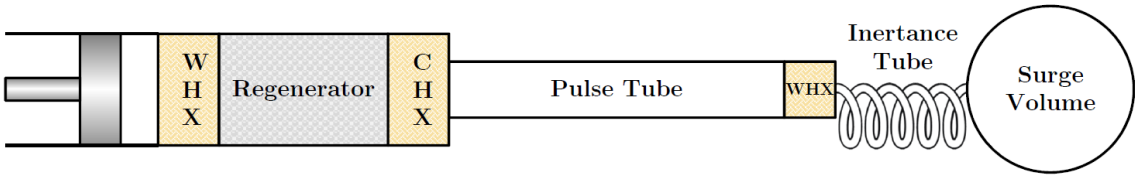

Figure 8. Schematic of Inertance Tube Pulse Tube Refrigerator [3]

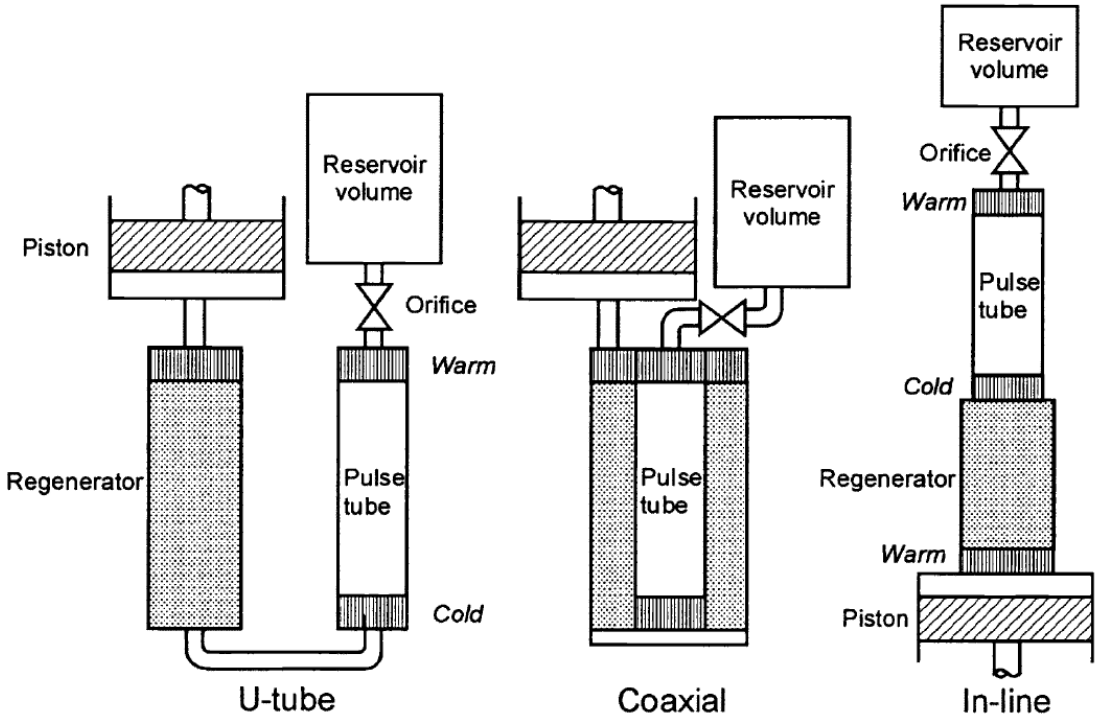

Figure 9. Pulse Tube Refrigerator Configurations from [10]

2.2 Regenerator Characteristics

The regenerator is widely considered to be the most crucial component of a Stirling or Pulse Tube cooler. It consists of a thin-walled, cylindrical shell packed with a porous matrix such as metal foam, wire mesh, beads, or powder. During the compression phase of the refrigeration cycle, the working fluid transfers thermal energy to the regenerator

filler material as it passes through the porous medium. During the expansion phase, the working fluid is forced back through the regenerator, absorbing thermal energy from the porous medium. The physical characteristics of the regenerator such as its length, diameter, porosity, and type of filler material all play a crucial role in its effectiveness. Regenerators must be carefully designed and optimized for a particular temperature range or operating frequency in order for the cryocooler to operate efficiently.

Essentially, the regenerator must be designed to provide adequate heat transfer between the working fluid and the porous filler material without having unacceptably high conduction in the axial direction or pressure drop from the inlet to the outlet. Since the regenerator sits between the warm and cold heat exchangers, one can generally assume that all the gas that enters the regenerator from the WHX is at the warm rejection temperature and all the gas that enters from the CHX is at the cold target temperature. Because of its location, any axial conduction through the regenerator will act as an additional heat load on the CHX and will subtract from the cooler's total cooling power. Axial conduction through the regenerator shell should obviously be minimized for the same reason. This is usually accomplished by selecting a low-conductivity metal such as stainless steel or Inconel brand steel as the regenerator housing and making the walls of the vessel as thin as possible given the operating pressure. In addition to the shell, axial conduction through the porous material itself must be minimized. Materials such as screen, foams, felts, and packed beds are often used because they allow for good convection heat transfer with the working fluid but have low thermal conductivity in the axial direction. Using materials with small characteristic solid lengths is also important. Since the working fluid is oscillating, heat can only penetrate a limited distance into the

solid during a single half-cycle. This is called the thermal penetration depth, and it depends on the solid material properties, fluid properties, and operating frequency of the cryocooler. Any solid material thicker than the thermal penetration depth will essentially be wasted space that does not contribute to the thermal storage of the porous medium. Figure 10 shows several common regenerator filler materials including wire mesh, metal foam, and micro-perforated disks. At extremely low temperatures (<50K) the heat capacity of many common regenerator filler materials begins to degrade. This has prompted the use of newer rare-earth materials such as Erbium-Praseodymium alloy (ErPr) which retains high thermal storage capacity even at cryogenic temperatures.

As previously stated, it is also essential that pressure drop through the regenerator be kept to a reasonable level. As the porosity of the medium is decreased the capacity for thermal storage increases, but so does the pressure drop. Frictional losses through the regenerator lead to greater power requirements from the compressor and less total mass passing through the porous zone each cycle. The pressure drop through the regenerator filler material can be predicted using hydrodynamic resistance parameters, which will be discussed in more detail in the following chapter. Some porous materials, such as packed sphere beds, have isotropic flow parameters meaning that the medium resists flow in every direction equally. Other materials, such as wire meshes, have anisotropic flow parameters since they are more resistive to flow in the radial direction than the axial [1]. While flow through the regenerator is predominately uni-directional in the axial direction, the flow parameters in the radial direction can have a large impact on the cooler performance. Large flow resistance in the radial direction can act to impede secondary or reversed flow in the porous zone by forcing the working fluid to move mostly in the axial

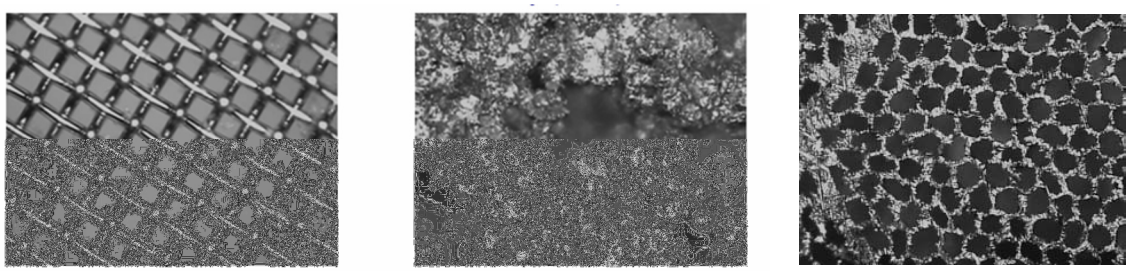

Figure 10. Typical porous regenerator filler materials: wire mesh (left), metal foam (middle) and perforated disks (right)

direction. This might be desirable in some designs, but high radial flow resistance can also exacerbate streaming effects by preventing the fluid velocity from equilibrating throughout the regenerator cross section. The hydrodynamic resistance characteristics of each regenerator filler material under investigation will be discussed in their respective sections, and their impact on overall cooler design will be addressed.

2.3 Porous Media Hydrodynamics

Realistic prediction of the regenerator performance depends heavily upon the accurate modeling of the fluid-solid hydrodynamic and thermal interactions within the porous filler material of the regenerator. While it is theoretically possible to model the entire PTC system including the porous material on a microscopic level using the conservation of mass, momentum, and energy equations, such an approach is computationally expensive and requires detailed knowledge of the microscopic geometry of the medium. A far more common approach is to convert the microscopic governing equations to the macroscopic level using volume averaging or a similar approach [22–26]. For the conservation of momentum equation under steady state conditions this

yields the extended Darcy- Forchheimer model equation for steady, incompressible flow in the axial direction [27]

$$\frac{dP}{dx} = -\frac{\mu}{K} u_D - \frac{c_f}{\sqrt{K}} \rho u_D^2 \tag{1}$$

where K represents the Darcy permeability, c_f represents the Forchheimer inertial coefficient, and u_D represents the Darcian velocity, or the averaged velocity over a gross cross-section of the porous medium, in the axial direction. Together, these are frequently referred to as closure parameters or hydrodynamic resistance parameters. These closure parameters are needed for determining the pressure drop and other hydrodynamic behavior of the fluid within the porous medium in order to optimize the regenerator design. Available widely-used computational tools such as Regen 3.3 [28] and Sage [4] , which are industry-standard design and analysis tools for regenerators and PTC systems, respectively, aim to maximize regenerator performance by using such pressure drop and heat transfer correlations.

There are currently two main methods for determining the permeability and inertial coefficients for a particular medium. One approach is to create microscopic or pore-level models of the regenerator filler material using Computational Fluid Dynamics (CFD) to determine the pressure drop characteristics and, by comparing the results to the macroscopic or volume-averaged equations, determine appropriate values for the closure parameters. This technique has been employed successfully by multiple researches including Kim [29] and Nakayama [30,31] who determined the hydrodynamic resistance parameters for a generic porous medium consisting of infinite square rods. Fumoto [32]

developed a three-dimensional numerical model in order to determine the pressure drop within a packed bed of spheres with varying diameters. Similarly, Palle and Aliabadi [33] modeled packed spheres within a rectangular channel. CFD simulations may also be used to model the heat transfer and thermal dispersion characteristics of porous media as shown by Pathak et al. [34,35] and Kuwahara et al. [36]. This approach is limited, however, because it relies on generalized or generic porous media structures. Rarely, if ever, will a porous medium of interest be arranged in a simple or repeatable pattern than lends itself easily to solid modeling in available software. Specific and detailed knowledge of the real geometric configuration of a porous medium is difficult to acquire, and often quite complicated. Some filler materials, including wire mesh and metal powders, are difficult to model accurately and lead to computationally expensive simulations. For these reasons, experimental measurements are frequently utilized.

Experimental regenerator testing has been utilized extensively by researchers for the determination of hydrodynamic closure relations. In order to apply the Forchheimer-extended Darcy model to PTC regenerators, Harvey [37] used a one-dimensional model for transient compressible flow within a porous medium

$$\frac{\partial(\rho u)}{\partial t}+\frac{\partial}{\partial x}(\rho u^2)+\frac{\partial P}{\partial x}+\left(\frac{\varepsilon\mu}{K}u+\frac{c_f\varepsilon^2\rho}{\sqrt{K}}u^2\right)=0 \tag{2}$$

where ε represents the porosity of the porous medium, and the last two terms on the left-hand side of the equation represent the viscous and inertial resistances of the medium, respectively. In the vast majority of cryocooler applications, the flow within the regenerator may be approximated as unidirectional in the axial direction. This allows for

easy comparison with experimentally measured pressure and mass flow data. Using this formulation, Harvey determined the hydrodynamic resistance parameters for several common regenerator filler materials including metal foam, #400SS mesh, #325SS mesh, and 60-micron perforated disks. Building upon the work of Harvey, Cha [1,38] determined the steady and oscillatory flow closure parameters in the radial and axial directions for a variety of porous media. Using a novel CFD-assisted methodology, Cha utilized the commercial CFD tool Fluent [5,6] to iteratively determine the closure parameters which lead to agreement between data and simulations. Cha also showed that the use of oscillatory versus steady flow closure parameters has a significant effect on the expected PTC performance. Cha's CFD-assisted experimental technique was later pursued by Clearman [39] and Landrum [40]. An issue of particular interest in these studies was the anisotropic behavior of widely-used screen mesh fillers. Other aspects of pulse tube cryocoolers (PTCs) were investigated by Conrad [21] in relation to miniature PTCs, by Pathak [41] with respect to large capacity two-stage PTCs, and Mulcahey [42] with respect to the effect of tilt angle with gravity on the basic phenomenology and performance of PTCs.

Recently, interest in new, rare-earth alloy regenerator fillers suitable for lower-temperature applications has grown especially in multistage PTCs where the regenerator of the final stage may need to operate at temperatures in the 10 – 20 K range or lower. Of particular interest is ErPr (erbium-praseodymium) alloy, which maintains a high heat capacity at temperatures at and below 20K. Pathak [43,44] experimentally determined the Darcy permeability and Forchheimer inertial coefficients for a packed-bed of 69μm average-diameter $Er_{0.5}Pr_{0.5}$ (alloys with 50% Er and 50% Pr) spheres in a prototypical

regenerator for steady and oscillatory flows of helium at room temperature for a range of frequencies, charge pressures, and gas velocities. Following an experimental approach similar to Cha, Pathak determined that the Darcy permeability, corresponding to the viscous resistance of the packed bed, depends only on the geometric configuration of the porous medium and remains relatively constant across the range of frequencies and charge pressures investigated. The Forchheimer coefficient, representing the inertial resistance of the flow through the porous medium, was found to vary with the mass flow rate within the regenerator, and was correlated with respect to the pore-based Reynolds number, given by Eq.(3) where the square root of the Darcy Permeability, K, is used as the length scale.

$$\mathrm{Re}_{\sqrt{K}} = \frac{\dot{m}\sqrt{K}}{\mu A_f} \tag{3}$$

In each of these studies, the hydrodynamic behavior of the regenerator depended heavily on the operating conditions of the PTC or experimental setup including the charge pressure, frequency, and filler material characteristics.

A key shortcoming of the work by Harvey, Cha, Pathak, and many other studies that have been published in the open literature is that all tests were conducted at room temperature, even though PTCs operate at temperatures well below ambient. Based on the derivation of the volume-average momentum equation, the experimentally determined closure parameters should not, in theory, be affected by the operating temperature assuming that the geometric configuration of the porous medium remains the same at ambient and cryogenic temperatures. Indeed, it is common practice in the industry to use

correlations for the hydrodynamic resistance parameters that have been developed at ambient temperature for models operating at cryogenic conditions. However, there is a pressing need to determine the closure parameters for these regenerator filler materials at cryogenic temperature and thereby verify, or otherwise remedy, the forgoing assumption. The objective of this work will be to determine the Darcy permeability and Forchheimer inertial coefficients for $Er_{0.5}Pr_{0.5}$ powder, #400 stainless steel mesh, and #325 stainless steel mesh at cryogenic temperatures for a range of mean pressures, frequencies, and velocity amplitudes and compare the results to those obtained at ambient conditions.

CHAPTER 3. EXPERIMENTAL METHODOLOGY

3.1 Overview

The general approach for the experimental determination of the hydrodynamic resistance parameters for porous media is to induce a flow of working fluid through a porous test section, measure the instantaneous pressure and mass flow rates at the inlet and outlet of the test section, and apply these measured values as boundary conditions to a numerical simulation to find the appropriate hydrodynamic resistance parameters that satisfy the conservation of mass and conservation of momentum equations. Typically, the working fluid will be high-purity helium as this is the most common working fluid for actual pulse-tube and Stirling cryocoolers. The flow may be steady or oscillating provided that the boundary conditions provided to the numerical simulation match the actual experiment. In this work, prototypical regenerators were constructed to serve as the porous test sections. The first regenerator was filled with 50% Erbium, 50% Praseodymium ($Er_{0.5}Pr_{0.5}$) rare-earth alloy in the form of a powder comprised of spherical particles with an average diameter of 55 microns. The second regenerator was filled with #400 (400 wires per inch) stainless steel mesh disks with a wire diameter of 30.5μm and thickness of 61μm, and the third regenerator was filled with #325 stainless steel mesh disks with a wire diameter of 35.6μm and thickness of 71.1μm. All regenerators were subjected to oscillating flow of high-purity helium in a closed-loop test section at charge pressures ranging from 0.1-2.86 MPa, frequencies of 30-70 Hz, and temperatures from 50-300 K. A summary of the regenerator filler materials is provided in Table 1.

Table 1. Summary of tested regenerator filler materials

Regenerator Number	Filler material	Description	Length (cm)	Porosity
1	$Er_{0.5}Pr_{0.5}$ powder	50% Er – 50% Pr alloy Packed sphere bed Sphere diameter: 55μm	1.66	0.370
2	#400 SS mesh	Stainless steel mesh Wire diameter: 30.5μm Thickness: 61.0μm	1.91	0.699
3	#325 SS mesh	Stainless steel mesh Wire Diameter: 35.6μm Thickness: 71.1μm	1.95	0.688

3.2 Apparatus

The test section and its vicinity for regenerator 1 are shown schematically in Figure 11, and the test section for regenerators 2 and 3 is shown in Figure 12. The test section consists of a stainless steel regenerator sandwiched between a heat exchanger and a rigid stainless steel surge volume with a Q-drive model 2S132W Pressure Wave Generator (PWG) upstream connected via a 0.91 m (3 ft) stainless steel transfer tube. A PowerFlex 700 power supply is used to specify the operating frequency and applied voltage of the PWG. The test section for regenerators 2 and 3 includes an extended surge volume to accommodate the higher mass flow rates that occur through the wire mesh regenerators. The heat exchanger, or Cold Heat Exchanger (CHX), is thermally synched with the 1st stage of a Sumitomo model RDK-408D2 GM cryocooler by a copper bus bar. The first stage cold head of the Sumitomo GM cryocooler is capable of delivering 50 Watts of cooling at 43 K, while the second stage provides 1 Watt of cooling power at 4.2 K. The interior of the CHX is packed with #100 mesh copper screens (porosity of 64.7%) to ensure adequate thermal contact and heat transfer with the helium working fluid. The

first regenerator is packed with $Er_{0.5}Pr_{0.5}$ micro spheres with 55μm mean particle diameter and porosity of 37%. The $Er_{0.5}Pr_{0.5}$ powder is retained by #400 SS mesh screens at the inlet and outlet which are reinforced by two #60 SS screens to prevent wear. Regenerators 2 and 3 consist of a packed bed of randomly stacked wire mesh screens with one #60 SS mesh disk upstream and downstream of the packed screen bed to provide structural support. All three regenerators have approximately 0.2 mm (0.07 in) deep void volumes created by retaining rings upstream and downstream of the packed bed. The total length of the porous matrices varies slightly between the regenerators as shown by Table 1. Indium wire is used to create cryogenic seals between components. First, the surfaces of the CHX, regenerator, and SV are polished to a mirror finish with high-grit sandpaper. Then, a single strand of indium wire is placed into a specialy designed groove on either side of the regenerator to form the seal. The assembly is compressed with a circular bolt pattern outside of the flow passage. PCB piezotronics brand pressure sensors (models 102A05 and 102A10) are installed in specially designed ports on the upstream and downstream sides of the CHX and SV. The gauge pressure within the PWG, also known as the charge pressure or mean operating pressure, was measured using a built-in Burdon tube pressure gauge with 1 bar increments, and the atmospheric pressure was measured with a Fisher Scientific barometer with 0.2 kPa increments. The experimental setup and the GM cryocooler are mounted inside of a vacuum-sealed dewar with modular feedthroughs (Figure 14), which is capable of maintaining an insulating vacuum of 10^{-6} torr in order to reduce conduction and convection loads from the surroundings. An image of the assembled test section is shown in Figure 13 for regenerators 2 and 3.

Instantaneous pressure measurements were made upstream and downstream of the regenerator test section in 2-second durations at a sample rate of 25.6 kHz for a total of 51200 samples per measurement. A minimum of 6 individual 2-second measurements were taken at each PWG setting. The oscillatory pressure measurements were analyzed using Matlab's FFT capability. Analysis shows that the time-dependent pressure can be adequately expressed in terms of the pressure amplitude and phase using the first five fundamental frequencies as follows

$$P(t) = \sum_{i=1}^{i=5} P_i \cos(n\pi ft + \phi_i) \tag{4}$$

where $n = 2,4,6,8,10$. Temperatures were measured using a LakeShore Cryotronics Cernox temperature sensor mounted to the CHX with thermal grease and a machine screw. Because cryogenic temperatures are desired for testing, hot-wire anemometry is not a suitable method for mass flow measurement as this would add an unacceptable heat source to the system. Therefore, the mass flow between the regenerator test section and the surge volume (SV) is calculated indirectly by considering the instantaneous pressure and temperature within the SV. Applying the conservation of energy equation to the surge volume leads to the following.

$$\frac{dE}{dt} = \dot{Q} - \dot{W} + \dot{m}_{in} h_{in} - \dot{m}_{out} h_{out} \tag{5}$$

Assuming the SV is rigid and adiabatic, the work and heat terms may be dropped, leading to

$$\frac{dE}{dt} = \dot{m}_{in} h_{in} - \dot{m}_{out} h_{out} \tag{6}$$

Neglecting the contributions of kinetic or potential energy and expressing the intensive enthalpy and energy in terms of the constant pressure and constant volume heat capacity yields

$$\frac{d}{dt}(\rho c_v \left(T - T_{ref}\right)V) = c_p \dot{m}\left(T - T_{ref}\right) \tag{7}$$

Note that the flow at any instant is either inward or outward, and when the flow is outward the fluid leaving the SV has the temperature equal to the SV temperature. Assuming perfect gas behavior and rearranging terms yields the following expressions for the mass flow rate into or out of the SV.

$$\dot{m}c_p T = \frac{d}{dt}\left(\frac{c_v PV}{R}\right) \tag{8}$$

$$\dot{m} = \frac{V}{\gamma RT}\frac{dP}{dt} \tag{9}$$

The time derivative of the SV pressure can be determined numerically from the collected data to calculate the instantaneous mass flow rate into the SV. A Fast Fourier Transform (FFT) is then performed in order to develop an equation for mass flow rate as a function of time as follows

$$\dot{m}(t) = \sum_{i=1}^{i=5} \dot{m}_i \cos(n\pi ft + \phi_i) \tag{10}$$

where, once again, $n = 2,4,6,8,10$. When the pressure at the inlet of the regenerator is higher than the outlet, the mass flow is positive from left to right, and when the outlet pressure is higher the mass flow is negative. The mass flow is greatest when the pressure difference between the inlet and outlet is highest, and the mass flow rate is zero when the inlet and outlet pressure are equal. The phase angle of the mass flow rate at the

downstream side of the regenerator test section can be determined from the amplitude and phase of the upstream and downstream pressure as follows

$$\phi_{\dot{m}} = \tan^{-1}\left(\frac{P_1 \sin(\phi_1) - P_2 \sin(\phi_2)}{P_1 \cos(\phi_1) - P_2 \cos(\phi_2)}\right) \tag{11}$$

where P_1 and P_2 are the upstream and downstream pressure amplitudes, respectively. The difference between the mean operating pressures at different locations along the test section is assumed to be negligible compared to the effect of the pressure amplitude and phase shift on the mass flow.

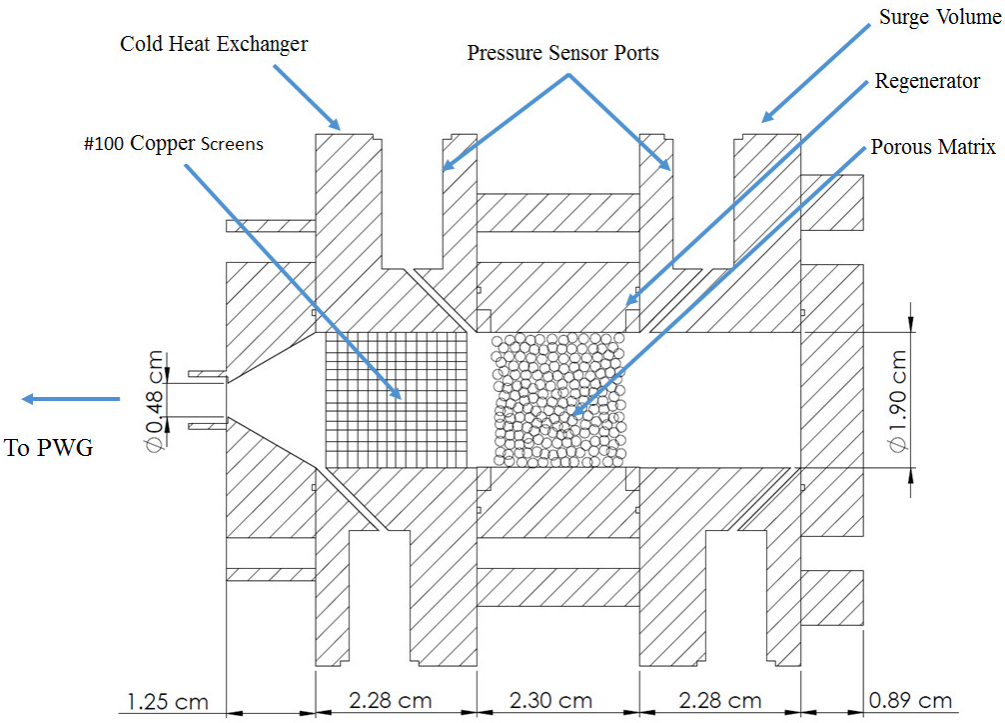

Figure 11. Schematic of experimental test section for $Er_{0.5}Pr_{0.5}$ regenerator

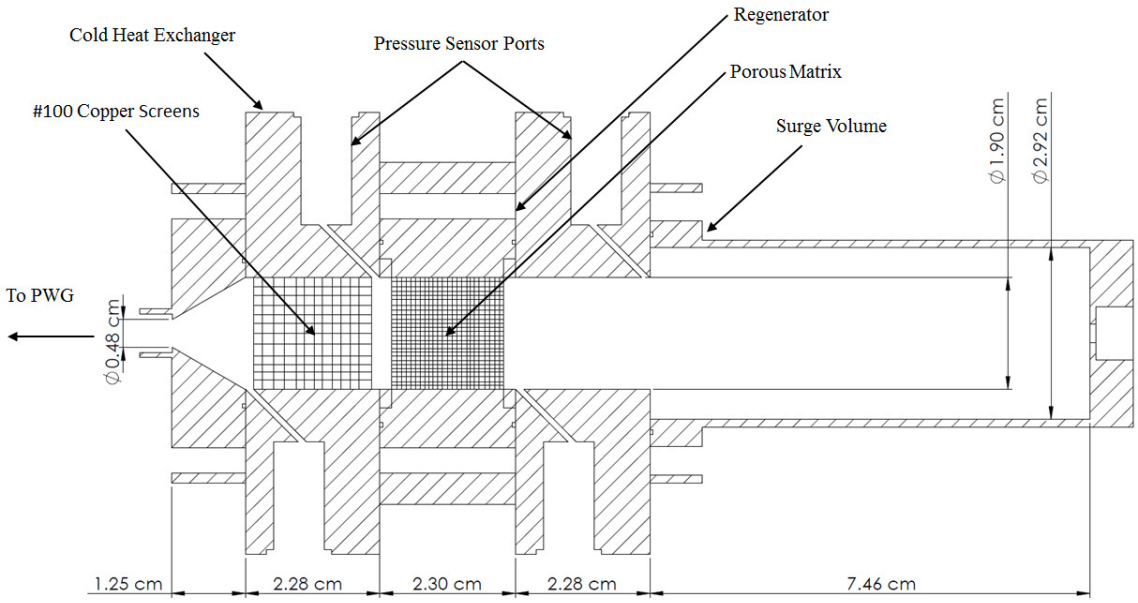

Figure 12. Schematic of experimental test section for #400SS mesh and #325SS mesh regenerators

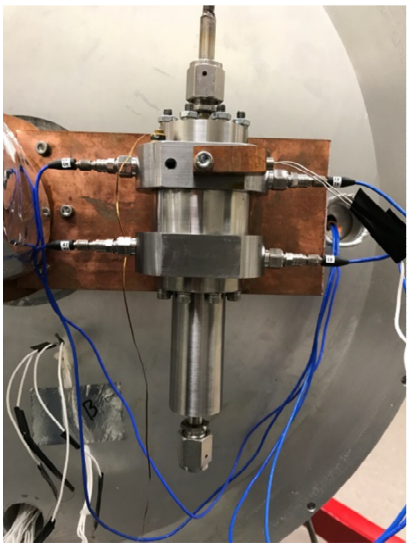

Figure 13. Experimental test section mounted to cold head with attached dynamic pressure transducers

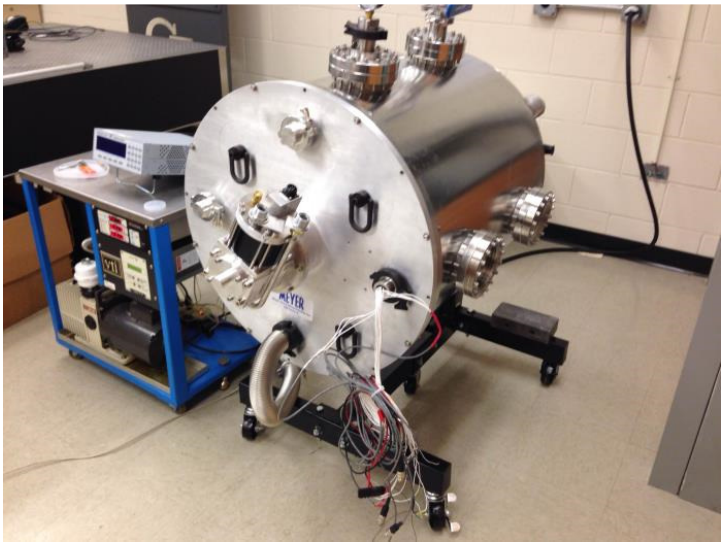

Figure 14. Vacuum-sealed dewar with modular feedthroughs and attached GM cryocooler

3.3 Uncertainty

The uncertainty of the dynamic pressure transducers is provided by the manufacture, PCB Piezotronics as follows [45]. The measurement resolution or random uncertainty, U_A, is given as ±0.014 kPa for the 102A05 and 102A10 model pressure sensors. The accuracy or systematic uncertainty, U_B, was determined from the sensor non-linearity, and varies slightly with the measurement range and individual sensor. Of the sensors used, the greatest non-linearity is given by the manufacturer as 0.3% of the full scale value. With a full scale range of 690 kPa, this gives a maximum systematic uncertainty of ±2.07 kPa. The combined uncertainty, U_C, is found according to Eq. (12) giving a final combined uncertainty of 2,070 Pa.

$$U_C = \sqrt{U_A^{\,2} + U_B^{\,2}} \tag{12}$$

For temperature measurements, the Cernox cryogenic temperature sensor has excellent accuracy and precision for the entire range of interest, with a sensor accuracy of ±40 mK and precision of ±180 mK at the worst-case temperature setting of 300K. This gives a maximum combined uncertainty of 0.2 K for all temperature measurements. The physical dimensions of the regenerator as shown in Figure 11 and Figure 12, namely the length and diameter, were machined to a precision of ±0.01 cm, which gives the compressible surge volume a total uncertainty of 0.206 cm^3.

The random and systematic uncertainties of the mass flow rates were determined through statistical analysis and error propagation analysis, respectively. The random uncertainty can be calculated for each measurement set point based on the sample

standard deviation, or SSD, given by Eq. (13) where N is the number of repeated measurements at each set point.

$$SSD = \sqrt{\frac{\sum \left(\overline{x} - x_i \right)^2}{N-1}}, \quad N = 6 \tag{13}$$

$$U_A = \frac{k_c SSD}{\sqrt{N}} \tag{14}$$

The random uncertainty is then calculated according to Eq. (14) where $k_c = 2.57$ is the coverage factor for a confidence interval of 95%. The systematic uncertainty of the experimental mass flow rates can be calculated using error propagation analysis according to Eq. (15)

$$U_{B_{\dot{m}}} = \sqrt{\left(\frac{\partial \dot{m}}{\partial V} U_{B_V} \right)^2 + \left(\frac{\partial \dot{m}}{\partial T} U_{B_T} \right)^2} \tag{15}$$

The uncertainties of the SV volume and SV temperature are provided above, and the influence coefficients in Eq. (15) are calculated according to Eq. (9). The combined uncertainty is calculated according to Eq. (12), which gives a combined uncertainty of approximately 3% for the entire charge pressure and temperature range of interest.

CHAPTER 4. MODELING METHODOLOGY

4.1 Overview

Once the time-varying pressure oscillations have been determined according to the steps in Chapter 3, the next step is to apply these measurements as boundary conditions to determine the appropriate hydrodynamic resistance parameters for the porous media. In this work, several commercially-available software tools were used to simulate the experimental results and compare to one another. First, Sage [4], an industry-standard tool for the modeling and optimization of Pulse Tube and Stirling cryocoolers, was used to determine the frictional pressure gradient, F, within the porous media. This term represents the total hydrodynamic effect of the porous medium under consideration and the terms in the Stokes stress tensor that cannot be resolved in 1D analysis. In order to deconstruct the total frictional pressure gradient into the viscous and inertial components for comparison with the Forchheimer-extended Darcy law for porous media, Eq. (1), dimensional analysis is used to express the total frictional pressure gradient as a quadratic function of the hydraulic diameter-based Reynolds number, Re_{d_H}. The viscous and inertial resistance parameters, corresponding to the Darcy and Forchheimer hydrodynamic resistance parameters, respectively, can then be extracted from the coefficients of the quadratic function as described in Section 4.3.4. The computational fluid dynamics (CFD) software, ANSYS Fluent [5,6] is then used to model the oscillating flow through the experimental test section using the viscous and inertial resistance parameters extracted from the Sage analysis. A schematic representation of the modeling methodology is presented in Figure 15.

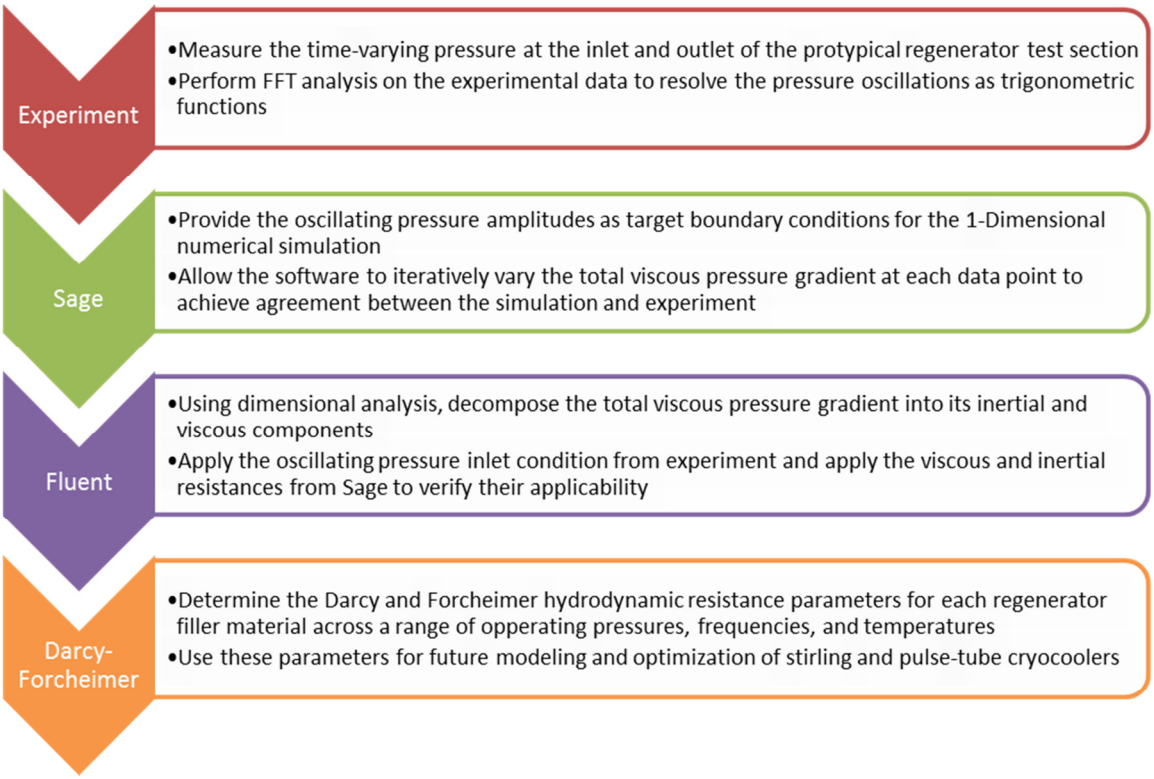

Figure 15. Graphical summary of experimental and simulation methodology for determination of hydrodynamic resistance parameters

4.2 Sage Modeling

Sage [4] is an industry-standard software tool developed by David Gedeon for the modeling and optimization of Stirling and Pulse Tube cryocoolers as well as other mechanical and fluid dynamics system that function based on hydrodynamic resistance and impedance networks. The Sage software package provides a graphical interface consisting of modular sub-models representing individual cryocooler components which can be thermally and hydrodynamically coupled to represent a cryocooler system. Available sub-models include compressors, heat exchanges, transfer lines, pulse tubes, surge volumes, and regenerators. The user can specify the physical dimensions, filler material, and wall material for each sub-model in the overall cryocooler model [4]. An

example of the Sage GUI is shown in Figure 16 representing a large-capacity pulse tube cryocooler developed by Ray Radebaugh at NIST. The figure shows how fluid flow between the components is represented by mass flow connections, and conduction paths are represented using heat flow connections. Canister type components, such as the heat exchangers/ rejecters and regenerator can be filled with a user-specified porous media to exchange heat with the working fluid. The compliance tube, sharp-edged orifice, and reservoir volume provide the appropriate hydrodynamic inertance to generate heat flow from the parasitic sink to the parasitic source.

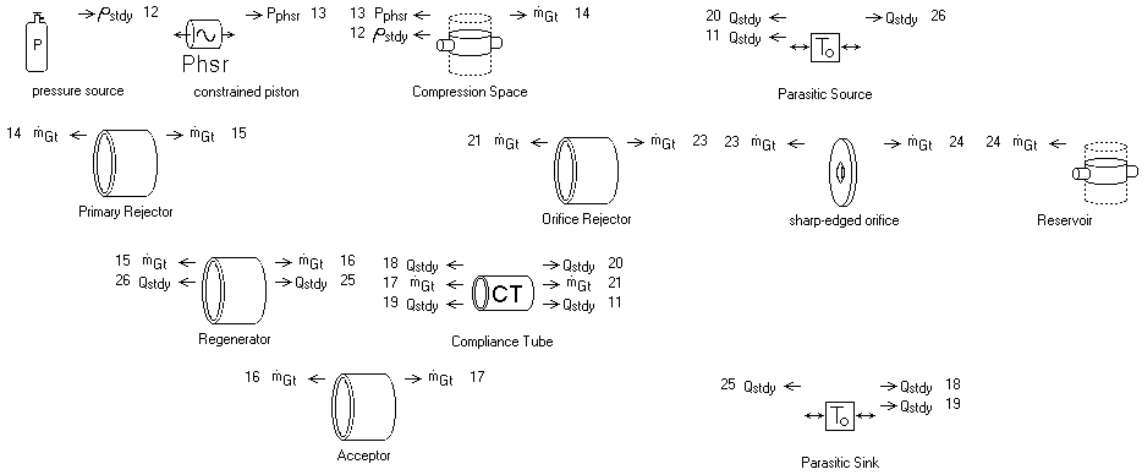

Figure 16. Graphical User Interface for Sage model NIST 1991

4.2.1 Governing Equations

Sage [4] predicts the cooling capacity of the completed cryocooler model by solving the conservation of mass, momentum, and energy equations in one dimension. Beginning with the general Navier-Stokes equations in integral form [46], Gedeon reduces the governing equations to a 1D form in the axial direction, which is the primary direction of

flow within the cryocooler, and allows the total cross-sectional area of the flow passage to vary with location. The governing equations for continuity, momentum, and energy are as follows.

$$\frac{\partial \rho A_f}{\partial t} + \frac{\partial \rho u A_f}{\partial x} = 0 \tag{16}$$

$$\frac{\partial \rho u A_f}{\partial t} + \frac{\partial u \rho u A_f}{\partial x} + \frac{\partial P}{\partial x} A_f - F A_f = 0 \tag{17}$$

$$\frac{\partial \rho e A_f}{\partial t} + P \frac{\partial A_f}{\partial t} + \frac{\partial}{\partial x}\left(u \rho e A_f + u P A_f + q\right) - Q_w = 0 \tag{18}$$

Equation (16) represents the conservation of mass where A_f is the flow area, ρ is the fluid density, x is the primary or axial direction, and u is the physical velocity component in the axial direction. The flow area within the cryocooler model is allowed to change owing to variations in the canister dimensions and different types of porous media present in the model. Equation (17) represents the conservation of momentum equation where P is thermodynamic pressure and F is the total frictional pressure gradient which also accounts for the viscous terms in the Stokes stress tensor since they cannot be resolved in a one-dimensional model. Equation (18) represents the conservation of energy of the working fluid.

The total frictional pressure gradient can be expressed in terms of the Darcy friction factor, f, and a local loss coefficient, K as follows

$$F = \frac{\Delta P}{L} = -\left(\frac{f}{d_h} + \frac{\mathrm{K}}{L} \right) \frac{\rho u |u|}{2} \tag{19}$$

where d_H is the hydraulic diameter and L is the length of the fluid domain under consideration. The hydraulic diameter is defined according to

$$d_h = \frac{4A_f}{S_x} \tag{20}$$

where A_f is the flow area as previously discussed and S_x is the wetted perimeter. For porous zones, the flow area depends on the cross-sectional area, A_c, and the porosity of the medium, ε.

$$\varepsilon = \frac{A_f}{A_c} \tag{21}$$

The wetted perimeter is based on the geometry of the flow passage and varies depending on the type of porous medium under consideration. For a typical regenerator, such as the ones in this study, the cross-sectional area will be constant along the length of the porous domain. Substituting the definition of flow area, Eq. (21), into Eq. (17) and dividing by the cross sectional area yields the following.

$$\frac{\partial \rho u}{\partial t} \varepsilon + \frac{\partial u \rho u}{\partial x} \varepsilon + \frac{\partial P}{\partial x} \varepsilon - F \varepsilon = 0 \tag{22}$$

When considering flow through a regenerator alone, the local loss coefficient in Eq. (19) may be neglected, yielding an expression for F solely in terms of the Darcy friction factor.

$$F = -\frac{f}{d_h}\frac{\rho u|u|}{2} \tag{23}$$

The Darcy friction factor for a particular porous medium must be determined empirically based on knowledge of the instantaneous flow conditions. Sage provides several built-in correlations for the simulation of various porous media to allow the user to simulate and optimize various cryocooler designs. The correlations provided by the Sage user manual [4], were determined by Gedeon experimentally according to the approach laid out in [47], and are also useful for comparison with the experimental results of this work.

Empirical correlations for the Darcy friction factor and by extension the total frictional pressure gradient in Sage are formulated according to the hydraulic-diameter Reynolds number

$$\mathrm{Re}_{d_h} = \frac{\rho|u|d_h}{\mu} \tag{24}$$

where μ is the viscosity of the helium working fluid and the hydraulic diameter serves as the appropriate length scale. It is important to note that the hydraulic diameter Reynolds number differs in magnitude from the pore-based Reynolds number used in other literature, where the square root of the Darcy Permeability, K, is used as the length scale.

4.2.2 Packed Sphere Matrix

The packed sphere matrix correlation reported in the Sage user manual [4] is used to compare to the results for the $Er_{0.5}Pr_{0.5}$ rare-earth prototype regenerator: regenerator 1. Sage defines the wetted perimeter for a packed bed of spheres as

$$S_x = \frac{6(1-\varepsilon)A_c}{d_s} \tag{25}$$

based on purely geometric considerations. The sphere diameter is represented by d_s, which for the $Er_{0.5}Pr_{0.5}$ regenerator is $55\mu m$. The empirical correlation for Darcy friction factor for a packed bed of spheres was determined experimentally by Gedeon as a modified form of the Ergun equation to be

$$f = \left(\frac{157}{\mathrm{Re}_{d_h}} + \frac{5.15}{\mathrm{Re}_{d_h}^{0.137}} \right) \left(\frac{\varepsilon}{0.39} \right)^{3.48} \tag{26}$$

Experiments were conducted using $173\mu m$ diameter spherical lead particles with porosities ranging from 0.38 to 0.43. In Eq. (26), the first term on the right hand side represents the laminar flow regime, where viscous forces dominate and the friction factor is linearly proportional to the inverse of the Reynolds number, similar to regular internal flow. As the Reynolds number increases above approximately 50, the second term on the right-hand side becomes equal in magnitude and eventually surpasses the first term as inertial effects become more important. Other correlations can be found in the literature specifically for packed-sphere beds. Two of the most widely used are the Ergun and Black-Kozeny equations represented by Eq. (27) and Eq. (28), respectively, where u_s

represents the superficial velocity defined by Eq.(29), which is identical to the Darcian velocity used in Eq. (1) .

$$\frac{\Delta P}{L} = \frac{150\mu}{{d_s}^2}\frac{(1-\varepsilon)^2}{\varepsilon^3}u_s + \frac{1.75\rho}{d_s}\frac{(1-\varepsilon)}{\varepsilon^3}{u_s}^2 \tag{27}$$

$$\frac{\Delta P}{L} = \frac{150\mu}{{d_s}^2}\frac{(1-\varepsilon)^2}{\varepsilon^3}u_s \tag{28}$$

$$u_s = \varepsilon u \tag{29}$$

In both formulations, the left hand side of the equation represents the total frictional pressure gradient, which is synonymous with the term F in the conservation of momentum equation given in Eq. (17). The first term on the right hand side of Eq. (27) represents the viscous effects of the porous medium on the flow, while the second term on the right hand side of Eq. (27) represents the inertial effects. For low velocity or laminar flow through a packed bed of spheres the second term on the right hand side of Eq. (27) can be neglected, yielding the Black-Kozeny equation given by Eq. (28).

4.2.3 Woven Screen Matrix

The woven screen matrix option in Sage is used to compare to the #400SS mesh and #325SS mesh experiments for regenerators 2 and 3, respectively. The wetted perimeter for a woven screen matrix is calculated as

$$S_x = \frac{4(1-\varepsilon)A_c}{d_w} \tag{30}$$

where d_w is the wire diameter, specified in Table 1. The total frictional pressure gradient for the woven screen matrix can be determined from Eq. (23), and the friction factor is provided by Gedeon [4] as follows

$$f = \frac{129}{\mathrm{Re}_{d_h}} + \frac{2.91}{\mathrm{Re}_{d_h}^{0.103}} \tag{31}$$

Similar to the packed sphere matrix, the friction factor for the woven screen matrix exhibits a $\mathrm{Re}_{d_h}^{-1}$ dependence at low flow rates, and begins to plateau at higher flow rates as inertial effects become more important.

4.2.4 Generic matrix

A generic porous matrix may also be used to represent unique filler materials or to develop one's own correlations for friction factor and total frictional pressure gradient. The generic matrix option accepts hydraulic diameter as a input and calculates the Darcy friction factor as follows

$$f = c_1 + c_2 \mathrm{Re}_{d_h}^{\ m} + \frac{c_3}{\mathrm{Re}_{d_h}} \tag{32}$$

where c_1, c_2, c_3, and m are all user-defined constants, and Re_{d_h} is the hydraulic diameter-based Reynolds number as previously defined.

Figure 17 shows the graphical interface of the Sage simulation used to model the experimental results for the $Er_{0.5}Pr_{0.5}$ rare-earth regenerator and Figure 18 shows the setup used to model the #325SS and #400SS woven mesh screens regenerators.

Comparison of Figure 17 with the schematic representation in Figure 11 shows how each component of the test section is represented within the Sage simulation. The Q-Drive Pressure Wave Generator (PWG) is modeled using the constrained piston and compression space sub-models. The pressure source component specifies the mean operating pressure or charge pressure of the test section in absolute terms. The Cold Heat Exchanger (CHX) and regenerator are represented as cylindrical canisters filled with porous media. For the CHX, this is #100 copper woven mesh screens which are modeled using the default Sage correlation for packed screen beds. The porous medium within the regenerator is represented as a generic porous matrix as previously described. The generic cylinder components upstream and downstream of the regenerator represent the small void spaces created by the stainless steel retaining rings used to contain the porous material. The transfer line and the tapered compliance tube upstream of the test section are thermally synced with the ambient rejection temperature of 300K, and the CHX, regenerator, and surge volume are thermally synced with the experimental cold set point, which was varied from 50-300K using the Sumitomo GM Cryocooler and the Cryocon cryogenic temperature controller with 50W attached heater. The entire experimental test section is modeled as a closed system with a reciprocating piston upstream and a closed surge volume downstream rather than specifying the dynamic pressure and mass flow rate oscillations with time like Cha [1] and Pathak [43]. This approach is advantageous for several reasons. Firstly, the reciprocating piston face couples the mass flow rate and pressure oscillations upstream of the regenerator. Computational approaches, in general, do not allow the pressure and mass flow rate boundary conditions to be specified simultaneously at the same inlet. Secondly, it eliminates the need for a second boundary

condition, so the experimentally measured mass flow rate calculated according to Eq. (9) can serve as a redundancy and sanity check against the simulation results.

The modeling methodology using Sage is as follows. First, the instantaneous pressure oscillations upstream and downstream of the regenerator are recorded using the method described in Section 3.2. Recall that the pressure oscillations recorded by the experimental apparatus are dynamic pressures, not absolute, meaning that an instantaneous pressure measurement of 0Pa is equal to the charge pressure or mean

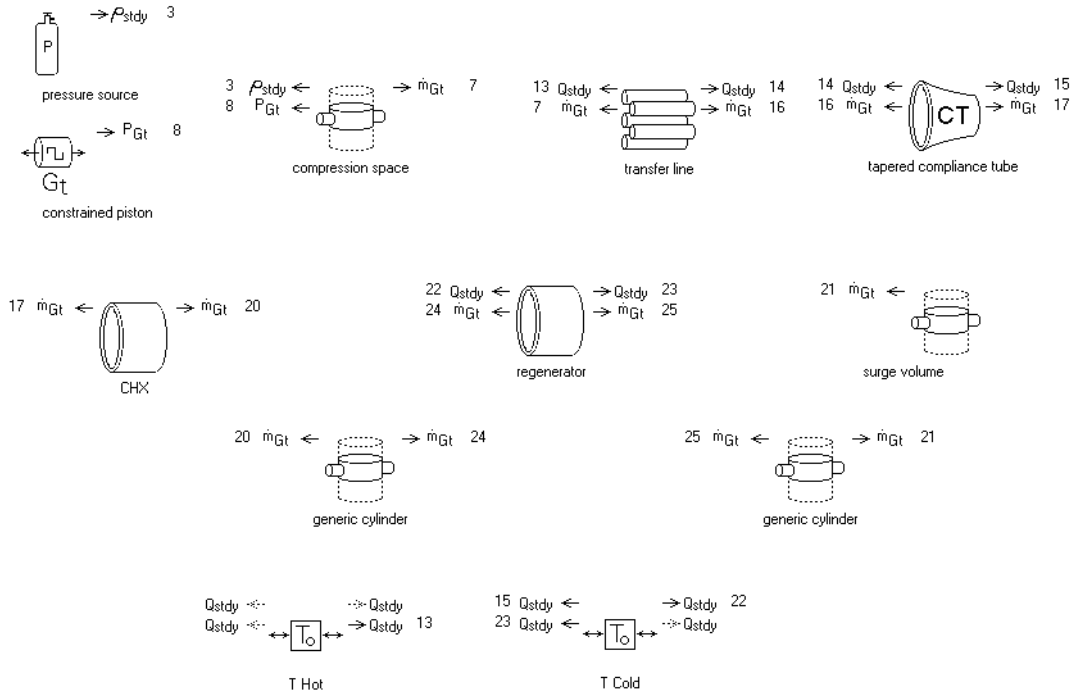

Figure 17. Graphical interface for Sage simulation of $Er_{0.5}Pr_{0.5}$ regenerator

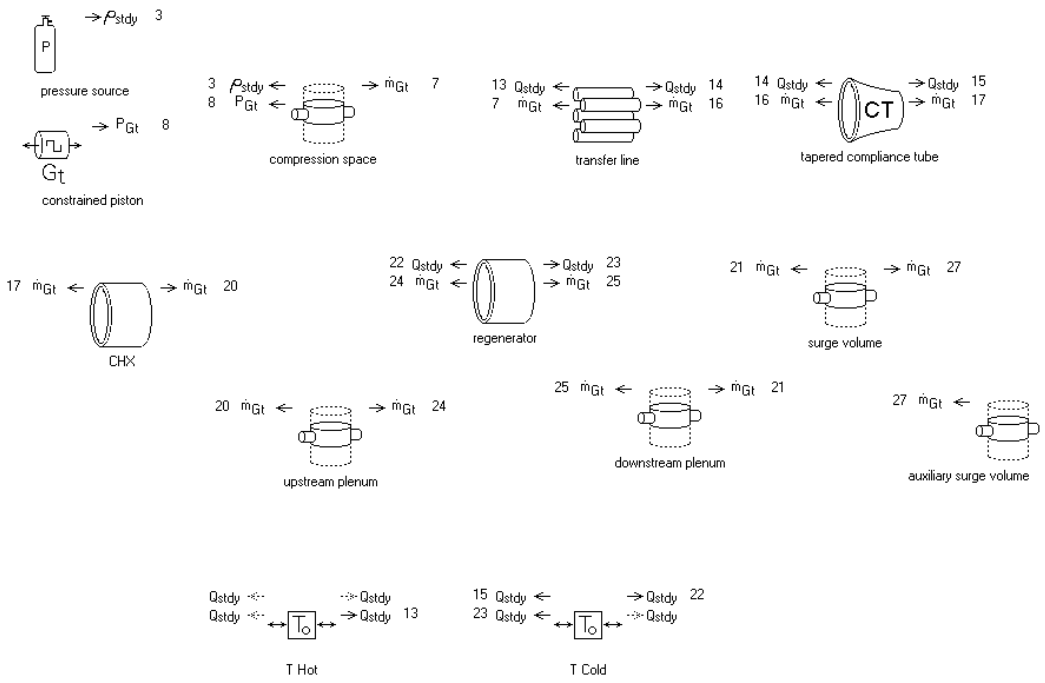

Figure 18. Graphical interface for Sage simulation of #400SS mesh and #325SS mesh regenerators

operating pressure in absolute terms specified by the pressure source sub component. A Fast Fourier Transform analysis is performed on the raw experimental data using Matlab's FFT functionality. The source code for the FFT analysis is included in Appendix A. The pressure amplitudes of the first harmonic frequency upstream and downstream of the regenerator are extracted from the FFT and are specified as target values in the Sage simulation. Using the built-in optimization tool in Sage, the stroke amplitude of the constrained piston sub model and the friction factor of the generic matrix within the regenerator are iteratively varied until the amplitudes of the first harmonic pressure oscillations upstream and downstream of the regenerator match the experimental values. For simulation purposes, only c_3 in Eq. (32) is varied during the optimization. Theoretically, the effect of the total frictional pressure gradient will be

negligible as the velocity approaches zero, so c_1 is neglected. The available literature also suggests that the c_3/Re_{d_h} term will dominate in low Reynolds number flows where laminar flow prevails [5]. The inclusion of the $c_2\,\mathrm{Re}^m$ term allows the simulation to track the behavior of the total frictional pressure drop more accurately at higher Reynolds number flows where inertial affects become significant, but it is neglected for this analysis were all experimental data points are well within the laminar domain. Once the optimization of the constant c_3 and the piston stroke amplitude are complete, the Darcy friction factor can be calculated according to Eq. (32)

4.3 CFD Modeling

4.3.1 Governing Equations

ANSYS Fluent is an industry-standard CFD tool for the modeling of two-dimensional and three-dimensional fluid flow and heat transfer [5,6]. Fluent uses various numerical techniques to solve the conservation of mass, momentum, and energy equations for both compressible or incompressible and steady or transient flow. The transient conservation of mass, momentum, and energy equations solved by Fluent are as follows [5,6]

$$\frac{\partial P}{\partial t}+\nabla\bullet\left(\rho\vec{u}\right)=0 \tag{33}$$

$$\frac{\partial}{\partial t}\left(\rho\vec{u}\right)+\nabla\bullet(\rho\vec{u}\vec{u})=-\nabla P+\nabla\bullet\left(\bar{\bar{\tau}}\right)+\rho\vec{g}+\vec{F} \tag{34}$$

$$\frac{\partial}{\partial t}(\rho E)+\nabla\bullet\left(\vec{u}\left(\rho E+P\right)\right)=\nabla\bullet\left(k\nabla T+\left(\bar{\bar{\tau}}\bullet\vec{u}\right)\right) \tag{35}$$

In the above equation, $\bar{\bar{\tau}}$ is the stress tensor and $\vec{F}$ represents the body forces acting on the fluid, including porous media effects. The conservation of energy equation presented in Eq. (35) does not include species diffusion or generation.

For the majority of cases, it is not computationally expedient to model the porous medium directly at the microscopic level. Such an approach is normally far too computationally expensive and can give vastly different results depending on the minute details of the geometric model. Instead, Fluent includes a porous media option which uses a volume-averaged approach similar to the Darcy-Forchheimer law presented in Eq. (1) to predict the pressure drop through the porous medium [5]. The porous medium effects are represented by the addition of a momentum source term given in terms of the superficial velocity, u_s, by Eq. (36).

$$S_i = -\left(\sum_{j=1}^{3} D_{ij} \mu u_{s_j} + \sum_{j=1}^{3} C_{ij} \frac{1}{2} \rho |u_s| u_{s_j} \right) \tag{36}$$

Superficial velocity is defined according to Eq. (29). The first term on the right hand side of Eq. (36) represents the viscous losses, which are synonymous with the Darcy term in Eq. (1), and the second term on the right hand side represents the inertial losses, which are synonymous with the Forchheimer term in Eq. (1). For the case of simple homogeneous porous media, Eq. (36) can be reduced to

$$S_i = -\left(\frac{\mu}{\alpha} u_{s_i} + C_2 \frac{1}{2} \rho |u_s| u_{s_i} \right) \tag{37}$$

where i represents the primary direction of flow, in this case the axial direction, α is the permeability with units of m^2, and C_2 is the inertial resistance with units of $1/\mathrm{m}$. Adding the momentum source term to Eq. (34) and assuming isotropic porosity yields the volume-averaged conservation of mass and momentum equations for the porous medium in terms of the physical velocity represented by Eq. (38) and (39), respectively.

$$\frac{\partial(\varepsilon\rho)}{\partial t}+\nabla\bullet\left(\varepsilon\rho\vec{u}\right)=0 \tag{38}$$

$$\frac{\partial\left(\varepsilon\rho\vec{u}\right)}{\partial t}+\nabla\bullet\left(\varepsilon\rho\vec{u}\vec{u}\right)=-\varepsilon\nabla P+\nabla\bullet(\varepsilon\bar{\bar{\tau}})+\varepsilon\vec{B}_f-\left(\frac{\varepsilon^2\mu}{\alpha}\vec{u}+\frac{\varepsilon^3 C_2}{2}\rho\left|\vec{u}\right|\vec{u}\right) \tag{39}$$

In Eq. (39), $\vec{B}_f$ represents the body forces such as gravity, and the last two terms on the right hand side represent the viscous and inertial resistances, which constitute the momentum source term given in Eq. (37). Comparison of Eq. (39) and Eq. (2) allows the viscous and inertial resistances in Fluent to be recast in terms of the commonly used Darcy term, K, and Forchheimer coefficient, c_f, as follows.

$$K=\alpha \tag{40}$$

$$c_f=\frac{C_2\sqrt{K}}{2} \tag{41}$$

Within the Fluent graphical user interface, the permeability, α, is specified by the viscous resistance term, β, which is simply the inverse of permeability with units of

$1/\mathrm{m}^2$. The inertial resistance, C_2, with units of $1/\mathrm{m}$ is specified directly within the graphical interface.

$$\beta = \frac{1}{\alpha} \tag{42}$$

Detailed descriptions of ANSYS Fluent theory and usage can be found in [6] and [5]. Details specific to the modeling of the experimental test section will be provided here for convenience.

4.3.2 Model Setup

The prototypical regenerator, retaining ring void space, and surge volume are modeled together using a 2D, axisymmetric model shown in Figure 19 and Figure 20. A transient, pressure-based solver is used to solve the governing conservation of mass, momentum, and energy equations. The flow is assumed to be laminar within the entire model according to the hydraulic diameter-based Reynolds number calculated from Eq. (24). The working fluid within the model is ideal helium. The pressure of the working fluid at each time step and location within the model is calculated based on the ideal gas law. This requires the activation of the energy equation within the Fluent model, even though the entire domain is assumed to be isothermal. A constant temperature boundary condition is applied at the inlet and walls of the axisymmetric model based on the experimental measurements. The operating pressure of the model is defined based on the mean operating pressure of the experimental test section, also known as the charge pressure, and the atmospheric pressure measurement. The oscillating pressure boundary condition at the inlet is added to the mean operating pressure at each time step to

determine the total, absolute pressure at the inlet of the model. The oscillating pressure inlet boundary condition is specified with a user defined function which defines the instantaneous pressure using a Fourier series of cosines where the pressure amplitude and phase of the first five harmonic frequencies are used. The text of the user defined function can be found in its entirety in Appendix B. Modeling the regenerator and surge volume together as a closed-ended system is advantageous because it eliminates the need for a second boundary condition. The interfaces between the regenerator, void space, and surge volume are simply modeled as interior regions. Figure 19 shows the Fluent model for regenerator 1, and Figure 20 shows the Fluent model for regenerators 2 and 3.

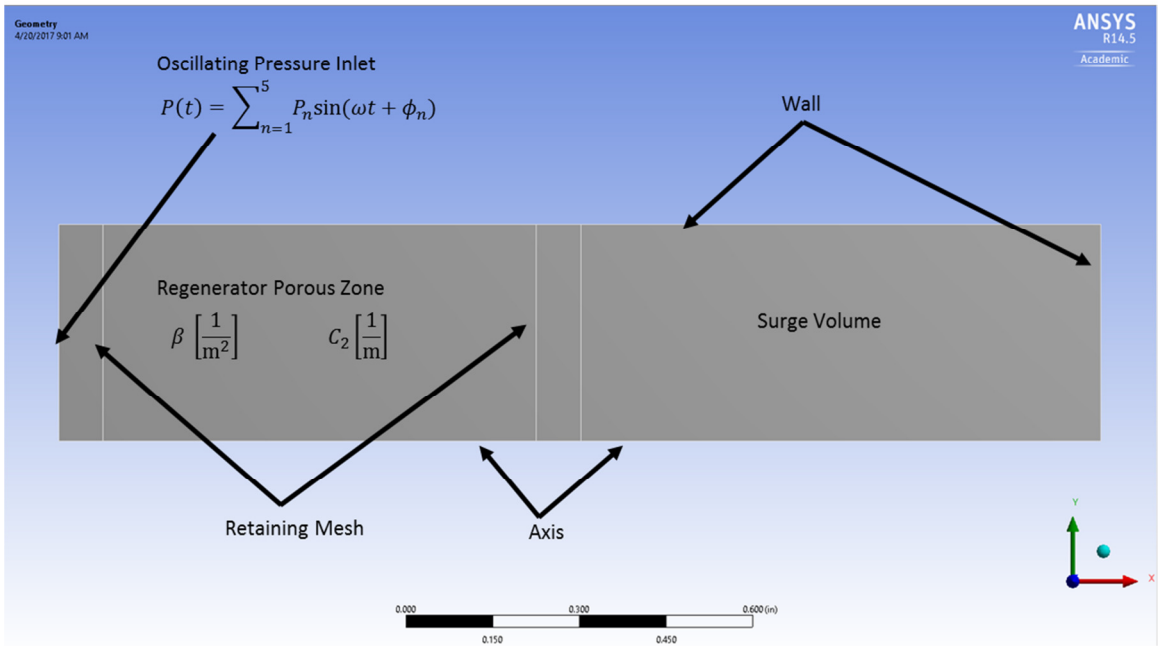

Figure 19. 2D, axisymmetric Fluent model of prototypical regenerator and surge volume with oscillating pressure inlet boundary condition for $Er_{0.5}Pr_{0.5}$ regenerator

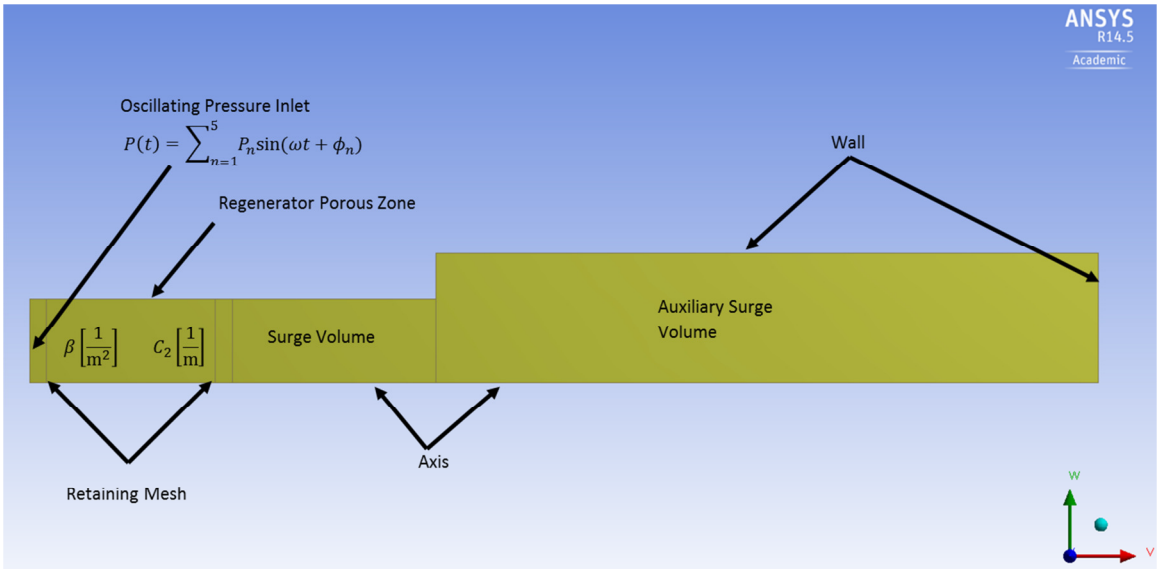

Figure 20. 2D, axisymmetric Fluent model of prototypical regenerator and surge volume with oscillating pressure inlet boundary condition for regenerators 2 and 3

4.3.3 Time Step and Mesh Size Sensitivity

Mesh size sensitivity analysis was performed for the 30Hz operating frequency at 30V input voltage, 1.14 MPa (150psig) charge pressure, and 300K operating temperature with the $Er_{0.5}Pr_{0.5}$ rare-earth regenerator filler material. Figures 21, 22, and 23 show the finished meshes for grid sizes of 0.635mm (0.025in), 0.254mm (0.010in), and 0.127mm (0.005in), respectively. As shown in Figure 19 and Figure 20, the oscillating pressure boundary condition is applied to the inlet of the regenerator with a user defined function. The hydrodynamic resistance parameters of the porous zone are defined according to the technique outlined in Section 4.3.4, and the pressure and mass flow rate at the outlet of the regenerator are monitored at each time step. The time step is specified based on the operating frequency of the simulation. In general, 150 time steps per period are sufficient to model oscillating laminar flow. For an operating frequency of 30Hz, a time step of

0.0002s was used with 500 time steps to simulate over 3 full periods. Convergence was evaluated based on the outlet mass flow rate and maximum outlet pressure of the regenerator. Results are shown in Table 2. Based on the analysis, a mesh size of 0.254mm (0.010in) was chosen and used for all simulations.

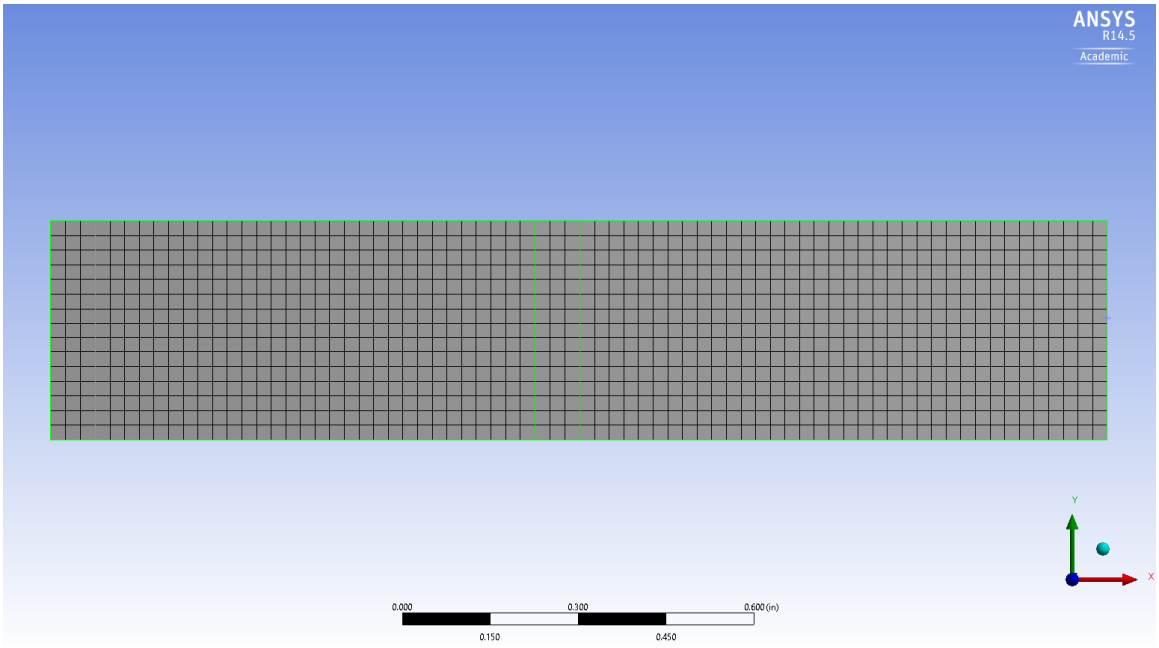

Figure 21. Mapped Face Mesh with 0.635mm (0.025in) Grid Size – Regular Mesh

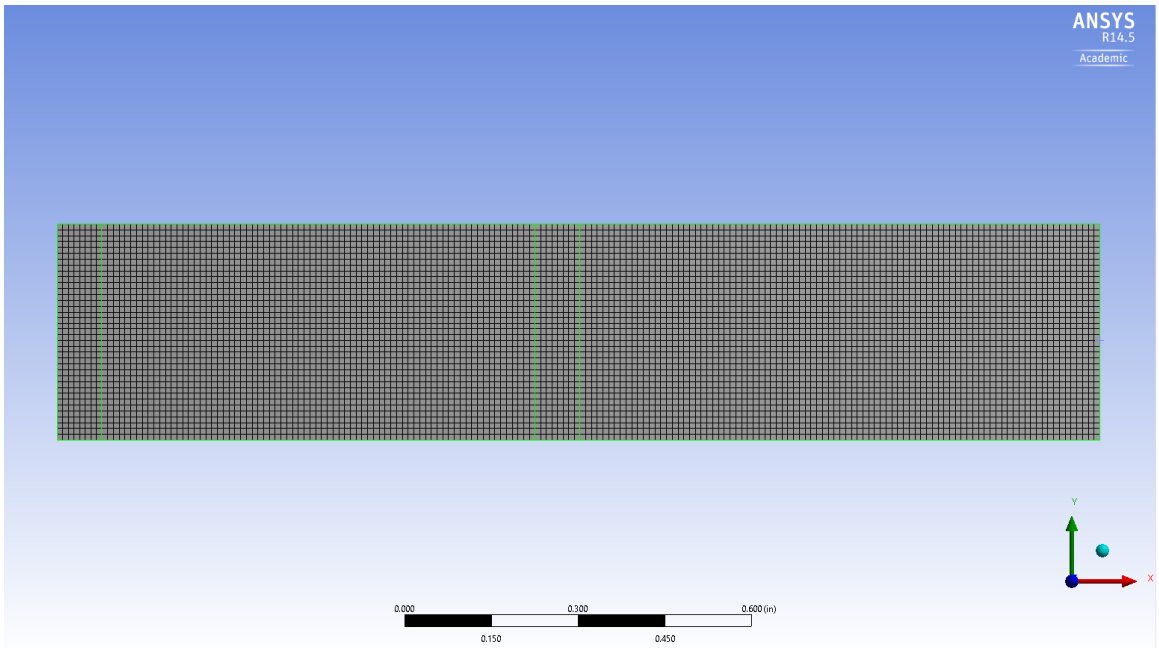

Figure 22. Mapped Face Mesh with 0.254mm (0.010in) Grid Size – Fine Mesh

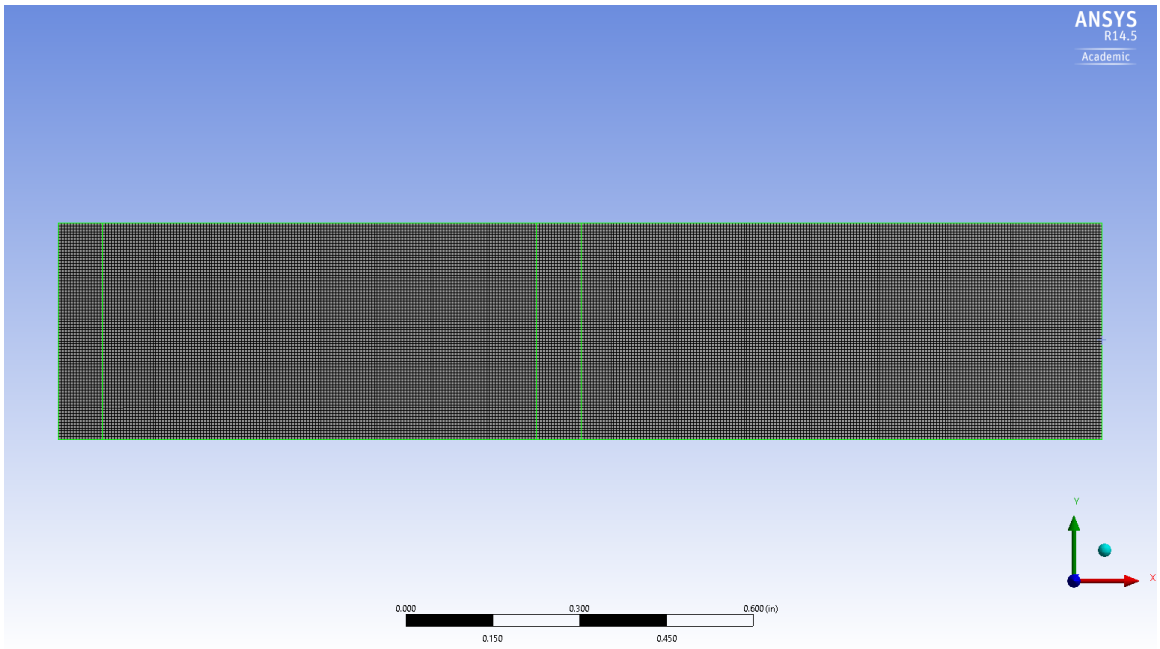

Figure 23. Mapped Face Mesh with 0.127mm (0.005in) Grid Size – Superfine Mesh

Table 2. Mesh Sensitivity with 30Hz, 30V, 1.14MPa, 300K Operating Condition

Mesh	Grid Size	Maximum Experimental Downstream Mass Flow Rate [kg/s]	Maximum Simulation Downstream Mass Flow Rate [kg/s]	Maximum Experimental Downstream Pressure [Pa]	Maximum Simulation Downstream Pressure [Pa]
Regular	0.635mm	1.30E-04	1.03E-04	8.16E+04	79710
Fine	0.254mm	1.30E-04	1.05E-04	8.16E+04	79750
Superfine	0.127mm	1.30E-04	1.05E-04	8.16E+04	79750

4.3.4 Porous Zone Hydrodynamic Resistance Parameters

Within the Cell Zone Conditions tab of the Fluent GUI, the user must specify the viscous resistance, $\beta = 1/\alpha$, and inertial resistance, C_2, of the porous zone as well as the porosity of the porous medium. The usual method for determining the hydrodynamic resistance parameters, as previously discussed in section 2.3, is to measure the pressure drop across the porous medium experimentally and then construct a computational model of the experimental domain, varying the hydrodynamic resistance parameters iteratively until the upstream and downstream pressures of the simulation match those of the experiment. This approach has been employed successfully by Cha and Pathak [1,38,43,44,48], however such an approach has an obvious draw back. The momentum source term representing the hydrodynamic effects of the porous medium, Eq. (37), is comprised of two parts: the viscous resistance term which is a function of the fluid velocity, u_{s_i}, and the inertial resistance term which is a function of the fluid velocity squared, $|u_s|u_{s_i}$. This means that for a specific flow velocity there can be multiple combinations of β and C_2

that produce the same frictional pressure gradient, represented by the momentum source term, S_i, and therefore produce the same upstream and downstream pressure oscillations.

To address this, the approach employed by Cha and Pathak was to neglect the inertial resistance $\left(C_2 = 0\right)$ for the lowest measurable mass flow rate and iteratively vary the viscous resistance until the pressure oscillations within the Fluent model matched the experimental values [38,44,48]. Based on Eq. (37) and Eq. (39) the viscous resistance should dominate over the inertial resistance for sufficiently low mass flow rates, and some literature suggests that the inertial resistance may be neglected for the entire laminar regime. While the viscous resistance component of the momentum source term does appear to dominate for the range of experimental values under investigation, at no point is the inertial resistance negligible, even for the lowest experimental mass flow rate possible with the available apparatus. This was determined by varying C_2 by several orders of magnitude while keeping β constant and recording the effects. Theoretically, if the inertial resistance is negligible due to the velocity-squared component in the momentum source term, then the simulation results should be the same for constant β values regardless of the value of C_2, but this was not the case.

Therefore the viscous and inertial resistance parameters for Fluent were determined from the total Frictional pressure gradient, F, and dimensionless friction factor, f, in Sage. Comparing Eq. (22) with Eq. (39) reveals that the total frictional pressure gradient in Sage is equivalent to the momentum source term for porous media in Fluent if one neglects the three-dimensional shear stresses, which are negligible compared to the other forces and are only relevant in the vicinity of the regenerator wall.

$$F = \frac{\Delta P}{L} = S_i = \frac{\varepsilon \mu}{\alpha} u + \frac{\varepsilon^2 C_2}{2} \rho u^2 \tag{43}$$

Equating the total frictional pressure gradient from Sage to the definition of the momentum source term in Fluent suggest that F can be correlated as a quadratic function of flow velocity, u, where the leading coefficient of the u^2 term will depend upon the inertial resistance of the medium and the leading coefficient of the u term will depend upon the viscous resistance of the medium. It would appear that F or S_i could simply be correlated with respect to flow velocity and that the appropriate values for α and C_2 could be extracted from the leading coefficients, but in practice, the physical properties of the fluid such as the density and viscosity of the fluid, which vary based on the mean operating pressure and temperature, make it impossible to correlate all of the experimental data points with a single function.

In order to recast the experimental data into a single correlation, Eq. (43) can be non-dimensionalized using the hydraulic diameter-based Reynolds number, Re_{d_h}, as follows.

$$S_i \frac{\rho d_h^3}{\mu^2} = \frac{\varepsilon d_h^2}{\alpha} \mathrm{Re}_{d_h} + \frac{\varepsilon^2 C_2 d_h}{2} \mathrm{Re}_{d_h}^2 \tag{44}$$

$$\Gamma = S_i \frac{\rho d_h^3}{\mu^2} \tag{45}$$

$$\mathrm{A} = \frac{\varepsilon d_h^2}{\alpha} \tag{46}$$

$$\mathrm{B} = \frac{\varepsilon^2 C_2 d_h}{2} \tag{47}$$

$$\Gamma = A\,\mathrm{Re}_{d_h} + B\,\mathrm{Re}_{d_h}^2 \tag{48}$$

For convenience, the dimensionless momentum source term has been assigned the arbitrary variable, Γ. Assigning the arbitrary coefficients A to the leading term of Re_{d_h} and B to the leading coefficient of $\mathrm{Re}_{d_h}^2$ yields the following expression for α and C_2 where the coefficients A and B can be extracted from the quadratic fit of the experimental data.

$$\alpha = \frac{\varepsilon d_h^2}{\mathrm{A}} \tag{49}$$

$$C_2 = \frac{2\mathrm{B}}{\varepsilon^2 d_h} \tag{50}$$

CHAPTER 5. RESULTS AND DISCUSSION

5.1 Regenerator 1: $Er_{0.5}Pr_{0.5}$ Powder

Regenerator filler materials made from rare-earth metals such as erbium-praseodymium alloy have been gaining in popularity in recent years for use in high-capacity, low-temperatures coolers. The advantage of ErPr over other more common metals such as lead is that it maintains high thermal storage capacity at temperatures well below 70K, where many other more common coolers operate. Regenerator 1 was packed with 55μm-diameter $Er_{0.5}Pr_{0.5}$ powder according to the process outlined in Section 3.2 to a porosity of 37%, which corresponds to a random packing of equally sized spheres. Packed sphere beds generally have much higher densities than packed screen regenerators. While there is no good way to control the exact packing arrangement of the spheres, various porosities can be achieved by using spheres of varying diameters. Several researches have provided pressure drop correlations for packed-sphere beds of varying porosity and sphere diameters using experimental and CFD-assisted methodologies [33,49,50]. In this work, only single-diameter randomly packed spheres are considered.

5.1.1 Experimental Results

The transient pressure oscillations at the inlet and outlet of regenerator 1 were measured and transformed according to the process outlined in Section 3.2. The regenerator was tested at mean operating pressures of 2.86 MPa (400 psig), 1.13 MPa (150 psig), and 0.10 MPa (0 psig) and frequencies of 30, 40, and 50 Hz. Measurements were performed at ambient and cryogenic temperatures for all charge pressures and

frequencies. Although the Sumitomo GM cryocooler is capable of reaching a no-load temperature of 32K, the operating temperature was limited by helium leakage from the test section at low temperatures. It is believed that a mismatch of thermal expansion coefficients may have led to gas leakage around the pressure sensor ports when the temperature went below about 100K. Helium leakage was worse at higher mean pressures, which led to a higher minimum test temperature for those cases. A better future solution may be to permanently install the pressor sensors using cryogenic epoxy. For the following results, 2.86 MPa was chosen to represent a typical operating pressure for a high-power Stirling or pulse-tube cooler, and 1.13 MPa was chosen to be compatible with previous results in the literature, specifically Pathak [48]. Finally, the lowest charge pressure, 0.10 MPa was chosen to minimize helium leakage from the test section to enable testing at lower temperatures.

Figures 24, 25, and 26 show the time-varying pressure oscillations for charge pressures of 2.86, 1.13, and 0.10 MPa, respectively. The pressure was recorded at the pressor sensor locations specified in Figure 11. In the following figures, the term "Upstream" refers to the side of the component that faces the pressure wave generator and "Downstream" refers to the side facing the surge volume. Although the pressure is only measured at the outer radius, it is assumed, and indeed verifiable with CFD analysis, that the instantaneous pressure is uniform through the cross section. The PCB brand 102A10 and 102A05 pressure transducers only measure the pressure amplitude, not the absolute pressure. An amplitude of zero in Figures 24, 25, and 26 indicates that the pressure at that point is simply equal to the charge pressure of the PWG. It is assumed that the mean operating pressure does not change significantly between the upstream and

downstream locations within the experimental test section. The pressure waves are the actual, raw experimental data acquired using Labview data acquisition software. Although it is customary to represent experiment data points as discreet markers, the extremely high sample rate makes it impossible to distinguish individual measurements, so the data is instead shown using smooth lines. The pressure waves are clearly not perfectly sinusoidal, but are instead represented by the first five harmonics of the FFT.

As expected, Figures 24, 25, and 26 indicate that the pressure amplitudes decrease in magnitude as one moves further downstream from the PWG. For brevity, results are shown at an operating frequency of 30Hz and 30V PWG voltage input, but many more measurements were taken. Although the pressure upstream or downstream of the regenerator may be higher at a specific moment in time due to the oscillatory nature of the flow, the amplitude of the pressure waves upstream, or the side facing the pressure wave generator, should always be higher. For all three charge pressures, the greatest drop in pressure amplitude occurs across the $Er_{0.5}Pr_{0.5}$ regenerator. This is to be expected since the $Er_{0.5}Pr_{0.5}$ regenerator is much less porous than the #100 copper mesh heat exchanger. In general, the pressure amplitudes across the regenerator are higher for higher charge pressures, and the pressure drop is higher at higher temperatures. One would also expect the amplitude at the upstream and downstream portions of the surge volume to be the same, since there is no porous media within that component. This is true for the 0.10 MPa case and for the 1.13 MPa case at 300K, but for the 2.86 MPa measurements and for 1.13 MPa at 75K the amplitude of pressure oscillations at the downstream portion of the surge volume exceeded the amplitude at the upstream portion. This may indicate that there are some higher-order harmonic effects present within the

surge volume at these operating conditions. The effect appears to be more pronounced when the mass flow rate exiting the regenerator is greater such as at higher charge pressures and lower operating temperatures. The effect can be reduced and eliminated by adjusting the frequency and amplitude of the PWG, which suggests that the pressure or mass flow rate waves are achieving some sort of resonance at certain operating conditions. It may also be possible to eliminate this issue by installing a more extensive inertance network downstream of the regenerator consisting of a pulse tube, inertance tube, and surge volume to simulate a real PTC, but this would make predicting the mass flow rate exiting the regenerator much more difficult. Although the higher pressure amplitude at the downstream side of the SV is unexpected, it does not appear to affect the mass flow rate through the regenerator or the determination of the appropriate hydrodynamic resistance parameters for the porous medium.

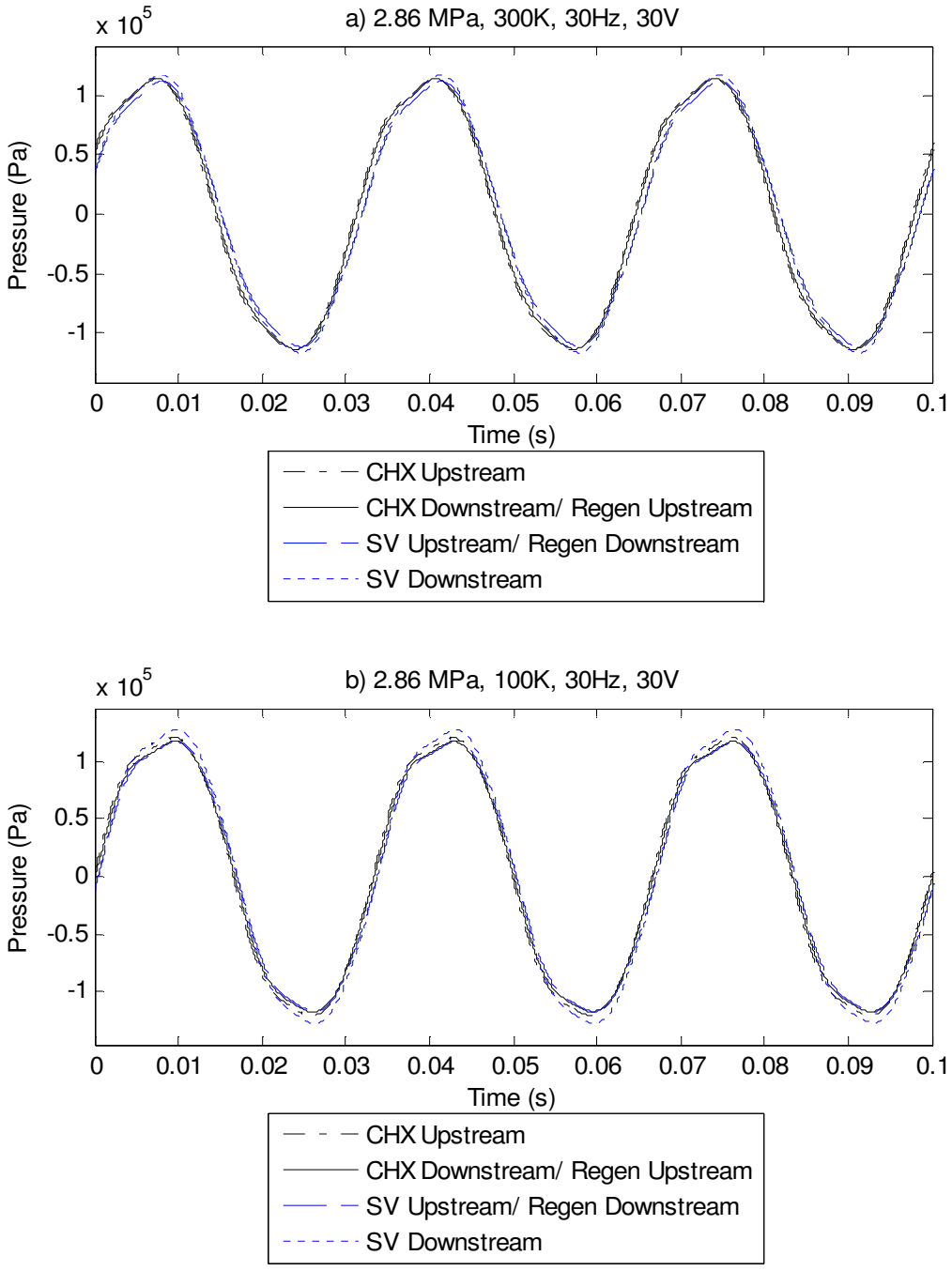

Figure 24. Instantaneous pressure across the $Er_{0.5}Pr_{0.5}$ regenerator at 2.86 MPa for a) 300K and b) 100K at 30Hz and 30V PWG input voltage

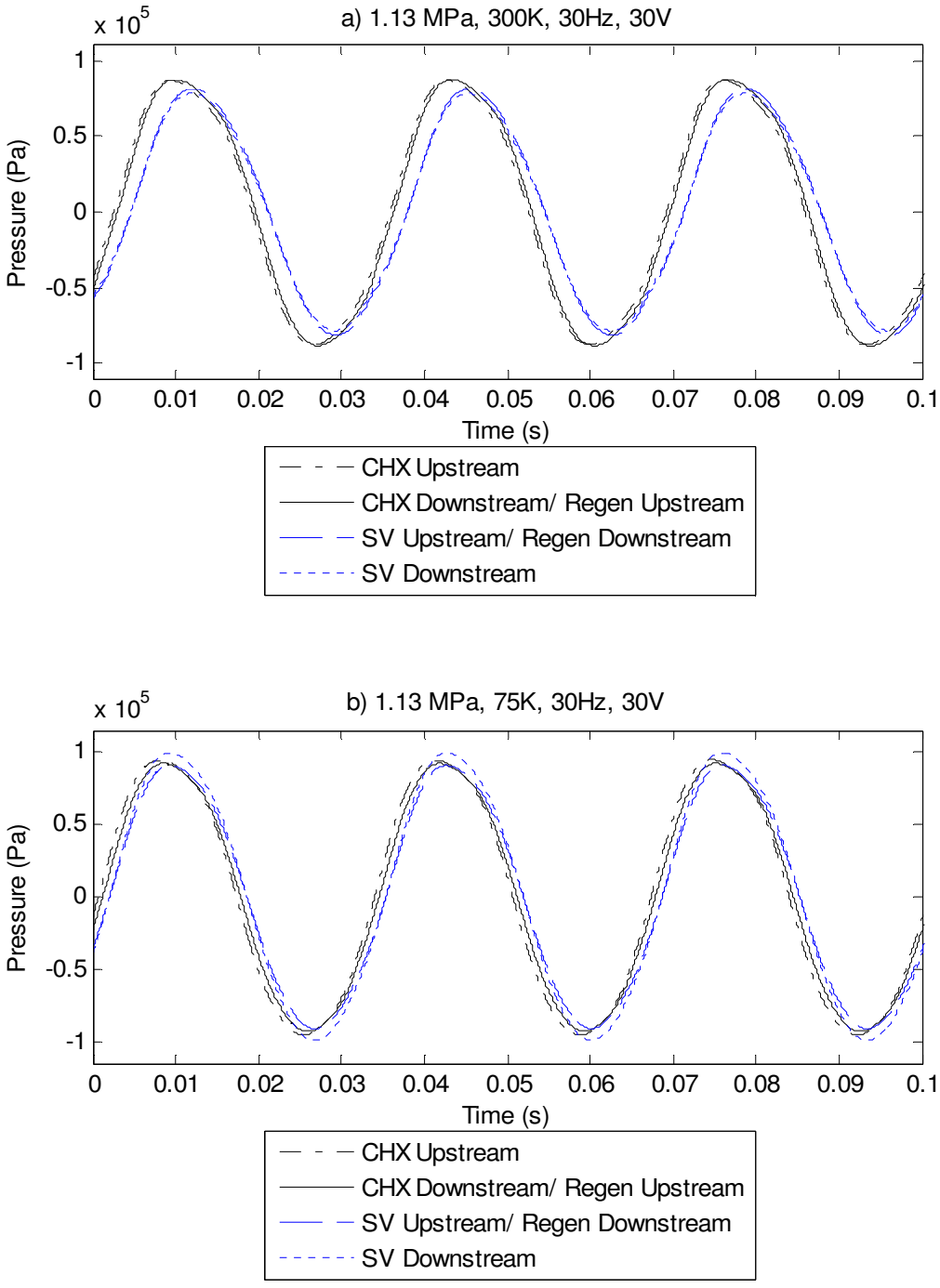

Figure 25. Instantaneous pressure across the $Er_{0.5}Pr_{0.5}$ regenerator at 1.13 MPa for a) 300K and b) 75K at 30Hz and 30V PWG input voltage

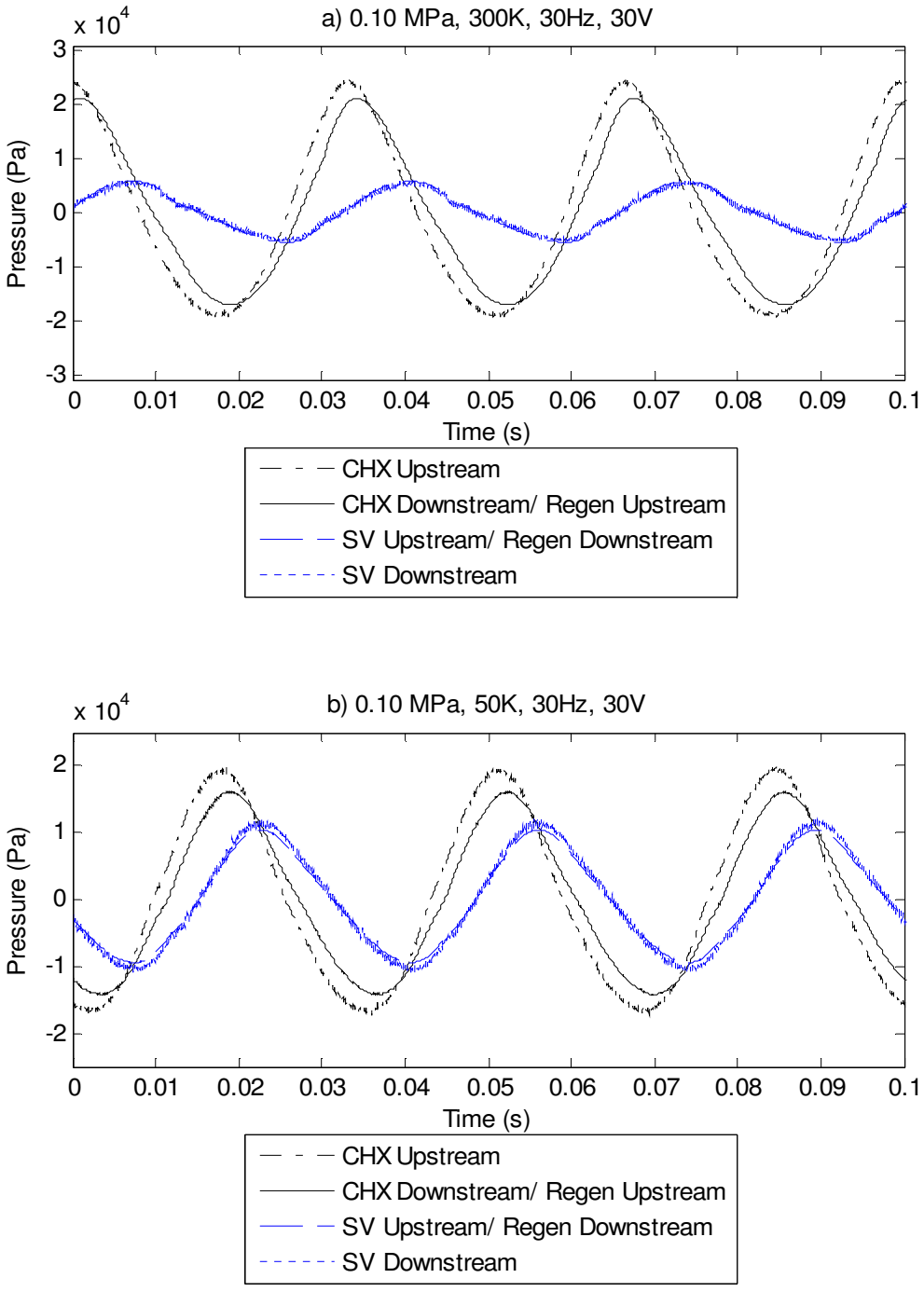

Figure 26. Instantaneous pressure across the $Er_{0.5}Pr_{0.5}$ regenerator at 0.10 MPa for a) 300K and b) 50K at 30Hz and 30V PWG input voltage

Figures 27, 28, and 29 show the time-varying pressure and mass flow rate across the regenerator for charge pressure of 2.86, 1.13, and 0.10, respectively. Once again, for brevity only a single frequency and voltage input are shown. As expected, the pressure amplitude downstream of the regenerator is consistently lower than the pressure amplitude upstream of the regenerator. The mass flow rate is calculated from the time derivative of the surge volume pressure according to Eq. (9) based on an energy balance of the surge volume. Because of this, the experimental mass flow rate is only measurable at the downstream location. When the upstream pressure is greater than the downstream pressure, the mass flow rate into the surge volume is positive, and when the downstream pressure is greater than the upstream pressure the mass flow rate into the surge volume is negative. When the pressures are equal, the mass flow rate is zero. Although the pressure drop across the regenerator does appear to be higher at higher temperatures, the mass flow rate is actually higher at lower temperatures due to the increased density of the working fluid. This also causes the mass flow rate to be higher at higher charge pressures for the same temperature.

According to the pressure-mass flow rate phase relationship represented by Eq.(11), the mass flow rate should be at its peak when the instantaneous pressure difference across the regenerator is the greatest. Indeed, this is the case with the experimental data. Figures 30, 31, and 32 show the experimental data for the instantaneous pressure difference across the regenerator and downstream mass flow rate versus flow time. The figures indicate that the peak mass flow rate coincides with the peak pressure drop across the regenerator as predicted by Eq. (11). At 2.86 MPa, the instantaneous pressure drop oscillations are clearly high-order sinusoids. Comparison of

Figure 30 with Figure 27 shows that the irregularities of the pressure drop oscillations agree with the curvature of the upstream and downstream pressure waves. If the first five harmonics of the Fourier transform are needed to accurately represent the upstream and downstream pressure oscillations, then it stands to reason that the difference between the upstream and downstream pressure would resemble a 10^{th} order harmonic, depending on the exact values of the amplitudes and phases. The pressure drop oscillations at 1.13 MPa appear more regular, presumably because the upstream and downstream pressures at 1.13 MPa more closely resemble pure sinusoids. The experimental mass flow rate and instantaneous pressure drop at 0.10 MPa are shown in Figure 32. The data at 0.10 MPa appear to be much noisier than for the other charge pressures due to the considerably lower magnitude of the mass flow rates at this charge pressure. However, the data still follows a clearly oscillates sinusoidaly and coincides with the instantaneous pressure drop across the regenerator.

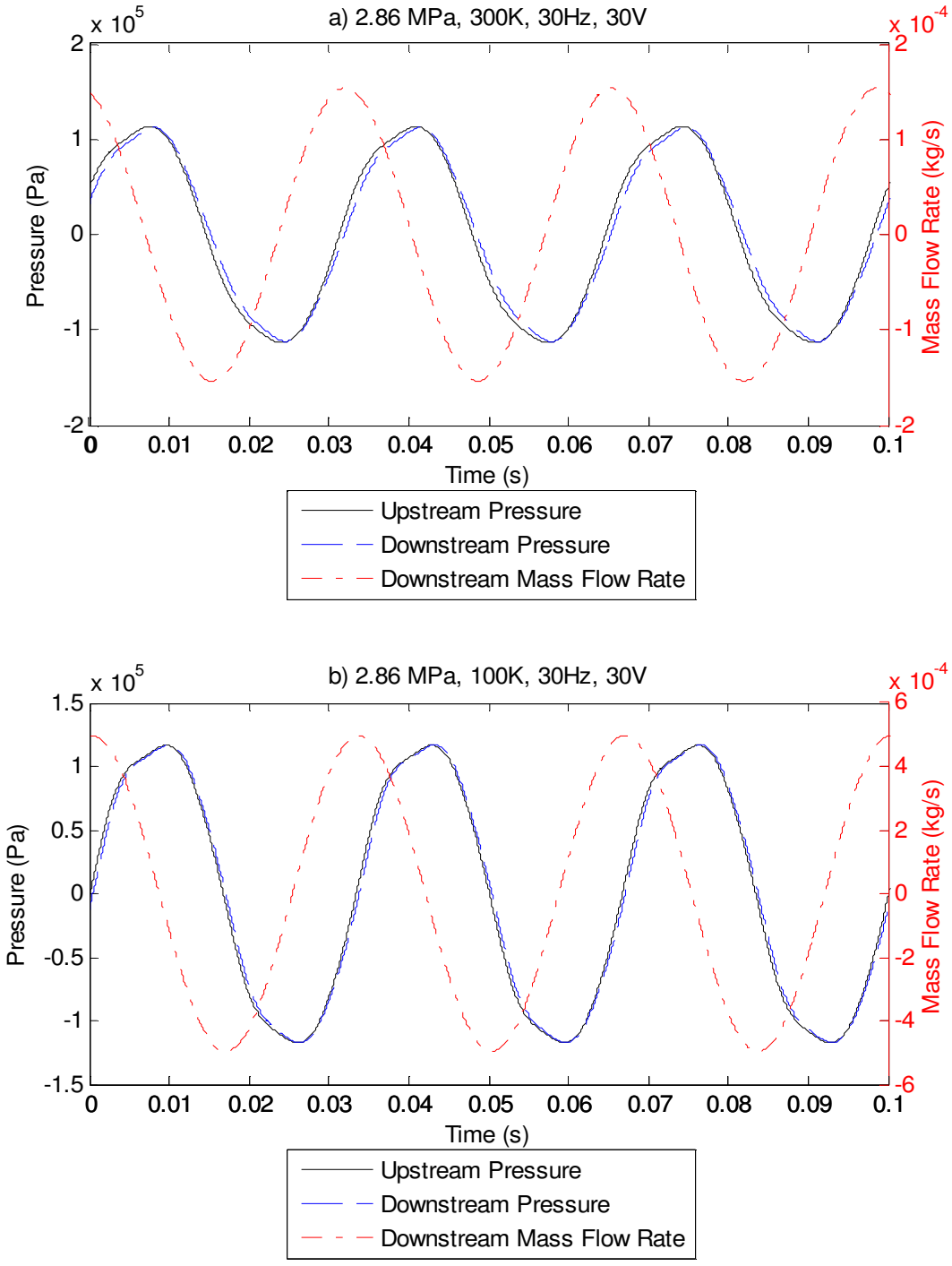

Figure 27. Transient pressure and mass flow rate oscillations for the $Er_{0.5}Pr_{0.5}$ regenerator at 2.86 MPa for a) 300K and b) 100K at 30Hz and 30V PWG voltage input

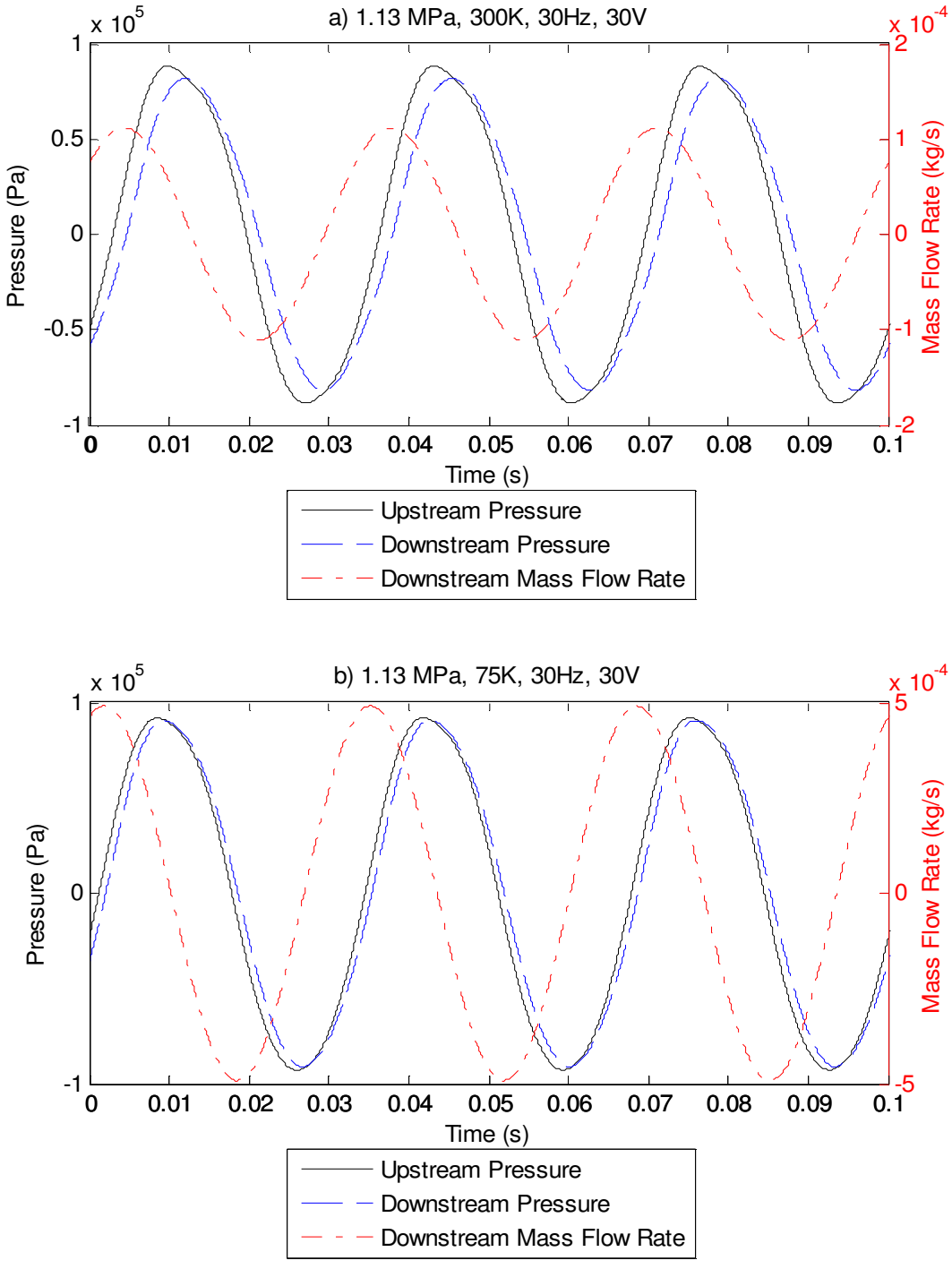

Figure 28. Transient pressure and mass flow rate oscillations for the $Er_{0.5}Pr_{0.5}$ regenerator at 1.13 MPa for a) 300K and b) 75K at 30Hz and 30V PWG voltage input

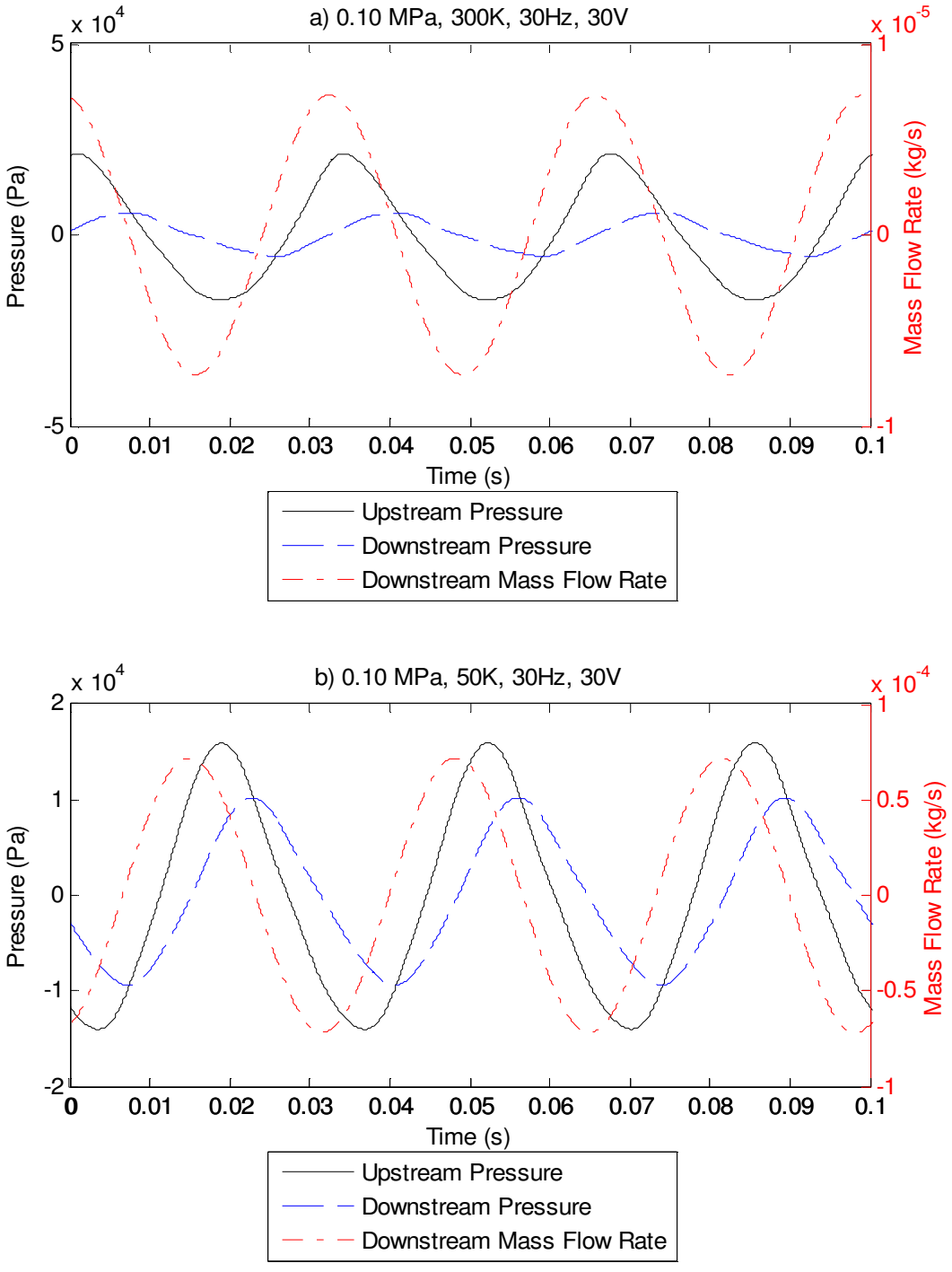

Figure 29. Transient pressure and mass flow rate oscillations for the $Er_{0.5}Pr_{0.5}$ regenerator at 0.10 MPa for a) 300K and b) 50K at 30Hz and 30V PWG voltage input

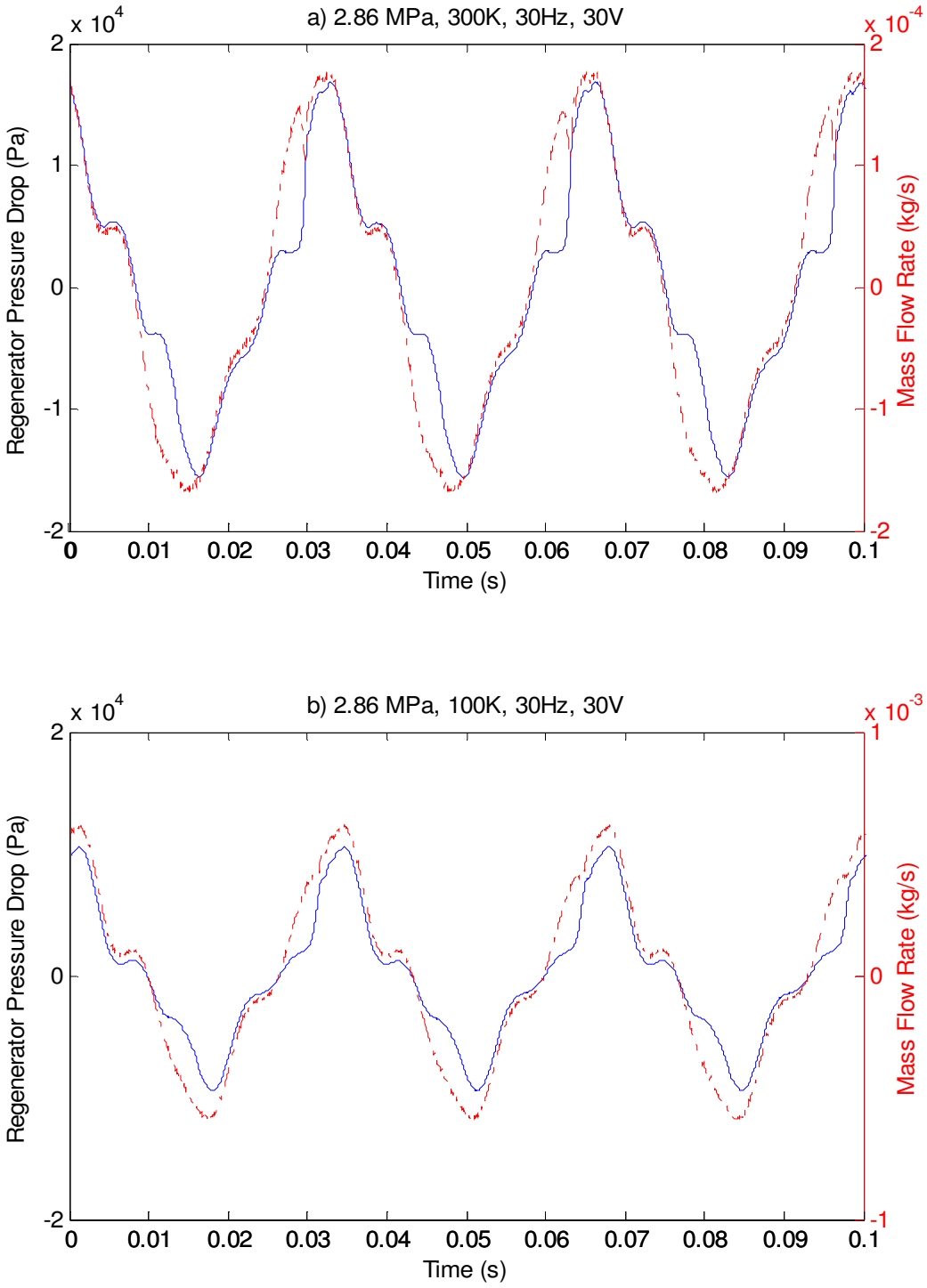

Figure 30. Regenerator Pressure Drop compared to downstream mass flow rate for the $Er_{0.5}Pr_{0.5}$ regenerator at 2.86 MPa for a) 300K and b) 100K at 30Hz and 30V PWG voltage input

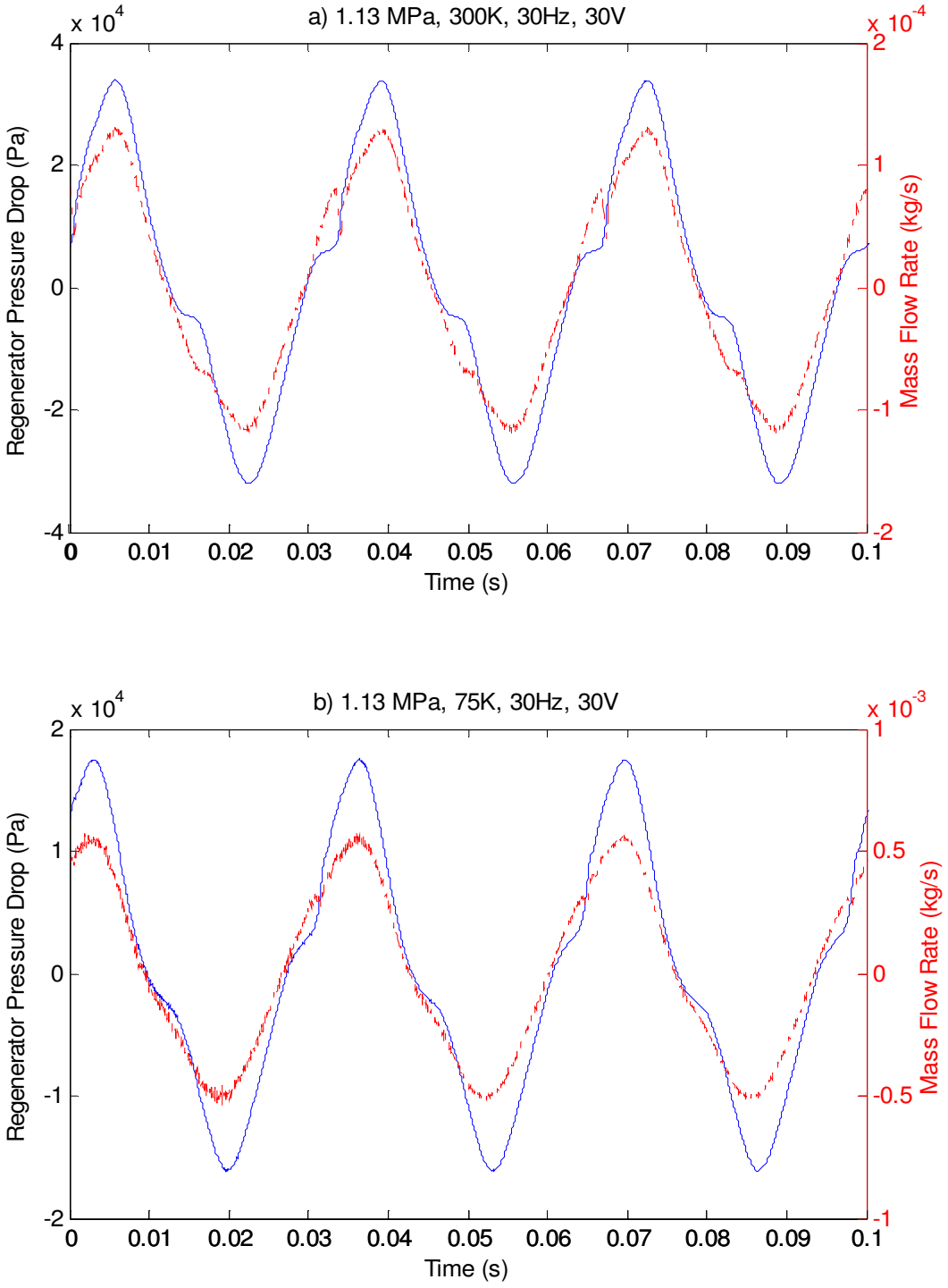

Figure 31. Regenerator Pressure Drop compared to downstream mass flow rate for the $Er_{0.5}Pr_{0.5}$ regenerator at 1.13 MPa for a) 300K and b) 75K at 30Hz and 30V PWG voltage input

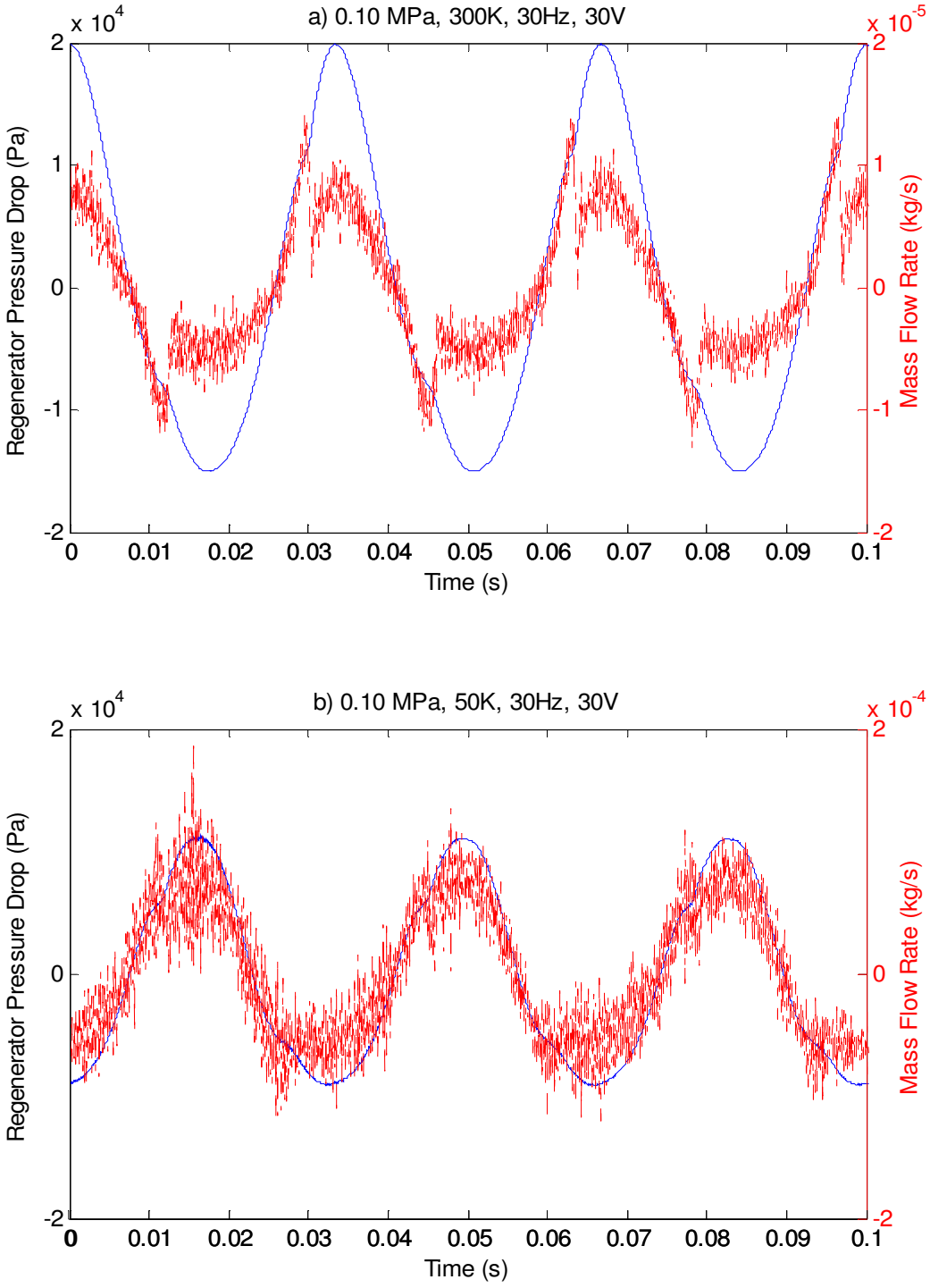

Figure 32. Regenerator Pressure Drop compared to downstream mass flow rate for the $Er_{0.5}Pr_{0.5}$ regenerator at 0.10 MPa for a) 300K and b) 50K at 30Hz and 30V PWG voltage input

Figures 33, 34, and 35 show the maximum instantaneous pressure drop across the regenerator as a function of the peak physical flow velocity for mean operating pressures of 2.86, 1.13, and 0.10 MPa, respectively. The peak velocity is simply calculated from the peak mass flow rate as follows

$$u_{\text{peak}} = \frac{\dot{m}_{\text{peak}}}{\rho A_f} \tag{51}$$

The results indicate that the pressure drop is independent of frequency when plotted vs. flow velocity so all experimental frequencies are shown together. The uncertainty bars are calculated according to section 3.3 as 0.3% of the full scale value of 690 kPa, which gives a total uncertainty of 2,070 Pa. The results indicate that the maximum pressure drop clearly varies based on operating pressure and temperature, and that the peak pressure drop is larger for higher charge pressures and operating temperatures.

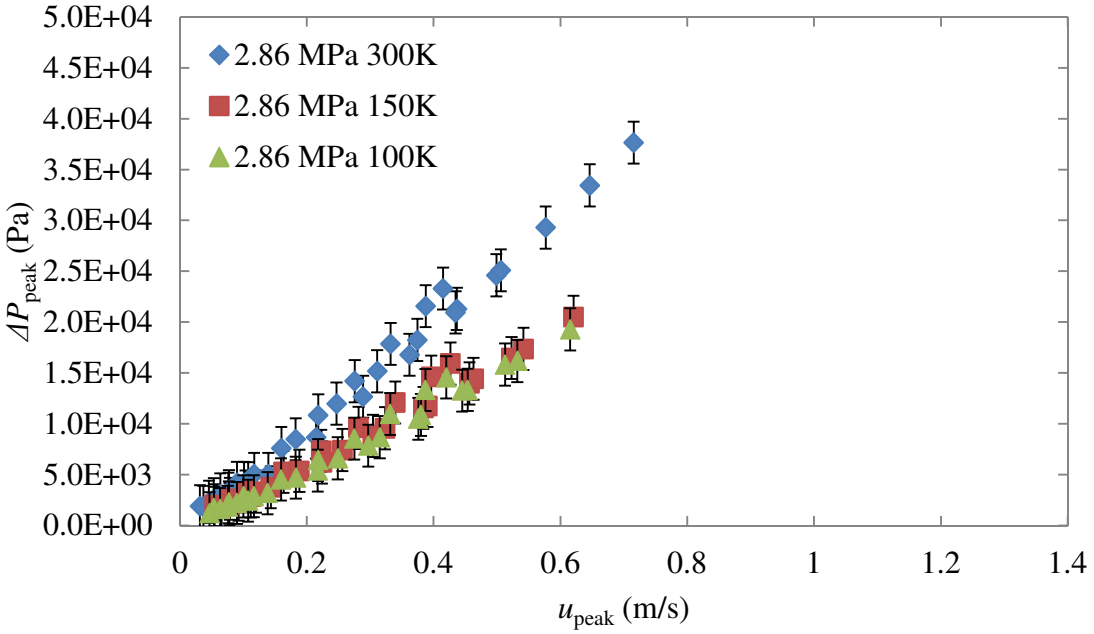

Figure 33. Maximum instantaneous pressure drop across the $Er_{0.5}Pr_{0.5}$ regenerator as a function of peak flow velocity at 2.86 MPa

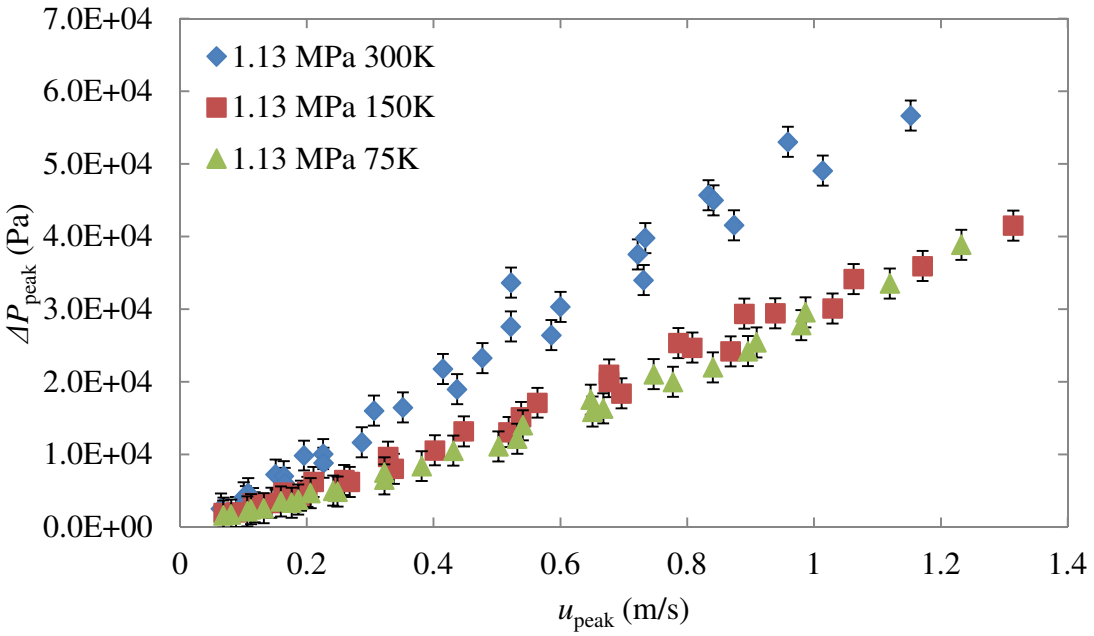

Figure 34. Maximum instantaneous pressure drop across the $Er_{0.5}Pr_{0.5}$ regenerator as a function of peak flow velocity at 1.13 MPa

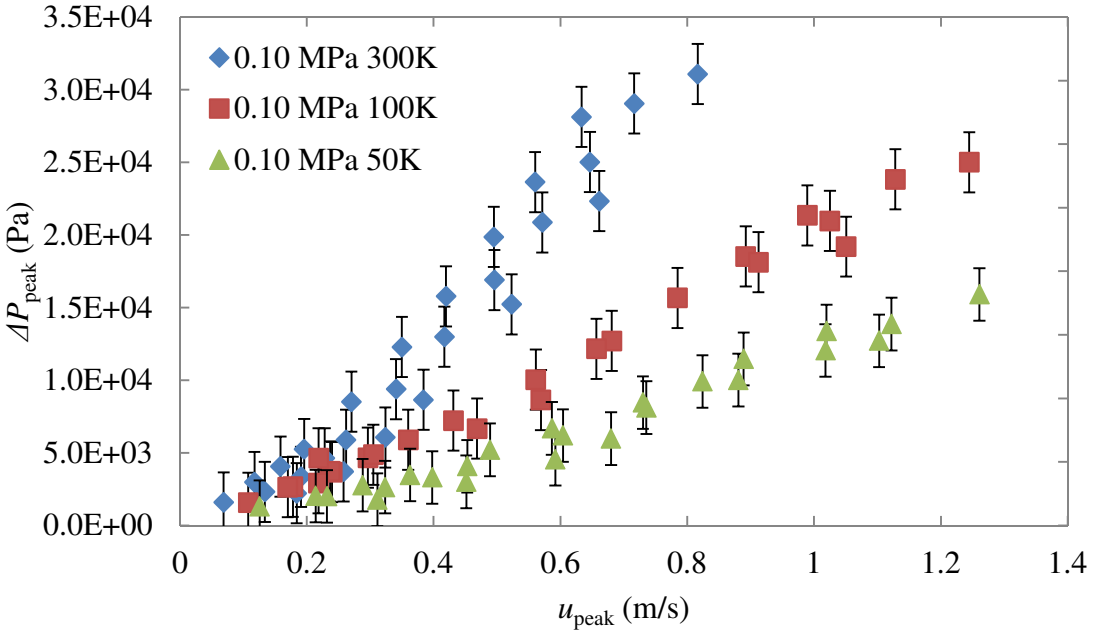

Figure 35. Maximum instantaneous pressure drop across the $Er_{0.5}Pr_{0.5}$ regenerator as a function of peak flow velocity at 0.10 MPa

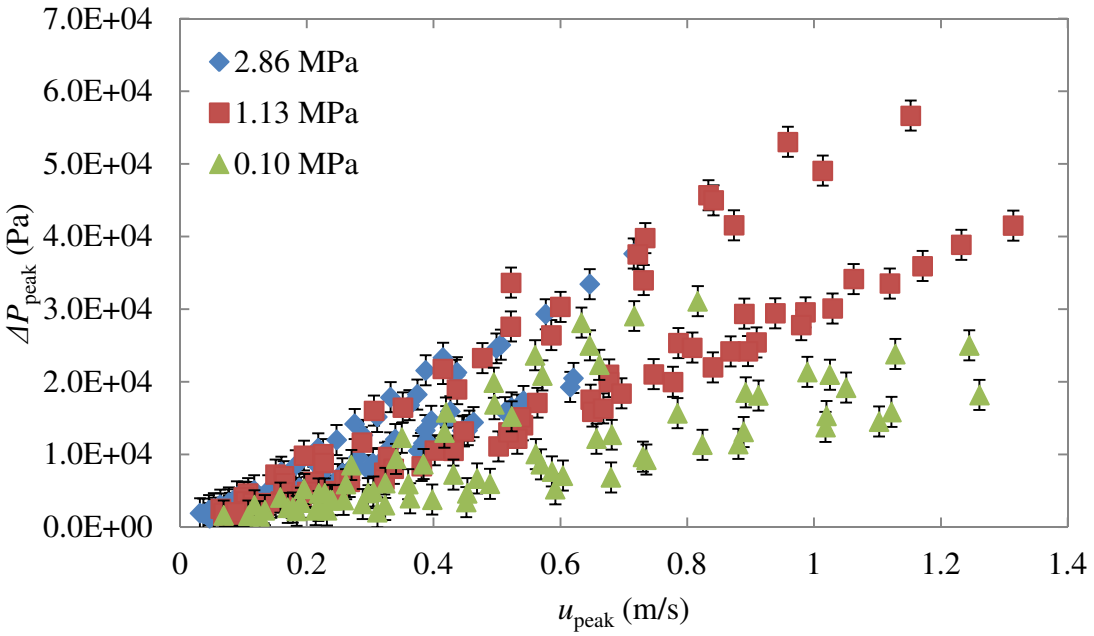

Figure 36. Maximum instantaneous pressure drop across the $Er_{0.5}Pr_{0.5}$ regenerator as a function of peak flow velocity at 2.86, 1.13, and 0.10 MPa

5.1.2 Sage Simulation Results

The experimentally measured maximum pressure drop and peak physical velocity for the $Er_{0.5}Pr_{0.5}$ regenerator are next used to evaluate the total friction pressure gradient in Sage, given by Eq.(19), and the Darcy friction factor in Sage, given by Eq.(23). According to Eq.(19), the total frictional pressure gradient at a given moment is simply the pressure drop across the regenerator at that moment divided by the regenerator length, which is given in Table 1. Figure 37 shows the results of the friction factor calculations using the experimental data as a function of the hydraulic-diameter Reynolds number given by Eq.(24). The results are plotted for 2.86, 1.13, and 0.10 MPa and compared to the correlation developed by Gedeon for packed sphere beds given by Eq.(26). The figure indicates that the experimental results agree very well with Gedeon's correlation for all charge pressures and temperatures. Gedeon's correlation was developed using data from experiments conducted at ambient conditions, which supports the belief that correlations developed at room temperature are indeed applicable at cryogenic temperature. Using the least-squares method, a new correlation was developed to match the experimental data and is given by Eq. (52) and is also shown in Figure 37.

$$f_{\text{Perrella}} = \frac{125}{\text{Re}_{d_h}} + 3.37 \tag{52}$$

The general trend of the data is linearly proportional to the inverse of the Reynolds number at low flow rates when viscous forces dominate, similar to the Darcy friction factor for internal pipe flow. As inertial forces become more important at Reynolds numbers above approximately 100, the Sage friction factor begins to plateau. The

experimental results also agree well with other well-stablished correlations for flow through packed spheres, namely the Ergun equation given by Eq.(27), and the Blake Kozeny equation, Eq.(28). The results of this comparison are shown in Figure 38.

Suitable values for the Sage friction factor can also be determined computationally using the software itself. Following the approach outlined in section 4.2, a working model of the entire test section including the $Er_{0.5}Pr_{0.5}$ regenerator was constructed as shown in Figure 17. Using the generic matrix option for the regenerator described by Eq.(32), the friction factor and compressor amplitude were iteratively varied using Sage's built-in optimization function until the pressure amplitude upstream and downstream of the regenerator matched the experimental results. The simulated values for Sage friction factor are shown in Figure 39. The figure shows that the simulated friction factor values also agree very well with Gedeon's correlation for all charge pressures and temperatures. The mass flow rate amplitudes calculated from the Sage simulations also agree with the experimental values to within a few percentage points. Figure 40 shows a comparison of the experimental and simulated Sage friction factors for the $Er_{0.5}Pr_{0.5}$ regenerator, and the two are almost identical.

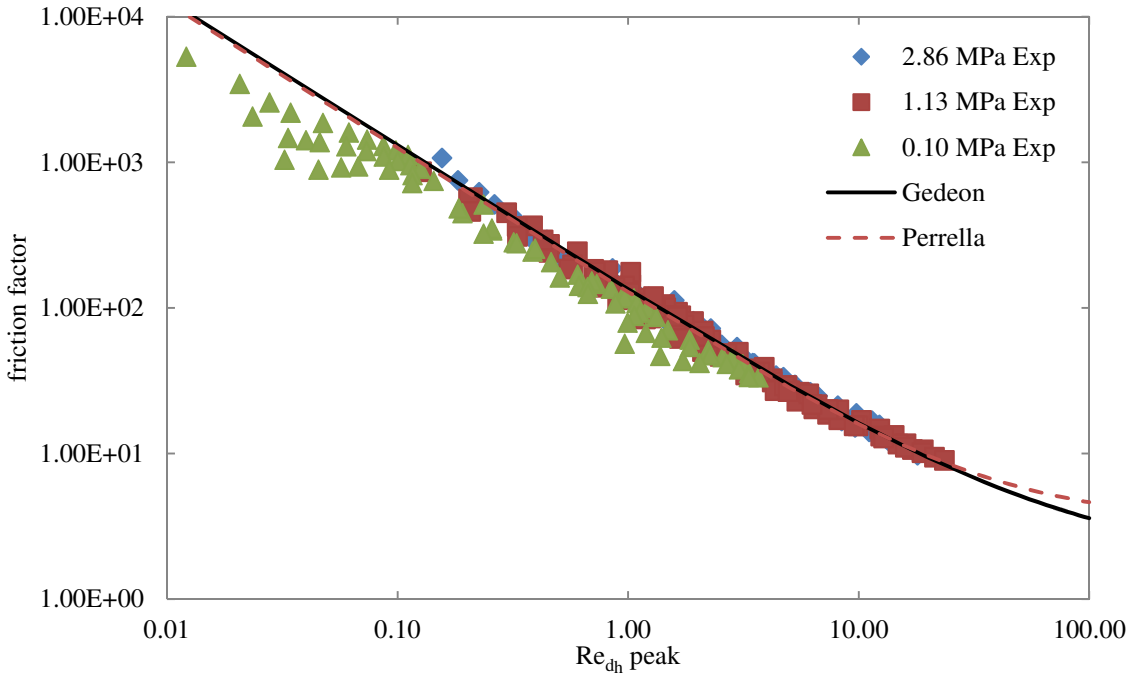

Figure 37. Experimental Sage friction factor for the $Er_{0.5}Pr_{0.5}$ regenerator compared to the correlation by Gedeon for packed spheres, Eq. (26), and Perrella, Eq.(52)

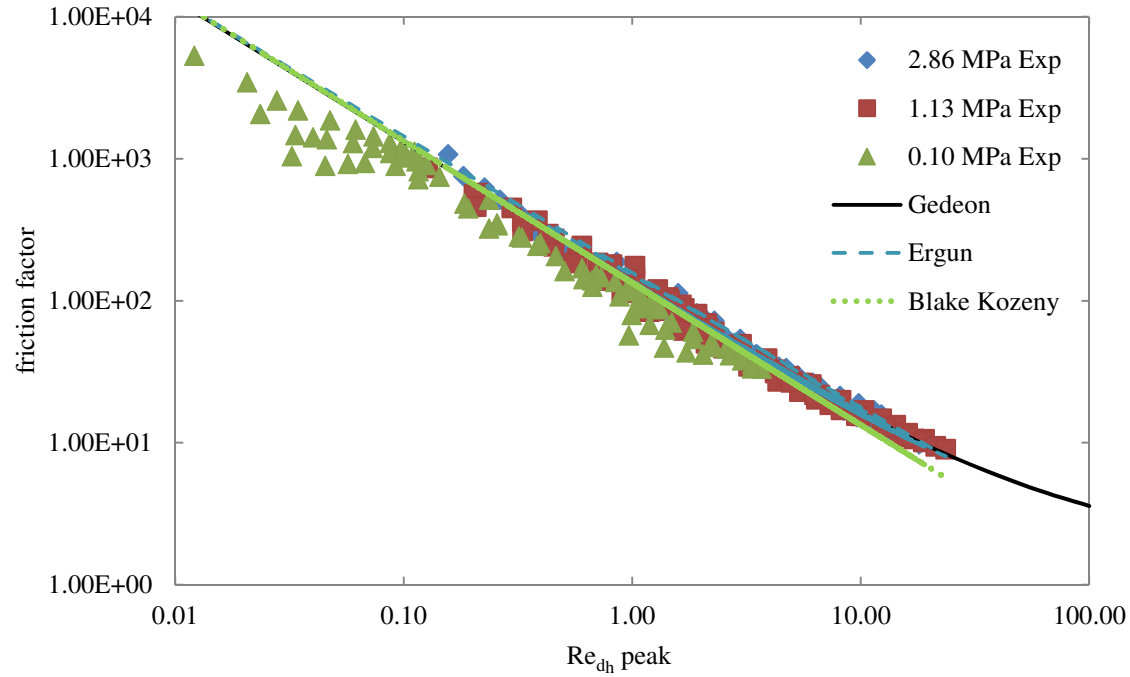

Figure 38. Experimental Sage friction factor for the $Er_{0.5}Pr_{0.5}$ regenerator compared to the correlation by Gedeon for packed spheres, Eq. (26); the Ergun equation, Eq. (27); and Black-Kozeny, (28)

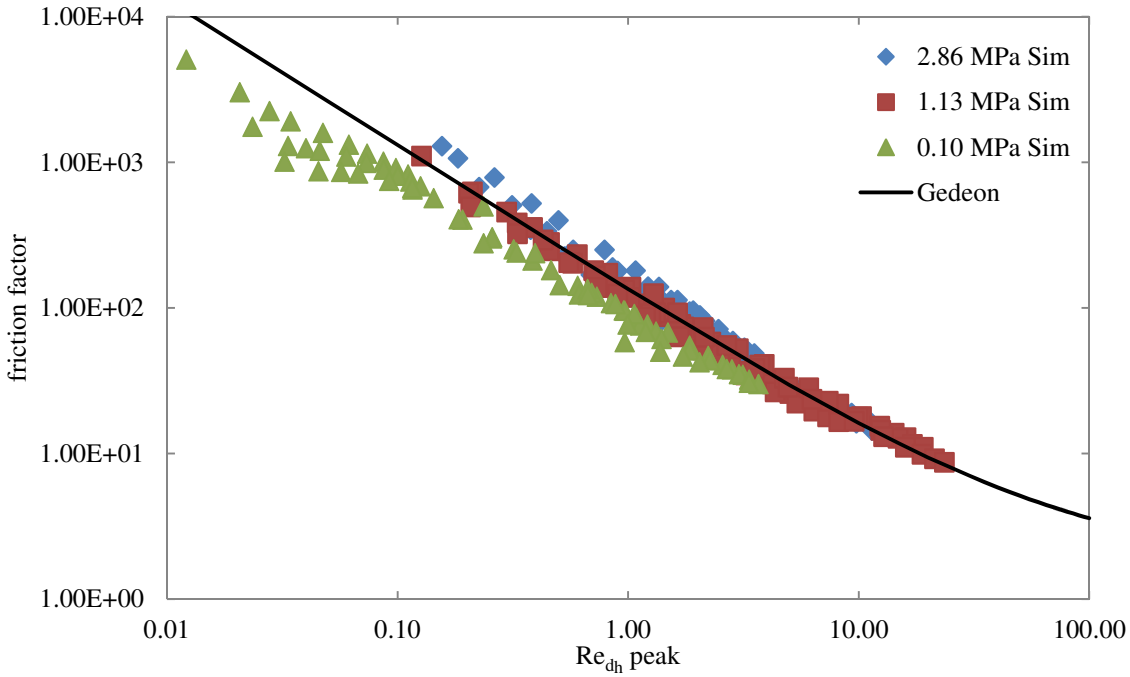

Figure 39. Simulated Sage friction factor for the $Er_{0.5}Pr_{0.5}$ regenerator compared to the correlation by Gedeon for packed spheres, Eq. (26)

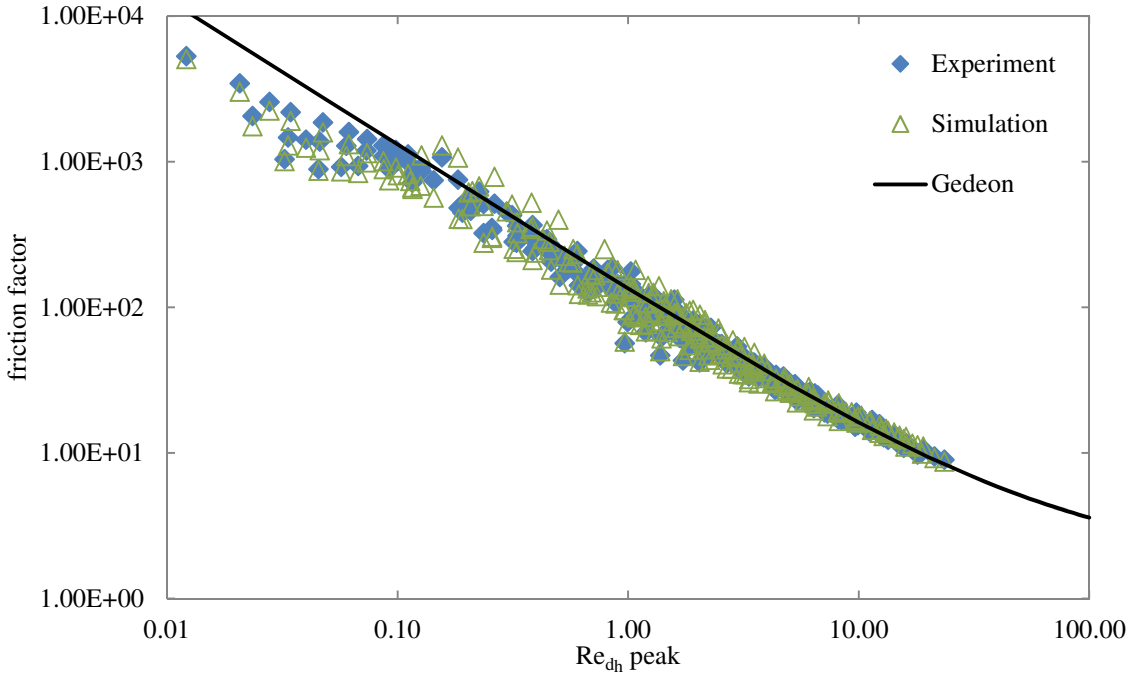

Figure 40. Comparison of Sage simulation and experimental friction factor for the $Er_{0.5}Pr_{0.5}$ regenerator

Although it appears that the results for the 0.10 MPa charge pressure do not agree as well as the 2.86 MPa and 1.13 MPa results, this may be due to a mistake in the charge pressure measurement. If the charge pressure is increased slightly to a value of 0.17 MPa, which may be more accurate based on a subsequent investigation, the low-pressure results agree with the high-pressure results and the correlation from Gedeon much better. Regardless of this, the correlation of Gedeon and that of Eq.(52) are indeed suitable for the entire charge pressure and temperature range under investigation.

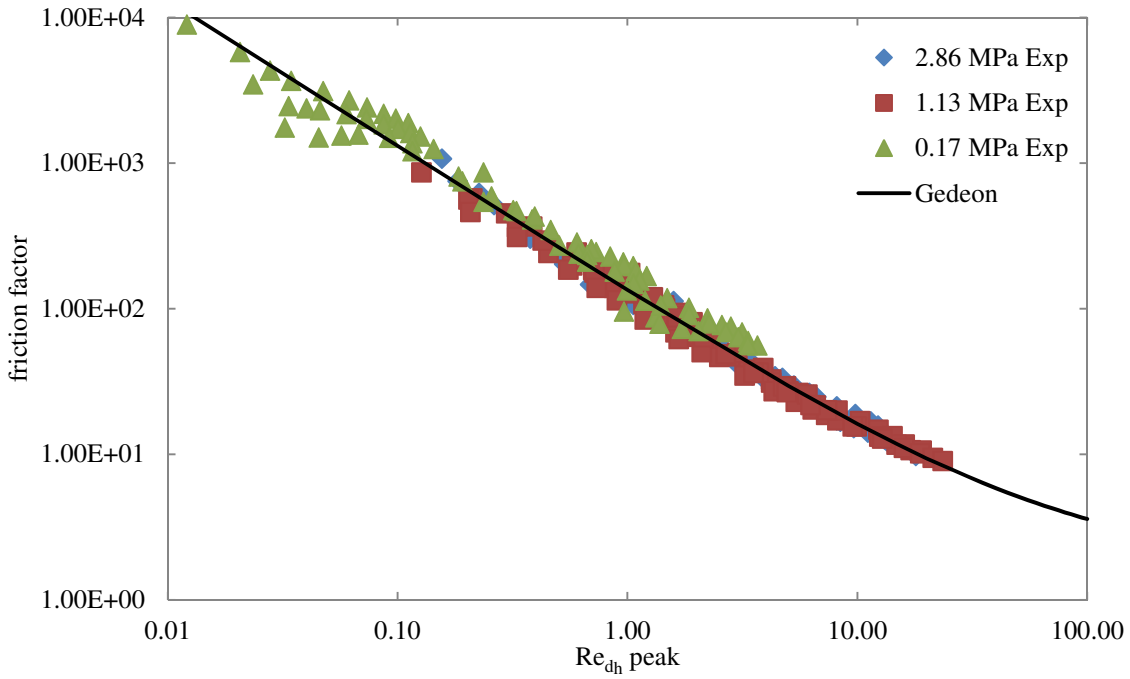

Figure 41. Experimental Sage friction factor for the $Er_{0.5}Pr_{0.5}$ regenerator with corrected gauge pressure for low-pressure runs compared to the correlation by Gedeon for packed spheres, Eq. (26)

5.1.3 CFD Simulation Results

One drawback of the Sage modelling approach is that it does not differentiate between the viscous and inertial components of the hydrodynamic resistance. It is often useful to define separate coefficients to these components such as in the Darcy-Forchheimer model represented by Eq.(1). In Fluent, for example, the hydrodynamic resistance is represented by a momentum source term defined by Eq.(37), which is composed of a viscous resistance, β, and inertial resistance, C_2. Recall that the viscous resistance specified in Fluent, β, is simply the inverse of the Fluent permeability, α, which is identical to the Darcy permeability, K. The momentum source term, S_i, is synonymous with the total frictional pressure gradient in Sage, F, and can be calculated from the maximum regenerator pressure drop. As figures 33, 34, and 35 indicate, the pressure drop across the regenerator will vary with charge pressure and temperature. Non-dimensionalizing the momentum source term according to Eq.(44) and assigning it the arbitrary variable , Γ, the data can be fit to a quadratic function of the Reynolds number, and the viscous and inertial resistances can be extracted according to Eq.(49) and Eq.(50). Figures 42-45 show the momentum source term from Fluent as well as the non-dimensionalized momentum source term for the $Er_{0.5}Pr_{0.5}$ regenerator at 2.86, 1.13, and 0.10 MPa for ambient and cryogenic temperatures. Quadratic fits are provided based on the least square method for each charge pressure and for the combined data. As the figures indicate, the non-dimensionalization collapses the data into a single trend line very nicely, allowing a single curve-fit to be developed for all of the experimental data without the need to distinguish between charge pressures and operating temperatures.

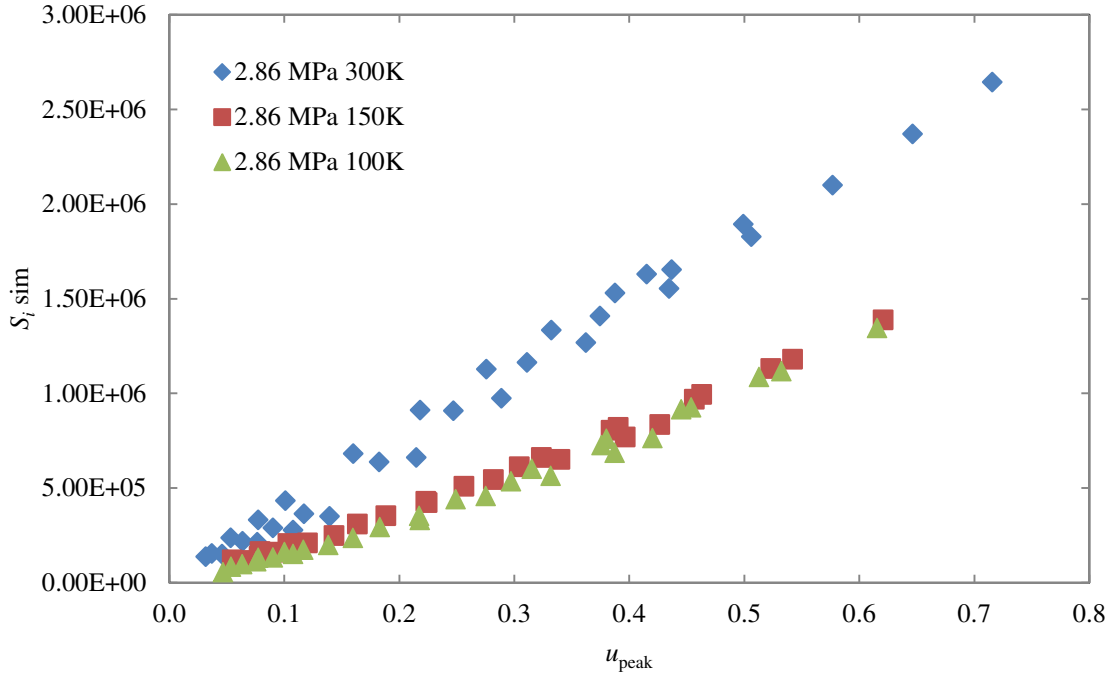

a) Fluent momentum source term at 2.86 MPa

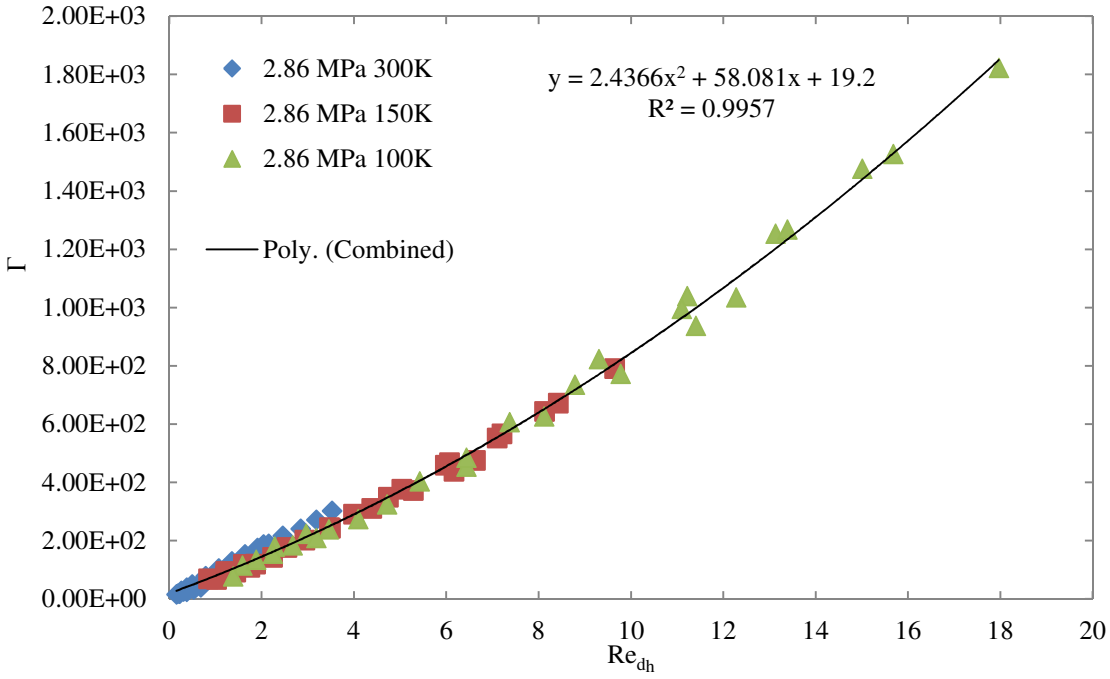

b) Dimensionless momentum source term at 2.86 MPa

Figure 42. $Er_{0.5}Pr_{0.5}$ regenerator a) momentum source term in Fluent, S_i, and b) non-dimensionalized momentum source term, Γ, calculated from Sage total frictional pressure gradient for 2.86 MPa at 300, 150, and 100K

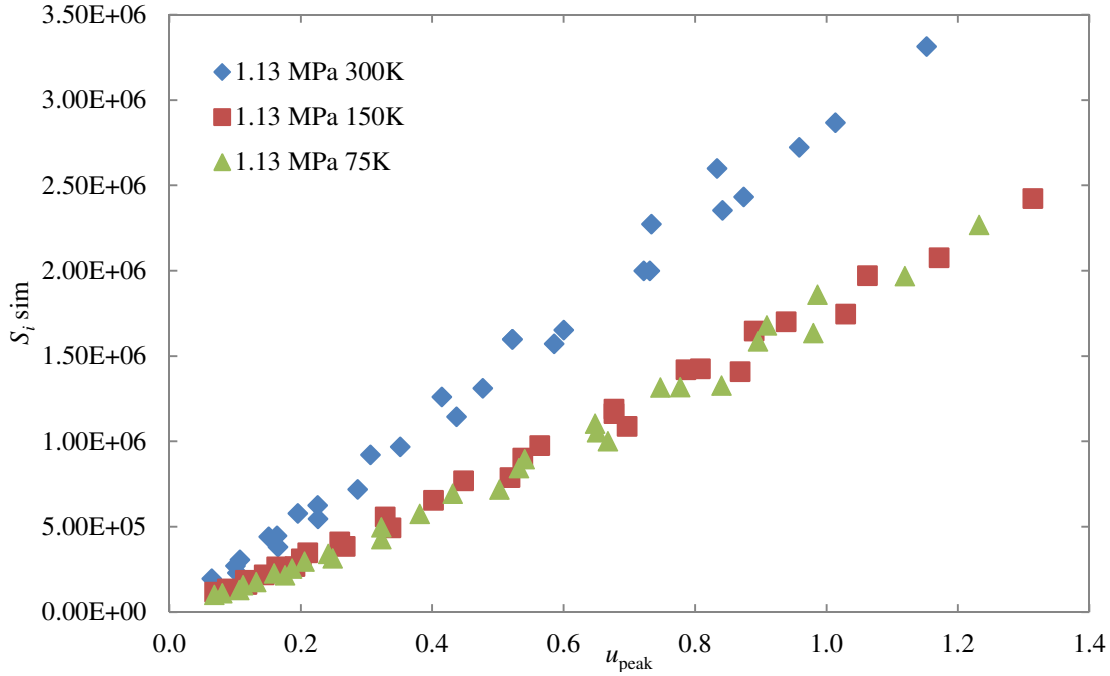

a) Fluent momentum source term at 1.13 MPa

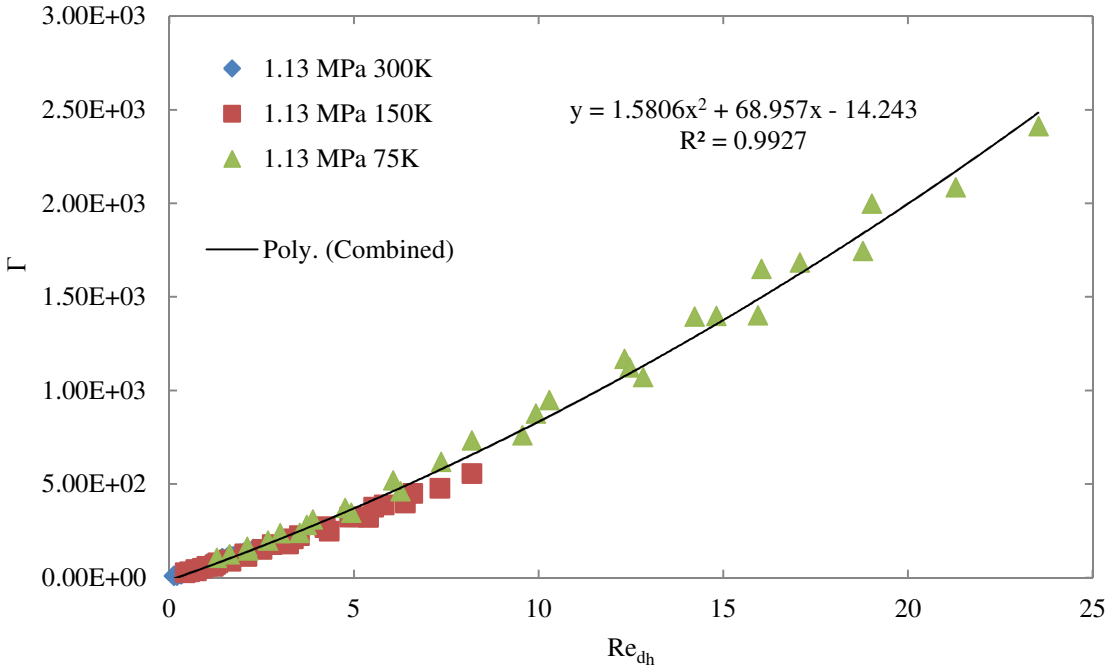

b) Dimensionless momentum source term at 1.13 MPa

Figure 43. $Er_{0.5}Pr_{0.5}$ regenerator a) momentum source term in Fluent, S_i, and b) non-dimensionalized momentum source term, Γ, calculated from Sage total frictional pressure gradient for 1.13 MPa at 300, 150, and 75K

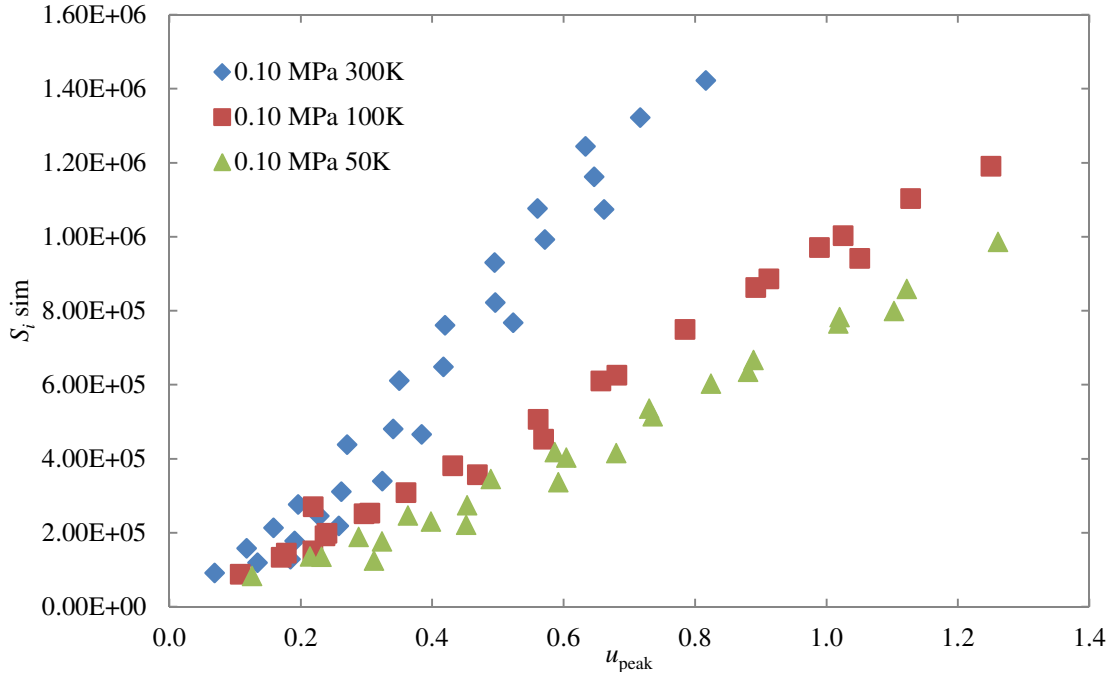

a) Fluent momentum source term at 0.10 MPa

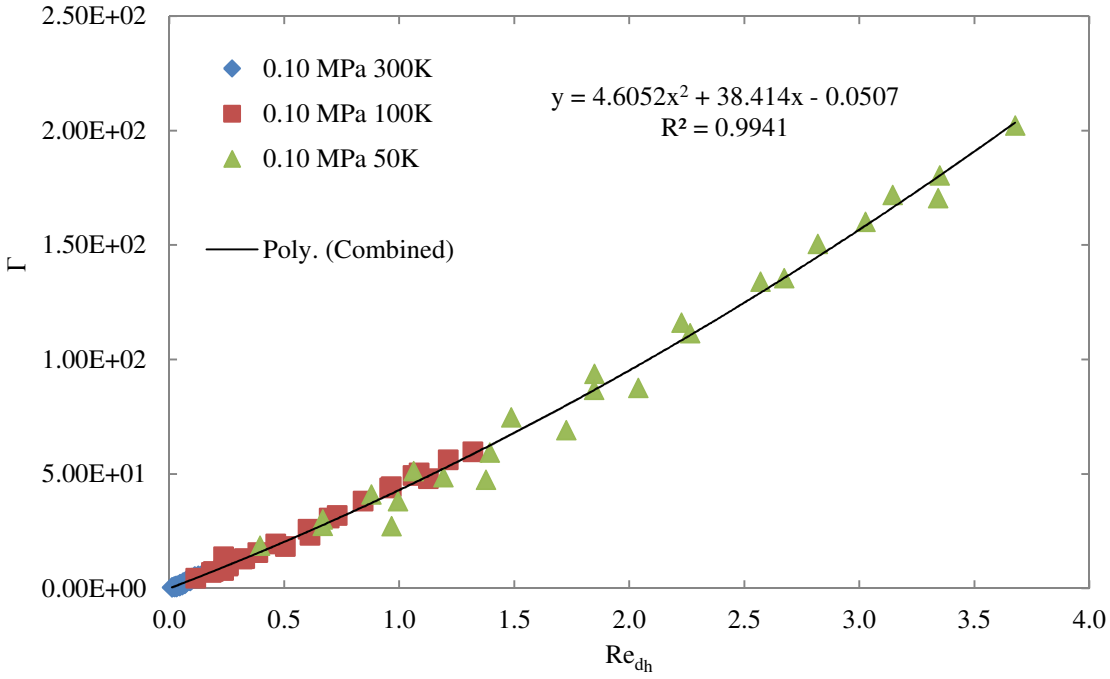

b) Dimensionless momentum source term at 0.10 MPa

Figure 44. $Er_{0.5}Pr_{0.5}$ regenerator a) momentum source term in Fluent, S_i, and b) non-dimensionalized momentum source term, Γ, calculated from Sage total frictional pressure gradient for 0.10 MPa at 300, 100, and 50K

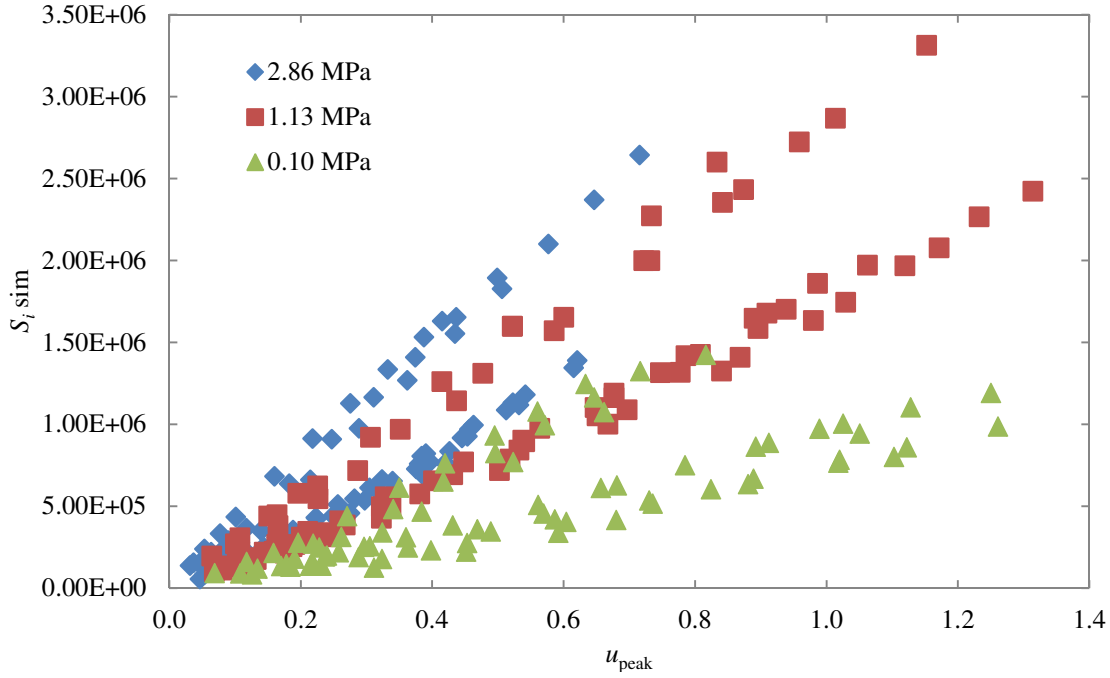

a) Fluent momentum source term at 2.86, 1.13, and 0.10 MPa

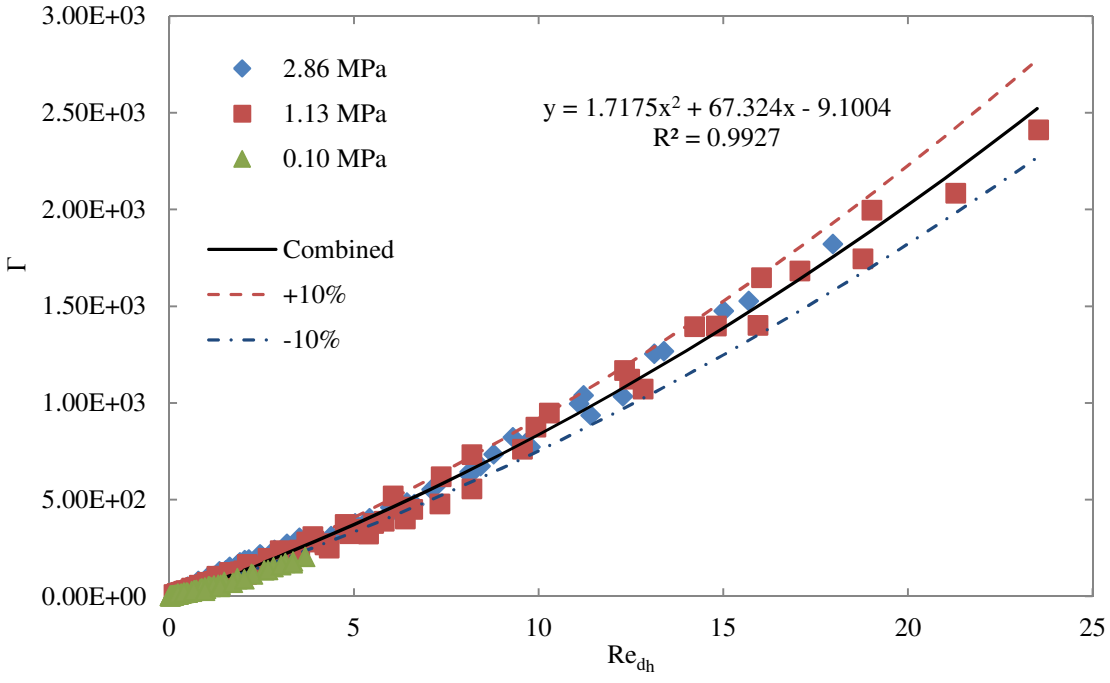

b) Dimensionless momentum source term at 2.86, 1.13, and 0.10 MPa

Figure 45. $Er_{0.5}Pr_{0.5}$ regenerator a) momentum source term in Fluent, S_i, and b) non-dimensionalized momentum source term, Γ, calculated from Sage total frictional pressure gradient for 2.86, 1.13, and 0.10 MPa

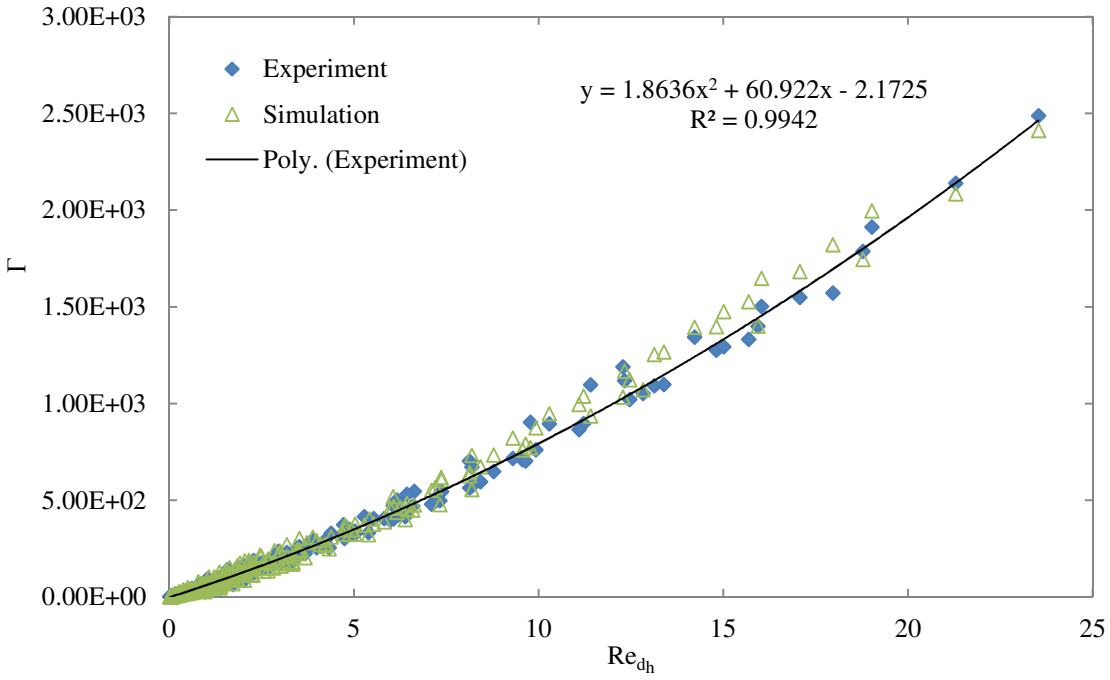

Figure 46. $Er_{0.5}Pr_{0.5}$ regenerator comparison of simulated and experiment dimensionless momentum source term for 2.86, 1.13, and 0.10 MPa

Figure 45 shows the combined data for all three charge pressures tested with the $Er_{0.5}Pr_{0.5}$ regenerator. The confidence lines in Figure 45b are equal to ±10% of the value of the quadratic best fit line. The figure shows that all the combined pressure data fall within this confidence band for the $Er_{0.5}Pr_{0.5}$ regenerator. Table 3 provides a summary of the viscous and inertial resistances in Fluent extracted from the quadratic fit of the non-dimensionalized momentum source terms for the $Er_{0.5}Pr_{0.5}$ regenerator. Results are provided for individual simulated charge pressures, the combined simulation data, and the experimental data. The Darcy permeability, K, and Forchheimer coefficient, c_f, are calculated according to Eq.(49) and Eq.(50), respectively.

Table 3. Summary of Fluent viscous and inertial resistance, Darcy Permeability and Forchheimer coefficient for $Er_{0.5}Pr_{0.5}$ regenerator

Pressure [MPa]	A	B	β [1/m^2]	C_2 [1/m]	K [m^2]	c_f
2.86	2.44	58.08	3.40E+11	1.66E+06	2.94E-12	1.42
1.13	1.58	68.96	4.03E+11	1.07E+06	2.48E-12	0.85
0.01	4.61	38.41	2.25E+11	3.13E+06	4.45E-12	3.30
Combined	1.72	67.32	3.94E+11	1.17E+06	2.54E-12	0.93
Experimental	1.86	60.92	3.56E+11	1.27E+06	2.81E-12	1.06
Pathak [48]	-	-	7.52E+09	-	1.33E-10	-

Using this approach, a single value for β and C_2 were found for any flow velocity for individual charge pressures or for the entire pressure range. This differs from the results of Pathak, who determined a single value for permeability, but allowed the Forchheimer coefficient to vary with flow velocity and pressure. The difference may be due to the different approaches used to determine the permeability and Forchheimer coefficients. Pathak used the lowest flow rate of his steady flow tests to determine the viscous resistance in Fluent by neglecting the inertial resistance at low flow velocities and only varying viscous resistance until the simulation matched his experimental results. Then, using the same viscous resistance from his steady flow tests for oscillating flow, he varied the inertial resistance to match his experimental results. Perhaps the viscous resistance determined at steady flow was not suitable for oscillating flow, or perhaps the low-flow rate used to determine the viscous resistance in the steady flow tests was not low enough to justify neglecting the inertial resistance. Pathak also used one oscillating mass flow rate BC and one oscillating pressure BC upstream and downstream of the regenerator, respectively, rather than a single pressure BC and closed system as outlined in Section 4.3.2. The experiments of Pathak also used $Er_{0.5}Pr_{0.5}$ particles with 69μm mean diameter and a regenerator of 38% porosity, which differs slightly from this study.

Table 4 shows the results of simulating the $Er_{0.5}Pr_{0.5}$ regenerator in Fluent using the viscous and inertial resistances from Table 3 for the individual charge pressures. The details of the Fluent simulation can be found in Section 4.3.2. The $Er_{0.5}Pr_{0.5}$ matrix was assumed to be isotropic given the random nature of the sphere packing. This means that the hydrodynamic resistance parameters, the viscous and inertial resistance, were given the same value in the axial and radial directions. A single frequency and PWG input voltage were chosen for each temperature/ charge pressure combination. The simulations showed excellent agreement with the experimental results particularly in terms of the downstream pressure amplitude. The downstream mass flow rate did not agree as well, but since the experimental mass flow rates agreed with the rates from the Sage simulations, the problem is likely with the Fluent simulation itself. It is believed that the pressure inlet boundary condition is not sufficient to capture the coupled nature of the pressure and mass flow. In the future, a moving wall boundary condition such as the one provided in Appendix C could be used instead and might provide better agreement.

Table 4. Summary of CFD simulation results using viscous and inertial resistances from Table 3 compared to experimental measurements for $Er_{0.5}Pr_{0.5}$ regenerator

Pressure [MPa]	Temperature [K]	$\dot{m}_{exp}$ [kg/s]	$\dot{m}_{sim}$ [kg/s]	Percent error	$P_{max_{exp}}$ [Pa]	$P_{max_{sim}}$ [Pa]	Percent error
2.86	300	1.74E-04	1.57E-04	9.92E-02	1.12E+05	1.12E+05	2.40E-03
2.86	150	4.07E-04	3.43E-04	1.57E-01	1.16E+05	1.15E+05	5.21E-03
2.86	100	6.12E-04	5.17E-04	1.56E-01	1.17E+05	1.16E+05	4.93E-03
1.13	300	1.30E-04	1.13E-04	1.27E-01	8.16E+04	8.45E+04	3.56E-02
1.13	150	2.87E-04	2.32E-04	1.90E-01	9.01E+04	9.02E+04	1.20E-03
1.13	75	5.70E-04	4.51E-04	2.08E-01	9.06E+04	9.09E+04	3.01E-03
0.26	300	7.31E-06	6.36E-06	1.30E-01	5.81E+03	6.32E+03	8.75E-02
0.26	100	3.66E-05	2.93E-05	2.01E-01	9.69E+03	9.92E+03	2.33E-02
0.26	50	7.41E-05	6.24E-05	1.57E-01	1.02E+04	1.04E+04	2.12E-02

Slightly different results for the Fluent hydrodynamic resistances, Darcy Permeability and Forchheimer coefficients can be obtained by forcing the y-intercept of the quadratic fit to zero. This approach might provide more appropriate results since, physically, the hydrodynamic resistance of the porous medium should be zero at zero flow velocity. The results are summarized in Table 5. The zero-intercept results agree fairly well with the non-zero-intercept results from Table 3, but there are slight differences. One might expect the intercept of the non-dimensionalized momentum source term, Γ, to equal zero naturally, without having to be forced, but this is not the case. This could be due to the bias error of the dynamic pressure transducers themselves or due to the error associated with the mean operating pressure measurement.

Table 5. Summary of Fluent viscous and inertial resistance, Darcy Permeability and Forchheimer coefficient with zero intercept for $Er_{0.5}Pr_{0.5}$ regenerator

Pressure [MPa]	A	B	β [1/m^2]	C_2 [1/m]	K [m^2]	c_f
2.86	2.09	64.19	3.75E+11	1.42E+06	2.66E-12	1.16
1.13	1.74	65.21	3.81E+11	1.18E+06	2.62E-12	0.96
0.10	4.62	38.34	2.24E+11	3.14E+06	4.46E-12	3.32
Combined	1.84	64.64	3.78E+11	1.25E+06	2.65E-12	1.02
Experimental	1.89	60.28	3.52E+11	1.28E+06	2.84E-12	1.08
Pathak [48]	-	-	7.52E+09	-	1.33E-10	-

5.2 Regenerator 2: #400SS Wire Mesh

Wire mesh screens are among the most common types of regenerator filler materials for a wide range of cryocooler sizes and operating temperatures. Packed beds of wire mesh screens provide good heat transfer between the working fluid and the heat exchanger walls without causing undue pressure drop or axial conduction. Mesh screens are typically woven, causing slight gaps in the radial direction, which allows gas to flow in the axial and radial directions to alleviate streaming effects. Typically, packed screen

beds will have porosities in the range of 0.67-0.72, although higher porosities can be achieved by compressing the woven mesh, allowing the screens to lay flush against one another. However, this can eliminate the radial flow paths for the working fluid and lead to undesirable pressure and velocity streaming. In this work, only woven screen meshes are considered. Various metals can be used for the mesh material including copper, steel, and bronze. The heat capacity and thermal conductivity of each determines its appropriate range of use. In some applications it is even possible to assemble a regenerator with multiple mesh metals so that the heat capacity and thermal conductivity of the wire mesh filler material can be tuned for different axial locations as the desired temperature gradient along the regenerator changes. In this study, 316 stainless steel was selected due to its wide availability and popularity as a regenerator filler material and as a point of comparison with previous studies such as those of Cha [1,38,39,51].

5.2.1 Experimental Results

The transient pressure oscillations at the inlet and outlet of regenerator 2 were measured and transformed according to the process outline in Section 3.2. The regenerator was tested at mean operating pressures of 2.86 MPa (400psig), 1.13 MPa (150psig), and 0.26 MPa (24psig) and frequencies of 50, 60, and 70 Hz. Measurements were performed at ambient and cryogenic temperatures for all charge pressures and frequencies. The experimental setup for regenerator 2 differs slightly from that of regenerator 1, as outlined in Section 3.2. As shown in Figure 12, a larger surge volume was used for testing regenerators 2 and 3 to accommodate the higher mass flow rates through the wire mesh regenerators compared to the packed-sphere $Er_{0.5}Pr_{0.5}$ regenerator. Figures 47, 48, and 49 show the instantaneous upstream and downstream pressure

oscillations across the CHX and regenerator 2 for 2.86, 1.13, and 0.26 MPa and 60 Hz operating frequency at ambient and cryogenic temperatures. The experimental results indicate that, unlike regenerator 1, the greatest drop in pressure amplitude occurs across the CHX and not the #400SS mesh regenerator. This seems reasonable considering that the porosity of the CHX is only 0.647 while the porosity of regenerator 2 is 0.699. The increased porosity is likely due to the smaller wire diameter and higher facial opening percentage of the #400SS mesh compared to the #100Cu mesh. Figures 50, 51, and 52 show the instantaneous upstream and downstream pressure oscillations across the regenerator and the instantaneous mass flow rates downstream. In general, the pressure amplitudes decrease with decreasing charge pressure and operating temperature, and the mass flow rate amplitudes increase with increasing charge pressure and decreasing operating temperature due to the increased density of the working fluid. As expected, the peak mass flow rate occurs when the instantaneous difference between the upstream and downstream pressure is greatest, and the mass flow rate is zero when the upstream and downstream pressure are equal. This agrees with the pressure-to-mass flow rate phase relationship described by Eq. (11). Figures 53, 54, and 55 compare the instantaneous pressure drop across regenerator 2 with the mass flow rate downstream of the regenerator. The results verify that the peak mass flow rate coincides with the peak pressure drop. Although the oscillations are not purely sinusoidal, the waves are much smoother and less erratic than the pressure drop and mass flow rate oscillations for the $Er_{0.5}Pr_{0.5}$ regenerator. This is likely due to the increased porosity and accompanying higher mass flow rate magnitude for the woven mesh regenerators.

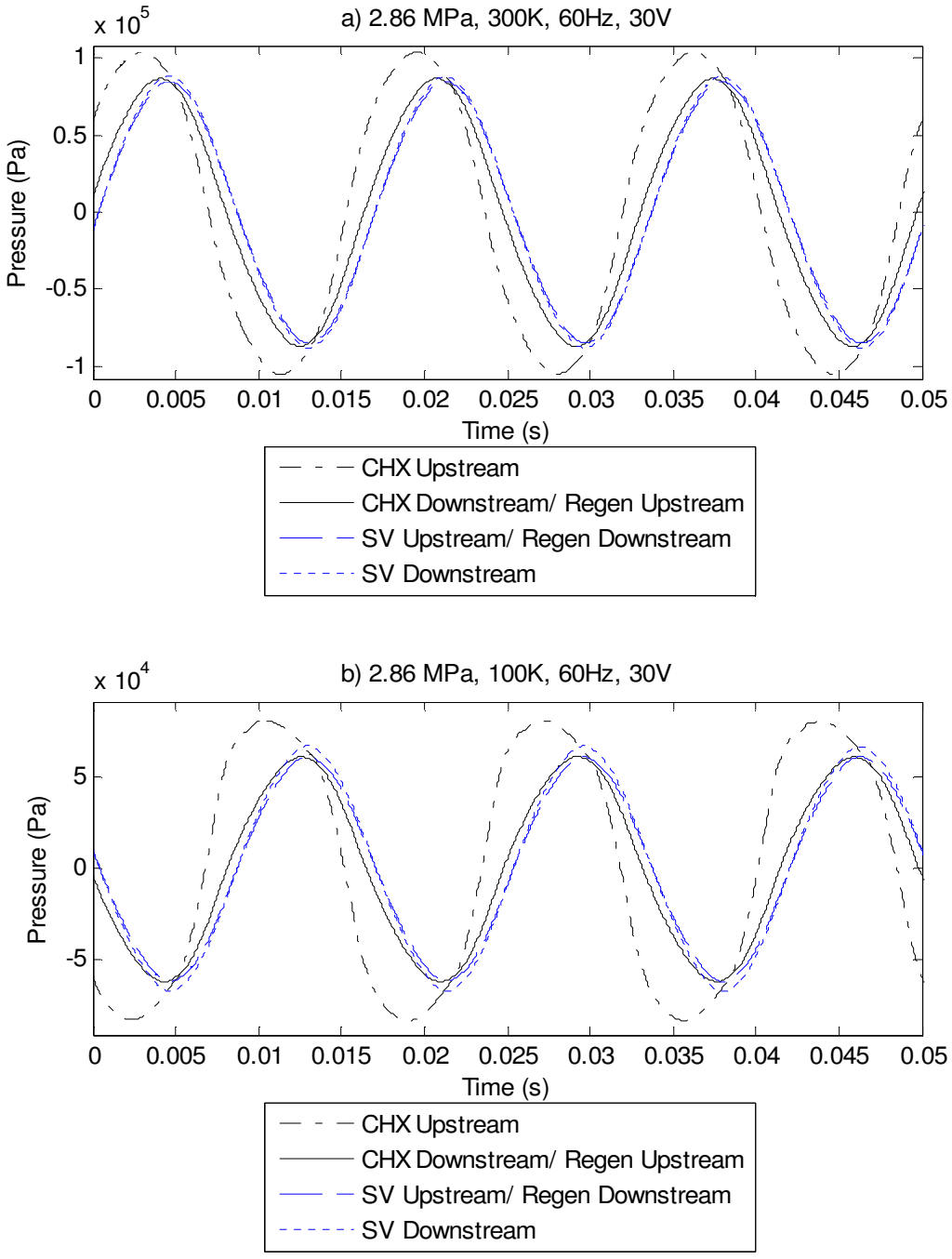

Figure 47. Instantaneous pressure across the #400SS mesh regenerator at 2.86 MPa for a) 300K and b) 100K at 60Hz and 30V PWG input voltage

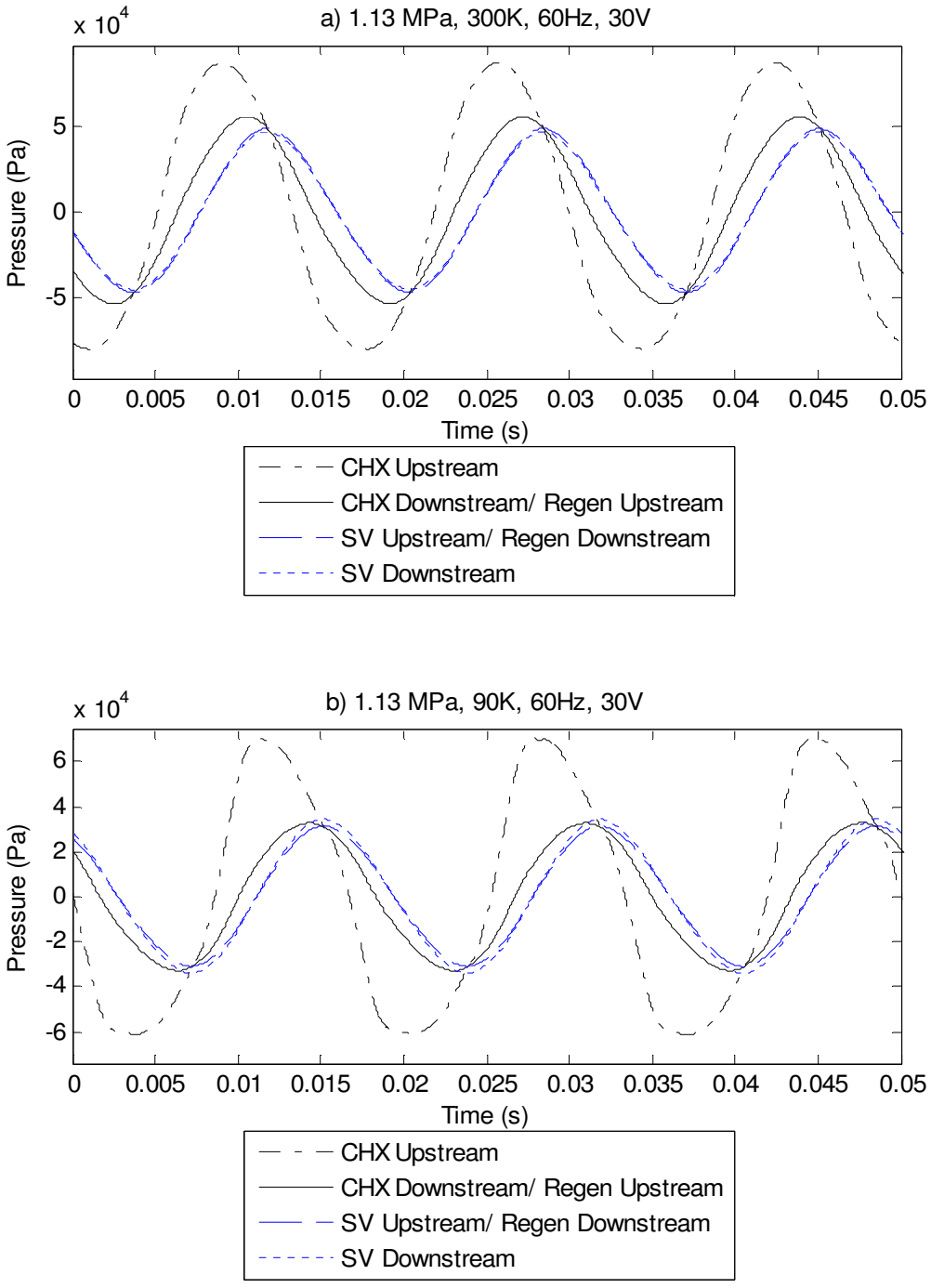

Figure 48. Instantaneous pressure across the #400SS mesh regenerator at 1.13 MPa for a) 300K and b) 90K at 60Hz and 30V PWG input voltage

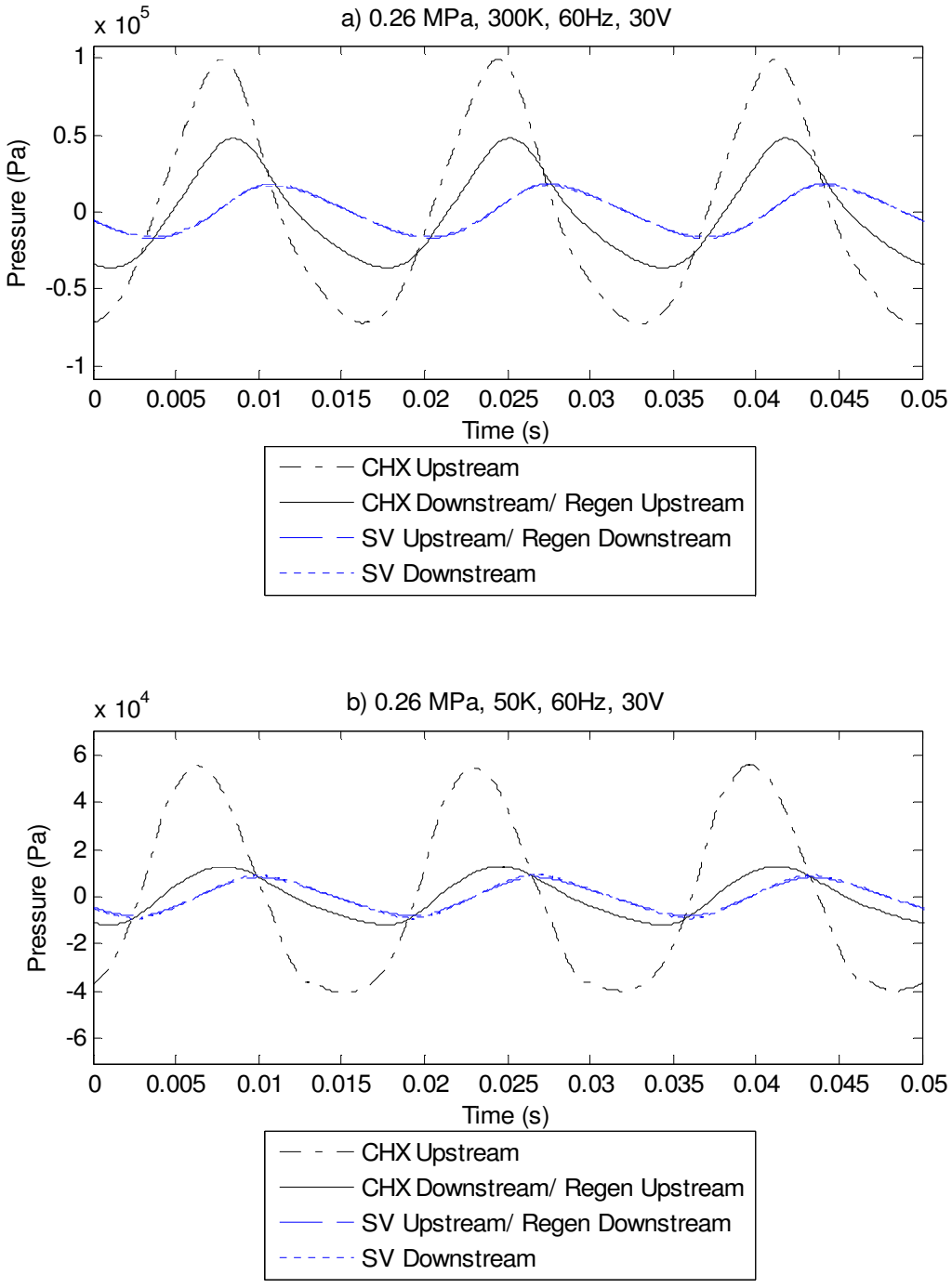

Figure 49. Instantaneous pressure across the #400SS mesh regenerator at 0.26 MPa for a) 300K and b) 50K at 60Hz and 30V PWG input voltage

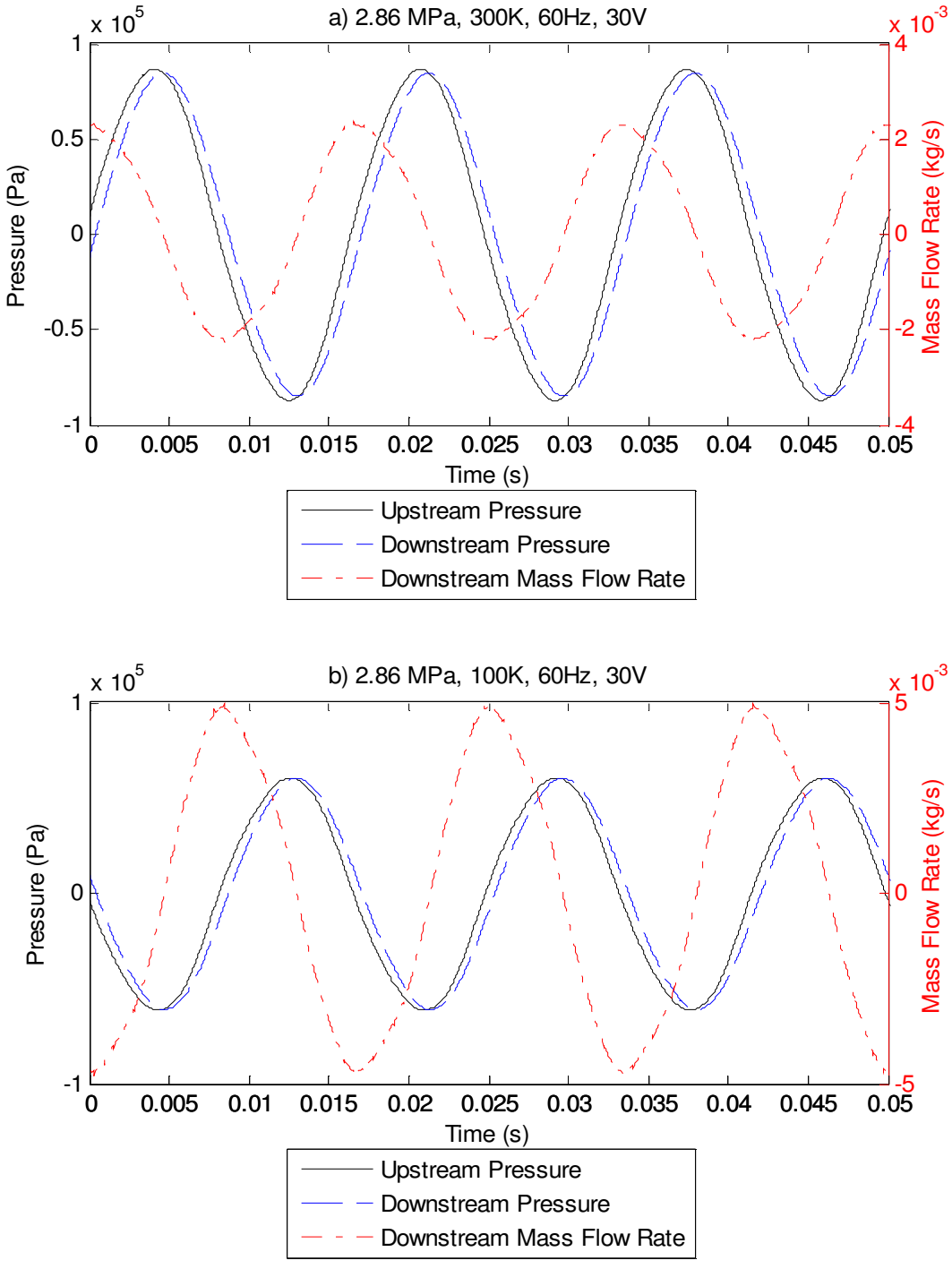

Figure 50. Transient pressure and mass flow rate oscillations for the #400SS mesh regenerator at 2.86 MPa for a) 300K and b) 100K at 60Hz and 30V PWG voltage input

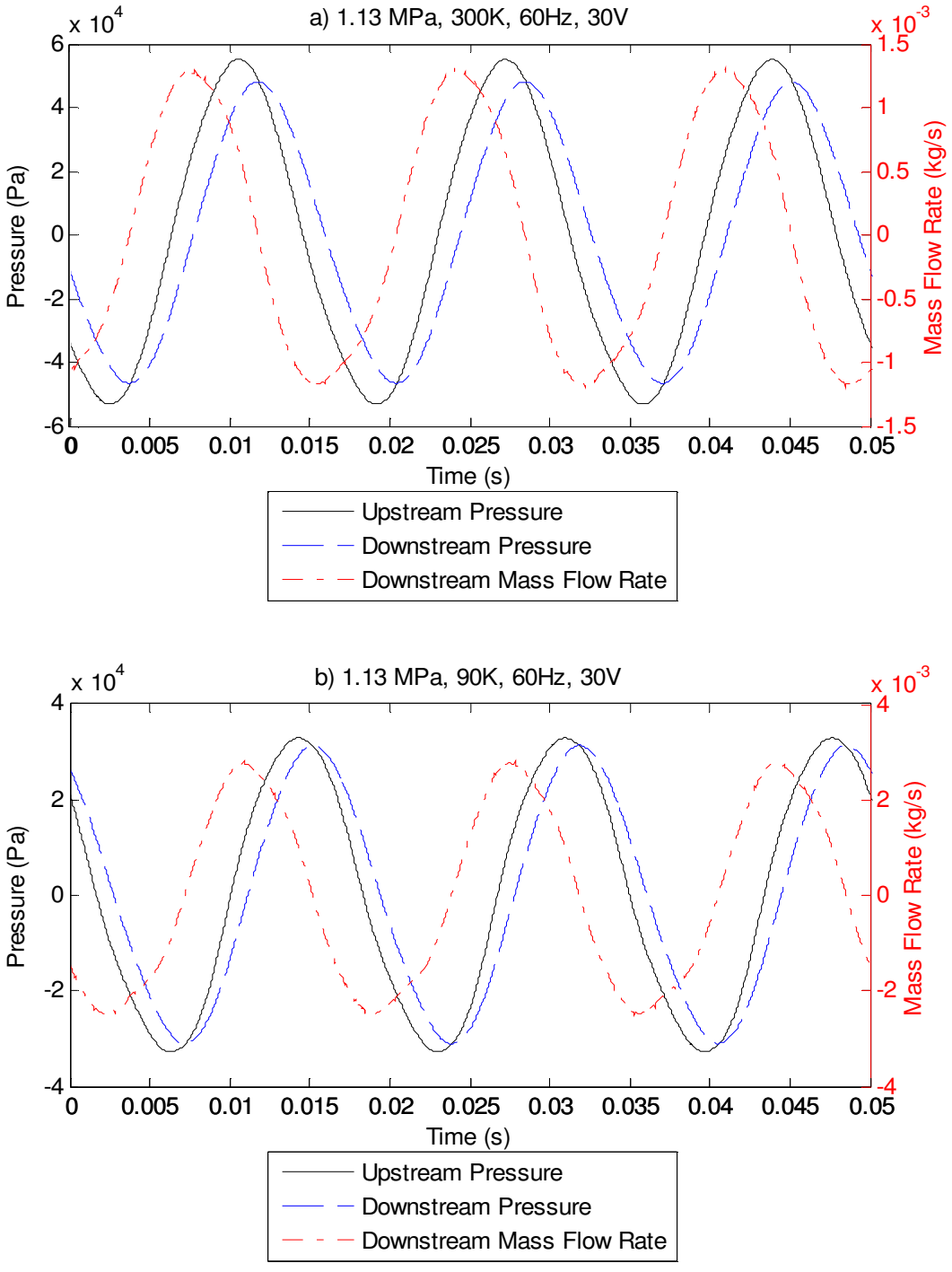

Figure 51. Transient pressure and mass flow rate oscillations oscillations for the #400SS mesh regenerator at 1.13 MPa for a) 300K and b) 75K at 60Hz and 30V PWG voltage input

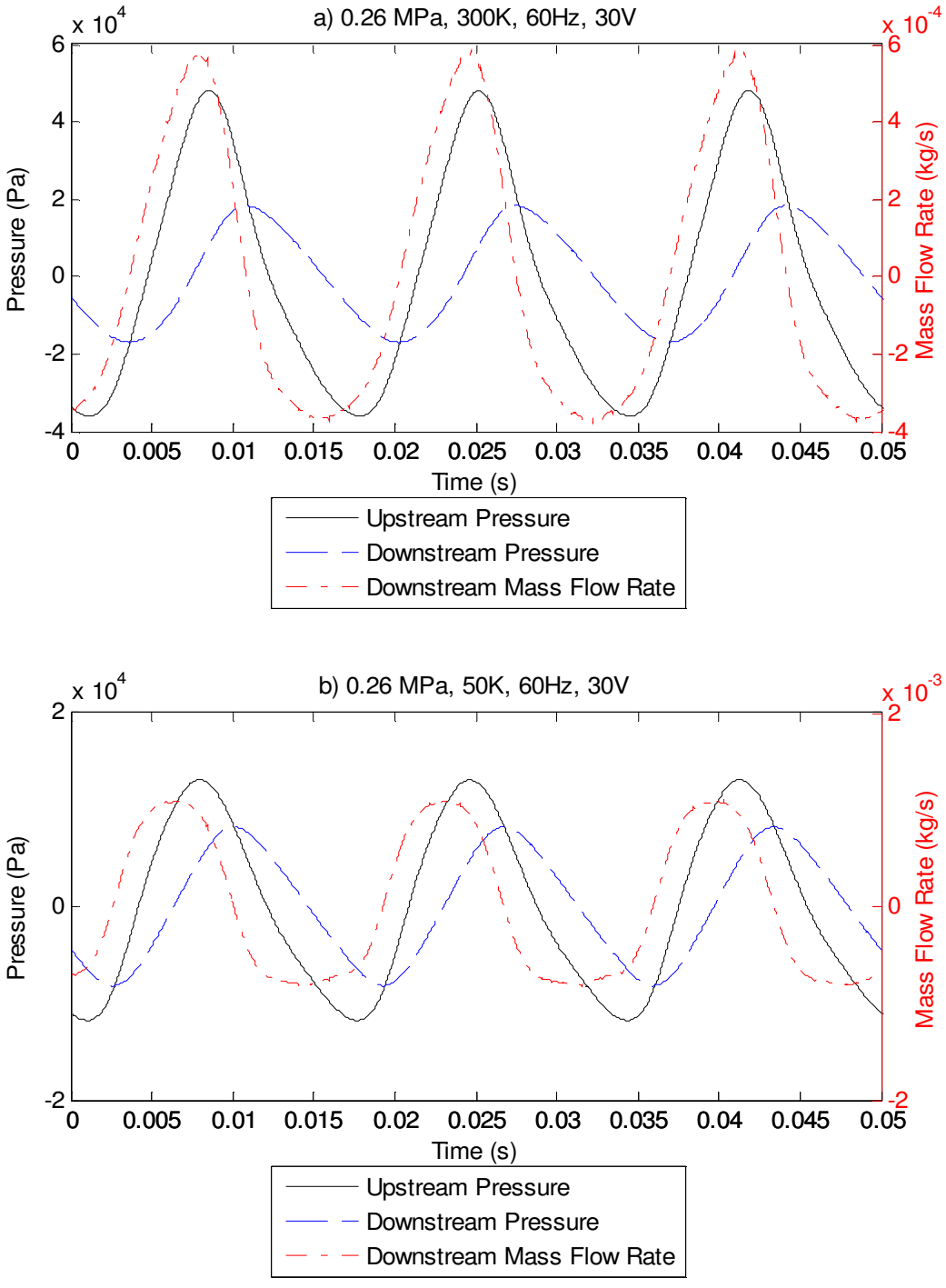

Figure 52. Transient pressure and mass flow rate oscillations oscillations for the #400SS mesh regenerator at 0.10 MPa for a) 300K and b) 50K at 60Hz and 30V PWG voltage input

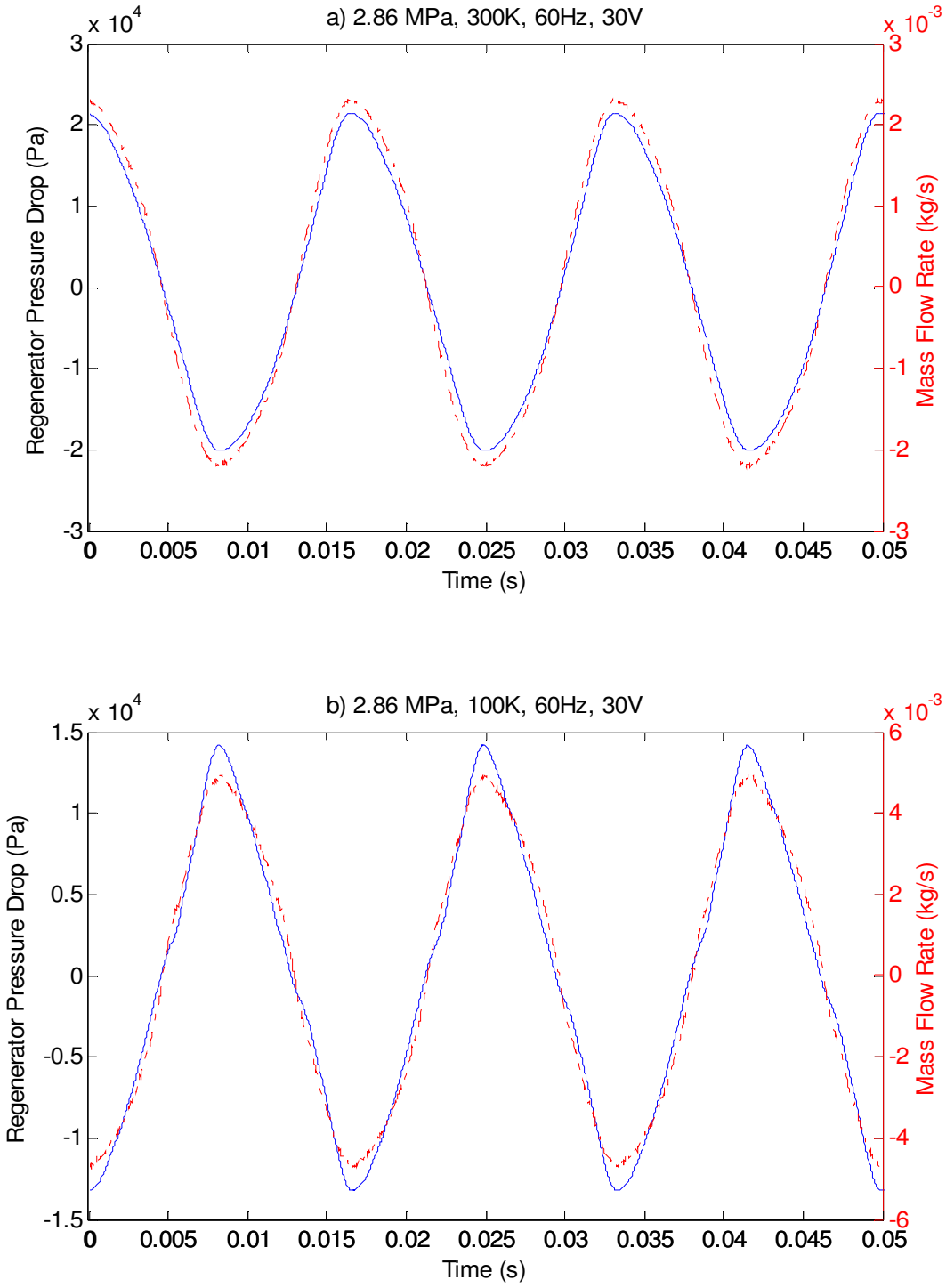

Figure 53. Regenerator Pressure Drop compared to downstream mass flow rate oscillations for the #400SS mesh regenerator at 2.86 MPa for a) 300K and b) 100K at 60Hz and 30V PWG voltage input

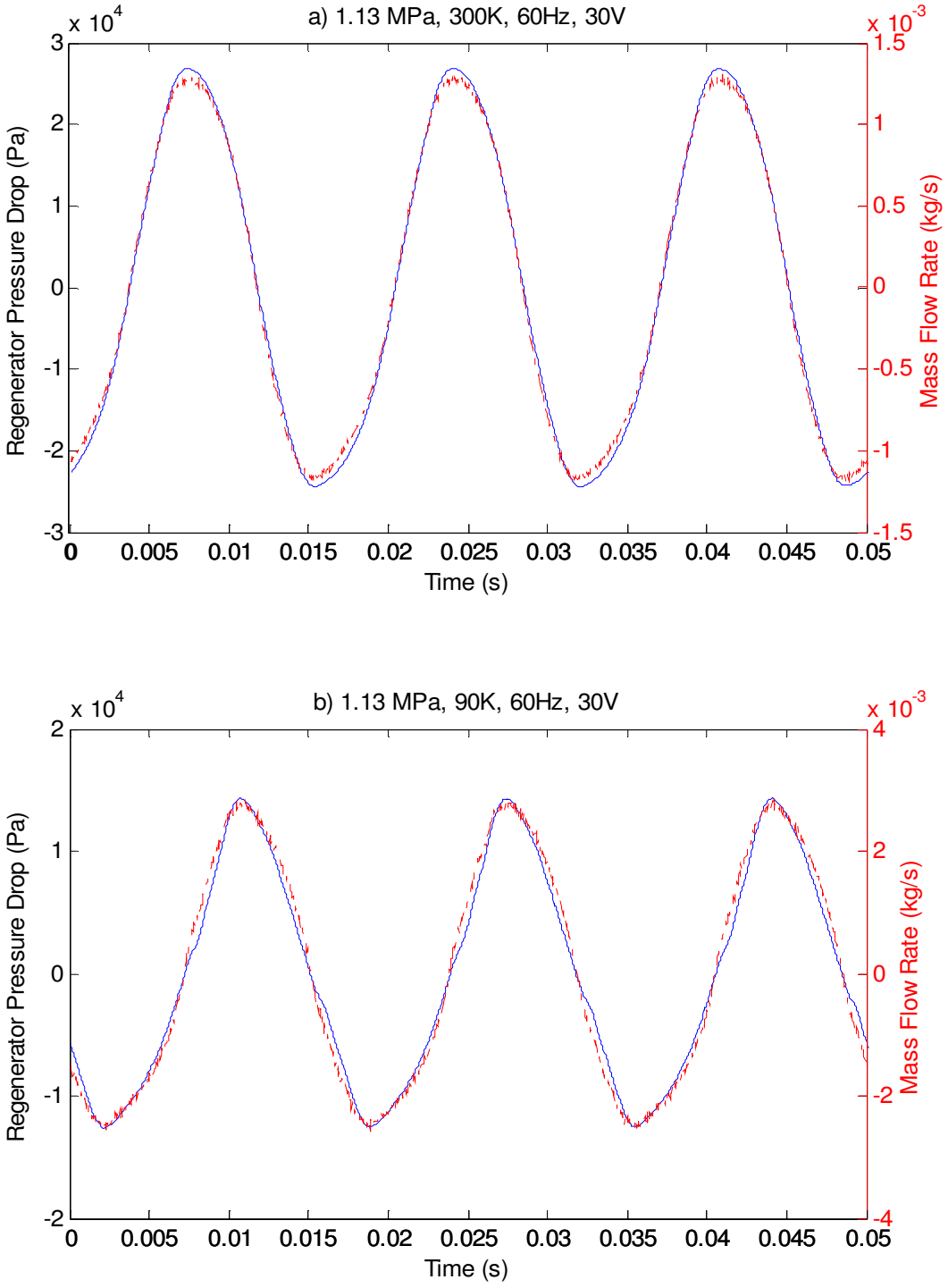

Figure 54. Regenerator Pressure Drop compared to downstream mass flow rate oscillations for the #400SS mesh regenerator at 1.13 MPa for a) 300K and b) 75K at 60Hz and 30V PWG voltage input

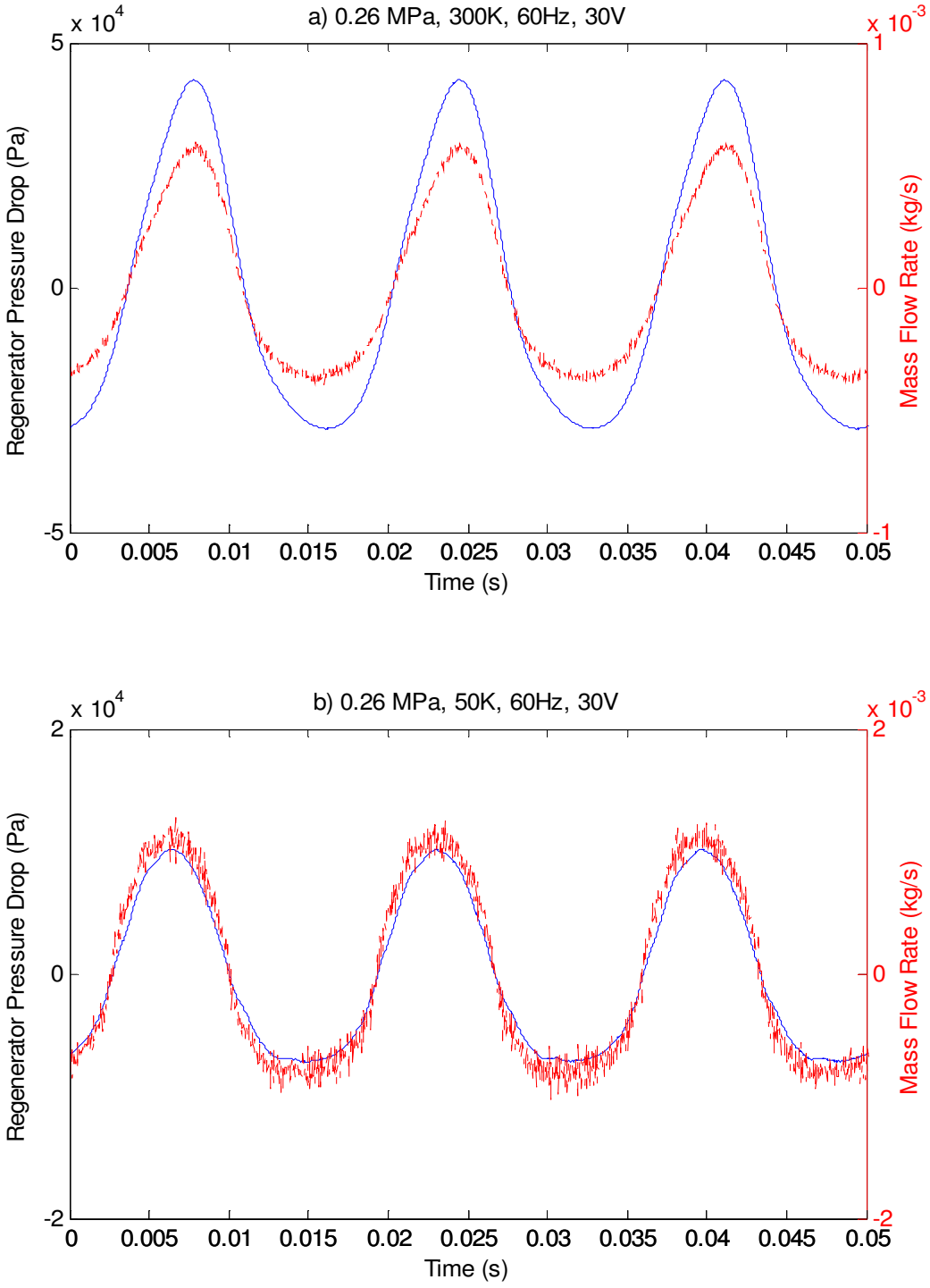

Figure 55. Regenerator Pressure Drop compared to downstream mass flow rate oscillations for the #400SS mesh regenerator at 0.10 MPa for a) 300K and b) 50K at 60Hz and 30V PWG voltage input

Figures 56, 57, and 58 show the maximum or peak instantaneous pressure drop across the #400SS mesh regenerator versus the peak flow velocity, where the peak flow velocity is calculated according to Eq. (51). The results indicate that the peak physical flow velocities for the #400SS mesh regenerator are generally higher than the $Er_{0.5}Pr_{0.5}$ regenerator at the same charge pressures and temperatures. This is to be expected given the different porosities and pore structures of the two regenerator filler materials. The results indicate that the pressure drop is independent of frequency when plotted vs. flow velocity so all experimental frequencies are shown together. The uncertainty bars are calculated according to section 3.3 as 0.3% of the full scale value of 690 kPa, which gives a total uncertainty of 2,700 Pa. The results indicate that the maximum pressure drop clearly varies based on operating pressure and temperature. The peak pressure drop is larger for higher charge pressures and operating temperatures, although the peak pressure drop does not vary with the operating temperature of the #400SS mesh regenerator as severely as for the $Er_{0.5}Pr_{0.5}$ regenerator. Figure 59 compares the peak pressure drop across regenerator 2 at 2.86, 1.13, and 0.26 MPa. While all of the results do obey the same general trend, it is clear that these dimensioned results cannot be expressed using a single correlation, which establishes the need for none-dimensionalization.

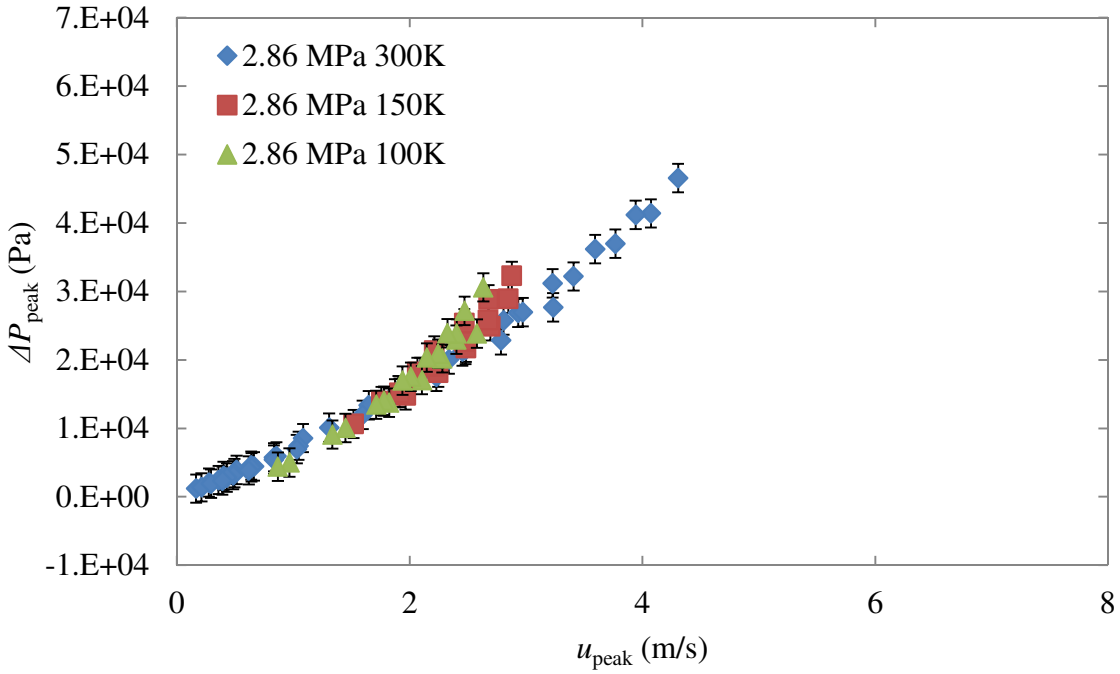

Figure 56. Maximum instantaneous pressure drop across the #400SS mesh regenerator as a function of peak flow velocity at 2.86 MPa

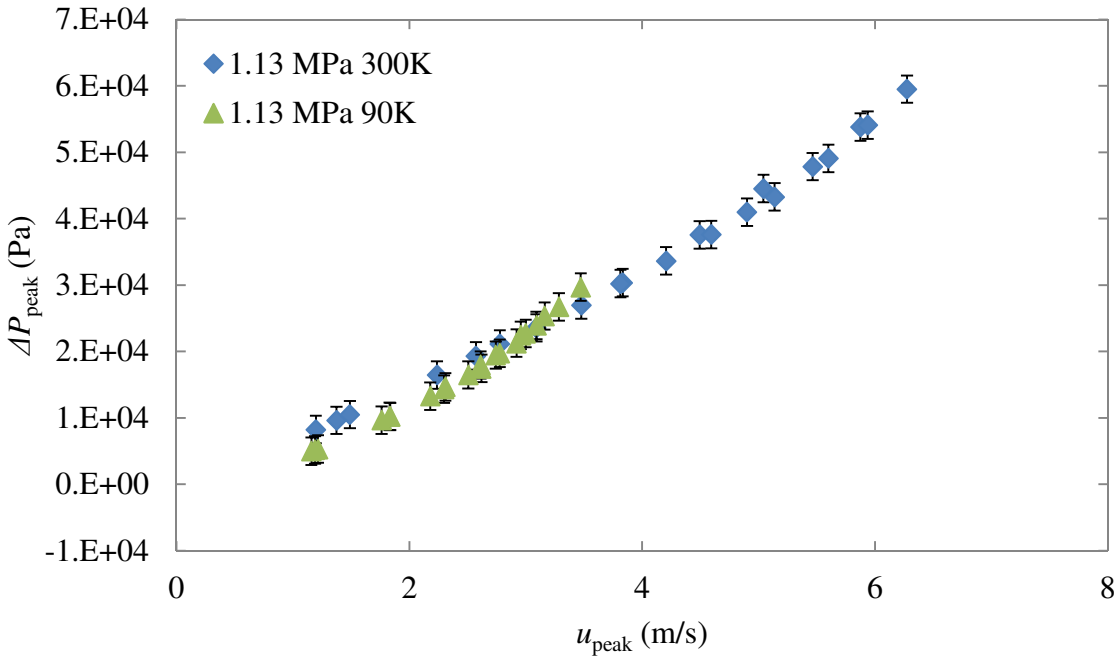

Figure 57. Maximum instantaneous pressure drop across the #400SS mesh regenerator as function of peak flow velocity at 1.13 MPa

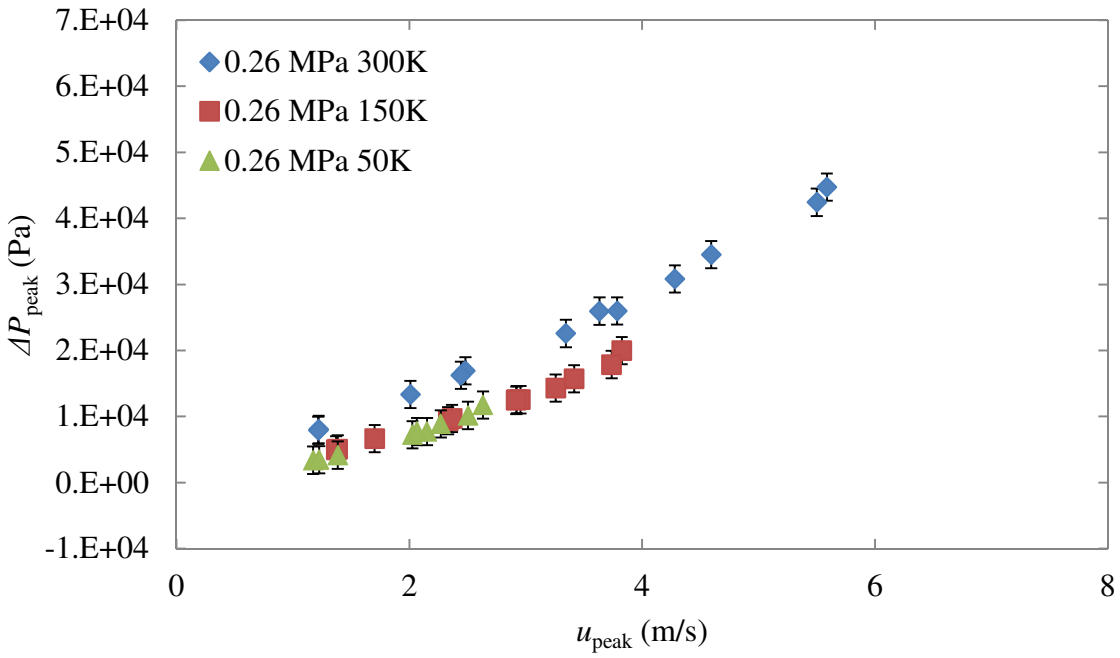

Figure 58. Maximum instantaneous pressure drop across the #400SS mesh regenerator as a function of peak flow velocity at 0.10 MPa

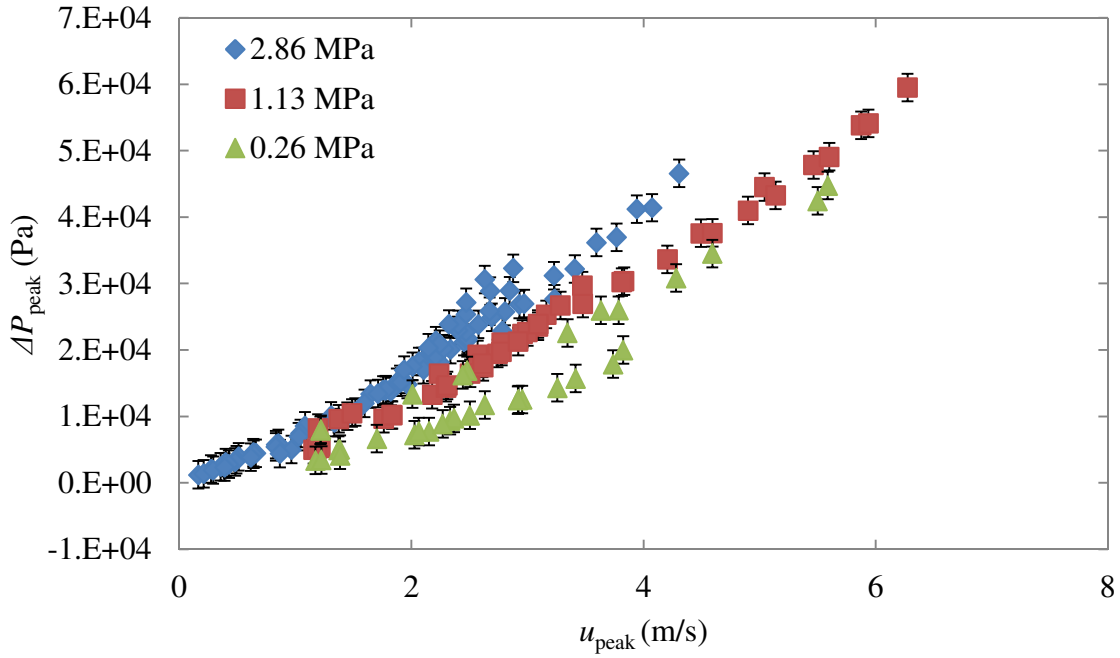

Figure 59. Maximum instantaneous pressure drop across the #400SS mesh regenerator as function of peak flow velocity at 2.86, 1.13, and 0.10 MPa

5.2.2 Sage Simulation Results

The experimentally measured maximum pressure drop and peak physical velocity for the #400SS regenerator can next be used to evaluate the total frictional pressure gradient in Sage, given by Eq.(19), and the Sage friction factor, given by Eq.(23). According to Eq.(19), the total frictional pressure gradient at a given moment is simply the pressure drop across the regenerator at that moment divided by the regenerator length, which is given in Table 1. Figure 60 shows the results for friction factors calculated using the experimental data as a function of the hydraulic-diameter Reynolds number given by Eq.(24). The results are plotted for 2.86, 1.13, and 0.26 MPa and compared to the correlation developed by Gedeon for packed mesh screens given by Eq. (31). Figure 60 shows that the experimental results agree very well with Gedeon's correlation for all charge pressures and temperatures. Since Gedeon's correlation was developed using data from experiments conducted at ambient conditions, this supports the belief that correlations developed at room temperature are indeed applicable at cryogenic temperatures for packed screen regenerators. Using the least-squares method, a new correlation was developed to match the experimental data and is given by Eq. (53) and is also shown in Figure 60.

$$f_{\text{Perrella}} = \frac{168}{\text{Re}_{d_h}} + 1.72 \tag{53}$$

The general trend of the data is linearly proportional to the inverse of the Reynolds number at low flow rates when viscous forces dominate, similar to the Darcy friction

factor for internal pipe flow. As inertial forces become more important at Reynolds numbers above approximately 100, the Sage friction factor begins to plateau.

Suitable values for the Sage friction factor can also be determined computationally using the Sage software itself. Following the approach outlined in section 4.2, a working model of the entire test section including the #400SS mesh regenerator was constructed as shown in Figure 18. Using the generic matrix option for the regenerator described by Eq.(32), the friction factor and PWG amplitude were iteratively varied using Sage's built-in optimization function until the pressure amplitudes upstream and downstream of the regenerator matched the experimental results. The simulated values for Sage friction factor are shown in Figure 61. The figure shows that the simulated friction factor values also agree very well with Gedeon's correlation for all charge pressures and temperatures. The mass flow rate amplitudes calculated from the Sage simulations also agree with the experimental values to within a few percentage points. Figure 62 shows a comparison of the experimental and simulated Sage friction factors for the #400SS mesh regenerator, demonstrating that the two are almost identical.

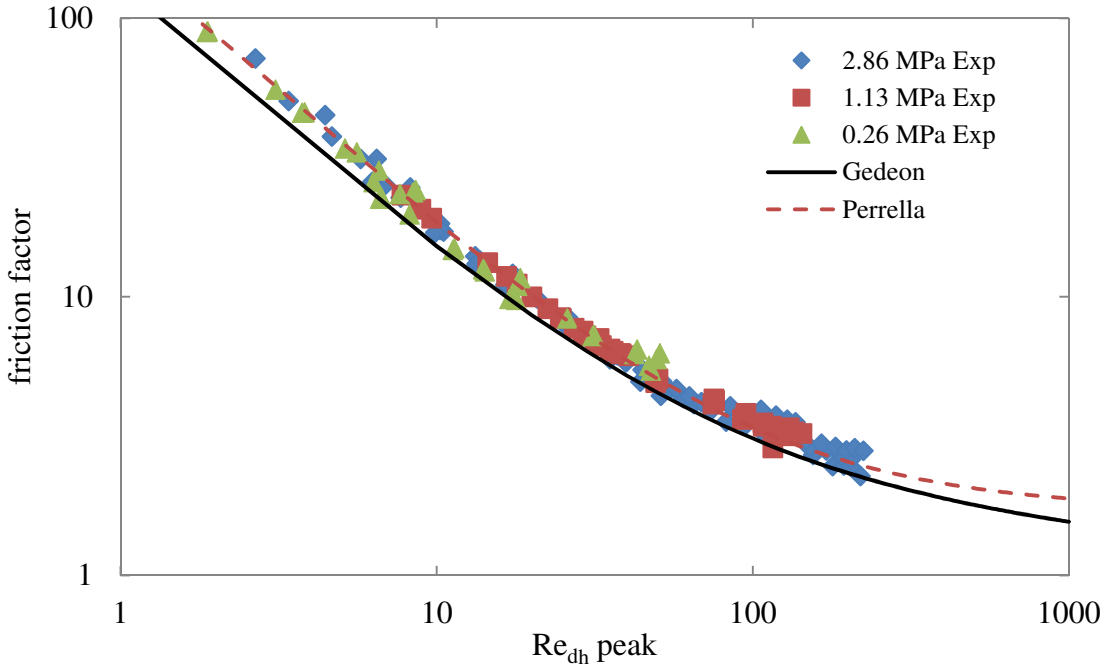

Figure 60. Experimental Sage friction factor for the #400SS mesh regenerator compared to the correlation by Gedeon for packed mesh screens, Eq. (31)

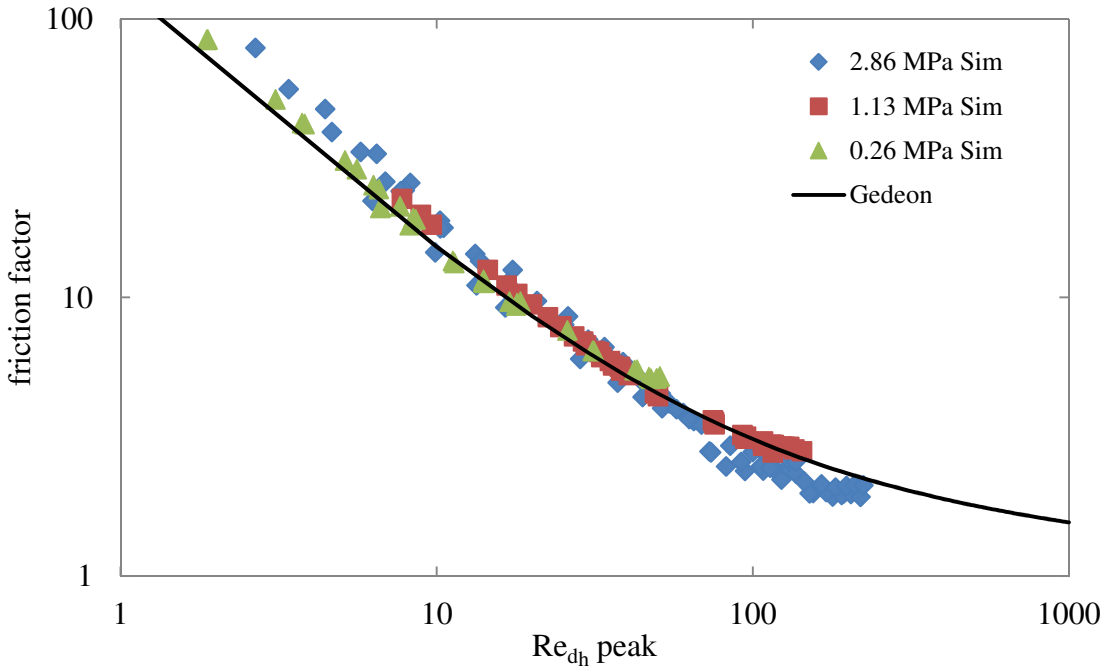

Figure 61. Simulated Sage friction factor for the #400SS regenerator compared to the correlation by Gedeon for packed mesh screens, Eq. (31)

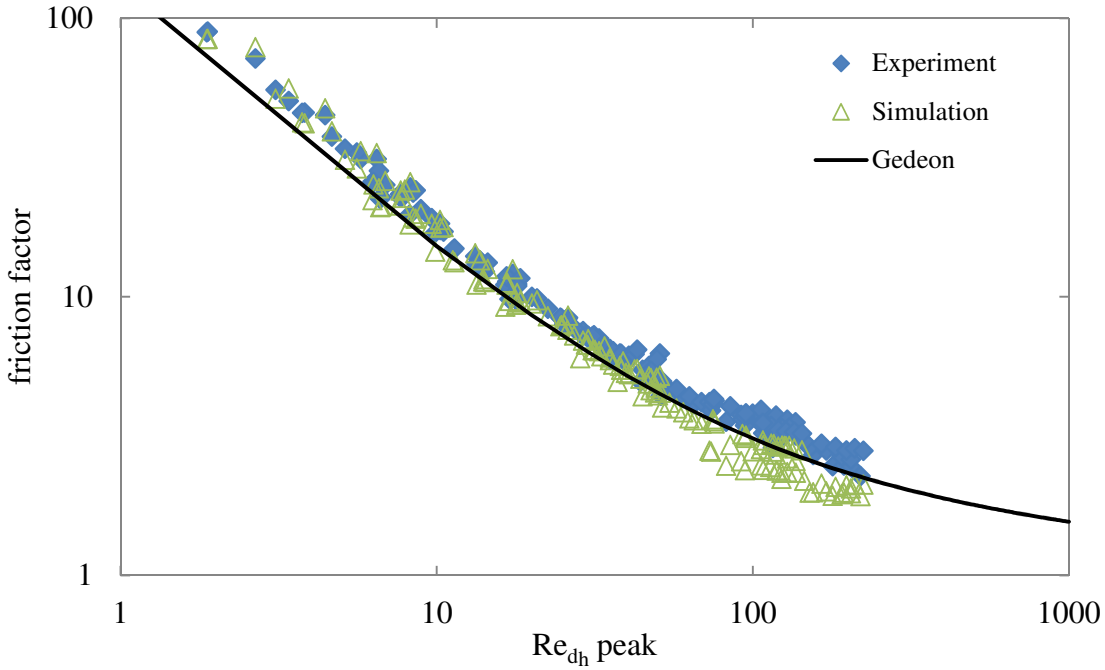

Figure 62. Comparison of Sage simulation and experimental friction factor for the #400SS regenerator as a function of hydraulic-diameter Reynolds number for 2.86, 1.13, and 0.26 MPa

5.2.3 CFD Simulation Results

Figures 63, 64, and 65 show the momentum source term in Fluent, S_i vs. the peak flow velocity and the non-dimensionalized momentum source term, Γ, vs. the hydraulic dimeter-based Reynolds number for 2.86, 1.13, and 0.26 MPa, respectively. The momentum source term in Fluent is identical to the total frictional pressure gradient, F, in Sage and is defined according to Eq. (37). The momentum source term represents the hydrodynamic resistance of the porous medium in Fluent, and is composed of a viscous resistance term, β, and an inertial resistance term, C_2. Based on Eq. (37), S_i will be a quadratic function of physical velocity, u, but differences in fluid properties at different charge pressures and operating temperatures make it impossible to develop a single

correlation for all operating conditions. It is therefore necessary to non-dimensionalize the momentum source term according to Eq. (44) based on the hydraulic-diameter and assign the non-dimensional term the arbitrary variable, Γ. Figures 63, 64, and 65 show how the non-dimensionalization of the momentum source term condenses the data into a single trend line which can be fitted with a quadratic correlation with very good agreement. Figure 66 presents the dimensional and non-dimensional momentum source terms for 2.86, 1.13, and 0.26 MPa for all frequencies and operating temperatures with a quadratic fit model for the combined data. This shows, once again, that the hydrodynamic resistance of the porous filler material is independent of the operating temperature. The error bars in The error bars in Figure 66 represent the value of the quadratic best-fit line ±10%. Figure 67 compares the experimental values for Γ calculated from the peak regenerator pressure drop to the simulated values using the Sage optimization software. The Sage simulation and experimental values for Γ follow the same general trend, although the experimental results are slightly higher for the same Reynolds number values.

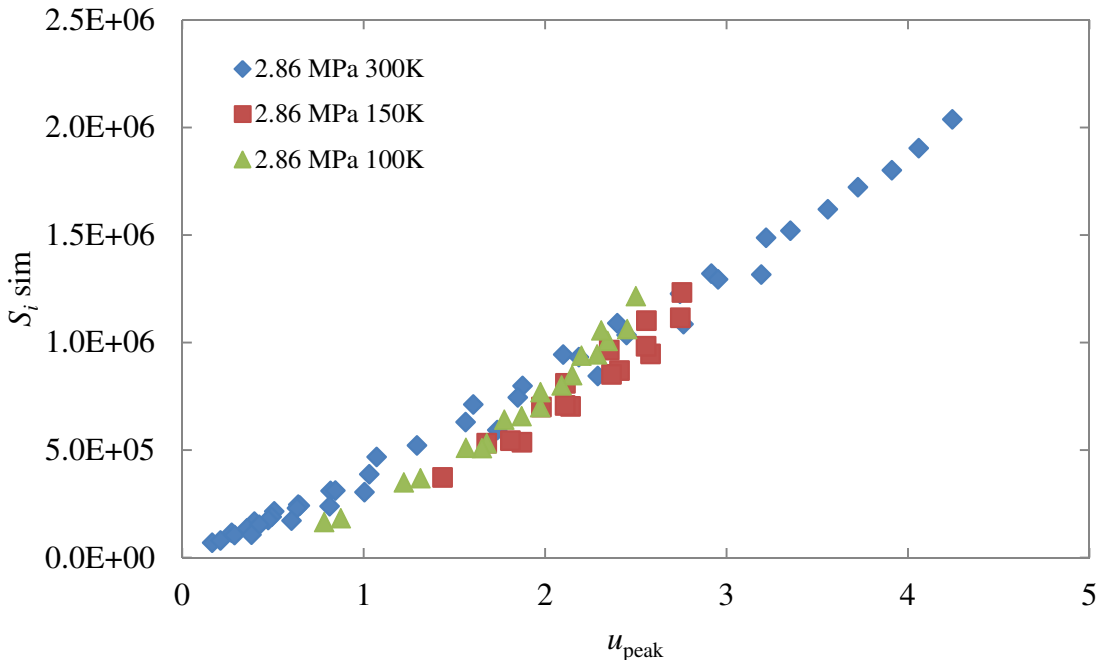

a) Fluent momentum source term at 2.86 MPa

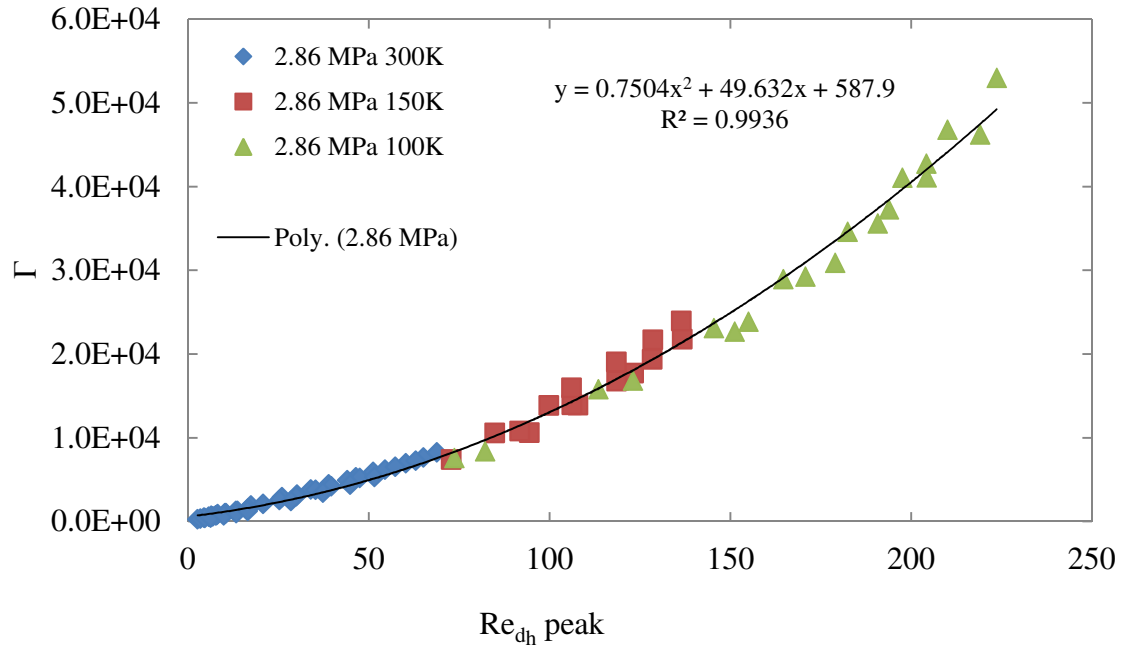

b) Dimensionless momentum source term at 2.86 MPa

Figure 63. #400SS mesh regenerator results for a) momentum source term in Fluent, S_i, and b) non-dimensionalized momentum source term, Γ, calculated from Sage total frictional pressure gradient for 2.86 MPa at 300, 150, and 100K

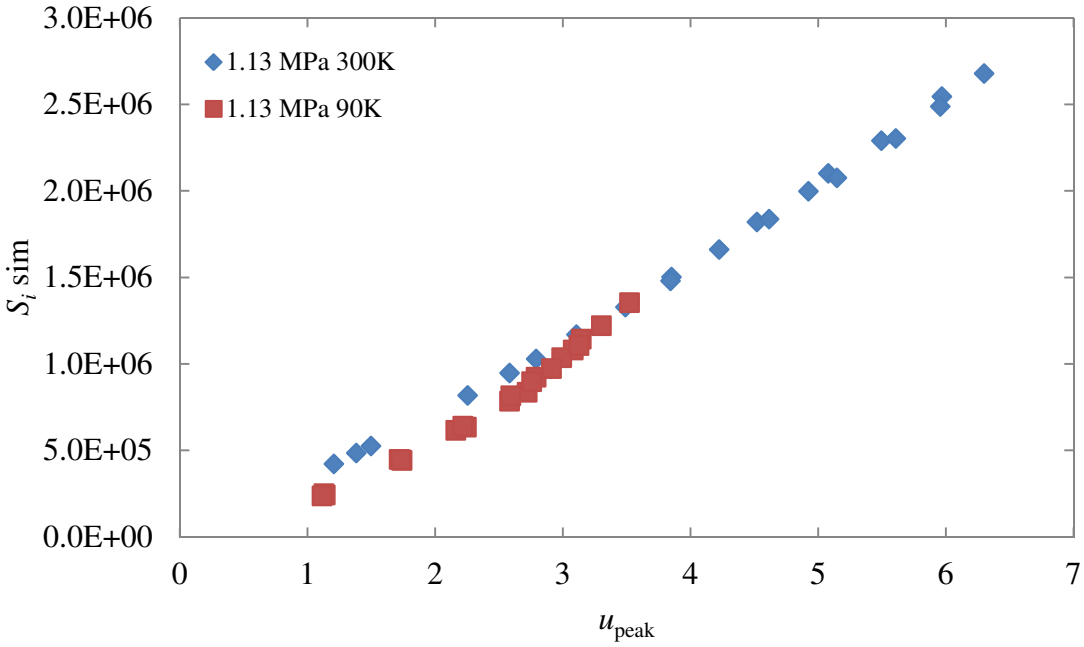

a) Fluent momentum source term at 1.13 MPa

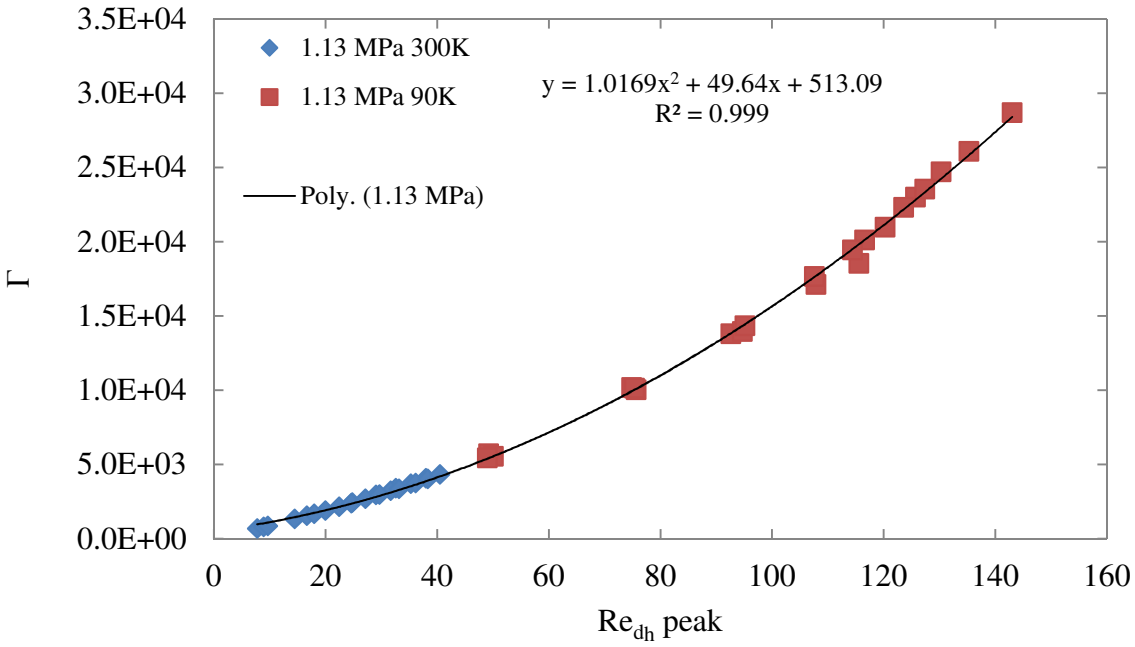

b) Dimensionless momentum source term at 1.13 MPa

Figure 64. #400SS mesh regenerator results for a) momentum source term in Fluent, S_i, and b) non-dimensionalized momentum source term, Γ, calculated from Sage total frictional pressure gradient for 1.13 MPa at 300, 150, and 75K

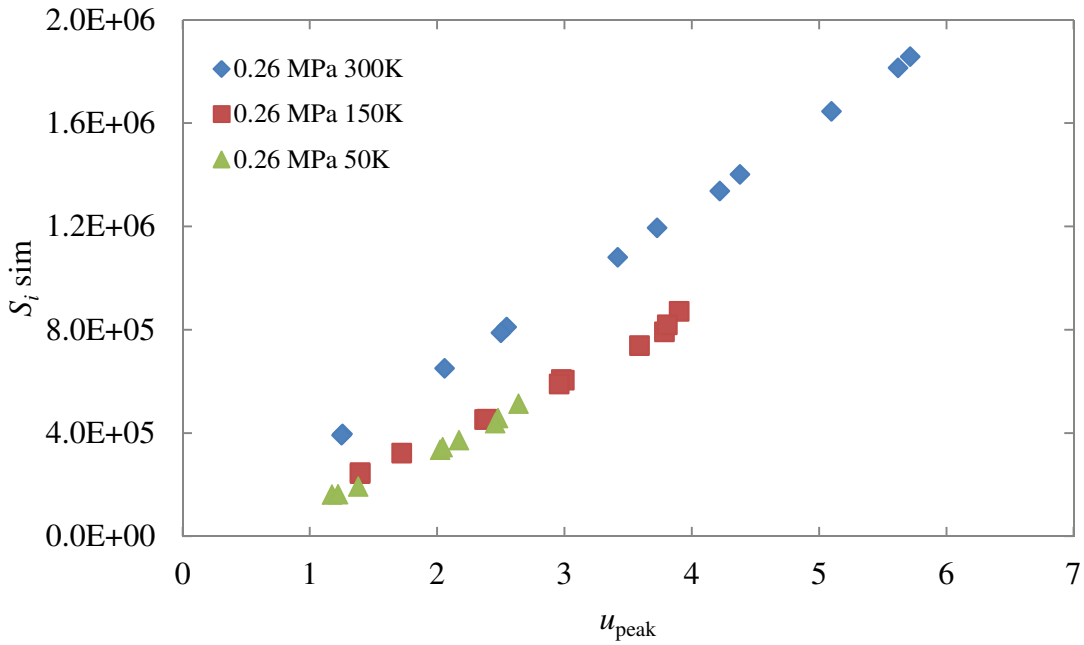

a) Fluent momentum source term at 0.10 MPa

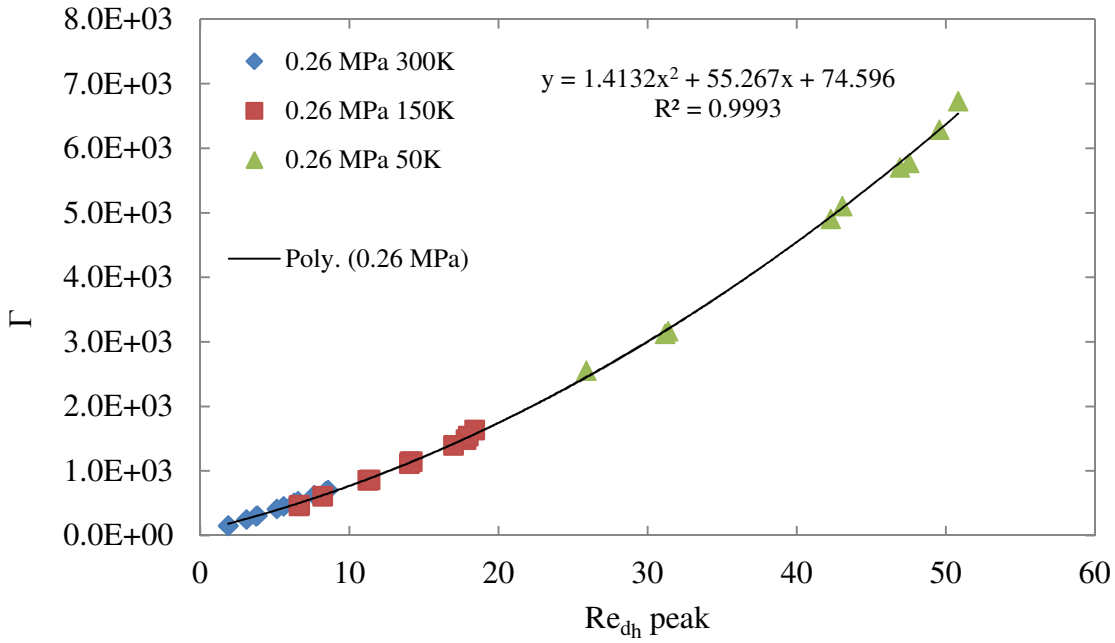

b) Dimensionless momentum source term at 0.10 MPa

Figure 65. #400SS mesh regenerator results for a) momentum source term in Fluent, S_i, and b) non-dimensionalized momentum source term, Γ, calculated from Sage total frictional pressure gradient for 0.10 MPa at 300, 100, and 50K

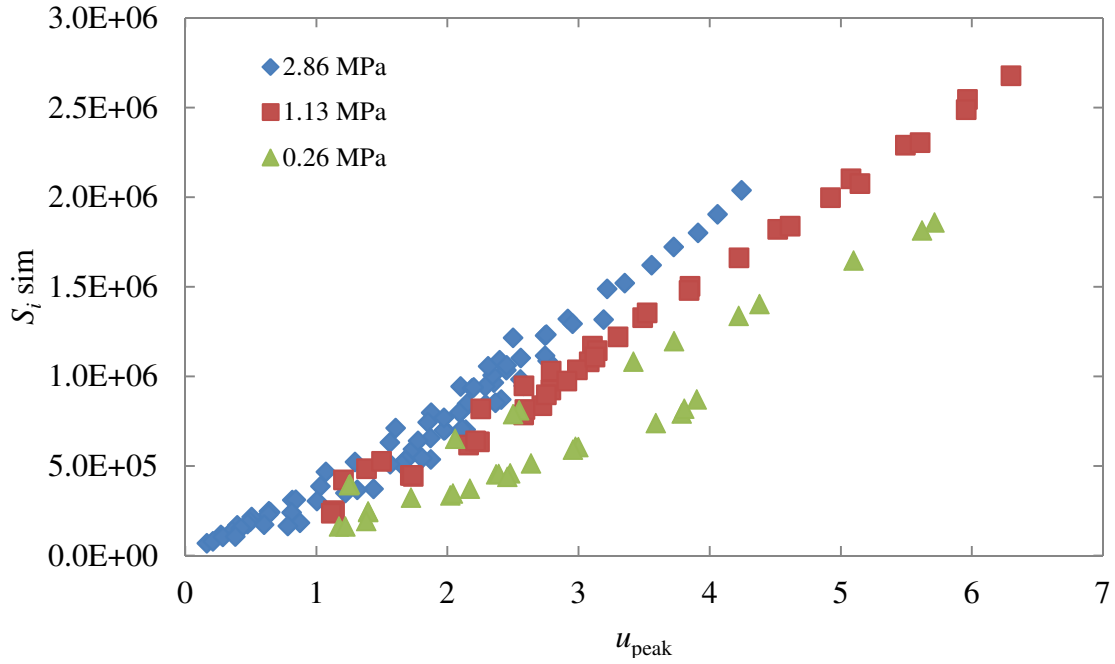

a) Fluent momentum source term at 2.86, 1.13, and 0.26 MPa

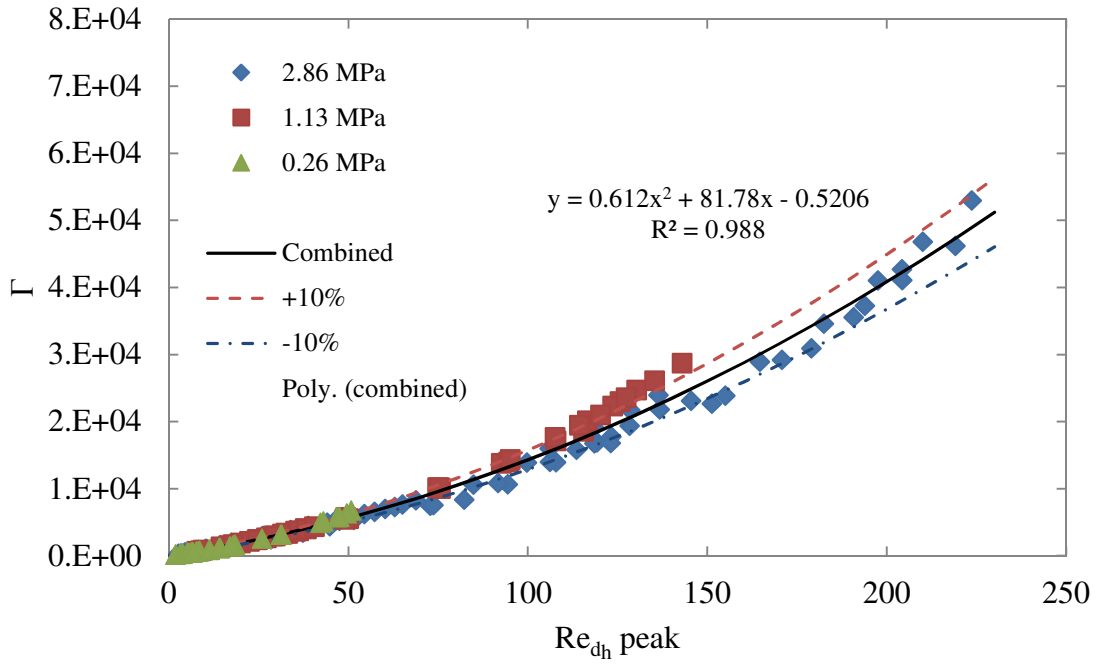

b) Dimensionless momentum source term at 2.86, 1.13, and 0.26 MPa

Figure 66. #400SS mesh regenerator results for a) momentum source term in Fluent, S_i, and b) non-dimensionalized momentum source term, Γ, calculated from Sage total frictional pressure gradient for 2.86, 1.13, and 0.26 MPa

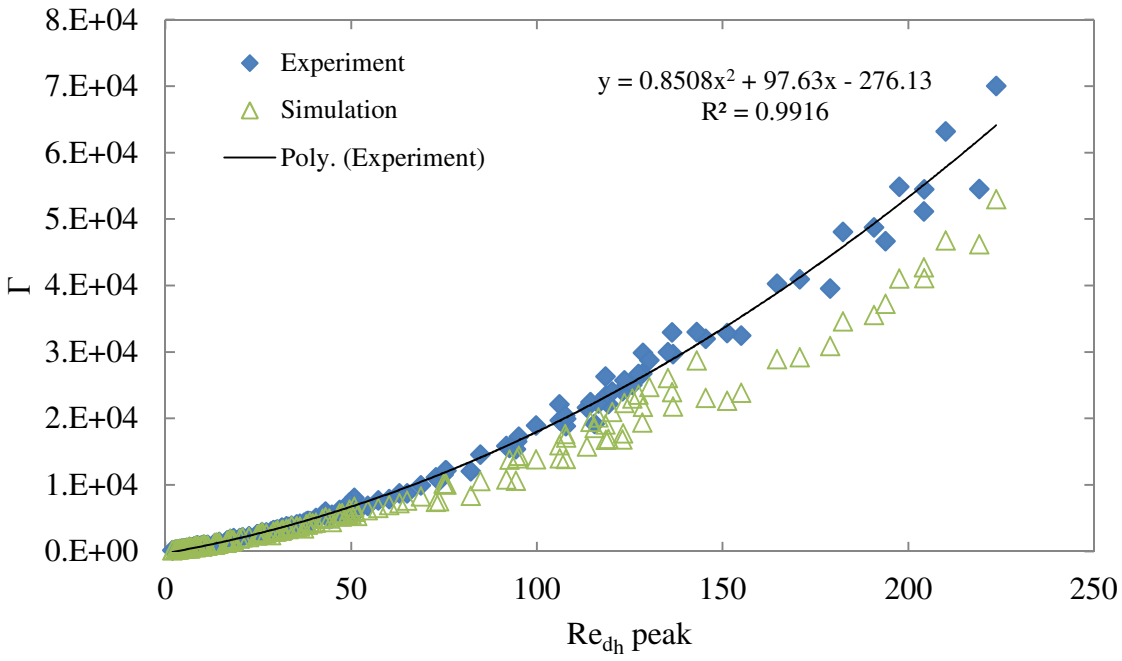

Figure 67. Comparison of Sage simulation and experiment dimensionless momentum source term at 2.86, 1.13, and 0.26 MPa for the #400SS mesh regenerator

Table 6 presents the viscous and inertial resistances in Fluent extracted from the quadratic model of the non-dimensionalized momentum source term according to Eq. (49) and Eq.(50). The Darcy permeability and Forchheimer coefficient are determined according to Eq.(40) and Eq.(41), respectively. The results are compared with those of Cha for #400SS non-sintered mesh [1]. As the results indicate, the hydrodynamic resistance parameters differ slightly based on mean operating pressure, but are all the same order of magnitude. The combined simulated hydrodynamic resistances also agree well with those calculated from the experimental results. The results from Cha are of similar magnitude, but differ from the current results by a factor of nearly two for some cases. This is most likely due to the different method that Cha used to determine the hydrodynamic resistances. Similar to Pathak [43], Cha determined the viscous resistance

first by neglecting the inertial resistance (setting $C_2 = 0$) for the case with the lowest mass flow rate magnitude. Unlike Pathak, however, Cha used the lowest oscillatory mass flow rate to determine the viscous resistance rather than the lowest steady-flow mass flow rate. This might explain why the results of Cha agree better with the current study than those of Pathak. Cha's results have a single value for inertial resistance and Forchheimer coefficient for all flow velocities, the same as this study.

Table 6. Summary of Fluent viscous and inertial resistance, Darcy Permeability and Forchheimer coefficient for #400SS mesh regenerator

Pressure [MPa]	A	B	β [1/m^2]	C_2 [1/m]	K [m^2]	c_f
2.86	0.75	49.63	1.42E+10	4.33E+04	7.06E-11	1.82E-01
1.13	1.01	49.64	1.42E+10	5.88E+04	7.05E-11	2.47E-01
0.26	1.41	55.26	1.58E+10	8.17E+04	6.34E-11	3.25E-01
Combined	0.61	81.78	2.34E+10	3.50E+04	4.28E-11	1.16E-01
Experimental	0.85	97.63	2.79E+10	4.92E+04	3.59E-11	1.47E-01
Cha [1]	-	-	3.97E+10	1.20E+05	2.52E-11	3.01E-01

The hydrodynamic resistance parameters from Table 6, specifically β and C_2 for the individual pressure calculations, were then used to simulate the oscillatory flow through regenerator 2 for several charge pressures and temperatures according to the approach outlined in Section 4.3.2. A single oscillating pressure boundary condition was applied to the inlet of the regenerator with a user defined function in the same fashion as Cha's study. Table 7 shows the results of the Fluent analysis in terms of the downstream mass flow rate and pressure amplitudes. For the results presented in Table 7, the porous medium was assumed to be isotropic, with the same values of viscous and inertial resistance applied to the axial and radial directions. This assumption is suspect since prior literature including studies by Cha, Kirkonnell, and Clearman [39] indicate that the

hydrodynamic resistance parameters in the radial direction tend to be higher than those in the axial direction by a factor of about three for woven screen matrices. However, it is generally believed that when the flow is primarily in the axial direction, as in this case, the error associated with applying axial hydrodynamic resistance parameters to the radial direction is negligible since very little flow actually moves in the radial direction [1].

Table 7. Summary of CFD simulation results using viscous and inertial resistances from Table 6 compared to experimental measurements for #400SS mesh regenerator

Pressure [MPa]	Temperature [K]	$\dot{m}_{exp}$ [kg/s]	$\dot{m}_{sim}$ [kg/s]	Percent error	$P_{max_{exp}}$ [Pa]	$P_{max_{sim}}$ [Pa]	Percent error
2.86	300	2.25E-03	1.76E-03	2.20E-01	8.46E+04	8.62E+04	1.79E-02
2.86	150	3.47E-03	2.76E-03	2.06E-01	6.49E+04	6.49E+04	3.35E-04
2.86	100	4.70E-03	3.85E-03	1.80E-01	6.03E+04	6.04E+04	9.35E-04
1.13	300	1.25E-03	1.02E-03	1.83E-01	4.81E+04	5.31E+04	1.04E-01
1.13	90	2.61E-03	2.10E-03	1.96E-01	3.14E+04	3.26E+04	3.99E-02
0.26	300	4.60E-04	3.99E-04	1.33E-01	1.83E+04	2.74E+04	5.00E-01
0.26	151	6.21E-04	4.83E-04	2.22E-01	1.24E+04	1.59E+04	2.87E-01
0.26	62	1.02E-03	7.93E-04	2.25E-01	8.22E+03	1.03E+04	2.58E-01

The Fluent simulations agree very well with experimental results for the highest charge pressure of 2.86 MPa, but less favorably for lower charge pressures. The percentage error of the downstream pressure amplitude is lowest for higher pressures and lower temperatures, which corresponds with higher mass flow rate amplitudes. Similar to the results for the $Er_{0.5}Pr_{0.5}$ regenerator, the simulated mass flow rate amplitudes show a consistent deviation from experiment of approximately 20%, which as previously discussed is most likely due to the inability of the oscillating pressure boundary condition to provide the appropriate coupled mass flow rate at the inlet. Unlike the $Er_{0.5}Pr_{0.5}$ results, however, the downstream pressure amplitudes sometimes differ by as much as 50%. This suggests that the simplifying assumption of isotropic hydrodynamic resistance for

the #400SS mesh regenerator is not appropriate, especially not for lower mass flow rate amplitudes. This makes physical sense as one can imagine that for higher mass flow rate amplitudes, the flow in the axial direction will dominate the flow in the radial direction, whereas secondary flows due to boundary effects or interfaces become more important as the mass flow rate amplitude decreases.

Table 8 shows the results of varying the radial viscous and inertial resistance in Fluent iteratively in order to achieve better agreement between the experimental and simulated values of the downstream pressure amplitude. The results indicate that excellent agreement between the experimental and simulated downstream pressure amplitudes was achieved by multiplying the axial viscous and inertial resistances by a factor of approximately 5/3 or 1.689 to get the radial values. This differs from the factor of ~3 determined by Cha et al., but in those studies the radial hydrodynamic resistance parameters where determined by directly measuring the pressure drop in the radial direction rather than iterating the computational simulation as was done here.

Table 8. Investigation of anisotropic hydrodynamic resistance for #400SS mesh at 0.26 MPa and 300K using combined α and C_2 from Table 6

Radial multiplication factor	$\dot{m}_{exp}$ [kg/s]	$\dot{m}_{sim}$ [kg/s]	Percent error	$P_{max\ exp}$ [Pa]	$P_{max_{sim}}$ [Pa]	Percent error
0	4.60E-04	3.33E-04	2.76E-01	1.83E+04	2.26E+04	2.36E-01
3	4.60E-04	2.07E-04	5.50E-01	1.83E+04	1.37E+04	2.52E-01
2	4.60E-04	2.53E-04	4.50E-01	1.83E+04	1.68E+04	7.86E-02
1.5	4.60E-04	2.87E-04	3.76E-01	1.83E+04	1.92E+04	5.17E-02
1.7	4.60E-04	2.75E-04	4.03E-01	1.83E+04	1.82E+04	2.01E-03

Table 9 shows the results for the anisotropic hydrodynamic resistance analysis for charge pressures of 0.26, 1.13, and 2.86 MPa all with a radial multiplication factor of 1.689 applied to the viscous and inertial resistances in Fluent. The results show good agreement in terms of the downstream pressure amplitude, and similar percent error for the downstream mass flow rate as the isotropic case. These results suggest that the radial multiplication factor for the hydrodynamic resistance in Fluent is independent of mean operating pressure. While instructive, these results are far from conclusive. Future researches could investigate further the effects of anisotropic hydrodynamic parameters on mass flow and pressure drop, but such an investigation is beyond the scope of this work.

Table 9. Investigation of anisotropic hydrodynamic resistance for #400SS mesh at 0.26, 1.13, and 2.86 MPa and 300K using Combined α and C_2 from Table 6

Pressure [MPa]	$\dot{m}_{exp}$ [kg/s]	$\dot{m}_{sim}$ [kg/s]	Percent error	$P_{max_{exp}}$ [Pa]	$P_{max_{sim}}$ [Pa]	Percent error
0.26	4.60E-04	2.75E-04	4.03E-01	1.83E+04	1.82E+04	2.01E-03
1.13	1.25E-03	9.14E-04	2.71E-01	4.81E+04	4.84E+04	6.61E-03
2.86	2.25E-03	1.70E-03	2.44E-01	8.46E+04	8.47E+04	1.12E-03

Similarly to the $Er_{0.5}Pr_{0.5}$ regenerator, slightly different results for the Fluent hydrodynamic resistances, Darcy Permeability and Forchheimer coefficients can be obtained by forcing the y-intercept of the quadratic fit to zero. This approach might provide more appropriate results since, physically, the hydrodynamic resistance of the porous medium should be zero at zero flow velocity. The results are summarized in Table 10. The zero-intercept results agree fairly well with the non-zero-intercept results from Table 6, but there are slight differences. One might expect the intercept of the non-

dimensionalized momentum source term, Γ, to equal zero naturally, without having to be forced, but this is not the case. Once again, this could be due to the bias error of the dynamic pressure transducers themselves or due to the error associated with the mean operating pressure measurement.

Table 10. Summary of Fluent viscous and inertial resistance, Darcy permeability and Forchheimer coefficients with zero intercept

Pressure [MPa]	A	B	β [1/m^2]	C_2 [1/m]	K [m^2]	c_f
2.86	0.70	61.98	1.77E+10	4.05E+04	5.65E-11	1.52E-01
1.13	0.91	66.98	1.91E+10	5.26E+04	5.23E-11	1.90E-01
0.26	1.28	62.85	1.79E+10	7.42E+04	5.57E-11	2.77E-01
Combined	0.61	81.77	2.33E+10	3.54E+04	4.28E-11	1.16E-01
Experimental	0.88	91.15	2.60E+10	5.08E+04	3.84E-11	1.57E-01
Cha [1]	-	-	3.97E+10	1.20E+05	2.52E-11	3.01E-01

5.3 Regenerator 3: #325SS Wire Mesh

Given the prevalence and popularity of wire mesh regenerator filler materials, it seemed prudent to test at least one other variety of wire mesh in addition to regenerator 2. For regenerator 3, #325 stainless steel was selected based on its wide use and to serve as another comparison with the work of Cha et al. [1,38,39,51]. The woven-screen matrix of regenerator 3 is similar in design and construction to regenerator 2, but with a larger wire diameter and mesh thickness, as shown in Table 1. The #325SS mesh will have similar pressure drop and heat transfer characteristics with the #400SS mesh, or other meshes of similar mesh density, including good heat transfer with the working fluid, limited conduction in the axial direction, and relatively small pressure drop across the length of the regenerator. The porosity of regenerator 2 is within the expected range for a packed-screen regenerator at 0.688, and likely possesses similar anisotropic behaviour as the #400SS mesh regenerator. In this study, however, only isotropic hydrodynamic resistance is considered since the primary focus of this study is to investigate the effects of cryogenic temperature on the hydrodynamic resistance parameters. Future work could focus on further investigating the radial flow properties of woven screen matrices at various temperatures and evaluate their relevance to cryocooler performance.

5.3.1 Experimental Results

The transient pressure oscillations at the inlet and outlet of regenerator 3 were measured and transformed according to the process outlined in Section 3.2. The regenerator was tested at mean operating pressures of 2.86 MPa (400psig), 1.13 MPa (150psig), and 0.23 MPa (20psig) and frequencies of 50, 60, and 70 Hz. Measurements

were performed at ambient and cryogenic temperatures for all charge pressures and frequencies.

The experimental setup for regenerator 3 is the same as that for regenerator 2, as outlined in Section 3.2. As shown in Figure 12, a larger surge volume was used for testing regenerators 2 and 3 to accommodate the higher mass flow rates through the wire mesh regenerators compared to the packed-sphere $Er_{0.5}Pr_{0.5}$ regenerator. Figures 68, 69, and 70 show the instantaneous upstream and downstream pressure oscillations across the CHX and regenerator 3 for 2.86, 1.13, and 0.23 MPa and 60 Hz operating frequency at ambient and cryogenic temperatures. The experimental results indicate that, like regenerator 2, the greatest drop in pressure amplitude occurs across the CHX and not the #325SS mesh regenerator. This seems reasonable considering that the porosity of the CHX is only 0.647 while the porosity of regenerator 3 is 0.688. The increased porosity is likely due to the smaller wire diameter and higher facial opening percentage of the #325SS mesh compared to the #100Cu mesh. The pressure drop across regenerator 3 for the cases shown does appear to be comparable to that of regenerator 2. Figures 71, 72, and 73 show the instantaneous upstream and downstream pressure oscillations across the regenerator and the instantaneous mass flow rate downstream. In general, the pressure amplitudes decrease with decreasing charge pressure and operating temperature, and the mass flow rate amplitudes increase with increasing charge pressure and decreasing operating temperature due to the increased density of the working fluid. As expected, the peak mass flow rate occurs when the instantaneous difference between the upstream and downstream pressure is greatest, and the mass flow rate is zero when the upstream and downstream pressures are equal. This agrees with the pressure-to-mass flow rate phase

relationship described by Eq. (10). Figures 74, 75, and 76 compare the instantaneous pressure drop across regenerator 3 with the mass flow rate downstream of the regenerator. The results verify that the peak mass flow rate coincides with the peak pressure drop. As with regenerator 2, although the oscillations are not purely sinusoidal, the waves are much smoother and less erratic than the pressure drop and mass flow rate oscillations for the $Er_{0.5}Pr_{0.5}$ regenerator. This is likely due to the increased porosity and accompanying higher mass flow rate magnitude for the woven mesh regenerators.

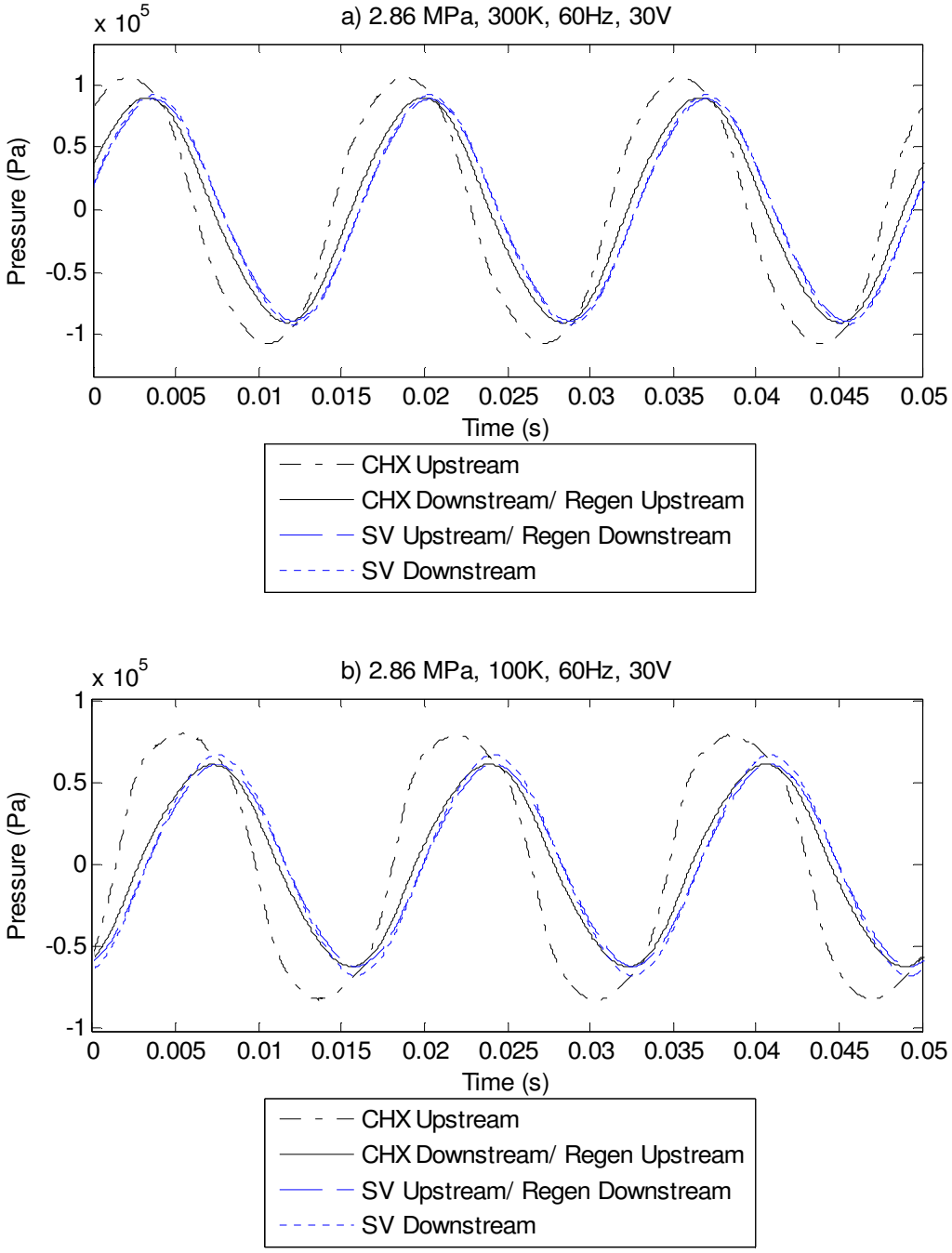

Figure 68. Instantaneous pressure across the #325SS mesh regenerator at 2.86 MPa for a) 300K and b) 100K at 60Hz and 30V PWG input voltage

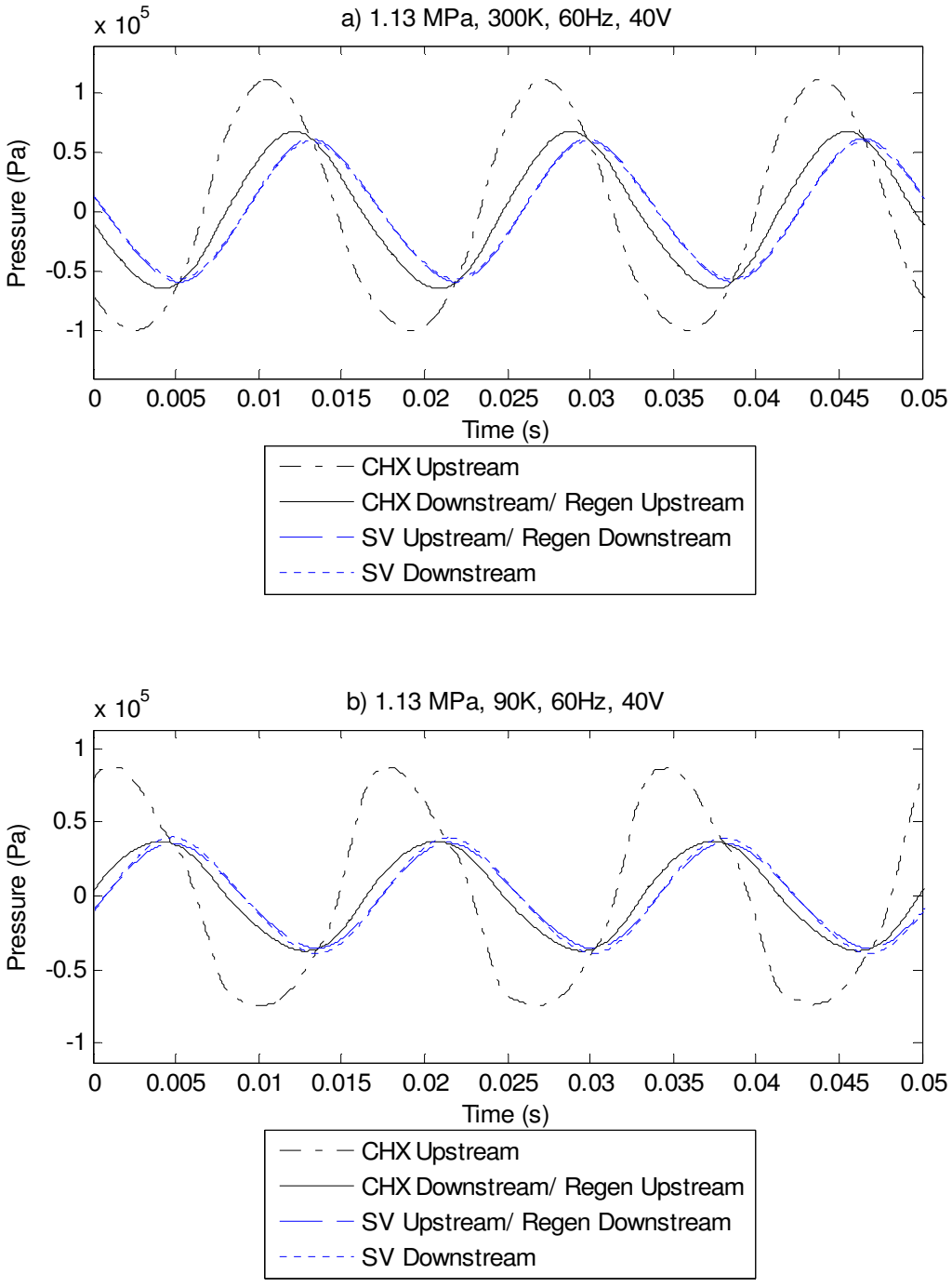

Figure 69. Instantaneous pressure across the #325SS mesh regenerator at 1.13 MPa for a) 300K and b) 90K at 60Hz and 40V PWG input voltage

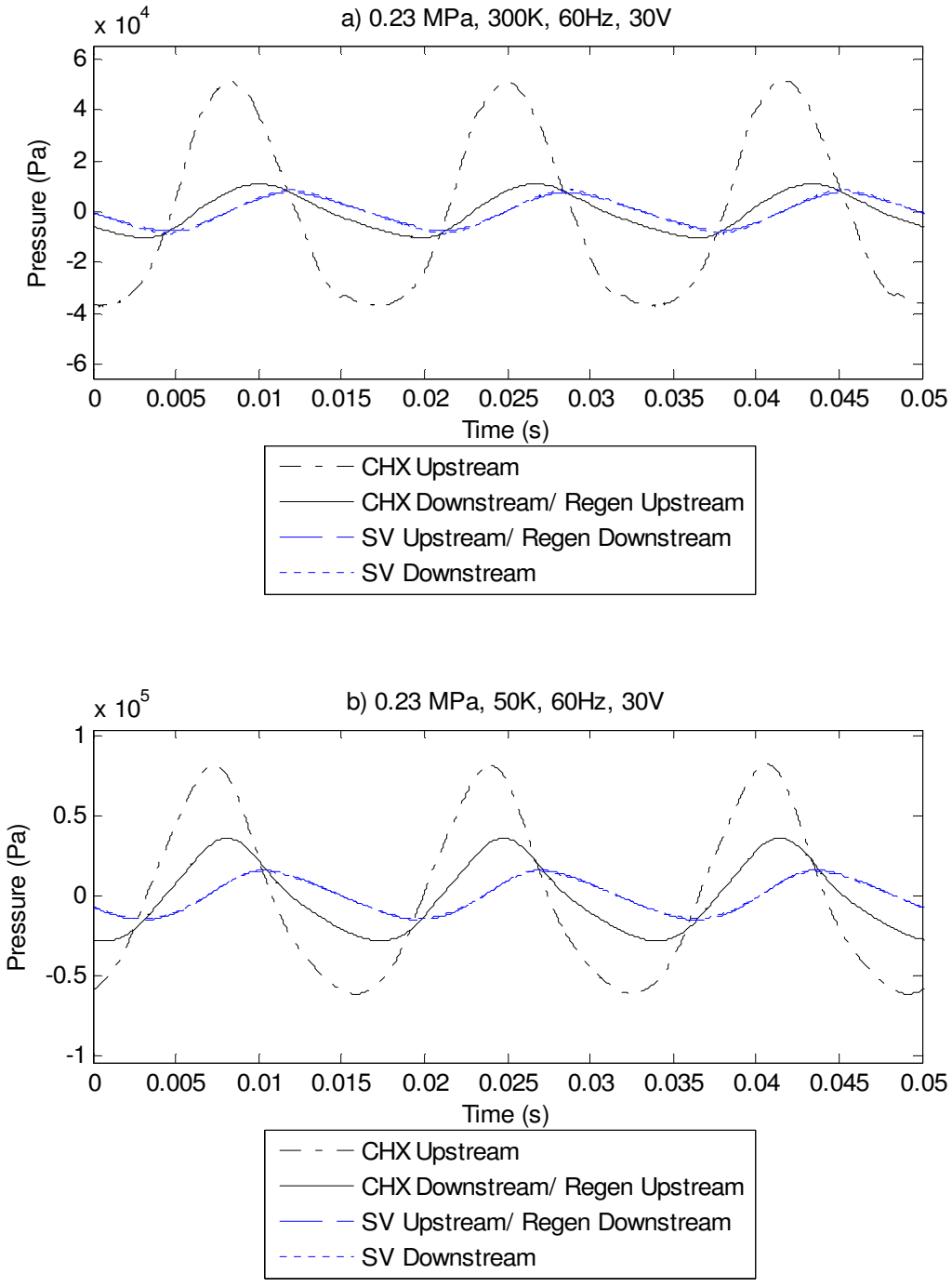

Figure 70. Instantaneous pressure across the #325SS mesh regenerator at 0.23 MPa for a) 300K and b) 50K at 60Hz and 30V PWG input voltage

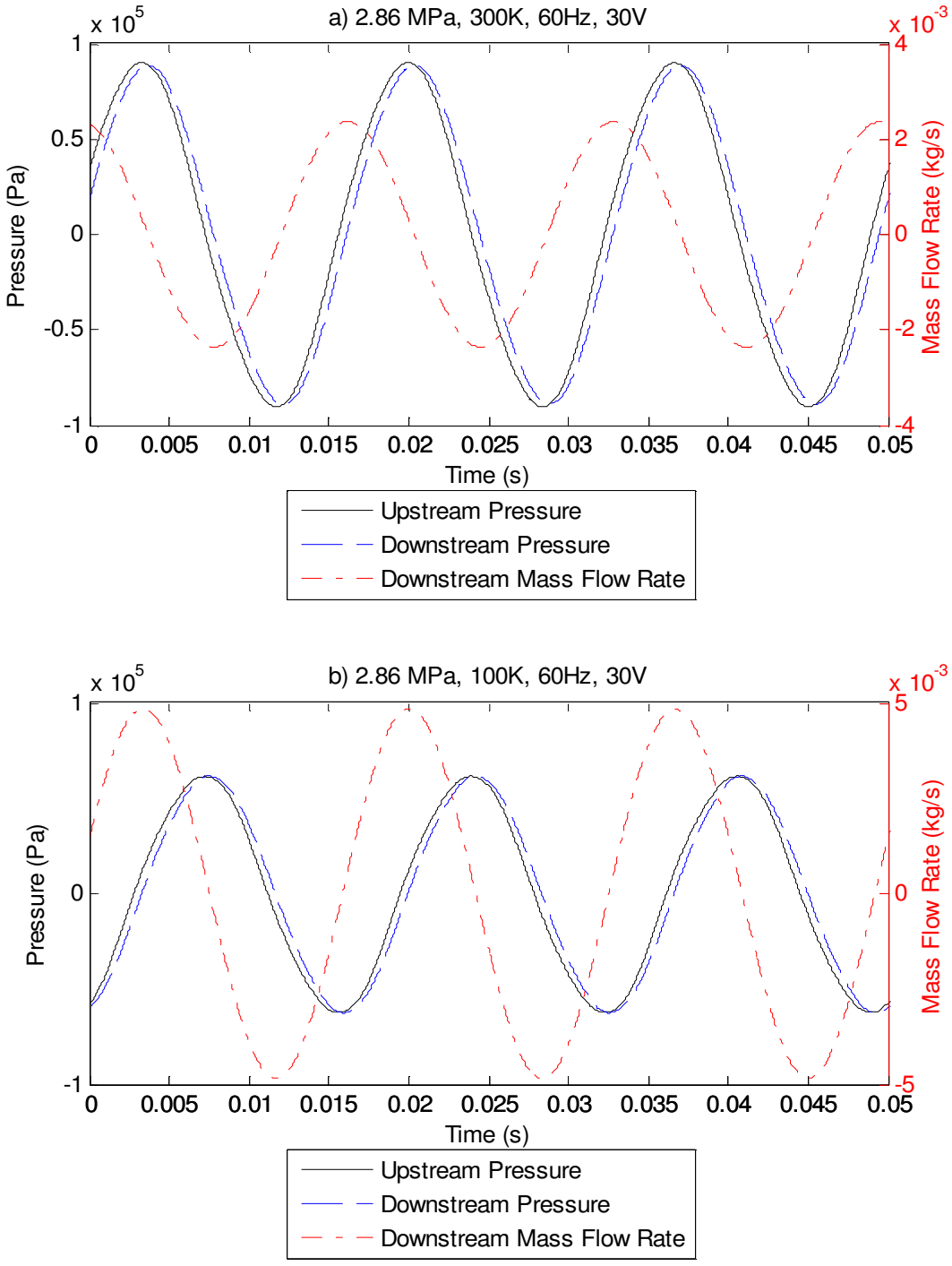

Figure 71. Transient pressure and mass flow rate oscillations for the #325SS mesh regenerator at 2.86 MPa for a) 300K and b) 100K at 60Hz and 30V PWG voltage input

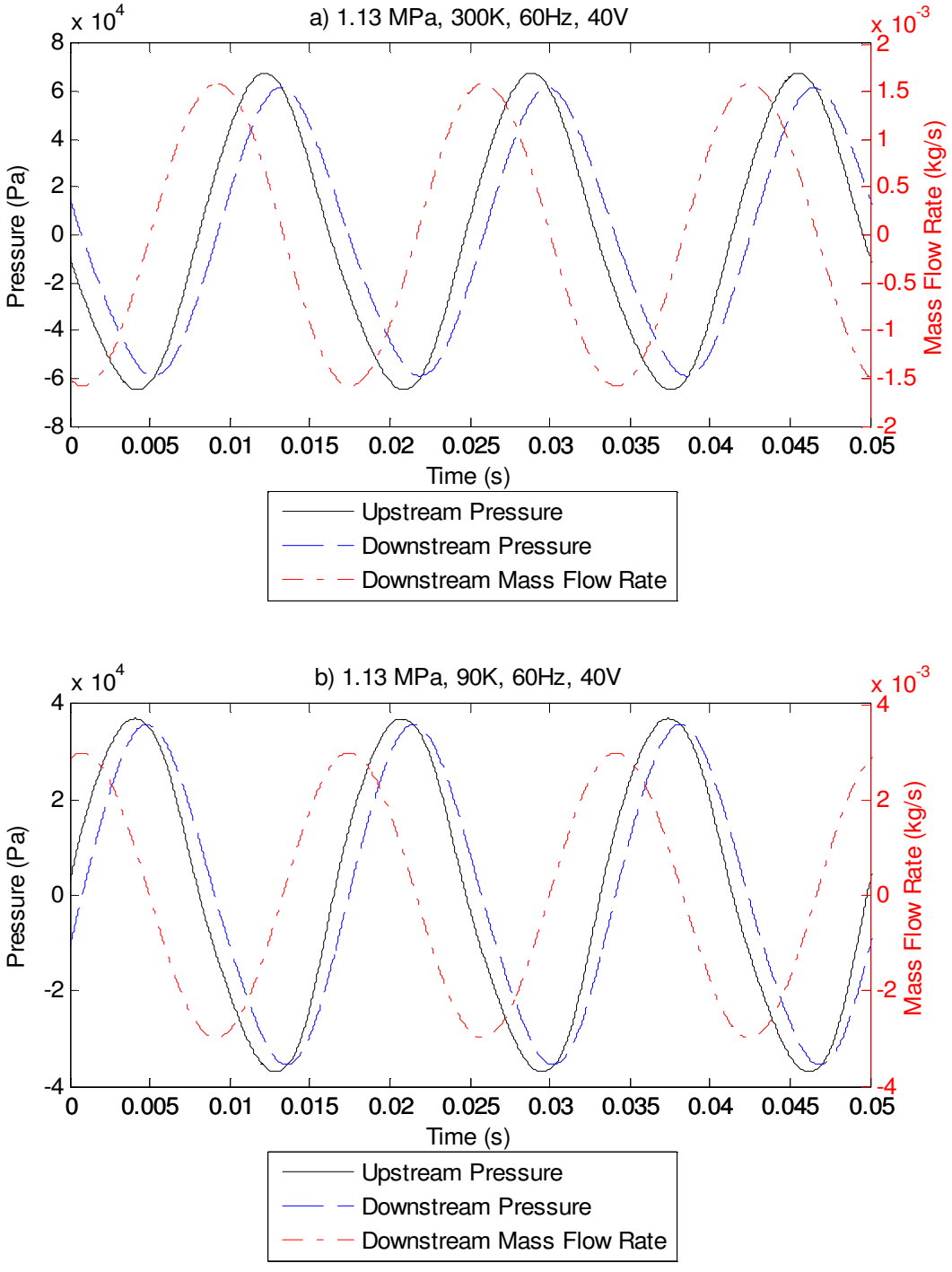

Figure 72. Transient pressure and mass flow rate oscillations for the #325SS mesh regenerator at 1.13 MPa for a) 300K and b) 90K at 60Hz and 40V PWG voltage input

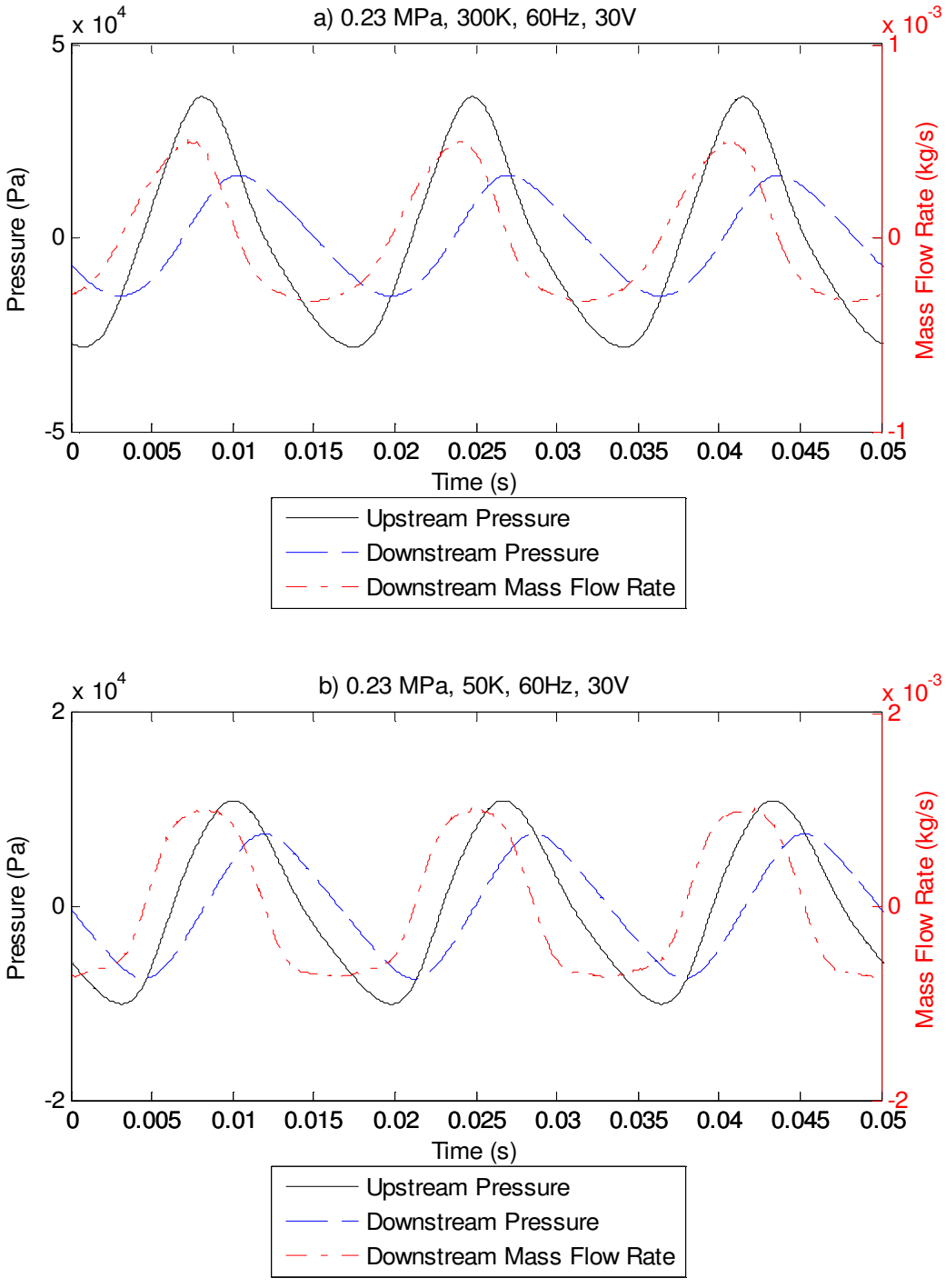

Figure 73. Transient pressure and mass flow rate oscillations for the #325SS mesh regenerator at 0.23 MPa for a) 300K and b) 50K at 60Hz and 30V PWG voltage input

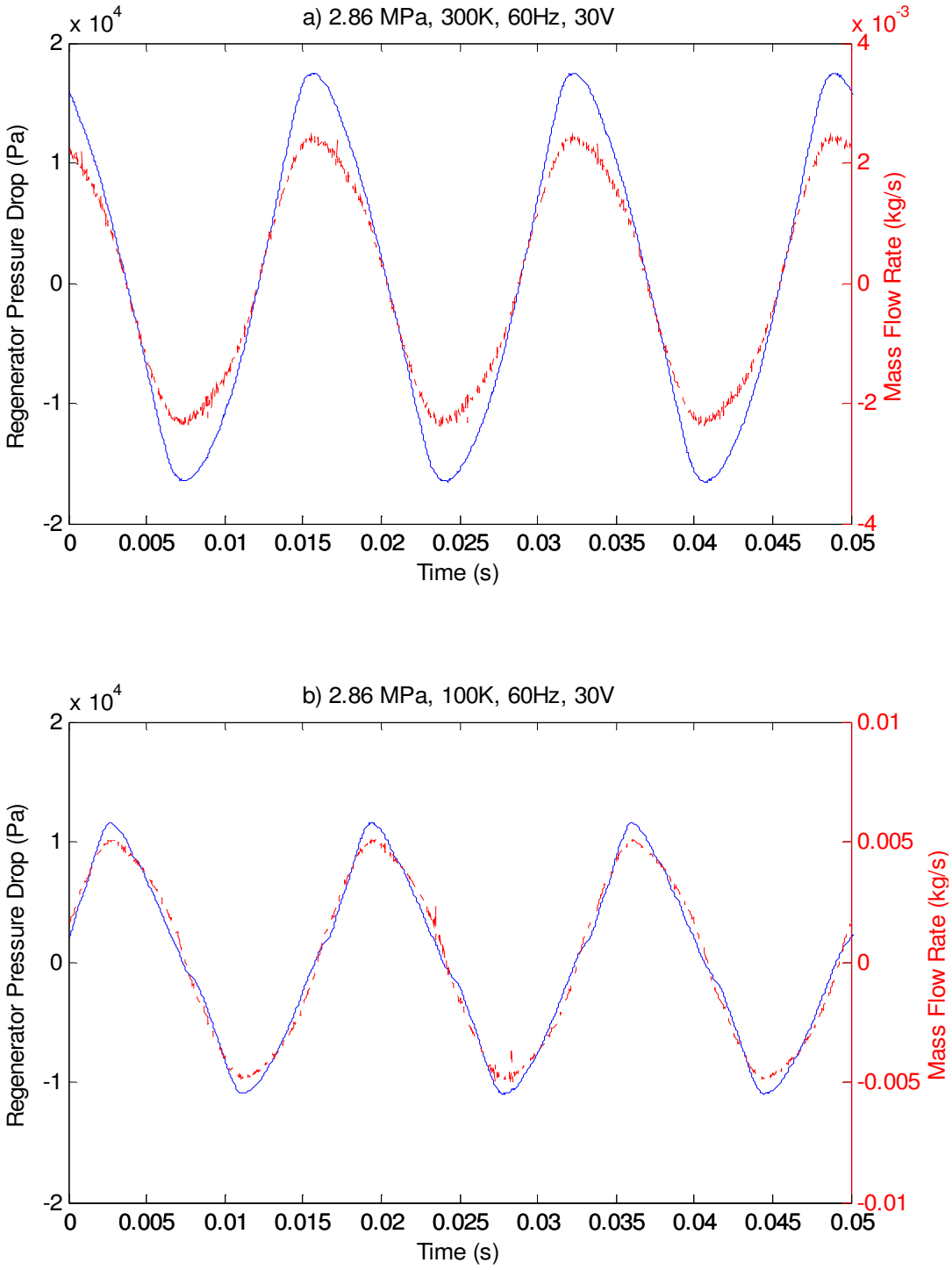

Figure 74. Regenerator Pressure Drop compared to downstream mass flow rate oscillations for the #325SS mesh regenerator at 2.86 MPa for a) 300K and b) 100K at 60Hz and 30V PWG voltage input

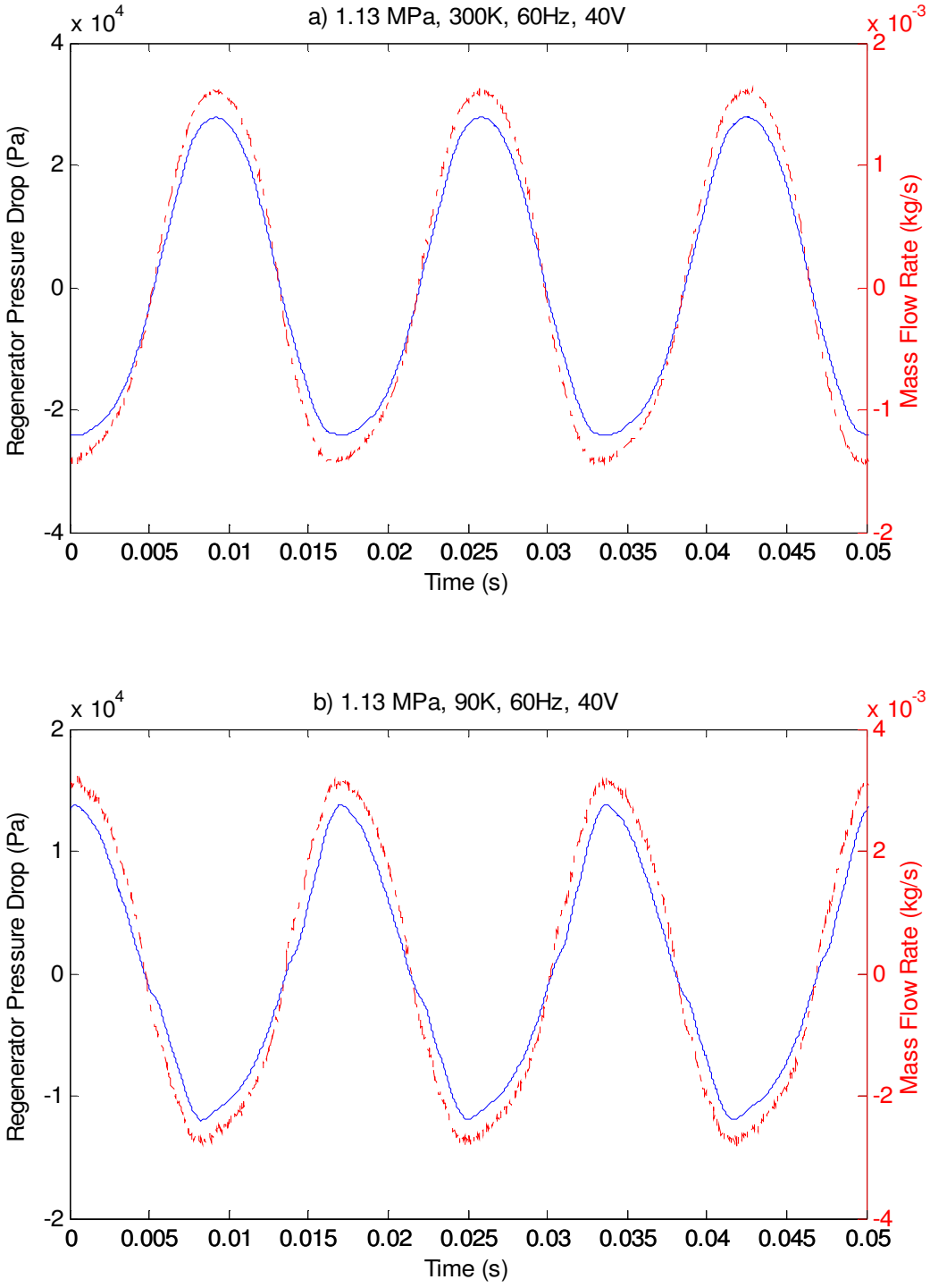

Figure 75. Regenerator Pressure Drop compared to downstream mass flow rate oscillations for the #325SS mesh regenerator at 1.13 MPa for a) 300K and b) 90K at 60Hz and 40V PWG voltage input

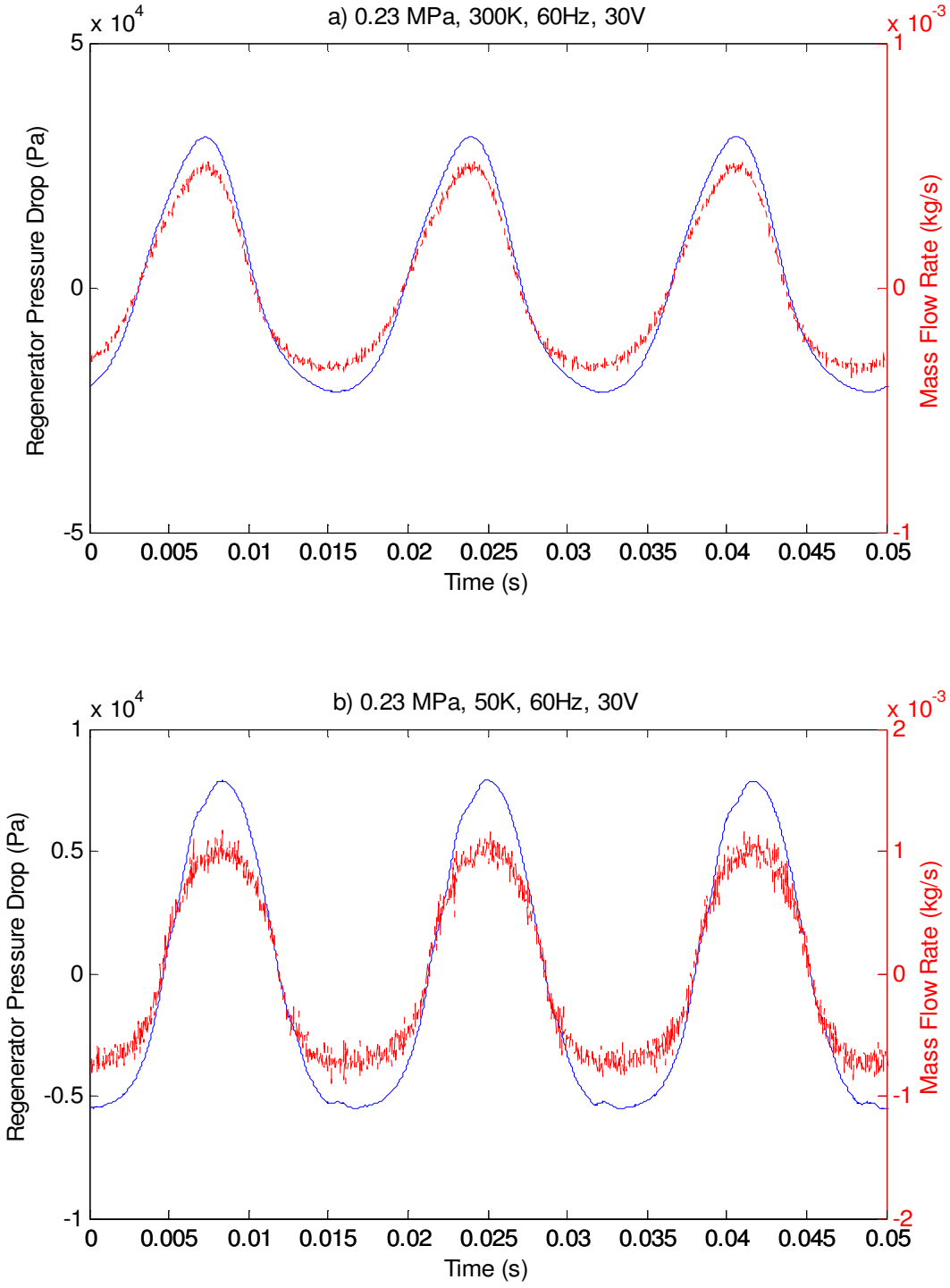

Figure 76. Regenerator Pressure Drop compared to downstream mass flow rate oscillations for the #325SS mesh regenerator at 0.23 MPa for a) 300K and b) 50K at 60Hz and 30V PWG voltage input

Figures 77, 78, and 79 show the maximum or peak instantaneous pressure drop across the #325SS mesh regenerator versus the peak flow velocity, where the peak flow velocity is calculated according to Eq. (51). The results indicate that the peak physical flow velocities for the #325SS mesh regenerator are generally higher than the $Er_{0.5}Pr_{0.5}$ regenerator at the same charge pressures and temperatures and comparable to the #400SS mesh regenerator. This is to be expected given the similar porosities and pore structures of the two wire mesh regenerator filler materials. The results indicate that the pressure drop is independent of frequency when plotted vs. flow velocity so all experimental frequencies are shown together. The uncertainty bars are calculated according to section 3.3 as 0.3% of the full scale value of 690 kPa, which gives a total uncertainty of 2,700 Pa. The results indicate that the maximum pressure drop clearly varies based on operating pressure and temperature. The peak pressure drop is larger for higher charge pressures and operating temperatures, although the peak pressure drop does not vary with the operating temperature of the #325SS mesh regenerator as severely as for the $Er_{0.5}Pr_{0.5}$ regenerator. Figure 59 compares the peak pressure drop across regenerator 3 at 2.86, 1.13, and 0.23 MPa. While all of the results do obey the same general trend, it is clear that these dimensioned results cannot be expressed using a single correlation, which establishes the need for non-dimensionalization.

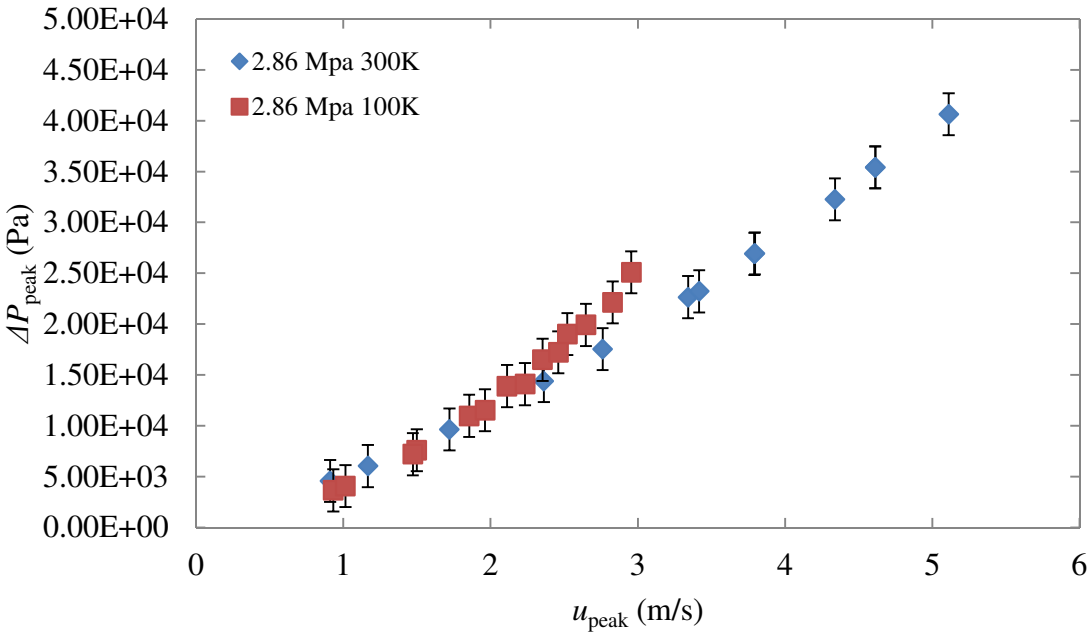

Figure 77. Maximum instantaneous pressure drop across the #325SS mesh regenerator as function of peak flow velocity at 2.86 MPa

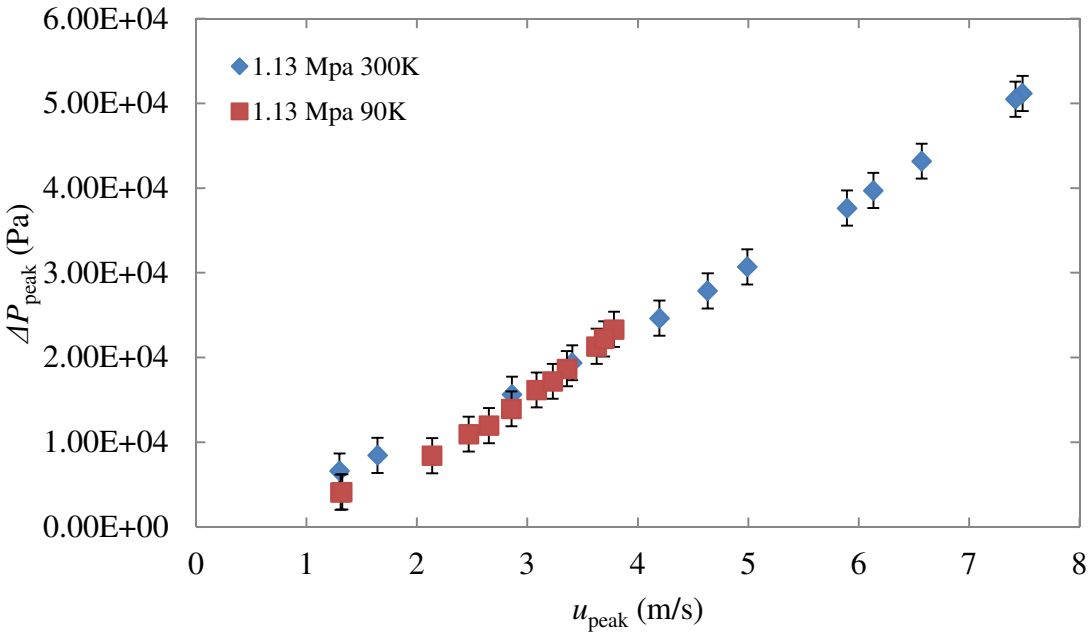

Figure 78. Maximum instantaneous pressure drop across the #325SS mesh regenerator as a function of peak flow velocity at 1.13 MPa

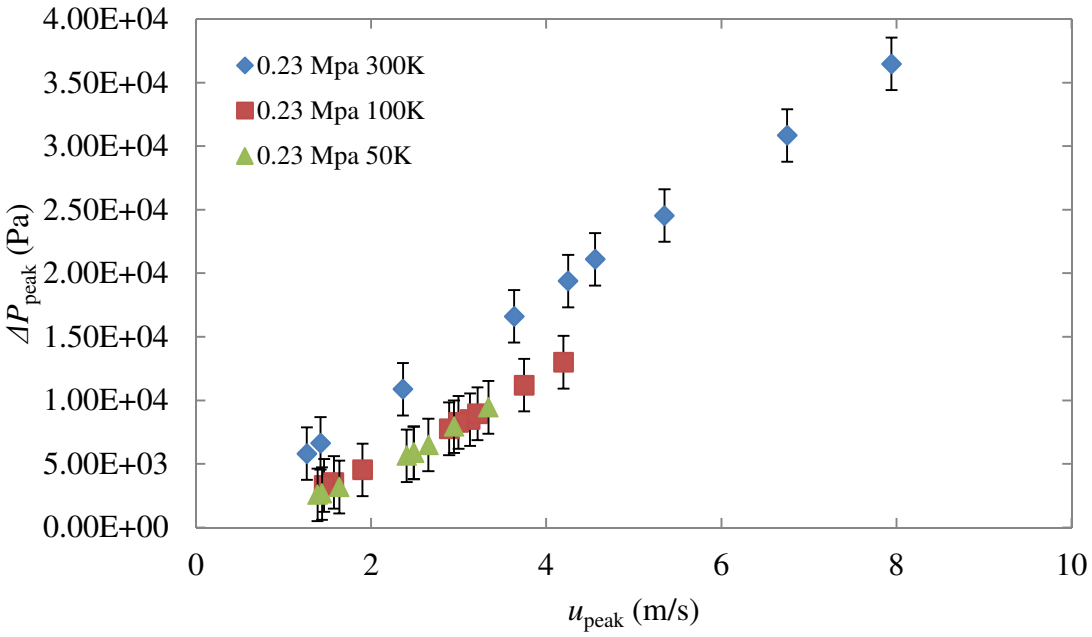

Figure 79. Maximum instantaneous pressure drop across the #325SS mesh regenerator as function of peak flow velocity at 0.23 MPa

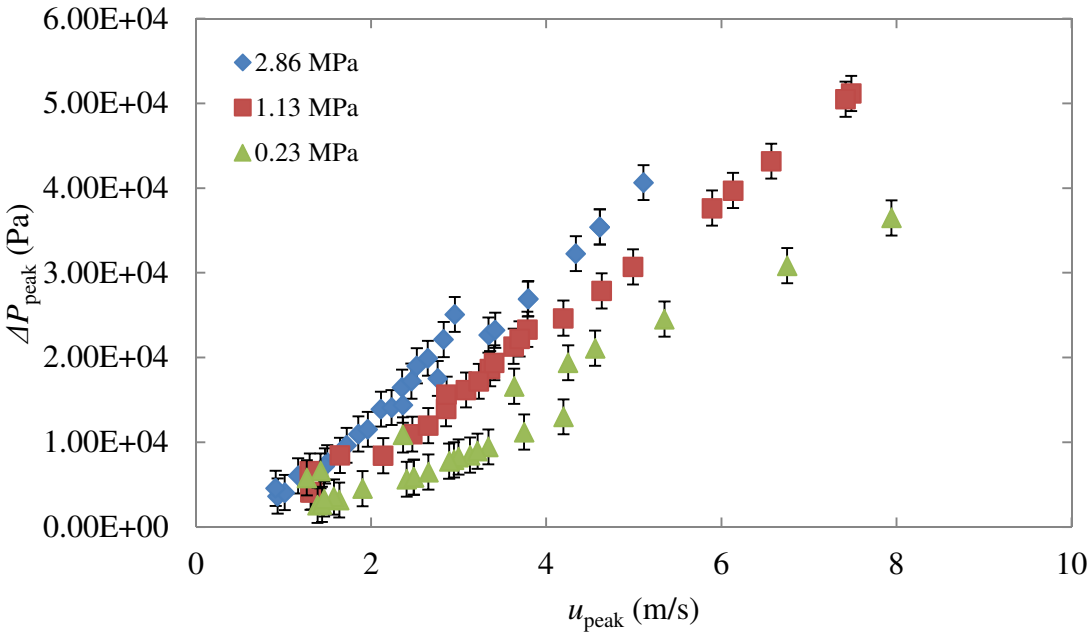

Figure 80. Maximum instantaneous pressure drop across the #325SS mesh regenerator as a function of peak flow velocity at 2.86, 1.13, and 0.23 MPa

5.3.2 Sage Simulation Results

In the same manner as before, the experimentally measured maximum pressure drop and peak physical velocity for the #325SS regenerator is used to evaluate the total friction pressure gradient in Sage, given by Eq.(19), and the Sage friction factor, given by Eq.(23). According to Eq.(19), the total frictional pressure gradient at a given moment is simply the pressure drop across the regenerator at that moment divided by the regenerator length, which is given in Table 1. Figure 81 shows the results for friction factor calculated using the experimental data as a function of the hydraulic-diameter Reynolds number given by Eq.(24). The results are plotted for 2.86, 1.13, and 0.23 MPa and compared to the correlation developed by Gedeon for packed mesh screens given by Eq. (31). The figure indicates that the experimental results agree very well with Gedeon's correlation for all charge pressures and temperatures, which again supports the belief that correlations developed at room temperature are indeed applicable at cryogenic temperatures for packed screen regenerators. Using the least-squares method, a new correlation was developed to match the experimental data for the #325SS regenerator and is given by Eq. (54) and is also shown in Figure 81.

$$f_{\text{Perrella}} = \frac{142}{\text{Re}_{d_h}} + 1.19 \tag{54}$$

As with the #400SS regenerator, the general trend of the data is linearly proportional to the inverse of the Reynolds number at low flow rates when viscous forces dominate, similar to the Darcy friction factor for internal pipe flow. As inertial forces become more

important at Reynolds numbers above approximately 100, the Sage friction factor begins to plateau.

Suitable values for the Sage friction factor can also be determined computationally using the Sage software itself. Given the definitive results in sections 5.1.2 and 5.2.2, it was deemed unnecessary to perform Sage analysis on every experimental data point in order to determine the appropriate values for friction factor for the #325SS wire mesh regenerator. Instead, the correlation provided by Eq.(54) was applied to selected points to verify its validity. Following the approach outlined in section 4.2, a working model of the entire test section including the #325SS mesh regenerator was constructed as shown in Figure 18. The generic matrix option described by Eq. (32) was selected to represent the regenerator, but instead of iteratively varying c_3 as before, the friction factor was defined according to Eq. (54) and only the PWG amplitude was varied using Sage's built-in optimization function in order to match the upstream regenerator pressure amplitude from the simulation with the experimental result. Select points were chosen for comparison, and the results are summarized in Table 11. The table shows that the simulation results agree extremely well with the experimental measurements, with the downstream pressure and mass flow rate amplitudes showing agreement to within only a few percentage points.

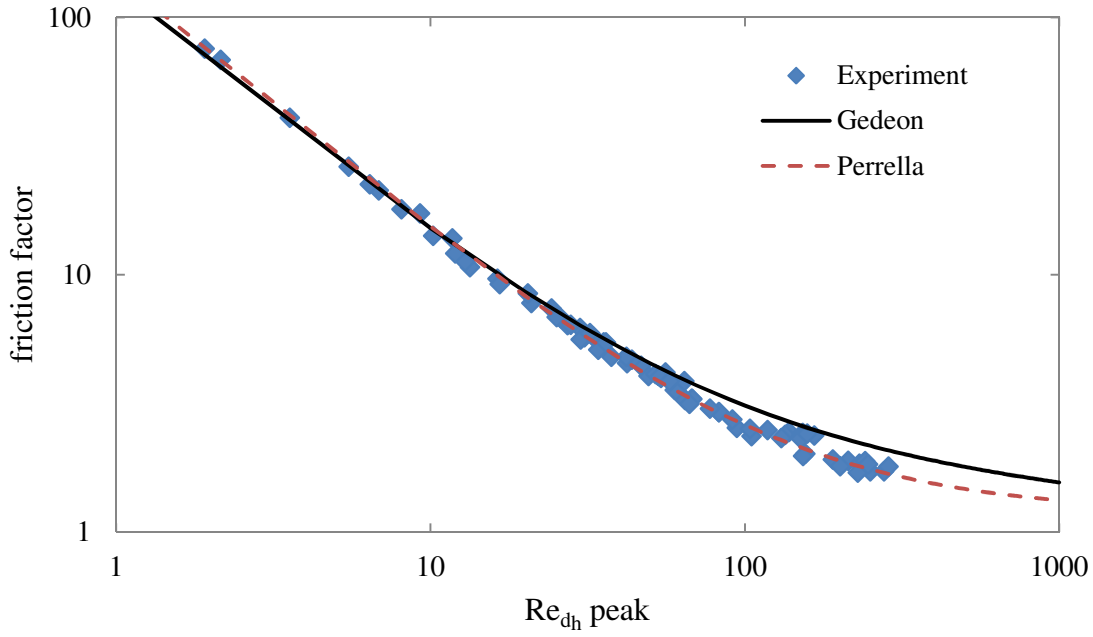

Figure 81. Experimental Sage friction factor for the #400SS mesh regenerator compared to the correlation by Gedeon for packed mesh screens, Eq. (31), and Perrella Eq. (54)

Table 11. Summary of Sage simulation results for the 325SS mesh regenerator using the generic matrix option with friction factor from Eq. (54) compared to experimental measurements

Pressure [MPa]	Temperature [K]	$\dot{m}_{exp}$ [kg/s]	$\dot{m}_{sim}$ [kg/s]	Percent error	$P_{max\ exp}$ [Pa]	$P_{max_{sim}}$ [Pa]	Percent error
2.86	300	2.36E-03	2.34E-03	2.07E-03	8.79E+04	8.81E+04	2.07E-03
2.86	100	4.84E-03	4.49E-03	7.17E-02	6.15E+04	6.15E+04	1.98E-03
1.13	300	1.58E-03	1.61E-03	1.97E-02	5.89E+04	5.96E+04	1.07E-02
1.13	90	2.98E-03	2.94E-03	1.26E-02	3.49E+04	3.55E+04	1.77E-02
0.23	300	4.07E-04	4.06E-04	3.40E-03	1.51E+04	1.47E+04	2.75E-02
0.23	100	7.15E-04	7.38E-04	3.09E-02	9.03E+03	9.24E+03	2.26E-02
0.23	62	9.31E-04	9.82E-04	5.49E-02	7.10E+03	7.52E+03	5.90E-02

5.3.3 CFD Simulation Results

Figures 82, 83, and 84 show the momentum source term in Fluent, S_i, vs. the peak flow velocity and the non-dimensionalized momentum source term, Γ, vs. the hydraulic dimeter-based Reynolds number for 2.86, 1.13, and 0.23 MPa, respectively. The momentum source term in Fluent is defined according to Eq.(37), and the non-dimensionalized momentum source term is defined according to Eq. (44). The figures show how the non-dimensionalization of the momentum source term condenses the data into a single trend line which can be fitted with a quadratic correlation with very good agreement. Figure 85 presents the dimensional and non-dimensional momentum source term for 2.86, 1.13, and 0.23 MPa for all frequencies and operating temperatures with a quadratic model for the combined data. The error bars in Figure 85 represent the quadratic fit of the data ±10%. This shows, once again, that the hydrodynamic resistance of the porous filler material is independent of the operating temperature.

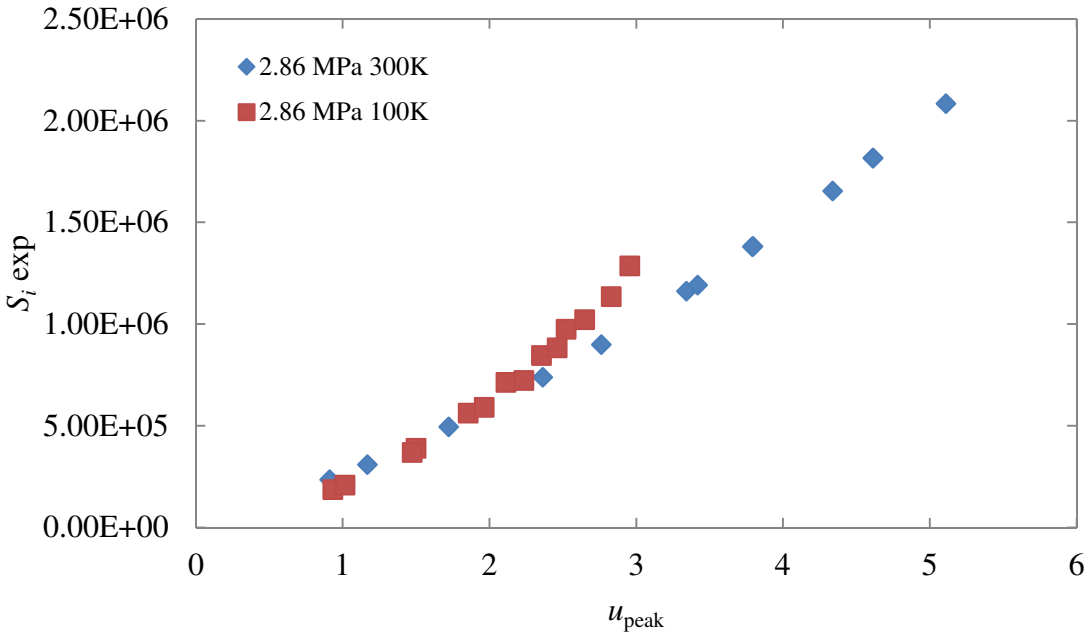

a) Fluent momentum source term at 2.86 MPa

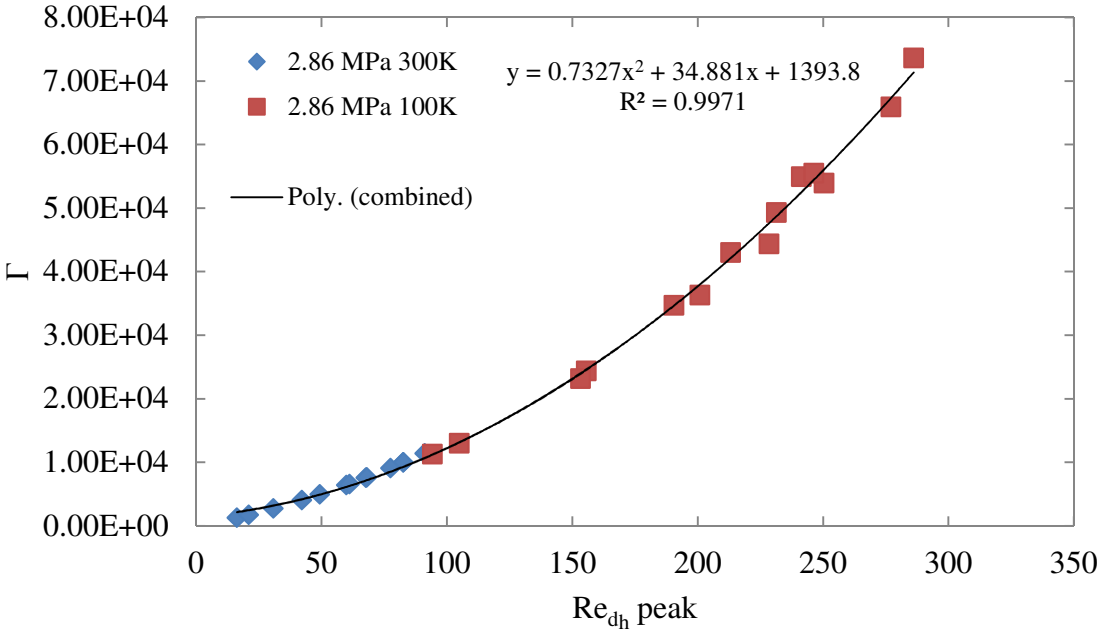

b) Dimensionless momentum source term at 2.86 MPa

Figure 82. #325SS mesh regenerator results for a) momentum source term in Fluent, S_i, and b) non-dimensionalized momentum source term, Γ, calculated from experimental total frictional pressure gradient for 2.86 MPa at 300K and 100K

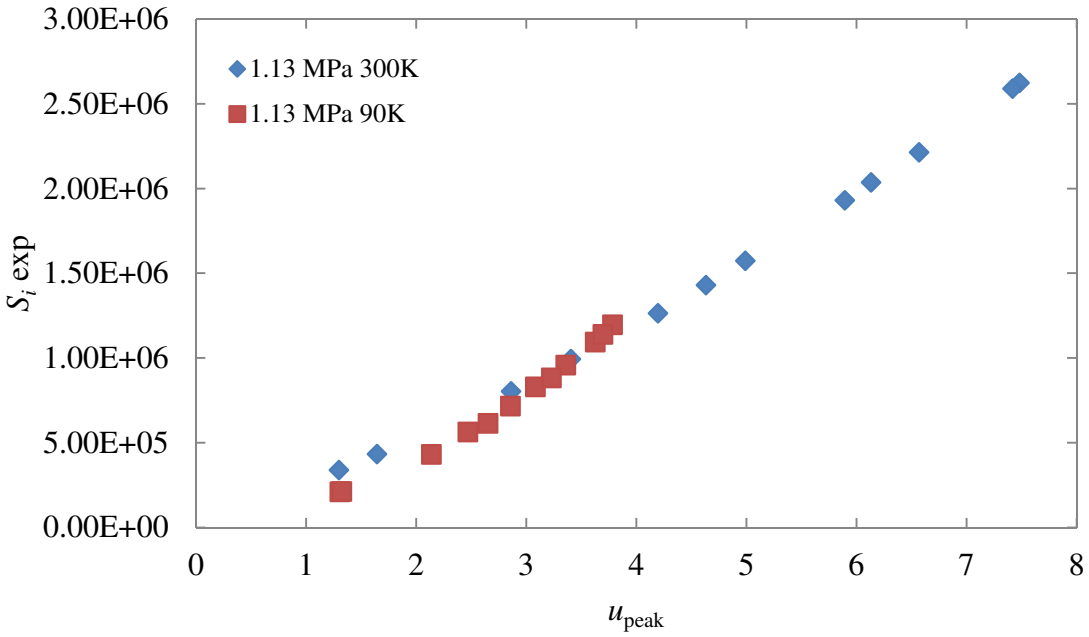

a) Fluent momentum source term at 1.13 MPa

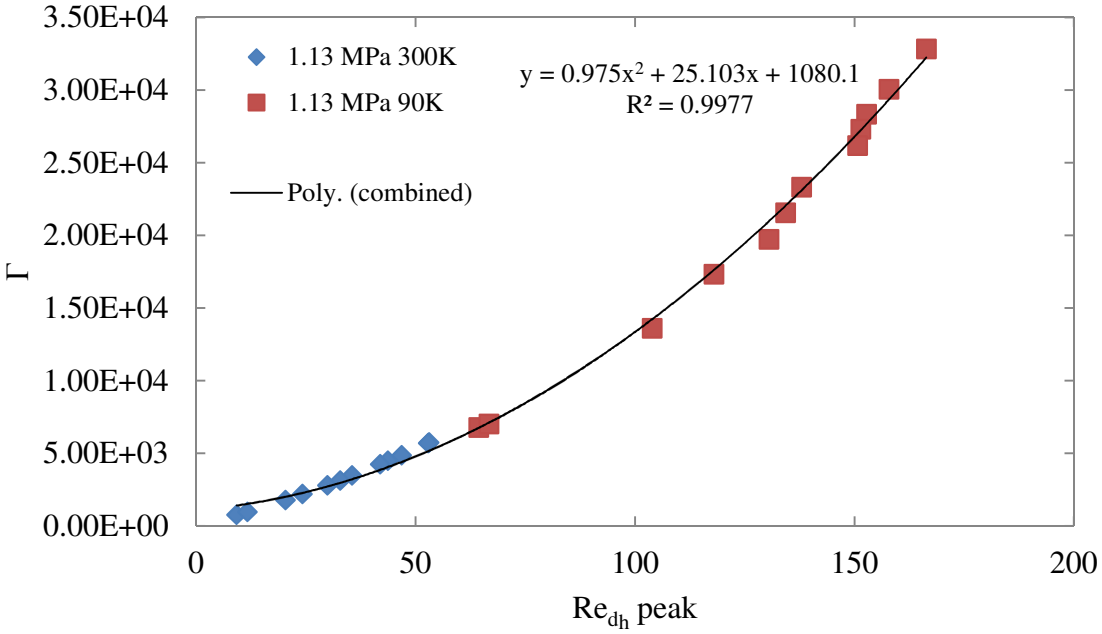

b) Dimensionless momentum source term at 1.13 MPa

Figure 83. #325SS mesh regenerator results for a) momentum source term in Fluent, S_i, and b) non-dimensionalized momentum source term, Γ, calculated from experimental total frictional pressure gradient for 1.13 MPa at 300K and 90K

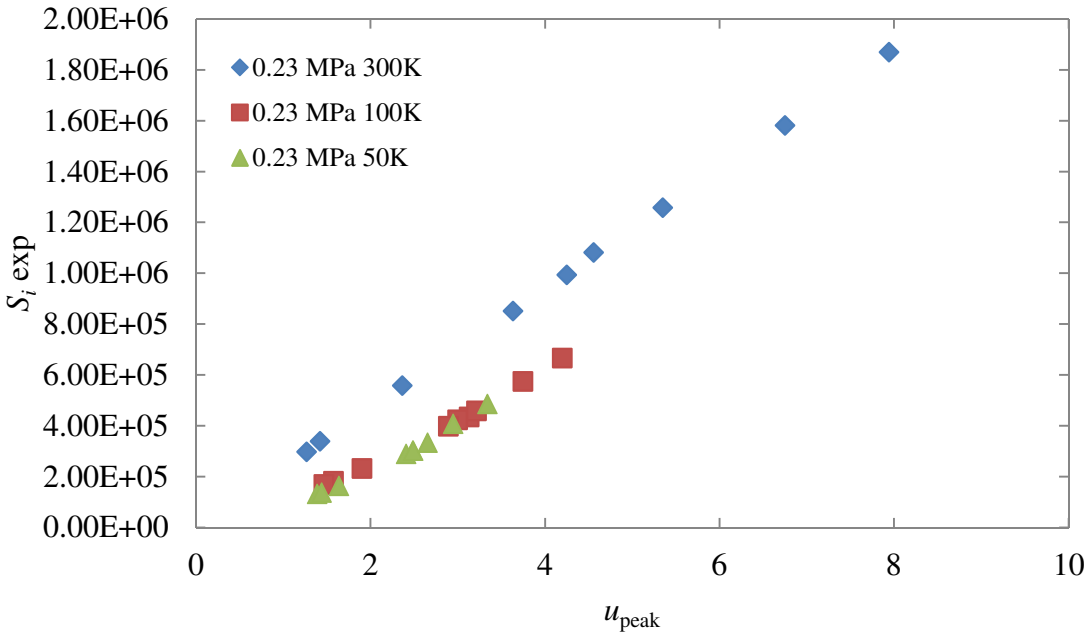

a) Fluent momentum source term at 0.23 MPa

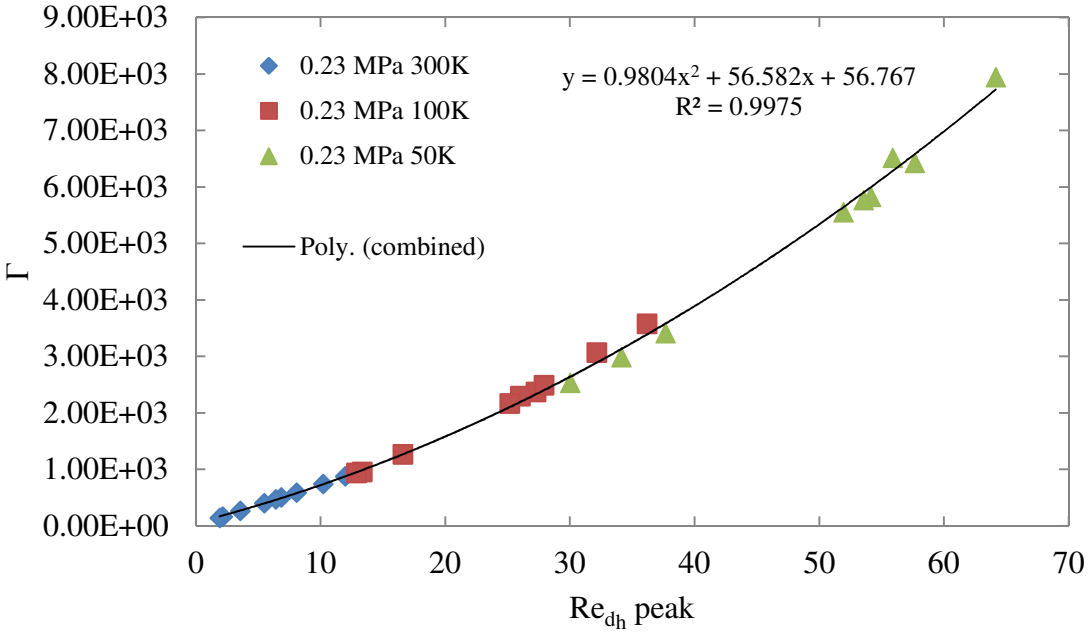

b) Dimensionless momentum source term at 0.23 MPa

Figure 84. #325SS mesh regenerator results for a) momentum source term in Fluent, S_i, and b) non-dimensionalized momentum source term, Γ, calculated from experimental total frictional pressure gradient for 0.23 MPa at 300K and 50K

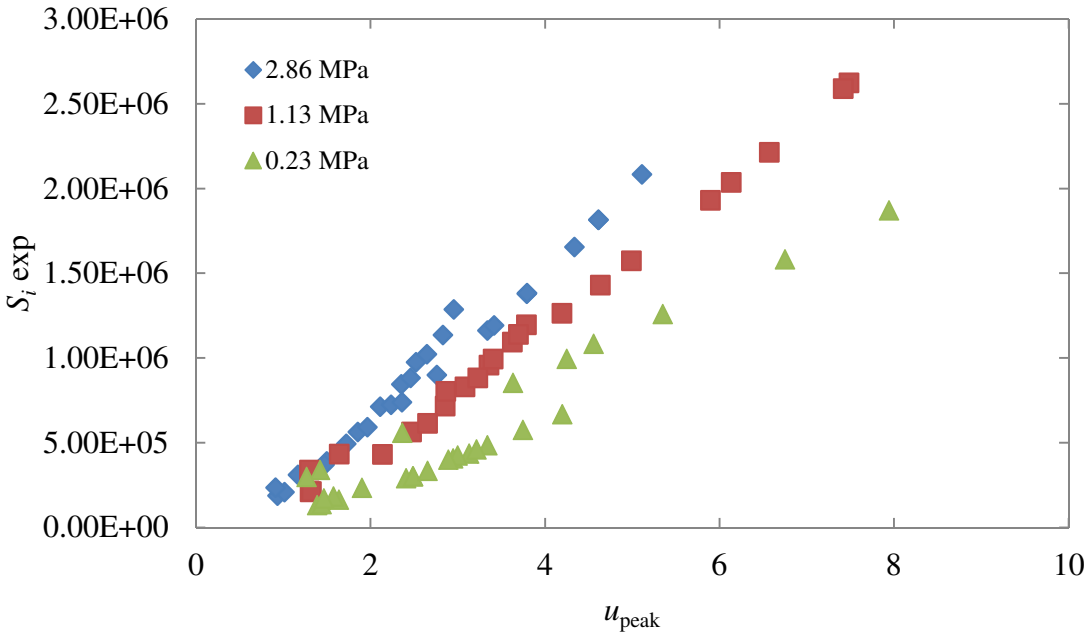

a) Fluent momentum source term at 2.86, 1.13, and 0.26 MPa

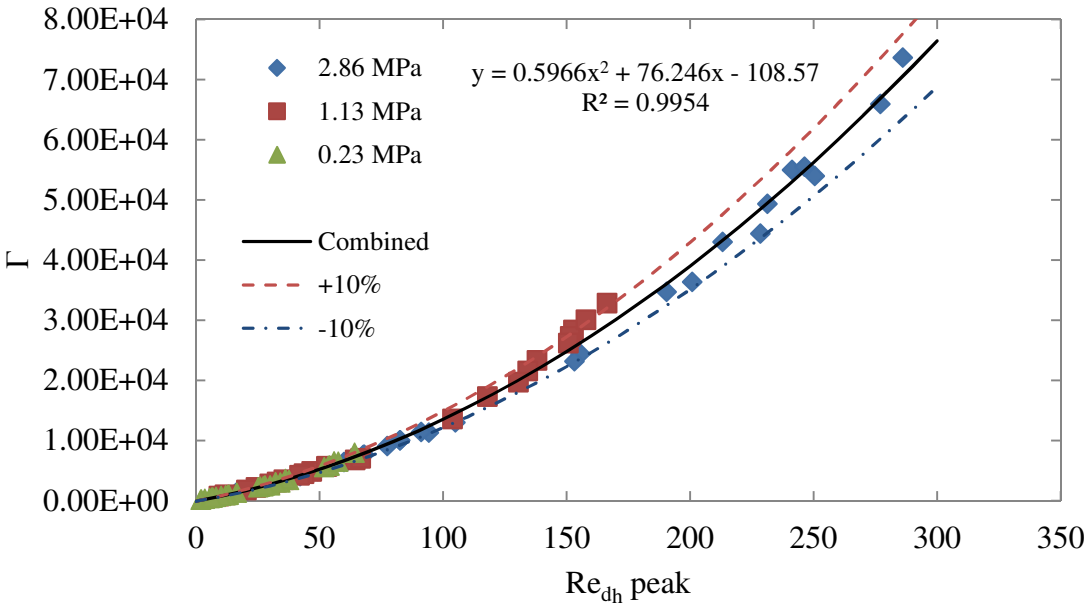

b) Dimensionless momentum source term at 2.86, 1.13, and 0.26 MPa

Figure 85. #325SS mesh regenerator results for a) momentum source term in Fluent, S_i, and b) non-dimensionalized momentum source term, Γ, calculated from experimental total frictional pressure gradient for 2.86, 1.13, and 0.23 MPa

Table 12 presents the viscous and inertial resistances in Fluent extracted from the quadratic model of the non-dimensionalized momentum source term according to Eq. (49) and Eq. (50). The Darcy permeability and Forchheimer coefficient are determined according to Eq. (40) and Eq. (41), respectively. The results are compared with those of Cha for #325SS non-sintered mesh [1]. As the results indicate, the hydrodynamic resistance parameters differ slightly based on mean operating pressure, but are all of similar orders of magnitude. The results for the #325SS mesh appear to show greater dependence on mean operating pressure than the results for the #400Ss mesh. All results for the #325SS regenerator are based on experimental measurements since Sage was not used to determine the simulated friction factor, but only to verify the experimental friction factor results. The results from Cha for un-sintered #325SS mesh are of similar magnitude and appear to agree more closely than for the #400SS regenerator. As with regenerator 2, this study provides a single value for inertial resistance and Forchheimer coefficient for all flow velocities, the same as Cha's results.

Table 12. Summary of Fluent viscous and inertial resistance, Darcy Permeability and Forchheimer coefficient for the #325SS mesh regenerator

Pressure [MPa]	A	B	β [1/m^2]	C_2 [1/m]	K [m^2]	c_f
2.86	0.73	34.88	8.25E+09	3.95E+04	1.21E-10	2.17E-01
1.13	0.98	25.10	5.93E+09	5.25E+04	1.69E-10	3.41E-01
0.23	0.98	56.58	1.34E+10	5.28E+04	7.48E-11	2.28E-01
Combined	0.60	76.25	1.80E+10	3.21E+04	5.55E-11	1.20E-01
Cha [1]	-	-	1.56E+10	6.70E+04	6.42E-11	2.69E-01

As with regenerator 2, slightly different results for the Fluent hydrodynamic resistances, Darcy Permeability and Forchheimer coefficients can be obtained by forcing the y-intercept of the quadratic fit to zero. This approach might provide more appropriate results since, physically, the hydrodynamic resistance of the porous medium should be zero at zero flow velocity. The results are summarized in Table 13. The zero-intercept results agree fairly well with the non-zero-intercept results from Table 12, but there are slight differences. One might expect the intercept of the non-dimensionalized momentum source term, Γ, to equal zero naturally, without having to be forced, but this is not the case. This could be due to the bias error of the dynamic pressure transducers themselves or due to the error associated with the mean operating pressure measurement.

Table 13. Summary of Fluent viscous and inertial resistance, Darcy Permeability and Forchheimer coefficient for the #325SS mesh regenerator with zero intercept

Pressure [MPa]	A	B	β [1/m^2]	C_2 [1/m]	K [m^2]	c_f
2.86	0.67	56.89	1.34E+10	3.59E+04	7.44E-11	1.55E-01
1.13	0.82	55.17	1.30E+10	4.42E+04	7.67E-11	1.94E-01
0.26	0.93	60.51	1.43E+10	5.00E+04	6.99E-11	2.09E-01
Combined	0.60	74.21	1.75E+10	3.25E+04	5.70E-11	1.23E-01
Cha [1]	-	-	1.56E+10	6.70E+04	6.42E-11	2.69E-01

5.3.4 Combined Wire Mesh Regenerator Results

For the purpose of modelling and optimizing regenerator and cryocooler designs, it is convenient to develop friction factor and other hydrodynamic resistance parameter correlations that are suitable across a wide range of wire mesh sizes. This is possible since the difference in pore structure between packed beds of differently sized mesh screens is accounted for by the hydraulic diameter, defined in Sage by Eq. (20). The hydraulic diameter depends on the cross-sectional flow area, A_f, and the wetted perimeter, S_x. The wetted perimeter is calculated for any mesh size based on the surface area of the wire and the volume of the mesh, which can be calculated geometrically based on the wire diameter, d_w, and porosity, ε, according to Eq. (30). Since all results are correlated based on the hydraulic diameter-based Reynolds number, Eq. (24), the differences in pore structure are already accounted for in the data.

Figure 86 shows the experimental Sage friction factor defined by Eq. (19) as a function of the hydraulic diameter-based Reynolds number for #400SS mesh and #325SS mesh for all charge pressures, frequencies, and temperatures. The results are compared to the correlation of Gedeon given by Eq. (31). The least-squares method was also used to develop a new correlation for the combined data set across the entire charge pressure and temperature range under consideration, and is given by Eq. (55).

$$f_{\text{Perrella}} = \frac{160}{\text{Re}_{d_h}} + 1.57 \tag{55}$$

The figure shows the experimentally determined friction factors for both the #400SS and the #325SS mesh agree very well with one another and with the correlation provided by Gedeon. The friction factor correlation provided by Eq. (55) also fits the data very well and is similar to that developed by Gedeon. In fact, the friction factor correlation determined from the combined data matches the correlation by Gedeon more closely than that of individual data sets. Since Eq. (55) is based on a wide range of mean operating pressures and temperatures from 50-300K, the agreement provides strong evidence that any such correlation for friction factor will indeed be independent of operating temperature.

Figure 87 shows the non-dimensionalized momentum source term for the #400SS mesh regenerator and the #325SS mesh regenerator as a function of the hydraulic diameter-based Reynolds number. Although the data sets do not agree perfectly, they still follow the same basic trend. It is not possible, however, to extract universal values for the viscous and inertial resistances of a generic mesh since the calculation of Γ itself depends on the hydraulic diameter, which varies with porosity and wire diameter.

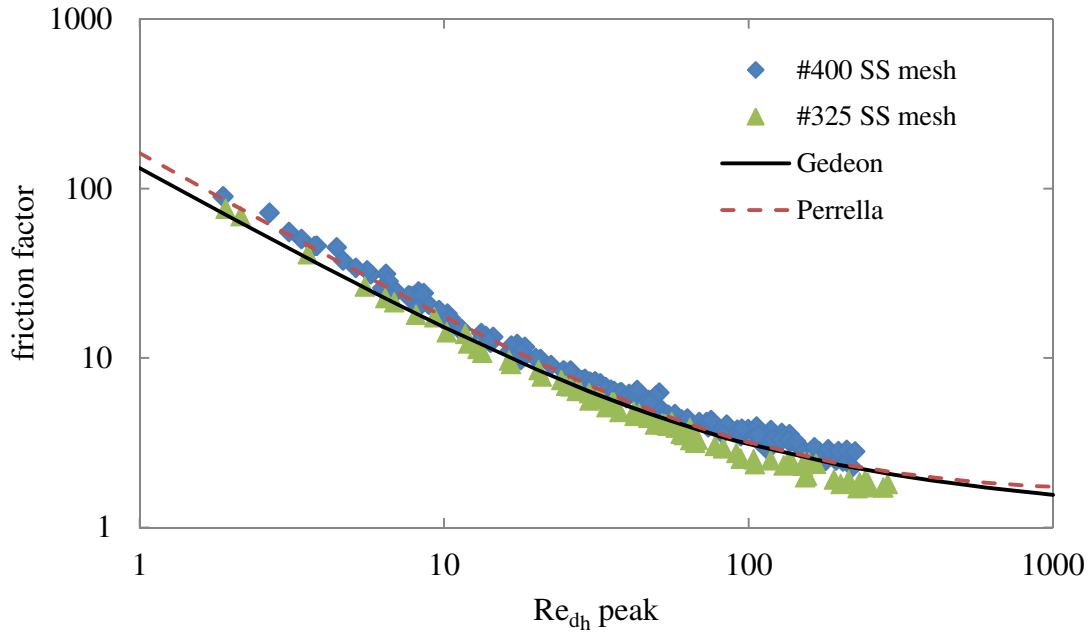

Figure 86. Experimental Sage friction factor for #400SS mesh and #325SS mesh vs. hydraulic diameter-based Reynolds number for all charge pressures and temperatures compared to the correlations of Gedeon, Eq. (31), and Perrella, Eq. (55)

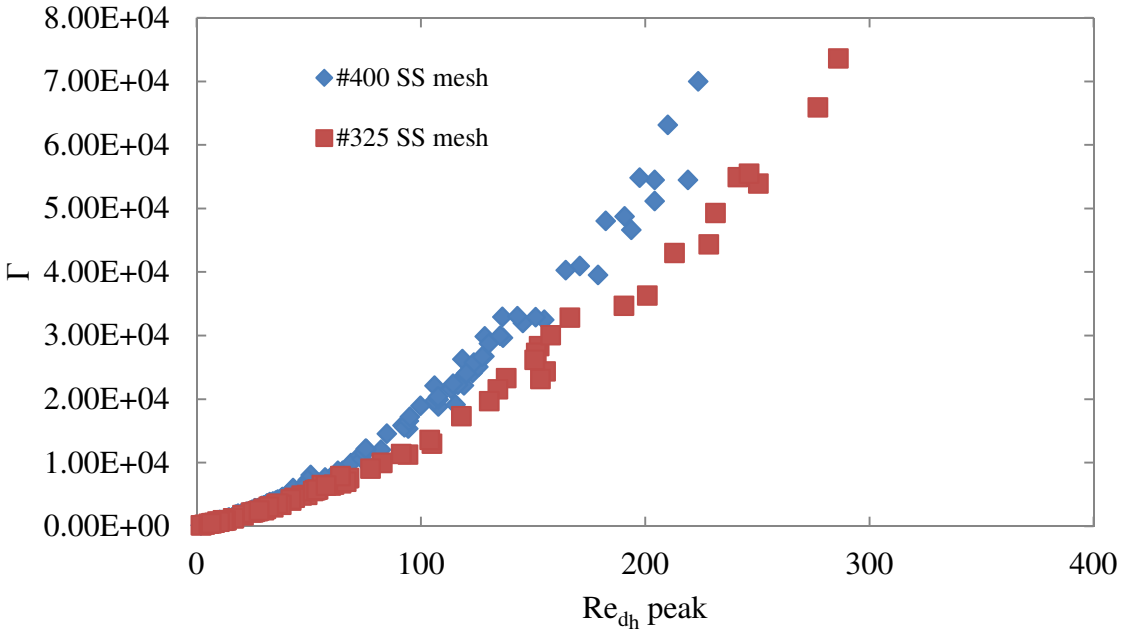

Figure 87. Experimental non-dimensionalized momentum source term in Fluent for #400SS mesh and #325SS mesh with quadratic fit

5.4 A Case Study: The Design of a Two-Stage 20W at 20K Cryocooler

The design of a two-stage pulse tube cryocoler is described in this section as a case study that demonstrates the critical role that the regenerator plays in PTCs, and elucidates the sensitivity of the overall performance of a PTC to the hydrodynamic characteristics of the regenerators. This work was motivated in part by a NASA Early Stage Innovations (ESI) project to develop a robust, high-capacity cryocooler for space missions. The motivation of the ESI project was to address NASA's desire to achieve zero-boil off for on-board cryo-propellant, namely liquid hydrogen and liquid oxygen, for deep space missions and solar system exploration. Typically, an exploratory spacecraft or satellite must store a significant amount of extra fuel to account for the cryogen that will be vaporized and exhausted by heat leakage to the craft. The fuel accounts for such a significant portion of the spacecraft's weight that replacing a portion of the extra fuel with a built-in cryocooler is an attractive option. To address this need, NASA solicited the design of a 5W at 20K cryocooler, which would be a significant improvement over the currently available 1W at 20K designs. The Georgia Tech Cryolab, in collaboration with the University of Wisconsin Madison Cryo Group (MCG), proposed a 2-stage, pulse tube cryocooler with a theoretical predicted cooling power of 5W at 20K. This work was then expanded to the design of a 20W at 20K cryocooler based on the same 2-stage pulse tube configuration. Separate effects testing of the advanced $Er_{0.5}Pr_{0.5}$ regenerator was completed as a compliment to the theoretical design.

5.4.1 5W at 20K Design

The design process began with the theoretical design of a 5W at 20K cryocooler, which was performed in the GT Cryolab by Mihir Pathak and Gilbran Alvarez. In order to achieve the extremely low target temperature of 20K, a two-stage design was proposed which utilized a single compressor and two separate inertance networks. A schematic of the proposed design is shown in Figure 88. The CHX of the second stage absorbs heat at 20K, and rejects heat at 80K to the CHX of the first stage of the PTC. The WHX of the first stage rejects heat to the ambient at 300K. A thermal bus bar connects the WHX of the second stage with the CHX of the first stage.

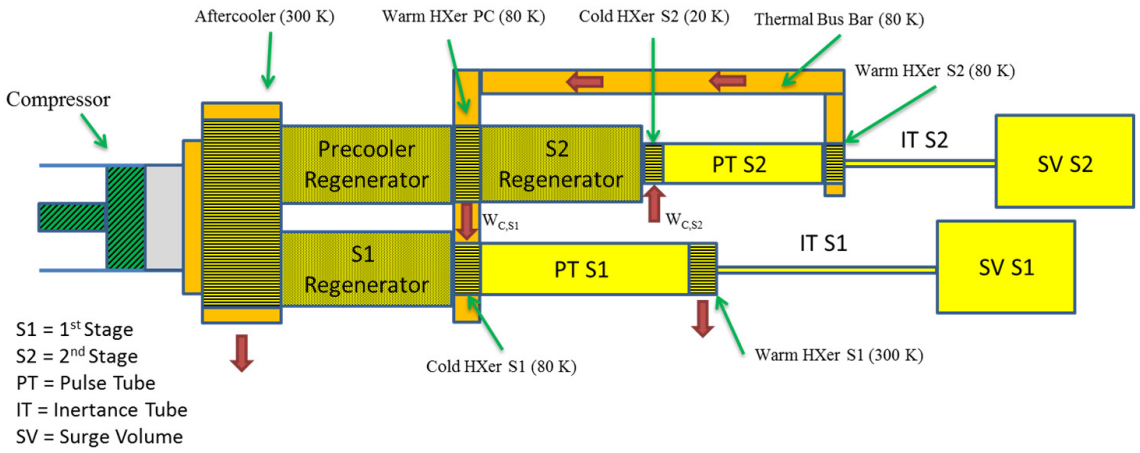

Figure 88. Schematic of proposed two-stage pulse tube cryocooler for 5W at 20K operation

Being the most crucial part of the cooler's design, the second stage regenerator, S2, was designed first using the computational software, REGEN 3.3 available from NIST. REGEN allows the user to predict the performance of a regenerator with a given temperature distribution, porous filler material, and operating conditions. Numerous iterations were performed using a variety of filler materials and operating frequencies,

and the results are summarized in Table 14. The tested materials included lead particles, stainless steel mesh, and $Er_{0.5}Pr_{0.5}$ particles at frequencies from 30-60Hz. As discussed in sections 2.2 and 5.1, $Er_{0.5}Pr_{0.5}$ is an attractive option for low temperature cryocoolers because it maintains its thermal storage capacity even at extremely low temperature. Based on the results, $Er_{0.5}Pr_{0.5}$ particles and an operating frequency of 30Hz were selected for further optimization. Based on the results summarized in

Table 15, a spherical particle diameter of 55μm was selected for simulation and separate-effects testing. The simulations in REGEN 3.3 assumed an optimum pressure-mass flow phase shift of -30^0 at the cold end of the regenerator. In the full system model, however, the actual phase shift differed slightly.

Table 14. Summary of simulation results for second-stage regenerator, S2, using REGEN 3.3

Material	**Frequency (Hz)**	**Max COP**
Er50Pr50	60	4.95%
Er50Pr50	50	5.56%
Er50Pr50	40	6.25%
Er50Pr50	30	6.93%
Material Distribution	**Frequency (Hz)**	**Max COP**
85% ErPr - 15% SS	30	1.90%
50% ErPr - 50% Pb	30	6%
66% ErPr - 33% Pb	30	6.40%
85% ErPr - 15% Pb	30	6.85%
Material Distribution	**Frequency (Hz)**	**Max COP**
Pb	60	3.70%
Pb	45	4.40%
Pb	30	4.90%

Table 15. Optimization of $Er_{0.5}Pr_{0.5}$particle diameter for second stage regenerator

Er50Pr50 Sphere Diameter	Max COP
30 microns	5.72%
40 microns	6.79%
50 microns	7.15%
60 microns	7.12%
70 microns	6.93%
80 microns	6.54%
90 microns	6.00%
100 microns	5.37%

The NIST code ISOHX was used to develop a preliminary design for the warm and cold heat exchangers of both stages, and the preliminary pulse tube, inertance tube, and surge volume dimensions were determined using analytical models. With this information, a system-level simulation of the entire two-stage cooler was constructed using Sage cryocooler modeling software [4]. The graphical interface of the completed Sage simulation is shown in Figure 89 and uses a generic model for a duel-opposed piston configuration. Using Sage's built-in optimization function, a series of iterations were performed where the various component dimensions and porous media characteristics were varied to gradually increase the cooling capacity and decrease the input power of the model until an optimum design was achieved. The results of this optimization are shown in Figures 90 and 91.

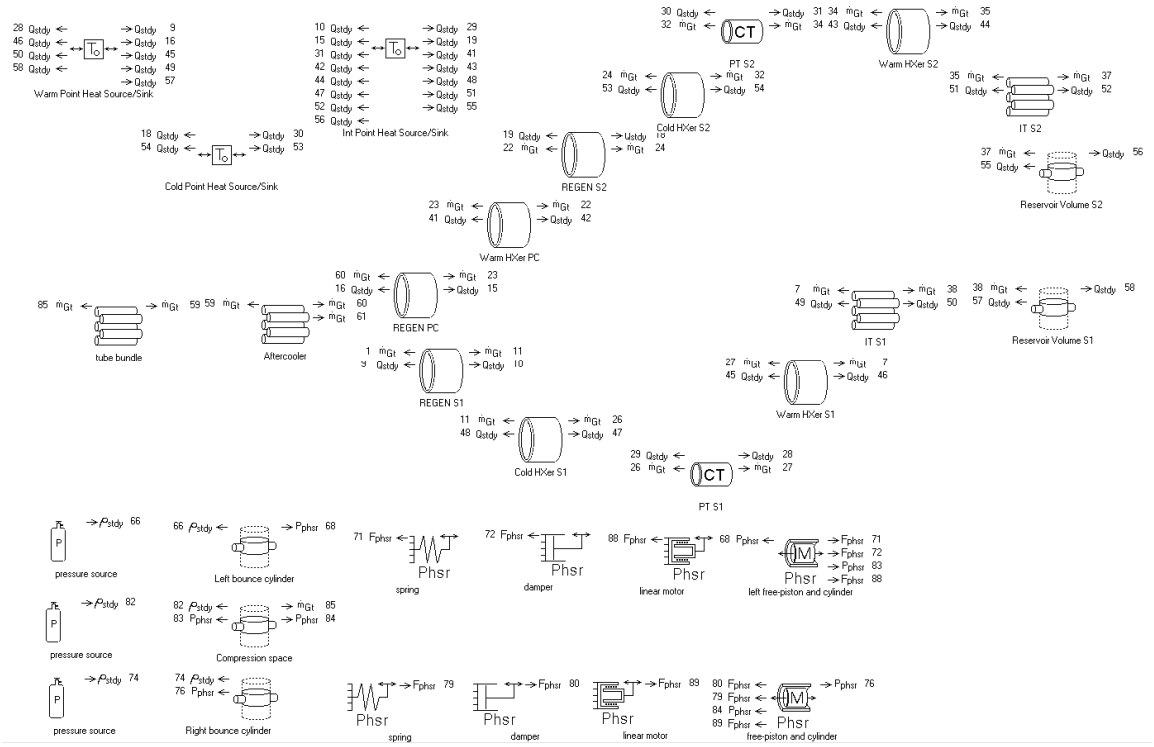

Figure 89. Graphical interface of completed Sage model for 5W at 20K two-stage PTC design

	Model A2		**Model A3**
Charge Pressure	3.0 MPa		2.5 MPa
Maximum Regenerator Diameter	5.5 cm		5.75 cm
Input Power	1473 W	→	1630 W
Cooling Power at 1st Stage (80K)	7.5 W		6 W
Cooling Power at 1st Stage (20K)	5 W		5 W

Figure 90. Optimization of charge pressure and regenerator diameter for 5W at 20K two-stage PTC design

	Model A4		Model A5
Cooling Power at 1st Stage (80K)	7.5 W		7.75 W
Cooling Power at 1st Stage (20K)	3 W		3 W
Input Power	1960 W	→	1840 W
1st Stage Cold End Temperature	80K		75K
Operating Frequency	47.5 Hz		47 Hz
Maximum Stroke Amplitude	10 mm		9.6 mm

Figure 91. Optimization of operating frequency and compressor stroke for 5W at 20K two-stage PTC design

5.4.2 20W at 20K Design

The theoretical design of a 5W at 20K two-stage pulse tube cryocooler served as the basis for designing a larger 20W at 20K cooler to address NASA's grand challenges and zero boil off targets for future missions. The basic approach to the 20W design was rather straight forward. In order to increase the cooling power of the cooler, the power input must also increase. This means that either the piston stroke or piston surface area must increase. In practice, the piston stroke will have a practical limit of 1-2 cm for most commercially available, magnetically driven duel apposed piston designs. Increasing the piston facial area increases the induced mass flow rate leaving the compressor and also increases the input power of the cooler. To simplify the analysis, the duel-opposed piston in Figure 89 was replaced with a single constrained piston as shown in Figure 92. The basic approach of the 20W at 20K design process was to gradually increase the input power and size of the individual cooler components such as the heat exchangers and regenerators while keeping the aspect ratios basically the same. Then, Sage's built in

optimization tool was used to recalculate the inertance tube and surge volume dimensions to provide the correct inertance network for the two stages. Once the desired cooling power was achieved, the input power was reduced by varying the piston stroke and charge pressure. While the Sage optimization software is powerful, it cannot converge on a single solution without realistic limits and initial guesses. This made the optimization process fairly slow, as only small changes could be made at a time in order for the software to converge properly for each iteration. Table 16 presents a summary of the operating conditions for a few select iterations taken from the hundreds that were performed. Based on the analysis, model 20W20K_4_37 was selected for further analysis.

While the theoretical design in Sage accomplished the stated goal of achieving 20W of cooling power at 20K, additional analysis reveals that the proposed dimensions and operating conditions of the theoretical model are not feasible when multi-dimensional flow effects are considered. Recall that the Sage modeling software only considers flow in the primary or axial direction. All governing equations including the conservation of mass, momentum, and energy are solved in one dimension. This automatically assumes that flow properties such as temperature, pressure, and velocity are all uniform through the cross section of each component. Such an approach is not capable of predicting secondary of three dimensional flow effects such as jetting and streaming. In an actual cooler, abrupt changes in flow area and sharp edges can cause swirling, jetting, and mixing effects that degrade the performance of the cooler. To investigate these issues, a 2D, axisymmetric model was made using ANSYS Fluent [5,6] based on the dimensions and boundary conditions of the 20W20K_4_37 Sage model by

GT Cryolab researcher Mallik Ahmed. The temperature contours for the first stage of the 20W at 20K cryocooler at flow times of 11.8 and 73.5 seconds are shown in Figures 93 and 94, respectively. The results indicate that extreme streaming occurs in the first stage pulse tube between the WHX and CHX, which would effectively kill the cooler by imposing an unacceptable heat load on the first stage CHX. This streaming effect is caused by the sudden step change in area between the first stage inertance tube and the WHX and pulse tube. The higher mass flow rates and larger pulse tube diameter necessary to achieve the desired cooling load for the 20W design only exacerbate the streaming behavior. In practice, longer heat exchangers could be used to help disperse the flow and alleviate jetting from the inertance tube, but this would also add additional frictional losses to the system. The Sage optimization was not capable of predicting the streaming effects within the pulse tube, so the simulation simply minimized the WHX and CHX to reduce the frictional losses through the system.

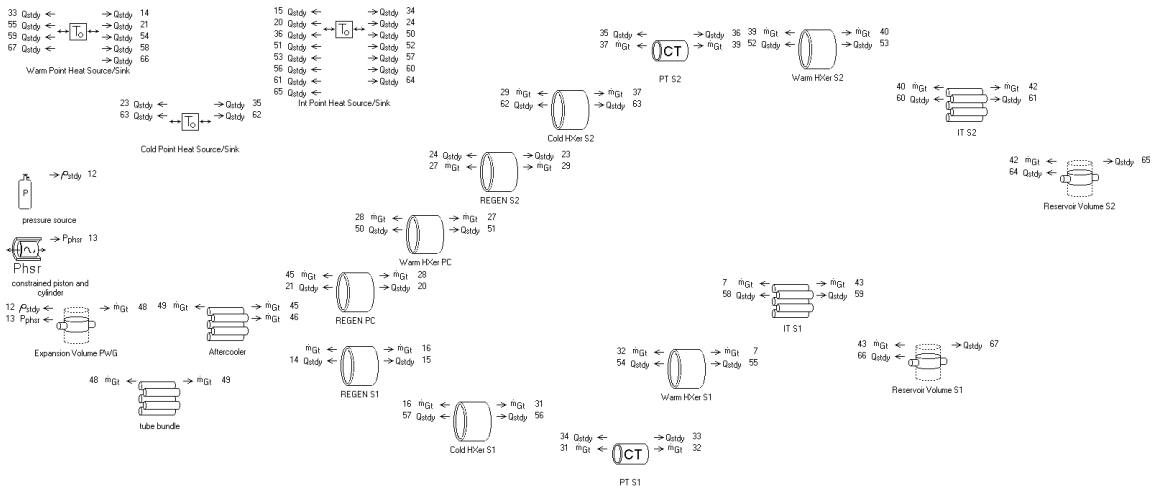

Figure 92. Graphical interface of Sage model for 20W at 20K two-stage PTC design

Table 16. Summary of 20W at 20K two-stage PTC optimization for selected iterations

	20W20K_4_1	**20W20K4_29**	**20W20K4_37**
Cooling Power at 1st Stage	20.15 W	20.00 W	20.30 W
Cooling Power at 2nd Stage	19.99 W	20.00 W	20.01 W
T_c at 1st Stage	20 K	20 K	20 K
T_c at 2nd Stage	80 K	80 K	80 K
Input Power	4455 W	3200 W	2625 W
Charge Pressure	3.87 MPa	3.91 MPa	3.61 MPa
Operating Frequency	30 Hz	30 Hz	30 Hz
Piston Stroke Amplitude	10.0 mm	7.3 mm	6.96 mm

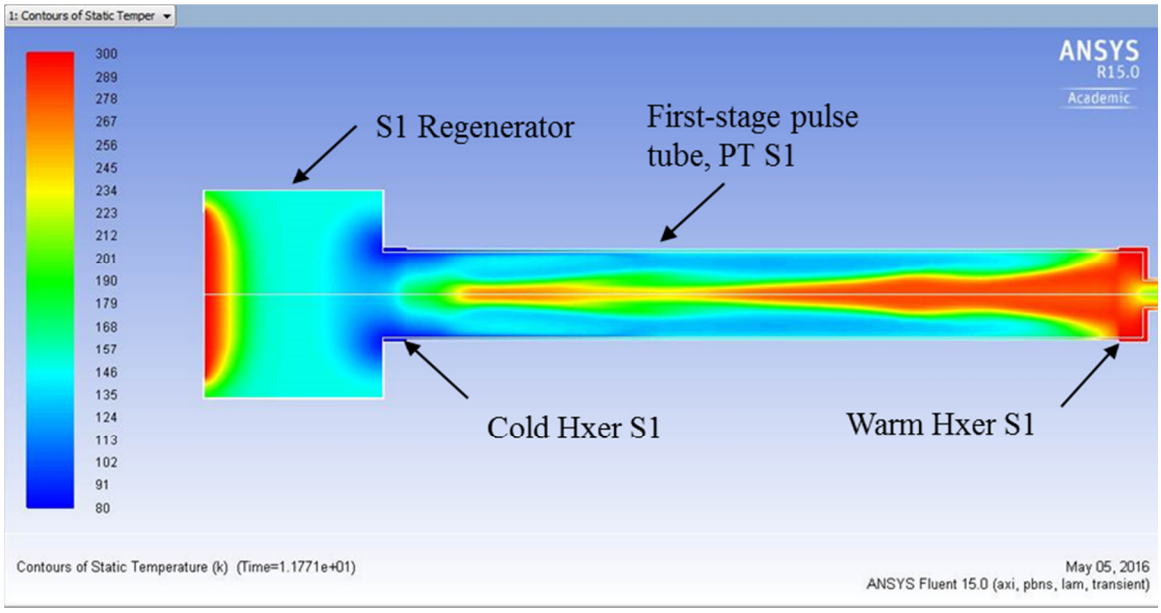

Figure 93. Temperature contours for first stage of 20W at 20K PTC at 11.8 s

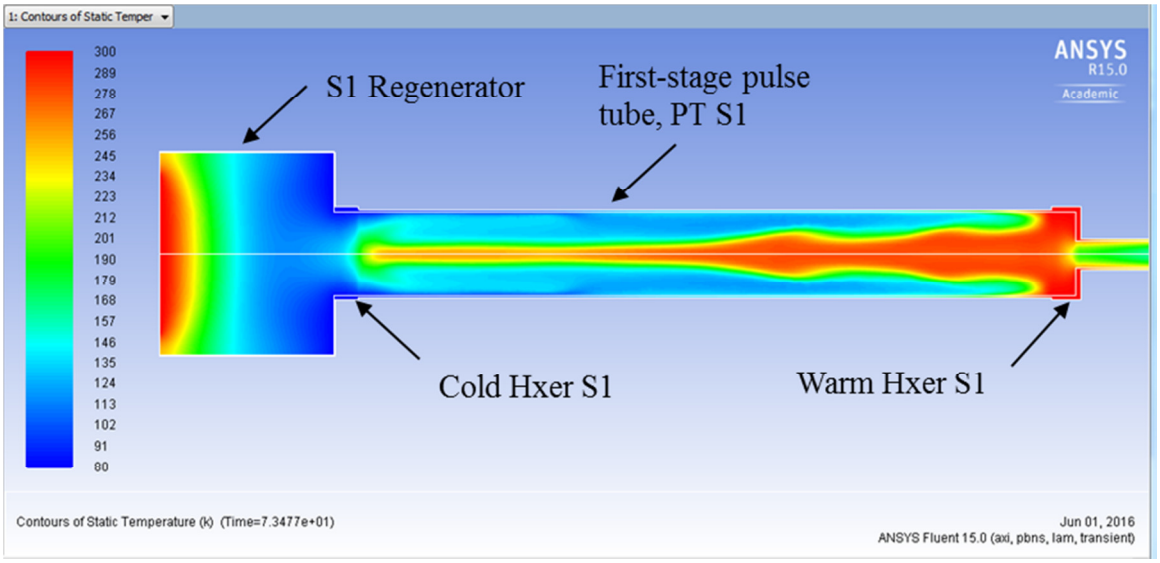

Figure 94. Temperature contours for first stage of 20W at 20K PTC at 73.5 s

5.4.3 Lessons Learned

It is clear from this design process that a 1D model alone, such as the one utilized by the Sage software [4], is not sufficient to accurately predict the realistic performance of a large-capacity cryocooler. Either 2D or 3D CFD tools such as ANSYS Fluent [5,6], or knowledge from prior experiences must be used in the design process to ensure that the physical dimensions of the proposed cryocooler design are practical when considering secondary flow effects. In addition to the streaming observed here, other secondary flow effects such as buoyancy-induced mixing should also be considered whenever the PTC components become especially large. To fulfill the original objective of the separate effects testing, the friction factor correlation developed in Section 5.1.2 given by Eq. (52) was applied to the second stage regenerator by replacing the packed-sphere subcomponent in Sage with the generic matrix option and optimizing the entire system.

A comparison of the results is shown in Table 17. Although the correlation for friction factor within a porous matrix of packed spheres provided in Sage by Gedeon, Eq (26), was shown to be very similar to the correlation developed in Section 5.1.2, the results indicate that even a slight change in the hydrodynamic resistance of the second stage regenerator has a significant effect on the cooling power of the system when not included as part of the original design. This is likely due to the coupled nature of the first and second stages of the PTC. Whenever the flow resistance of a component in one stage of the cooler is adjusted, even slightly, it has a dramatic effect on the proportion of flow that is driven through either stage of the cooler. For future investigations, an alternative to the coupled-compressor design might help to alleviate this issue.

The desired cooling power can be achieved by adjusting the inertance networks of the first and second stages through additional optimization as shown in Table 17. However, the increased cooling power of the second stage is accompanied by an increase in the compressor input power and also requires an adjustment in operating frequency. This is unexpected considering that the results for the Darcy friction factor shown in Section 5.1.2 agreed well with the correlation provided by Gedeon for packed sphere beds [4]. One possible explanation is that while the correlation provided by this work, Eq.(52), and that of Gedeon, Eq.(26), agree well at low Reynolds numbers, they do diverge slightly for values above 10, and the mean Reynolds number within the second-stage regenerator of the simulated Sage model is approximately 30. The divergence is due to the fact that Eq.(52) does not possess a second term to tract the friction factor behavior at higher Reynolds numbers as does Eq.(26). Furthermore, the correlation of Gedeon was developed based on experiments conducted at higher flow rates and with a

larger mean particle diameter than the current study. As with any discipline within fluid dynamics, it is essential to use correlations that are developed based on the expected operating conditions of the system. It appears that the Sage simulation software is especially sensitive to small changes in flow resistance through the regenerators, so special care should be taken to use appropriate correlations for friction factor based on the specifications of the porous media or to develop one's own when no suitable correlations exist.

Table 17. Comparison of packed-sphere and generic matrix second stage regenerator results for 20W at 20K PTC design using friction factor from Eq. (52)

	Packed-sphere S2 Regenerator	**Generic matrix S2 Regenerator**	**Optimized S2 Regenerator**
Cooling Power at 1st Stage	20.30 W	6.66 W	20.00 W
Cooling Power at 2nd Stage	20.01 W	32.06 W	19.99 W
T_c at 1st Stage	20 K	20 K	20 K
T_c at 2nd Stage	80 K	80 K	80 K
Input Power	2625 W	2790 W	4079 W
Charge Pressure	3.61 MPa	3.53 MPa	2.93 MPa
Operating Frequency	30 Hz	30 Hz	10.6 Hz
Piston Stroke Amplitude	6.96 mm	7.07 mm	11.8 mm

CHAPTER 6. CONCLUSIONS AND RECOMMENDATIONS FOR FUTURE WORK

6.1 Summary

The purpose of this work was to examine the effect of temperature on the hydrodynamic resistance parameters of porous media, specifically media for use in advanced cryocooler regenerators, and determine whether the correlations for predicting the aforementioned hydrodynamic resistance parameters that have been developed by past researches at ambient temperatures are also applicable at cryogenic temperatures at which typical cryocooler regenerators operate. Several porous filler materials for use in high-performance cryocooler regenerators including 55μm-diameter $Er_{0.5}Pr_{0.5}$ powder, #400 stainless steel wire mesh, and #325 stainless steel wire mesh were tested with periodic flow of high-purity helium at multiple mean pressures and frequencies for operating temperatures ranging from 50-300K. For each regenerator, the Darcy friction factor, f, was calculated based on the maximum instantaneous pressure drop across the regenerator and correlated as a function of the hydraulic diameter-based Reynolds number, Re_{d_h}. The results showed that for each of the regenerator filler materials under consideration, the dimensionless friction factor was independent of mean operating pressure, frequency, and temperature. The accuracy of the calculated friction factors for each of the regenerators was verified using the cryocooler modeling software, Sage [4]. A complete system-level model was created for each regenerator and its surrounding test section components in order to simulate the steady-periodic flow of the helium working fluid through the regenerator. The results showed excellent agreement between the

experimental and simulation results in terms of both pressure amplitudes on the upstream and downstream sides of the regenerator and the mass flow rate amplitude on the downstream side of the regenerator. Empirical correlations for friction factor were developed for each regenerator based on the least squares method and are applicable for the entire range of mean pressures, frequencies, and temperatures under consideration. The results also show suitable agreement with correlations developed by other authors at ambient temperatures, specifically those of Gedeon [47].

The viscous and inertial components of the pressure drop through each porous medium were determined by comparing the experimental measurements and the Darcy friction factor from the Sage simulations to the governing equations for porous media provided by the CFD software, ANSYS Fluent [5,6]. First, the momentum source term, S_i, which represents the total frictional pressure gradient within the porous zone, was calculated based on the maximum instantaneous pressure drop across the regenerator and the length of the porous zone. The momentum source term was then non-dimensionalized based on the hydraulic diameter of the porous medium and the physical properties of the working fluid, specifically the density and viscosity of the high-purity helium. This non-dimensionalized momentum source term was assigned the arbitrary variable Γ and was correlated as a function of the hydraulic diameter-based Reynolds number. The developed correlations for the non-dimensionalized momentum source term were shown to be independent of charge pressure, frequency, and temperature and displayed a second-order dependence on the hydraulic diameter-based Reynolds number. A trendline was created using the least-squares approach, and the coefficients of the quadratic model were used to calculate the viscous resistance, β, and inertial resistance,

C_2, which are used in ANSYS Fluent to predict the momentum source term and , by extension, and total frictional pressure gradient in the porous medium. Comparison of the momentum equation in Fluent, including the momentum source term, with the Forchheimer-extended Darcy law for flow through a porous medium allowed the Darcy permeability, K, to be calculated from the viscous resistance, β, and the Forchheimer inertial coefficient, c_f, to be calculated from the inertial resistance, C_2, for each of the three regenerator filler materials under consideration.

A closed-system CFD model was constructed to test the validity of the calculated viscous and inertial resistances for the packed sphere and wire mesh regenerators. An oscillating pressure boundary condition was applied at the regenerator inlet, and the porous media were assumed to be isotropic. This was a valid assumption for the $Er_{0.5}Pr_{0.5}$ regenerator given the random packing of the spherical particles. Although packed screen beds are known to have anisotropic hydrodynamic resistance parameters, it is still possible to approximate the medium as isotropic provided that the flow is primarily in the axial direction. For the $Er_{0.5}Pr_{0.5}$ regenerator, the Fluent simulations agreed well with the experimental results for different mean pressures and temperatures in terms of the pressure amplitude on the downstream side of the regenerator. The simulations and experiments agreed less favorably in terms of the mass flow rate amplitude on the downstream side of the regenerator. Given that the Sage simulation was able to match both the pressure and mass flow rate amplitudes on the downstream side of the regenerator, it is believed that the discrepancy between the experimental and simulated mass flow rate amplitudes in Fluent is likely due to the inability of the oscillating pressure boundary condition to adequately couple the upstream pressure with the

appropriate mass flow rate. For better agreement, a moving wall boundary condition at the regenerator inlet should be used.

For the #400SS regenerator, the Fluent simulations agreed well with the experimental results at high pressures and low temperatures in terms of the downstream pressure amplitude, but disagreed for low pressures and high temperatures. Since the mass flow rate through the #400SS regenerator is higher at higher pressures and lower temperatures, it is believed that the assumption of unidirectional flow is less valid for low mass flow rate amplitudes than for high. If radial flow does occur within the regenerator, then the assumption of isotropic hydrodynamic resistance for the #400SS regenerator would have a negative effect on the simulation results. To test this, the radial viscous and inertial resistances for the simulation of the #400SS regenerator were increased until agreement with the experimental results was achieved. Tests at several mean pressures indicated that the radial viscous and inertial resistances are greater than their axial counterparts by a factor of approximately 1.7. Test and simulation results for the #325SS wire mesh regenerator indicated similar hydrodynamic resistance to the #400SS wire mesh regenerator, allowing the friction factor for both wire mesh regenerators to be correlated based on the hydraulic diameter-based Reynolds number.

To demonstrate the importance of the regenerator hydrodynamic resistance on the overall performance of a pulse tube cryocooler, a case study was performed on the design and optimization of a 20W at 20K, two-stage pulse tube cryocooler. First, a 5W at 20K design was developed using industry-standard tools for cryocooler design and optimization including Regen 3.3 and ISOHX from NIST, and Sage cryocooler modeling software. Being the most important component of the cooler, the second stage

regenerator was designed first using Regen 3.3. Based on this analysis, $Er_{0.5}Pr_{0.5}$ rare-earth alloy with a mean particle diameter of 55μm was selected as the porous filler material due to its high heat capacity at cryogenic temperature. The heat exchangers were optimized using ISOHX software from NIST, and the inertance networks for both stages were approximated using analytical methods available in the literature. A complete, system-level model was then created in Sage to further optimize the cooler design utilizing Sage's built-in optimization software. Following an iterative approach, the 5W at 20K design was then modified to produce 20W of cooling at 20K by increasing the compressor input power as well as the size of the various components including the regenerators, heat exchangers, and pulse tubes.

Three-dimensional modeling of the 20W at 20K design revealed that the increased size of the various components and particularly the pulse tubes allowed undesirable secondary flow effects such as streaming to manifest themselves in ways that were not predicted by the one-dimensional Sage simulation. This result illustrated the need to perform 3D CFD analysis in tandem with 1D scoping and optimization simulations to ensure a realistic and workable final design. Finally, the correlation developed for the friction factor of the $Er_{0.5}Pr_{0.5}$ regenerator in this study was applied to the Sage model of the 20W at 20K cryocooler to assess the effect of adjusting the regenerator hydrodynamic resistance. Although the correlations for $Er_{0.5}Pr_{0.5}$ from this study closely matched the correlation for packed-sphere matrices included in the Sage software, the performance of the cooler was significantly different when the new correlation was applied. This demonstrated that even small changes in the hydrodynamic resistance of the cryocooler regenerator can have a significant impact on the overall cooler performance.

6.2 Contributions

The first significant contribution of this work is the development of a system and methodology for accurately measuring the pressure drop and mass flow rate across porous media at cryogenic temperatures. Past investigations of the hydrodynamic resistance parameters of various regenerator filler materials were mostly conducted at ambient temperatures precisely because experimentation at cryogenic temperatures is so difficult. Careful selection of the various temperature and dynamic pressure sensors used in this study was crucial in ensuring the accurate measurement of the porous media flow parameters, and the careful and meticulous construction of the test section and associated apparatus was necessary to eliminate undesirable complications such as gas leakage and heating from the ambient. Rigorous vacuum and baking procedures were also required to eliminate contamination and ensure the purity of the helium working fluid. These techniques ensured the reliable acquisition of cryogenic temperature and pressure measurements to analyze the porous media hydrodynamics at temperatures well below ambient. Application of the methods developed here will allow future testing by the GT Cryolab of additional regenerator filler materials and other crucial cryocooler components at cryogenic temperature.

Most importantly, this work verified the assumption that the hydrodynamic resistance parameters for the porous filler materials of cryocooler regenerators are independent of temperature, and that the correlations developed by past researchers at ambient temperatures are indeed applicable at cryogenic conditions. Repeated analysis of several regenerator filler materials at multiple charge pressures, frequencies, and temperatures showed that when the flow characteristics were properly non-

dimensionalized according to the hydraulic diameter-based Reynolds number, the hydrodynamic resistances of the porous filler materials were independent of charge pressure, frequency, and temperature. Correlations for the Darcy friction factor used in the Sage simulation software were developed for the entire range of experiments and were shown to agree very well with correlations developed by past researchers at ambient temperature conditions, specifically those of Gedeon [4]. The viscous and inertial resistances of the porous media for use in the CFD software ANSYS Fluent [5,6] were also determined for each regenerator filler material across the entire experimental range and found to be independent of temperature. Finally, the values for the viscous and inertial resistance of each material were used to determine the well-known Darcy permeability, K, and Forchheimer inertial coefficient, c_f, commonly found in the literature for predicting the hydrodynamic resistance of generic porous media and were also shown to be independent of temperature.

6.3 Future Work

The most obvious extension of this work would be to expand the methodology outlined here to other regenerator filler materials. Testing proposed regenerator filler materials at cryogenic temperatures adds confidence that the regenerator filler will perform as expected when operating at its actual design point. There are several cutting edge regenerator filler materials that will require additional testing to evaluate their performance in high-capacity and low-temperature cryocoolers. These included mixed-diameter sphere beds, flattened wire mesh screens, and micro-channel tube bundles to name a few. Many of these state-of-the-art filler materials are extensively used in

industry before their hydrodynamic properties and flow characteristics are completely understood, and there is a pressing need to perform thorough pressure drop and flow rate experiments on these materials to aid in the design and optimization of future cutting-edge Stirling and pulse tube cryocoolers. The approach outlined here can be applied to new materials to develop correlations for the Darcy friction factor for use in one-dimensional modeling software such as Sage, and to determine the individual viscous and inertial resistance of the materials for use in multi-dimensional CFD simulations such as ANSYS Fluent. With some modifications and improvements to the experimental test section, it may be possible to perform experiments in the 20K range as well to simulate the operation of low-temperature cryocoolers.

Another area of future interest is the appropriate selection of oscillating boundary conditions in order to accurately recreate the pressure to mass flow rate phase relationship of an actual cryocooler. In the Sage analysis described in Section 4.2, the pressure wave generator was represented by an actual moving piston, which automatically coupled the mass flow rate to the appropriate pressure amplitude. This led to excellent agreement between the experimental and simulation results in terms of both pressure and mass flow rate amplitude. For the CFD results, however, the oscillating pressure boundary condition at the inlet of the regenerator was not sufficient to recreate the appropriate pressure and mass flow rate coupling downstream of the regenerator. Applying a moving wall boundary condition upstream of the regenerator would more accurately represent the actual flow within a cryocooler regenerator that is created by the oscillating piston of a pressure wave generator. Such an approach would couple the

pressure to the mass flow rate at the inlet and should lead to better agreement between experiments and simulations for the downstream flow conditions as well.

More work could also be done in the area of anisotropic hydrodynamic resistance parameters. The work by Cha el al. [1], for example, that investigated anisotropic porous media measured the pressure drop in the radial direction directly to determine the radial viscous and inertial resistance, but assumed isotropic behavior when simulating the axial flow results. Based on the results of this study, however, it is clear that the radial viscous and inertial resistance of the porous medium can affect the pressure and mass flow rate in the axial direction even when the flow is primarily but not completely uni-directional. Additional transient CFD simulation could be performed to determine the amount of radial flow that occurs in a typical regenerator configuration and investigate how geometric features such as step changes in flow area and sharp edges influence these secondary flows. Systematic analysis would be needed to evaluate the magnitude of the hydrodynamic resistance parameters in the radial direction and asses how they differ from the primary or axial hydrodynamic resistance parameters. This would be of particular interest to the industry given the fact that radial flow parameters have significant influence on cryocooler hydrodynamic effects such as jetting and streaming.

APPENDIX A. DATA IMPORT AND FFT

```
% Matthew Perrella
% 8/22/2016
% GT Cryolab

% This code imports raw data from Labview .lvm files, performs a Fast
% Forier Trasform, and computes the pressure amplitudes, phases, outlet
% mass flow rate and pressure maximums

clear all
close all
clc

% ErPr Raw Data

data=lvm_import('E:\Cryolab\NASA Project Documents\Er50Pr50
Experiments\SepEff 09_08_16 300K\30Hz150psig30V.lvm',0);
% data=lvm_import('E:\Cryolab\NASA Project Documents\Er50Pr50
Experiments\SepEff 09_09_16 75K\30Hz150psig30V.lvm',0);
% data=lvm_import('E:\Cryolab\NASA Project Documents\Er50Pr50
Experiments\SepEff 09_22_16 150K\30Hz150psig40V.lvm',0);

% data=lvm_import('E:\Cryolab\NASA Project Documents\Er50Pr50
Experiments\SepEff 05_10_16 300K\40Hz150psig40V.lvm',0);
% data=lvm_import('E:\Cryolab\NASA Project Documents\Er50Pr50
Experiments\SepEff 05_11_16 70K\40Hz150psig40V.lvm',0);
% data=lvm_import('E:\Cryolab\NASA Project Documents\Er50Pr50
Experiments\SepEff 09_22_16 150K\40Hz150psig40V.lvm',0);

% data=lvm_import('E:\Cryolab\NASA Project Documents\Er50Pr50
Experiments\SepEff 05_10_16 300K\50Hz150psig40V.lvm',0);
% data=lvm_import('E:\Cryolab\NASA Project Documents\Er50Pr50
Experiments\SepEff 05_12_16 75K\50Hz150psi40V.lvm',0);
% data=lvm_import('E:\Cryolab\NASA Project Documents\Er50Pr50
Experiments\SepEff 09_22_16 150K\50Hz150psig40V.lvm',0);

% data=lvm_import('E:\Cryolab\NASA Project Documents\Er50Pr50
Experiments\SepEff 10_06_16 300K\30Hz400psig30V.lvm',0);
% data=lvm_import('E:\Cryolab\NASA Project Documents\Er50Pr50
Experiments\SepEff 10_06_16 150K\50Hz400psig40V.lvm',0);
% data=lvm_import('E:\Cryolab\NASA Project Documents\Er50Pr50
Experiments\SepEff 10_12_16 100K\30Hz400psig30V.lvm',0);

% data=lvm_import('E:\Cryolab\NASA Project Documents\Er50Pr50
Experiments\SepEff 03_08_17 50K\30Hz0psig30V.lvm',0);
% data=lvm_import('E:\Cryolab\NASA Project Documents\Er50Pr50
Experiments\SepEff 03_13_17 100K\50Hz0psig25V.lvm',0);
% data=lvm_import('E:\Cryolab\NASA Project Documents\Er50Pr50
Experiments\SepEff 03_13_17 300K\30Hz0psig30V.lvm',0);

% SS400 Raw Data Old
```

```
% data=lvm_import('E:\Cryolab\NASA Project Documents\SS400
Experiments\SepEff 04_04_17 300K\30Hz400psig40V.lvm',0);
% data=lvm_import('E:\Cryolab\NASA Project Documents\SS400
Experiments\SepEff 04_05_17 150K\30Hz400psig40V.lvm',0);
% data=lvm_import('E:\Cryolab\NASA Project Documents\SS400
Experiments\SepEff 04_06_17 90K\30Hz400psig40V.lvm',0);

% data=lvm_import('E:\Cryolab\NASA Project Documents\SS400
Experiments\SepEff 04_19_17 300K\30Hz150psig40V.lvm',0);
% data=lvm_import('E:\Cryolab\NASA Project Documents\SS400
Experiments\SepEff 04_13_17 80K\30Hz150psig40V.lvm',0);

% SS400 Raw Data

% data=lvm_import('E:\Cryolab\NASA Project Documents\SS400
Experiments\SepEff 06_01_17 300K\60Hz400psig30V.lvm',0);
% data=lvm_import('E:\Cryolab\NASA Project Documents\SS400
Experiments\SepEff 06_02_17 150K\70Hz400psig80V.lvm',0);
% data=lvm_import('E:\Cryolab\NASA Project Documents\SS400
Experiments\SepEff 06_13_17 100K\60Hz400psig30V.lvm',0);

% data=lvm_import('E:\Cryolab\NASA Project Documents\SS400
Experiments\SepEff 06_21_17 300K\60Hz150psig30V.lvm',0);
% data=lvm_import('E:\Cryolab\NASA Project Documents\SS400
Experiments\SepEff 06_16_17 90K\60Hz150psig30V.lvm',0);

% data=lvm_import('E:\Cryolab\NASA Project Documents\SS400
Experiments\SepEff 06_26_17 300K\60Hz0psig30V.lvm',0);
% data=lvm_import('E:\Cryolab\NASA Project Documents\SS400
Experiments\SepEff 06_23_17 150K\70Hz0psig40V.lvm',0);
% data=lvm_import('E:\Cryolab\NASA Project Documents\SS400
Experiments\SepEff 06_22_17 50K\60Hz0psig30V.lvm',0);

% SS325 Raw Data

% data=lvm_import('E:\Cryolab\NASA Project Documents\SS325
Experiments\SepEff 07_17_17 100K\60Hz400psig30V.lvm',0);
% data=lvm_import('E:\Cryolab\NASA Project Documents\SS325
Experiments\SepEff 07_18_17 300K\60Hz400psig30V.lvm',0);

% data=lvm_import('E:\Cryolab\NASA Project Documents\SS325
Experiments\SepEff 07_19_17 90K\60Hz150psig40V.lvm',0);
% data=lvm_import('E:\Cryolab\NASA Project Documents\SS325
Experiments\SepEff 07_20_17 300K\60Hz150psig40V.lvm',0);

% data=lvm_import('E:\Cryolab\NASA Project Documents\SS325
Experiments\SepEff 07_22_17 50K\60Hz0psig30V.lvm',0);
% data=lvm_import('E:\Cryolab\NASA Project Documents\SS325
Experiments\SepEff 07_24_17 100K\70Hz0psig40V.lvm',0);
% data=lvm_import('E:\Cryolab\NASA Project Documents\SS325
Experiments\SepEff 07_24_17 300K\60Hz0psig30V.lvm',0);


% Specify 1st Harmonic Frequency
FH=30;
```

```
% Sample Size
SampleSize=51200;
% Sample Frequency
SampleFrequency=25600; % Hz

% nn=9;
% X=data.Segment1.data((51200*nn-51199):(51200*nn),:);

DATA=data.Segment1.data;
[Rows,Colums]=size(DATA);
NumberOfSamples=Rows/SampleSize;
temp=DATA(Rows-SampleSize+1,6);

t=DATA(1:SampleSize,1);
nn=NumberOfSamples;
X=DATA((51200*nn-51199):(51200*nn),:);

chx_up = X(:,2);
chx_dwn = X(:,3);
sv_up = X(:,4);
sv_dwn = X(:,5);

tf = t(end);
dt = t(2) - t(1);
fs = 1/dt;
N = length(t);
df = fs/N;

% Take Fast Fourier Transform
CHX_D_trans=fft(chx_dwn);
SV_U_trans=fft(sv_up);

% Find magnitude
CHX_D_mag = 2/N*abs(CHX_D_trans);
SV_U_mag = 2/N*abs(SV_U_trans);

% Find Phase
CHX_D_phs=unwrap(angle(CHX_D_trans));
SV_U_phs=unwrap(angle(SV_U_trans));

% Define Frequency Vector
freq = 0:df:fs - df;



% Select amplitude and phase of 1st-5th harmonics
CHX_DS_amp1=CHX_D_mag(freq==FH);
CHX_DS_amp2=CHX_D_mag(freq==FH*2);
CHX_DS_amp3=CHX_D_mag(freq==FH*3);
CHX_DS_amp4=CHX_D_mag(freq==FH*4);
CHX_DS_amp5=CHX_D_mag(freq==FH*5);

SV_US_amp1=SV_U_mag(freq==FH);
```

```
SV_US_amp2=SV_U_mag(freq==FH*2);
SV_US_amp3=SV_U_mag(freq==FH*3);
SV_US_amp4=SV_U_mag(freq==FH*4);
SV_US_amp5=SV_U_mag(freq==FH*5);

CHX_DS_phs1=CHX_D_phs(freq==FH);
CHX_DS_phs2=CHX_D_phs(freq==FH*2);
CHX_DS_phs3=CHX_D_phs(freq==FH*3);
CHX_DS_phs4=CHX_D_phs(freq==FH*4);
CHX_DS_phs5=CHX_D_phs(freq==FH*5);

SV_US_phs1=SV_U_phs(freq==FH);
SV_US_phs2=SV_U_phs(freq==FH*2);
SV_US_phs3=SV_U_phs(freq==FH*3);
SV_US_phs4=SV_U_phs(freq==FH*4);
SV_US_phs5=SV_U_phs(freq==FH*5);

% Create models based on 1st, 1st-3rd, and 1st-5th harmonics
chx_dwn_mdl1=CHX_DS_amp1*cos(2*pi*FH.*t+CHX_DS_phs1);
chx_dwn_mdl2=CHX_DS_amp1*cos(2*pi*FH.*t+CHX_DS_phs1)+CHX_DS_amp2*cos(2*
pi*FH*2.*t+CHX_DS_phs2)+CHX_DS_amp3*cos(2*pi*FH*3.*t+CHX_DS_phs3);
chx_dwn_mdl3=CHX_DS_amp1*cos(2*pi*FH.*t+CHX_DS_phs1)+CHX_DS_amp2*cos(2*
pi*FH*2.*t+CHX_DS_phs2)+CHX_DS_amp3*cos(2*pi*FH*3.*t+CHX_DS_phs3)+CHX_D
S_amp4*cos(2*pi*FH*4.*t+CHX_DS_phs4)+CHX_DS_amp5*cos(2*pi*FH*5.*t+CHX_D
S_phs5);

sv_up_mdl1=SV_US_amp1*cos(2*pi*FH.*t+SV_US_phs1);
sv_up_mdl2=SV_US_amp1*cos(2*pi*FH.*t+SV_US_phs1)+SV_US_amp2*cos(2*pi*FH
*2.*t+SV_US_phs2)+SV_US_amp3*cos(2*pi*FH*3.*t+SV_US_phs3);
sv_up_mdl3=SV_US_amp1*cos(2*pi*FH.*t+SV_US_phs1)+SV_US_amp2*cos(2*pi*FH
*2.*t+SV_US_phs2)+SV_US_amp3*cos(2*pi*FH*3.*t+SV_US_phs3)+SV_US_amp4*co
s(2*pi*FH*4.*t+SV_US_phs4)+SV_US_amp5*cos(2*pi*FH*5.*t+SV_US_phs5);

% Determine Regenerator Upstream and Downstream Pressure maxima
P_max_US=max(chx_dwn_mdl3);
P_max_DS=max(sv_up_mdl3);

% Plot in time domain
figure(1)
plot(t,chx_up,'k-.',t, chx_dwn,'k-',t,sv_up,'b--',t,sv_dwn,'b:')
legend('CHX Upstream', 'CHX Downstream/ Regen Upstream','SV Upstream/
Regen Downstream','SV Downstream','Location','SouthOutside')
Y_min=max(chx_up)*-1.25; Y_max=max(chx_up)*1.25;
axis([0 0.05 Y_min Y_max])
xlabel('Time (s)')
ylabel('Pressure (Pa)')

% title('a) 0.23 MPa, 300K, 60Hz, 30V')
title('b) 0.23 MPa, 50K, 60Hz, 30V')
set(1,'units','inches','pos',[7 6 6 3.5]);

% Plot in frequency domain
figure(2)
semilogy(freq, SV_U_mag, 'r', freq, CHX_D_mag, 'b')
legend('SV Up', 'Chx Down')
```

```
set(gca, 'xlim', [0 fs/2])

% Plot models vs data
figure(3)
plot(t,chx_dwn,'k.',t,chx_dwn_mdl1,'r',t,chx_dwn_mdl2,'b',t,chx_dwn_mdl
3,'g','LineWidth',1,'MarkerSize',10)
legend('CHX Downstream Data','CHX Downstream 1st Harmonic','CHX
Downstream 1st-3rd Harmonics','CHX Downstream 1st-5th Harmonics')
xlabel('time (s)')
ylabel('Dynamic Pressure (Pa)')
xlim([0 0.2])

% Find SV Pressure Derivative Numerically using data and model
dP_dt_data=(sv_up(2:length(sv_up))-sv_up(1:length(sv_up)-1))./dt;
dP_dt_mdl1=(sv_up_mdl3(2:length(sv_up_mdl3))-
sv_up_mdl3(1:length(sv_up_mdl3)-1))./dt;
% dP_dt_mdl1=(sv_up_mdl1(2:length(sv_up_mdl1))-
sv_up_mdl1(1:length(sv_up_mdl1)-1))./dt;
t_mass=t(1:length(t)-1);

% Find SV Pressure Derivative analytically
syms sv_up_sym t_sym
%
sv_up_sym=SV_US_amp1*cos(2*pi*FH*t_sym+SV_US_phs1)+SV_US_amp2*cos(2*pi*
FH*2*t_sym+SV_US_phs2)+SV_US_amp3*cos(2*pi*FH*3*t_sym+SV_US_phs3)+SV_US
_amp4*cos(2*pi*FH*4*t_sym+SV_US_phs4)+SV_US_amp5*cos(2*pi*FH*5*t_sym+SV
_US_phs5);
sv_up_sym=SV_US_amp1*cos(2*pi*FH*t_sym+SV_US_phs1);
dP_dt_sym=diff(sv_up_sym,t_sym);
t_sym=t_mass;
dP_dt_anyl=eval(dP_dt_sym);

figure(4)
plot(t_mass,dP_dt_data,'b',t_mass,dP_dt_mdl1,'r',t_mass,dP_dt_anyl,'g')
legend('dP_dt data','dP_dt model','dP_dt analytical')
xlim([0 0.2]);

% Determine mass flow rate
gamma=1.667;
R_He=2077; % Pa m^3/(kg K)
% V=7.24*10^-6; % m^3
% Volume for ErPr
% V=7.5*10^-6; % m^3
% Volume for SS
V=7.42*10^-5; %m^3
T=temp; % K
P_mean=1135538.6; % Pa
nu=R_He*T/P_mean;
rho=1/nu;
m_dot_data=V/(gamma*R_He*T).*dP_dt_data; % kg/s
m_dot_mdl1=V/(gamma*R_He*T).*dP_dt_mdl1; % kg/s
m_dot_anyl=V/(gamma*R_He*T).*dP_dt_anyl; % kg/s

% Perform fft analysis on mass flow rate measurement
% m_dot_trans=fft(m_dot_data);
m_dot_trans=fft(m_dot_anyl);
```

```
m_dot_mag=2/(N-1)*abs(m_dot_trans);
m_dot_phs=unwrap(angle(m_dot_trans));

df2 = fs/(N-1);
freq2 = 0:df2:fs - df2;
figure(5)
semilogy(freq2, m_dot_mag)
set(gca, 'xlim', [0 fs/2])

m_dot_amp1=m_dot_mag(freq==FH);
m_dot_amp2=m_dot_mag(freq==FH*2);
m_dot_amp3=m_dot_mag(freq==FH*3);
m_dot_amp4=m_dot_mag(freq==FH*4);
m_dot_amp5=m_dot_mag(freq==FH*5);

m_dot_phs1=m_dot_phs(freq==FH);
m_dot_phs2=m_dot_phs(freq==FH*2);
m_dot_phs3=m_dot_phs(freq==FH*3);
m_dot_phs4=m_dot_phs(freq==FH*4);
m_dot_phs5=m_dot_phs(freq==FH*5);

m_dot_mdl2=m_dot_amp1*cos(2*pi*FH.*t_mass+m_dot_phs1)+m_dot_amp2*cos(2*
pi*FH*2.*t_mass+m_dot_phs2)+m_dot_amp3*cos(2*pi*FH*3.*t_mass+m_dot_phs3
)+m_dot_amp4*cos(2*pi*FH*4.*t_mass+m_dot_phs4)+m_dot_amp5*cos(2*pi*FH*5
.*t_mass+m_dot_phs5);

figure(6)
plot(t_mass,m_dot_data,'b',t_mass,m_dot_mdl1,'r',t_mass,m_dot_mdl2,'g')
xlim([0 0.2]);
legend('m dot data','m dot mdl','m dot fft')

% m_dot_max=max(m_dot_mdl2);
% m_dot_min=min(m_dot_mdl2);

m_dot_max=max(m_dot_mdl1);
m_dot_min=min(m_dot_mdl1);

% Calculate instantaneous pressure differencial across regenerator
Delta_P_regen_data=chx_dwn(1:length(t)-1)-sv_up(1:length(t)-1);
Delta_P_regen_mdl=chx_dwn_mdl3(1:length(t)-1)-sv_up_mdl3(1:length(t)-
1);
figure(7)
[ax,p1,p2]=plotyy(t_mass,Delta_P_regen_data,t_mass,m_dot_mdl2,'plot','p
lot');
xlabel(ax(1),'Time (s)')
ylabel(ax(1),'Regenerator Pressure Drop (Pa)')
ylabel(ax(2),'Mass Flow Rate (kg/s)')
xlim(ax(1),[0 0.05])
xlim(ax(2),[0 0.05])
grid off

set(p1,'LineStyle','-','Color','b'); set(p2,'LineStyle','-
.','Color','r'), set(ax,{'ycolor'},{'k';'r'});

% title('a) 0.23 MPa, 300K, 60Hz, 30V')
```

```
title('b) 0.23 MPa, 50K, 60Hz, 30V')

set(7,'units','inches','pos',[7 6 6 3.5]);

% Plot Regen pressure drop vs mass flow rate
figure(8)
Upstream=chx_dwn_mdl3(1:length(chx_dwn_mdl3)-1);
Downstream=sv_up_mdl3(1:length(sv_up_mdl3)-1);
combined=[Upstream,Downstream];
% combined=[chx_dwn_mdl3(1:length(chx_dwn_mdl3)-
1),sv_up_mdl3(1:length(sv_up_mdl3)-1)];
plot(t_mass,Upstream,'k-')
hold on
[ax2,p3,p4]=plotyy(t_mass,Downstream,t_mass,m_dot_mdl2,'plot','plot');
set(p3,'LineStyle','--','Color','b'); set(p4,'LineStyle','-
.','Color','r'), set(ax2,{'ycolor'},{'k';'r'});
% hold on
% plot(t_mass,Upstream,'k')
xlabel(ax2(1),'Time (s)')
ylabel(ax2(1),'Pressure (Pa)')
ylabel(ax2(2),'Mass Flow Rate (kg/s)')

title('a) 0.23 MPa, 300K, 60Hz, 30V')
% title('b) 0.23 MPa, 50K, 60Hz, 30V')

legend('Upstream Pressure','Downstream Pressure','Downstream Mass Flow
Rate','Location','SouthOutside')
% legend BOXOFF
xlim(ax2(1),[0 0.05]);
xlim(ax2(2),[0 0.05]);
% ylim(ax2(1),[-1.5E5 1.5E5]);
% ylim(ax2(2),[-9E-3 9E-3]);
grid off
set(8,'units','inches','pos',[7 6 6 3.5]);

% Plot Regen Delta_P vs. m_dot
figure(9)
plot(abs(m_dot_data),abs(Delta_P_regen_data));
figure(10)
plot(abs(m_dot_mdl2),abs(Delta_P_regen_mdl));

% calculate friction factor
L=0.001661; % m
A_cs=pi*0.01905^2/4; % m^2
d_sphere=55*10^-6; % m
epsilon=0.37;
S_x=6*(1-epsilon)*A_cs/d_sphere;
d_H=4*A_cs/S_x;

% rho=1.18621;
v_max=m_dot_max/rho/A_cs;
Delta_P_regen_max=Delta_P_regen_mdl(find(m_dot_mdl2==m_dot_max));
f=Delta_P_regen_max/L*d_H*2/rho/v_max^2

PHI_PM=CHX_DS_phs1-m_dot_phs1; % rad
```

```
T
m_dot_maxDS=m_dot_max;
m_dot_minDS=m_dot_min;
fprintf('m_dot_maxDS=\n%.5E\n\n',m_dot_maxDS)
fprintf('m_dot_minDS=\n%.5E\n\n',m_dot_minDS)
P_max_US
P_max_DS
P_amp1_US=CHX_DS_amp1
P_amp1_DS=SV_US_amp1
m_dot_amp1DS=m_dot_amp1;
fprintf('m_dot_amp1DS=\n%.5E\n\n',m_dot_amp1DS)
Delta_P_max=max(Delta_P_regen_mdl)
```

APPENDIX B. OSCILLATING PRESSURE BC UDF

```
#include "udf.h"

#define freq 30
#define P_amp_1 9.577284811127838e+03
#define P_phi_1 -9.704026936979709
#define P_amp_2 34.595225266925340
#define P_phi_2 -17.300961538486707
#define P_amp_3 4.060997140398168e+02
#define P_phi_3 -6.176557286482854
#define P_amp_4 59.650339352164080
#define P_phi_4 -11.462327177754650
#define P_amp_5 2.335525306839417e+02
#define P_phi_5 -23.451913927361257

#define P2_amp_1 9.250638120601740e+03
#define P2_phi_1 -9.854570906133090
#define P2_amp_2 1.923109502444599e+02
#define P2_phi_2 -7.691284200308830
#define P2_amp_3 3.505535057983406e+02
#define P2_phi_3 -6.681451991228741
#define P2_amp_4 1.427694654970456e+02
#define P2_phi_4 1.441421009811057
#define P2_amp_5 2.401800894973338e+02
#define P2_phi_5 -23.956829692681605

DEFINE_PROFILE(unst_p_inlet, thread, position)
{
 face_t f;
 real t = CURRENT_TIME;
  real omega  = 2*M_PI*freq;
 begin_f_loop(f, thread)
  {
  F_PROFILE(f, thread, position) =
(P_amp_1*cos(1*omega*t+P_phi_1)+P_amp_2*cos(2*omega*t+P_phi_2)+P_amp_3*cos(3*omega*t+P_
phi_3)+P_amp_4*cos(4*omega*t+P_phi_4)+P_amp_5*cos(5*omega*t+P_phi_5));
  }
 end_f_loop(f,thread)
}

DEFINE_PROFILE(unst_p_outlet, thread, position)
{
 face_t f;
 real t = CURRENT_TIME;
  real omega  = 2*M_PI*freq;
 begin_f_loop(f, thread)
  {
  F_PROFILE(f, thread, position) =
(P2_amp_1*cos(1*omega*t+P2_phi_1)+P2_amp_2*cos(2*omega*t+P2_phi_2)+P2_amp_3*cos(3*omega
*t+P2_phi_3)+P2_amp_4*cos(4*omega*t+P2_phi_4)+P2_amp_5*cos(5*omega*t+P2_phi_5));
  }
 end_f_loop(f,thread)
}
```

APPENDIX C. MOVING WALL BC UDF

```
#include "udf.h"

DEFINE_CG_MOTION(inlet_motion, dt, vel, omega, time, dtime)
{
  real freq=60;
  real w=2.0*M_PI*freq;
  real Xcomp=0.0001;

  /* reset velocities */
  NV_S (vel, =, 0.0);
  NV_S (omega, =, 0.0);

  vel[0] = w*Xcomp*cos(w*time);
}


DEFINE_CG_MOTION(outlet_motion, dt, vel, omega, time, dtime)
{
  real freq = 60;
  real w = 2.0*M_PI*freq;
  real Xcomp=0.0001;

  /* reset velocities */
  NV_S (vel, =, 0.0);
  NV_S (omega, =, 0.0);

  vel[0] = w*Xcomp*cos(w*time);
}
```

REFERENCES

[1] Cha, J. J., 2007, "Hydrodynamic Parameters of Micro Porous Media for Steady and Oscillatory Flow : Application To Cryocooler Regenerators," Ph.D. thesis, Mechancial Engineering, Georgia Institute of Technology.

[2] Conrad, T. J., 2011, "Miniaturized Pulse Tube Refrigerators," Ph.D. thesis, Mechancial Engineering, Georgia Institute of Technology.

[3] Mulcahey, T. I., 2014, "Convective Instability of Oscillatory Flow in Pulse Tube Cryocoolers Due to Asymmetric Gravitational Body Force," Ph.D. thesis, Mechancial Engineering, Georgia Institute of Technology.

[4] Gedeon, D., 2016, Sage User's Guide, Gedeon Associates, Athens, OH.

[5] ANSYS, 2016, ANSYS Fluent User's Guide, ANSYS, Inc., USA, Canonsburg, PA.

[6] ANSYS, 2016, Ansys Fluent Theory Guide, ANSYS, Inc., USA, Canonsburg, PA.

[7] Radebaugh, R., 2008, "Foundations of Cryocoolers," Cryogenic Technologies Group, National Institute of Standards and Technology, Boulder, CO.

[8] Radebaugh, R., 2000, "Development of the Pulse Tube Refrigerator as an Efficient and Reliable Cryocooler," Inst. Refrig., p. 1999.

[9] Organ, A. J., 1992, Thermodynamics and gas dynamics of the Stirling cycle

machine, Cambridge University Press.

[10] Radebaugh, R., 2000, “Pulse tube cryocoolers for cooling infrared sensors,” Proc. SPIE, **4130**, pp. 363–379.

[11] KIRK, A. C., 1874, “ON THE MECHANICAL PRODUCTION OF COLD. (INCLUDES PLATES AND APPENDIX).,” Minutes Proc. Inst. Civ. Eng., **37**(1874), pp. 244–282.

[12] Köhler, J. W. L., and Jonkers, C. O., 1954, “Fundamentals of the gas refrigeration machine,” Philips Tech. Rev, **16**(3), pp. 69–78.

[13] Gifford, W. E., and Longsworth, R. C., 1964, “Pulse-Tube Refrigeration.”

[14] Longsworth, R. C., 1967, “An Experimental Investigation of Pulse Tube Refrigeration Heat Pumping Rates,” Advances in Cryogenic Engineering: Proceedings of the 1966 Cryogenic Engineering Conference University of Colorado Engineering Research Center and Cryogenics Division NBS Institute for Materials Research Boulder, Colorado June 13--15, 1966, K.D. Timmerhaus, ed., Springer US, Boston, MA, pp. 608–618.

[15] Mikulin, E. I., Tarasov, A. A., and Shkrebyonock, M. P., 1984, “Low-Temperature Expansion Pulse Tubes,” Advances in Cryogenic Engineering: Volume 29, R.W. Fast, ed., Springer US, Boston, MA, pp. 629–637.

[16] Radebaugh, R., Zimmerman, J., Smith, D. R., and Louie, B., 1986, “A Comparison of Three Types of Pulse Tube Refrigerators: New Methods for

Reaching 60K," Advances in Cryogenic Engineering: Volume 31, R.W. Fast, ed., Springer US, Boston, MA, pp. 779–789.

[17] Godshalk, K. M., Jin, C., Kwong, Y. K., Hershberg, E. L., Swift, G. W., and Radebaugh, R., 1996, "Characterization of 350 Hz Thermoacoustic Driven Orifice Pulse Tube Refrigerator with Measurements of the Phase of the Mass Flow and Pressure," Advances in Cryogenic Engineering: Part A, P. Kittel, ed., Springer US, Boston, MA, pp. 1411–1418.

[18] Zhu, S. W., Zhou, S. L., Yoshimura, N., and Matsubara, Y., 1997, "Phase Shift Effect of the Long Neck Tube for the Pulse Tube Refrigerator," Cryocoolers 9, R.G. Ross, ed., Springer US, Boston, MA, pp. 269–278.

[19] Olson, J. R., and Swift, G. W., 1997, "Acoustic streaming in pulse tube refrigerators: tapered pulse tubes," Cryogenics (Guildf)., **37**(12), pp. 769–776.

[20] Roach, P. R., and Kashani, A., 1998, "Pulse Tube Coolers with an Inertance Tube: Theory, Modeling, and Practice," Advances in Cryogenic Engineering, P. Kittel, ed., Springer US, Boston, MA, pp. 1895–1902.

[21] Conrad, T. J., Ghiaasiaan, S. M., and Kirkconnell, C. S., "Simulation of Boundary Layer Effects in the Pulse Tube of a Miniature Cryocooler," pp. 267–274.

[22] Ochoa-Tapia, J. A., and Whitaker, S., 1995, "Momentum transfer at the boundary between a porous medium and a homogeneous fluid-I. Theoretical development," Int. J. Heat Mass Transf., **38**(14), pp. 2635–2646.

[23] Ochoa-Tapia, J. A., and Whitaker, S., 1997, "Heat transfer at the boundary between a porous medium and a homogeneous fluid," Int. J. Heat Mass Transf., **40**(11), pp. 2691–2707.

[24] Ochoa-Tapia, J. A., and Whitaker, S., 1995, "Momentum transfer at the boundary between a porous medium and a homogeneous fluid—II. Comparison with experiment," Int. J. Heat Mass Transf., **38**(14), pp. 2647–2655.

[25] Whitaker, S., 1999, The method of Volume Averaging. Theory and Applications of Transport in Porous Media, Kluwer Academic Publishers.

[26] Whitaker, S., 1996, "The Forchheimer equation: A theoretical development," Transp. Porous Media, **25**(1), pp. 27–61.

[27] Vafai, K., and Tien, C. L., 1981, "Boundary and inertia effects on flow and heat transfer in porous media," Int. J. Heat Mass Transf., **24**(2), pp. 195–203.

[28] Gary, J., Gallagher, A. O., Radebaugh, R., Huang, Y., and Marquardt, E., 2008, REGEN3 . 3 : USER MANUAL, National Institute of Science and Technology, Boulder, CO.

[29] Kim, S.-M., and Ghiaasiaan, S. M., 2009, "Numerical Modeling of Laminar Pulsating Flow in Porous Media," J. Fluids Eng., **131**(4), p. 41203.

[30] Nakayama, a., Kuwahara, F., Umemoto, T., and Hayashi, T., 2002, "Heat and Fluid Flow Within an Anisotropic Porous Medium," J. Heat Transfer, **124**(4), p. 746.

[31] Nakayama, a, and Kuwahara, F., 2014, "A macroscopic Turbulence Model for Flow in a Porous Medium," **121**(June 1999), pp. 427–433.

[32] Fumoto, Y., 2012, "A Three-Dimensional Numerical Model for Determining the Pressure Drops in Porous Media Consisting of Obstacles of Different Sizes," Open Transp. Phenom. J., **4**(1), pp. 1–8.

[33] Palle, S., and Aliabadi, S., 2013, "Direct simulation of structured wall bounded packed beds using hybrid FE/FV methods," Comput. Fluids, **88**, pp. 730–742.

[34] Pathak, M. G., and Ghiaasiaan, S. M., 2011, "Convective heat transfer and thermal dispersion during laminar pulsating flow in porous media," Int. J. Therm. Sci., **50**(4), pp. 440–448.

[35] Pathak, M. G., Mulcahey, T. I., and Ghiaasiaan, S. M., 2013, "Conjugate heat transfer during oscillatory laminar flow in porous media," Int. J. Heat Mass Transf., **66**, pp. 23–30.

[36] Kuwahara, F., Nakayama, a., and Koyama, H., 1996, "A Numerical Study of Thermal Dispersion in Porous Media," J. Heat Transfer, **118**(3), p. 756.

[37] Harvey, J. P., 2003, "Oscillatory Compressible Flow and Heat Transfer in Porous Media – Application To Cryocooler Regenerators," Ph.D. thesis, Mechancial Engineering, Georgia Institute of Technology.

[38] Cha, J. S., Ghiaasiaan, S. M., and Kirkconnell, C. S., 2008, "Oscillatory flow in microporous media applied in pulse - tube and Stirling - cycle cryocooler

regenerators," Exp. Therm. Fluid Sci., **32**(6), pp. 1264–1278.

[39] Clearman, W. M., Cha, J. S., Ghiaasiaan, S. M., and Kirkconnell, C. S., 2008, "Anisotropic steady-flow hydrodynamic parameters of microporous media applied to pulse tube and Stirling cryocooler regenerators," Cryogenics (Guildf)., **48**(3–4), pp. 112–121.

[40] Landrum, E. C., Conrad, T. J., Ghiaasiaan, S. M., and Kirkconnell, C. S., 2010, "Hydrodynamic parameters of mesh fillers relevant to miniature regenerative cryocoolers," Cryogenics (Guildf)., **50**(6–7), pp. 373–380.

[41] Pathak, M. G., Ghiaasiaan, S. M., Radebaugh, R., Kashani, A., Feller, J., and Field, M., 2012, "The Design and Development of a High-Capacity Cryocooler Regenerator for Space Exploration," (September), pp. 1–8.

[42] Mulcahey, T. I., Conrad, T. J., Ghiaasiaan, S. M., and Pathak, M. G., 2014, "Investigation of gravitational effects in pulse tube cryocoolers using 3-D CFD," **1002**, pp. 1002–1009.

[43] Pathak, M. G., 2013, "Periodic Flow Physics in Porous Media of Regenerative Cryocoolers," Ph.D. thesis, Mechancial Engineering, Georgia Institute of Technology.

[44] Pathak, M. G., Patel, V. C., Ghiaasiaan, S. M., Mulcahey, T. I., Helvensteijn, B. P., Kashani, a., and Feller, J. R., 2013, "Hydrodynamic parameters for ErPr cryocooler regenerator fillers under steady and periodic flow conditions," Cryogenics (Guildf)., **58**, pp. 68–77.

[45] Piezotronics, P. C. B., “Model 102A14 Cryogenic ICP ® pressure sensor , 5000 psi , 1 mV / psi , 3 / 8-24 mtg thd , Installation and Operating Manual.”

[46] Cabannes, J. A. H., Keller, M. H. H. B., and Rusanov, J. K. S. A. O. V. V, 1985, “Springer Series in Computational Physics.”

[47] Gedeon, D., and Wood, J. G., 1996, “Oscillating-Flow Regenerator Test Rig: Hardware and Theory With Derived Correlations for Screens and Felts,” NASA-Lewis Contract. Rep. 198422, (February).

[48] Pathak, M. G., Helvensteijn, B. P., Patel, V. C., Ghiaasiaan, S. M., Mulcahey, T. I., Kashani, A., and Feller, J. R., “Hydrodynamic Resistance Parameters for ErPr Rare-Earth Regenerator Material under Steady and Periodic Flow Conditions.”

[49] MacDonald, M. J., Chu, C. ???F, Guilloit, P. P., and Ng, K. M., 1991, “A generalized Blake-Kozeny equation for multisized spherical particles,” AIChE J., **37**(10), pp. 1583–1588.

[50] Calis, H. P. A., Nijenhuis, J., Paikert, B. C., Dautzenberg, F. M., and Bleek, C. M. Van Den, 2001, “CFD modelling and experimental validation of pressure drop and # ow pro " le in a novel structured catalytic reactor packing,” Chem. Eng. Sci., **56**, pp. 1713–1720.

[51] Cha, J. S., Ghiaasiaan, S. M., Desai, P. V., Harvey, J. P., and Kirkconnell, C. S., 2006, “Multi-dimensional flow effects in pulse tube refrigerators,” Cryogenics (Guildf)., **46**(9), pp. 658–665.